AN ABSTRACT OF THE THESIS OF

Christopher Northrup Kennard Mooers for the Doctor of Philosophy
(Name) (Degree)

in OCEANOGRAPHY presented on 5 June 1969
(Major) (Date)

Title: THE INTERACTION OF AN INTERNAL TIDE WITH THE FRONTAL ZONE IN A COASTAL UPWELLING REGION

Redacted for privacy

Abstract Approved:
Robert Lloyd Smith

The question of how an internal tide interacts with the frontal zone in a coastal upwelling region is examined theoretically and is studied with field observations. A linear, self-adjoint governing equation is derived for inertial-internal waves propagating transverse to a frontal region. The effects of horizontal density gradients and horizontal and vertical shears of the mean alongshore flow are included, as well as the customary effects of vertical density gradients and of the Earth's rotation. The frontal interaction affects the lines of constant phase and the passband for inertial-internal waves.

The temporal conservation of energy law, the variational principle, and the spatial conservation law are derived for the case of variable bottom topography, a free surface, and with frontal interaction. These results are used to set the mixed initial-boundary value problem for inertial-internal waves in a coastal region.

The method of characteristics is used to solve the mixed initial-boundary value problem for the inertial-internal wave equation with constant coefficients. The solution technique developed involves the use of the boundary conditions to analytically extend the given Cauchy data. Cases are considered with and without the frontal interaction and for waves propagating in regions with parallel boundaries and with a wedge-shape. The slope of the isopycnals affects the slope of the characteristics. A significant asymmetry in the upgoing and downgoing characteristics is introduced when the slope of the isopycnals is in the same order of magnitude as the slope that the characteristics would have without the frontal interaction. An extension of the method of characteristics is used to solve the mixed initial-boundary value problem formally when the inertial-internal wave equation has variable coefficients. Two frontal models are examined which produce analytical coefficients in the governing equation.

A technique is developed for the spectrum analysis of pairs of complex-valued velocity series (hodographs) sampled at different spatial points. It separates the spectra into clockwise and anticlockwise rotating components and allows the calculation of the coherence squared and phase of each component. The coherence squared is invariant under coordinate rotation.

Through the use of a moored array of recording sensors, and of hydrographic samples, field observations were conducted during

August-September 1966 over the Oregon continental shelf at 45° N. The array had ten-kilometer horizontal spacings between three array sites. The array sites extended seaward from 10 kilometers offshore. At each site, two sets of sensors were separated vertically by 40 meters.

Evidence is presented to show that

i) The mean flow, computed for a two-week period, was equatorward and onshore immediately above the permanent frontal layer and poleward and onshore at the base of the permanent frontal layer.

ii) The observed vertical shear in the mean alongshore flow agreed with that given by the thermal wind equation; i. e., the baroclinic component of the mean alongshore flow in the subsurface frontal region was in approximate geostrophic equilibrium.

iii) The dynamic stability was lowest near the base of the permanent frontal layer. The Richardson number attained critically low values, which were associated with the semidiurnal internal tide.

On the basis of this and other evidence, a schematic model is proposed for the mean cross-stream flow in the frontal zone.

The statistical evidence from the moored, recording sensors indicates that:

i) The semidiurnal internal tide had a vertical amplitude of about five meters and a horizontal speed of about 5 cm/sec. This motion propagated onshore as a progressive wave and had an onshore-offshore wavelength of about 30 kilometers in the vicinity of the array; its coherency over a wavelength was generally low, suggesting the occurrence of many wave frequencies not in phase within a measurement bandwidth, unsteadiness of the wave motion, phase modulation by the time-varying flow regime, or unsteady wave generation.

ii) The largest inertial velocity component, with an amplitude of about 3 cm/sec, was found at the boundary between the continental shelf and slope. A substantial fraction of the inertial motion was temporally coherent for 36 days at that site.

iii) Spectral peaks were present at higher harmonics of the tidal motions, especially at the three and four cycles per day frequencies. Spatially coherent tidal harmonics existed, suggesting the occurrence of nonlinear effects.

The Interaction of an Internal Tide with the Frontal Zone of a Coastal Upwelling Region

by

Christopher Northrup Kennard Mooers

A THESIS

submitted to

Oregon State University

in partial fulfillment of
the requirements for the
degree of

Doctor of Philosophy

June 1970

APPROVED:

Redacted for privacy

Assistant Professor of Oceanography

in charge of major

Redacted for privacy

Chairman of the Department of Oceanography

Redacted for privacy

Dean of Graduate School

Date thesis is presented 5 June 1969

Typed by Clover Redfern for Christopher Northrup Kennard Mooers

Figures drafted by William E. Gilbert

ACKNOWLEDGMENT

I am grateful to the National Science Foundation for three years of graduate fellowship support and one year of assistantship support, under NSF Grant GA1435, which have allowed the completion of my transition from a military career to a scientific profession. ONR Contract Nonr1286(10) has provided support for the final eight months of the dissertation preparation. NSF Grants GP4472, GA331, and GA1435 provided support for the OSU Coastal Oceanography project, a portion of which is represented by the observational and statistical effort of this study.

The computer facilities of Western Data Processing Center, University of California at Los Angeles, were used extensively for a first examination of the energy spectra. The subsequent calculations were performed at the Computer Center, Oregon State University.

The patience, challenge, and wisdom offered by Drs. Robert L. Smith, June G. Pattullo, and Michael S. Longuet-Higgins in supporting and moderating this work are gratefully acknowledged. The cooperation and assistance of the numerous staff members and students associated with the coastal oceanography project over the past four years are deeply appreciated. In particular, the dedicated assistance of Miss Lillie M. Muller in completing the computer calculations is thoroughly appreciated. The penetrating review given a draft

of this dissertation by Dr. G. Stephen Pond was very helpful.

The benefits of a solitary sojourn in Walsh Cottage (my "Walden"), Woods Hole Oceanographic Institution, Woods Hole, Massachusetts, where this dissertation was essentially prepared over a period of two-and-one-half months, are gratefully acknowledged.

An interpretation of a dissertation draft by Dr. David S. Burch, Department of Physics, Oregon State University, prompted a thorough discussion of the physics of the oceanographic problem.

Three members, in particular, of Oregon State University's Department of Mathematics, while not responsible for the mathematical work in the thesis, played a key role in developing my mathematical literacy: Dr. Philip M. Anselone, for introducing me to the theory of partial differential equations; Dr. Arvid T. Lonseth, for broadening my interests in mathematical analysis as applied to physics; and Dr. Ronald B. Guenther, for further exposure to the theory of partial differential equations and for serving as an effective "sounding board" for my intuitive development.

Tolerance is a two-way street (Buena Ambiguedad, 1698).

TABLE OF CONTENTS

Chapter Page

LIST OF FIGURES

LIST OF TABLES

LIST OF ABBREVIATIONS

AGE - the adjoint governing equation

BC - a boundary condition

CD - the Cauchy data

CGE - the canonical governing equation

CIVP - a characteristic initial value problem

COM - the reduced conservation of mass equation

CP - a Cauchy problem

CR - the characteristic relation

EE - the energy equation

EOC - the equation of continuity

EOM - the equation of motion

FBC - the free boundary condition

GE - the governing equation

LBC - the lossy boundary condition

LHS - lefthand side of an equation

MIBVP - mixed initial-boundary value problem

RBC - the rigid boundary condition

RHS - righthand side of an equation

SGE - the symmetric governing equation

SHM - simple harmonic motion

SOV - separation of variables

VE - the vorticity equation

WLOG - without loss of generality

LIST OF SYMBOLS

Explanatory notes:

i) All symbols are defined as they are introduced,

ii) Of necessity, there is some use of symbols for more than one quantity,

and

iii) The below list includes the most frequently used symbols.

a - depth scale of density variation

b - eastward scale of density variation

$\vec{c}_g$ - group velocity

c_h - horizontal phase speed

$\vec{c}_p$ - phase velocity

f - the cyclic frequency in cycles/second, unless otherwise specified

$\vec{f}$ - Coriolis parameter, f_h and f_v are its horizontal and vertical components, respectively

g - gravitational acceleration

i - $(-1)^{1/2}$

k - eastward wave number

ℓ - northward wave number

m - upward wave number

p - the fluid pressure

r - slope of an isotach in x, z plane

s - slope of an isopycnal in x, z plane

t - time

u - eastward component of velocity

v - northward component of velocity

w - upward component of velocity

x - eastward spatial coordinate

y - northward spatial coordinate

z - upward spatial coordinate

$z_B(x)$ - vertical coordinate of the sea bottom

C - the initial line (x=0)

CE - the extended initial line

D - the domain of interest

E - the static stability

E - the total energy (E = KE+ PE) per unit volume

$F^{(x)}$ - the x-directed horizontal energy flux in a vertical water column

F - one element of the Cauchy data

G - the other element of the Cauchy data

H - the water depth

I_D - the downgoing Riemann invariant

I_U - the upgoing Riemann invariant

J - the action integral

KE - the kinetic energy per unit volume

L - the horizontal coordinate of the coastline measured from the seaward edge of the continental shelf ($x = 0$)

L( ) - linear operator corresponding to the GE

M ( ) - linear operator corresponding to the AGE

M - the horizontal analogue of N

N - the Väisälä-Brunt frequency ($N^2 = E$)

PE - the potential energy per unit volume

PE_s - the total potential energy of the sea surface,

$$PE_s = \int_{x=0}^{L} V_s \, dx$$

$P_{xx}(\sigma)$ - autospectrum of x

$\tilde{P}_{xy}(\sigma)$ - cross spectrum of x and y

$P_{xy}(\sigma)$ - cospectrum of x and y

$Q_{xy}(\sigma)$ - quadrature spectrum of x and y

$R_{xx}(\tau)$ - autovariance function of x

$R_{xy}(\tau)$ - covariance frunction of x and y

R - a sub-domain of D

Rf - the flux Richardson number

Ri - the gradient Richardson number, i.e., the dynamic stability

T - the wave period

$\vec{U}$ - the total three-dimensional velocity vector

V_S - the potential energy of the sea surface per unit x-distance

$\overline{W}$ - the Riemann-Green function

W - the complex-valued horizontal velocity, $W = u + iv$

α - a characteristic, $\alpha = \eta - \zeta$

β - a characteristic, $\beta = \eta + \zeta$

ϵ - eccentricity of a hodograph

ζ - vertical particle displacement

η - vertical displacement of the sea surface

ζ - downgoing characteristic

η - upgoing characteristic

θ - a phase angle

λ - absolute value of the slope of the characteristics in a symmetric case

λ_1 - slope of the upgoing characteristic in an asymmetric case

λ_2 - slope of the downgoing characteristic in an asymmetrical case

$\lambda^{(h)}$ - horizontal wavelength

ξ - horizontal particle displacement

μ - dynamic molecular viscosity

ν - kinematic molecular viscosity ($\nu = \frac{\mu}{\rho_o}$)

π - the pressure variable with the Boussinesq approximation ($\pi = \frac{p}{\rho_o}$)

ρ - the mass density

σ - the angular frequency in radians/sec

σ_t - sigma-t, the density anomaly

τ - lag time

ϕ - a phase angle

χ - quantity which tends to be conserved as a function of x,

$$\chi(x) = \int_{z_B(x)}^{\eta(x)} (L_H(x) - L_V(x))dz$$

ψ - the stream function

$\vec{\omega}$ - the vorticity

Γ - the boundary of R

Λ_H - the horizontal Lagrangian per unit volume

Λ_V - the vertical Lagrangian per unit volume

Λ - the total Lagrangian per unit volume, $\Lambda = \Lambda_H + \Lambda_V$

$\overline{\Lambda}_o$ - The Lagrangian for a water column,

$$\overline{\Lambda_o(x)} = \int \Lambda(x, z)dz - V_s(x)$$

$(\tilde{})$ - complex-valued quantity

$()^*$ - complex conjugation operation

FRONTISPIECE

"Three phenomena are basic factors in the hydrodynamics of the geophysical fluids:

(1) their stratification,

(2) the curvature of the level surfaces,

(3) the rotation of the Earth (or planet).

It requires little observational material to establish the existence of these three factors, but their dynamic interaction in the fluid is so complex that even large amounts of observational material are of little help in understanding the situation. A theoretical analysis appears to be the only way to clarify it" (Eckart, 1960, p. 94-95).

"Oceanography is an observational science" (Cox, 1968).

"I should like to make it clear, finally, that I am not belittling the survey type of oceanography, nor even purely theoretical speculation. I am pleading that more attention be given to a difficult middle ground: the testing of hypotheses. I have not explored this middle ground very thoroughly, and the few examples given in this book may not even be the important ones; but perhaps they are illustrative of the point of view in which attention is directed not toward a purely descriptive art, nor toward analytical refinements of idealized oceans, but toward an understanding of the physical processes which control the hydrodynamics of oceanic circulation. Too much of the theory of oceanography has depended upon purely hypothetical physical processes. Many of the hypotheses suggested have a peculiar dreamlike quality, and it behooves us to submit them to especial scrutiny and to test them by observation" (Stommel, 1965, p. 178).

THE INTERACTION OF AN INTERNAL TIDE WITH THE FRONTAL ZONE IN A COASTAL UPWELLING REGION

I. INTRODUCTION

A. General

The thesis of this dissertation is that the semidiurnal internal tide interacts with the mean flow of the frontal zone in a coastal upwelling region to produce critically low dynamic stability for the mean flow and to modify the internal tide as well.[1] The basis for this thesis was the observation in September 1965 (Collins, Mooers, Stevenson, Smith, and Pattullo, 1968) that the semidiurnal tide was strongly baroclinic over Oregon's continental shelf in the presence of coastal upwelling. The thesis is investigated by two paths of inquiry: the development of a hydrodynamical theory for the interaction, and the examination of observational evidence relevant to the interaction. For these inquiries it is necessary to have an understanding of

i) The mean flow in the frontal zone of a coastal upwelling region.

ii) The tidal and other long wave motions in a density stratified ocean near a coastal barrier on a rotating sphere.

---

[1] The heuristic notion that an internal tide influences coastal upwelling was originally advanced by Defant (1949) from observations off northwest Africa.

iii) The physics of inertial-internal waves.[2]

iv) The mathematics of the solution theory for inertial-internal waves in a wedge-shaped region with variable density stratification.

v) The spectral properties of the existent time-dependent motions.

B. The Frontal Zone in a Coastal Upwelling Region

Off the west coast of North America, as off the west coast of most continents, the predominant, mesoscale physical process at low and mid-latitudes is that of coastal upwelling[3] in the hemispheric summer. Because of the Earth's rotation, equatorward winds produce both equatorward and offshore flow in the "surface layer." In addition, there is at least occasionally observed a poleward flow in the "lower layer" over the continental shelf and slope (Collins et al., 1968 and Chapter X).

Figure 1 is a schematic portrayal of the mean flow field for the

---

[2]The term inertial-internal wave refers to the class of body waves that can exist in a fluid which is influenced by both the Earth's rotation (inertial) and the Ocean's density stratification (internal). The semidiurnal internal, or baroclinic, tide is one specific wave in this class for Oregon's latitude and coastal density field; it is the most significant inertial-internal wave in this study.

[3]Coastal upwelling is a process by which water from a depth of up to several hundred meters offshore is introduced into the upper few meters of the water column near shore; the process is thought to be generally, but not exclusively, wind induced.

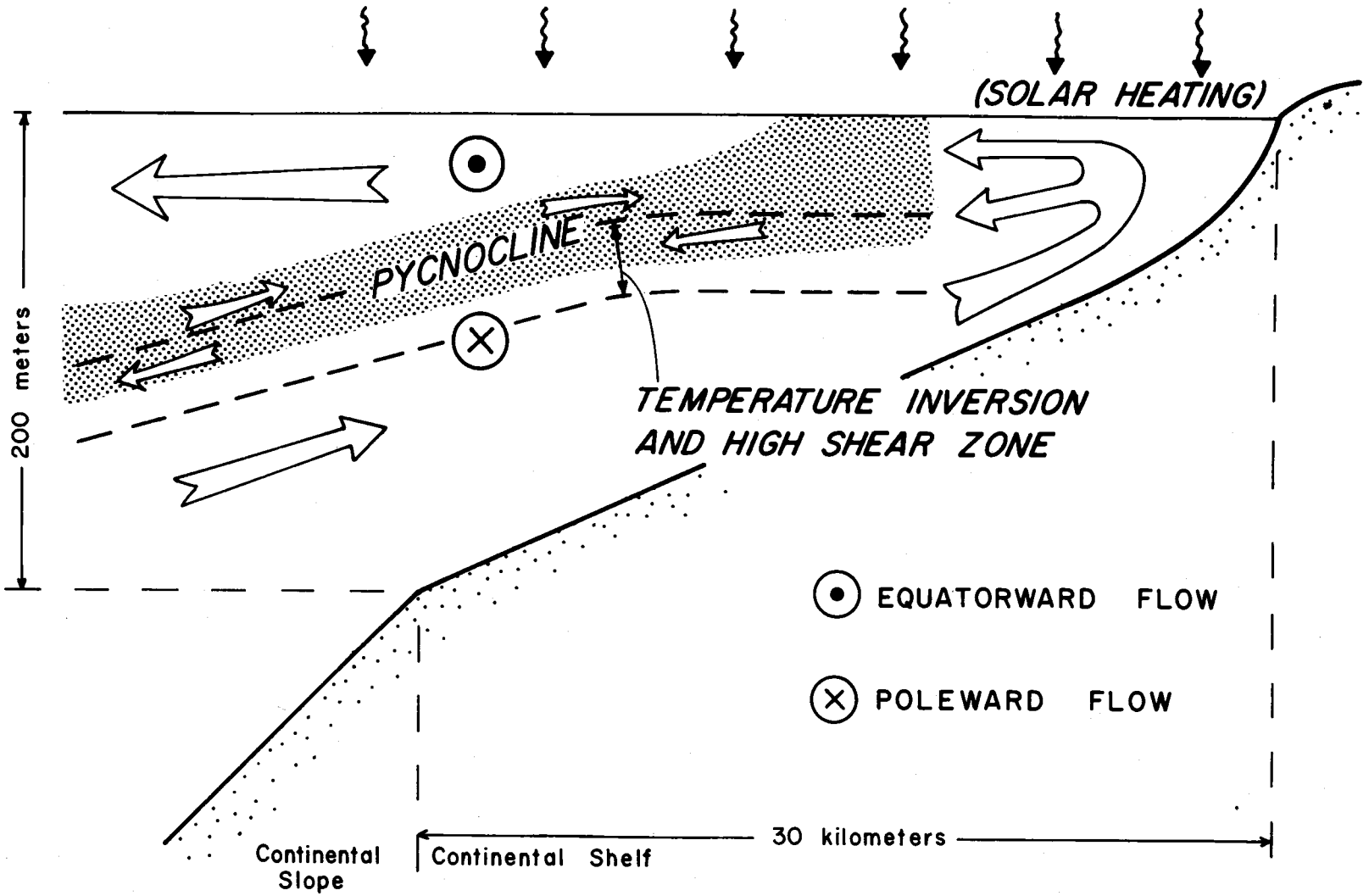

Figure 1. The mean flow field of the frontal zone in the coastal upwelling region off Oregon.

frontal zone in the coastal upwelling region off Oregon; the figure is the simple model upon which the theory is formulated and the observations of the mean flow are interpreted. A more intricate pattern for the cross-stream[4] flow is introduced in Chapter X. The coastal region is strongly density stratified, and the permanent pycnocline rises inshore, forming an inclined frontal layer during the upwelling season. The frontal layer tends to break the surface, forming a surface front; the surface front occurs 5 to 25 kilometers offshore in a quasi-steady fashion. The frontal layer descends from near the surface to a depth of about 100 meters 50 kilometers offshore, roughly paralleling the sloping bottom of the continental shelf. The subregion of the coastal upwelling region significantly influenced by the phenomena associated with the inclined frontal layer is referred to as the frontal zone. The alongshore flow described is similar to the more familiar flows parallel to frontal surfaces in the atmosphere. The wind stress acting on the sea surface plays a role for coastal upwelling fronts analogous to that of frictional drag at the Earth's surface for atmospheric surface fronts.

The frontal zone has significant horizontal density gradients and is a region of relatively intense divergence and convergence in

[4]The cross-stream flow is the flow component in the vertical plane normal to the alongshore flow, thus it is also normal to the bottom contours.

the cross-stream flow, and so also of relatively intense vorticity. The inclined frontal layer is vulnerable to annihilation, a process termed frontolysis. Yet the frontal layer is a quasi-steady phenomenon, hence it must be sustained by a transverse circulation (see the small arrows in Figure 1), a process termed frontogenesis. Turbulent mixing is expected to occur in the frontal zone in order to form the water mass of the frontal layer. The occurrence of turbulent mixing suggests that hydrodynamic instability mechanisms may be significant in the frontal zone.

Since the wind field is neither steady nor statistically stationary, coastal upwelling itself is neither steady nor statistically stationary. Coastal upwelling does have at least three generalized phases: inception, steady-state, and decay. All phases may occur several times in an upwelling season and may be overlapping, since the wind field fluctuates on various time scales.

In addition to purely transient phenomena, there may be very long-period (time scale of a month), free or forced motions present whose relation to coastal upwelling is unknown. Observations indicate that there are also shorter period phenomena superimposed on the "mean" coastal upwelling flow regime: several-day periodicities (time scale of a week), inertial[5] and tidal motions (time scale of a

[5]A pure inertial motion is barotropic and has a period equal to one-half pendulum day; the inertial period at the latitude of this study, 44° 50' to 44° 56'N, is about 16.9 hours.

day), and Väisälä-Brunt oscillations (time scale of minutes). Semidiurnal baroclinic motions are striking: the semidiurnal horizontal speeds are the same order of magnitude as those of the "mean" flow. The interaction of the semidiurnal baroclinic motions (internal tides) with the coastal upwelling frontal zone has been selected for examination, though the other wave motions present may also have significant interactions.

A simple model of the propagation of a surface tide from south to north along the west coast of North America is shown in Figure 2a. In the presence of density stratification, as the semidiurnal surface tide propagates alongshore, the internal tide is generated over the continental slope, Figure 2b. The internal tide then propagates in the onshore and offshore directions, Figure 2c. The reason that the internal tide is more strongly refracted in shallow water than the surface tide is that the onshore-offshore wave number for the internal tide is much greater than either the onshore-offshore or the alongshore wave number for the surface tide, while the alongshore wavenumber of the internal tide is probably equal to that of the surface tide. This subject is discussed fully in Appendix I. The coordinate system is defined in the figure; x is positive onshore, y is positive poleward, and z is positive upward. The origin is on the sea surface at the seaward edge of the continental shelf off Depoe Bay, Oregon.

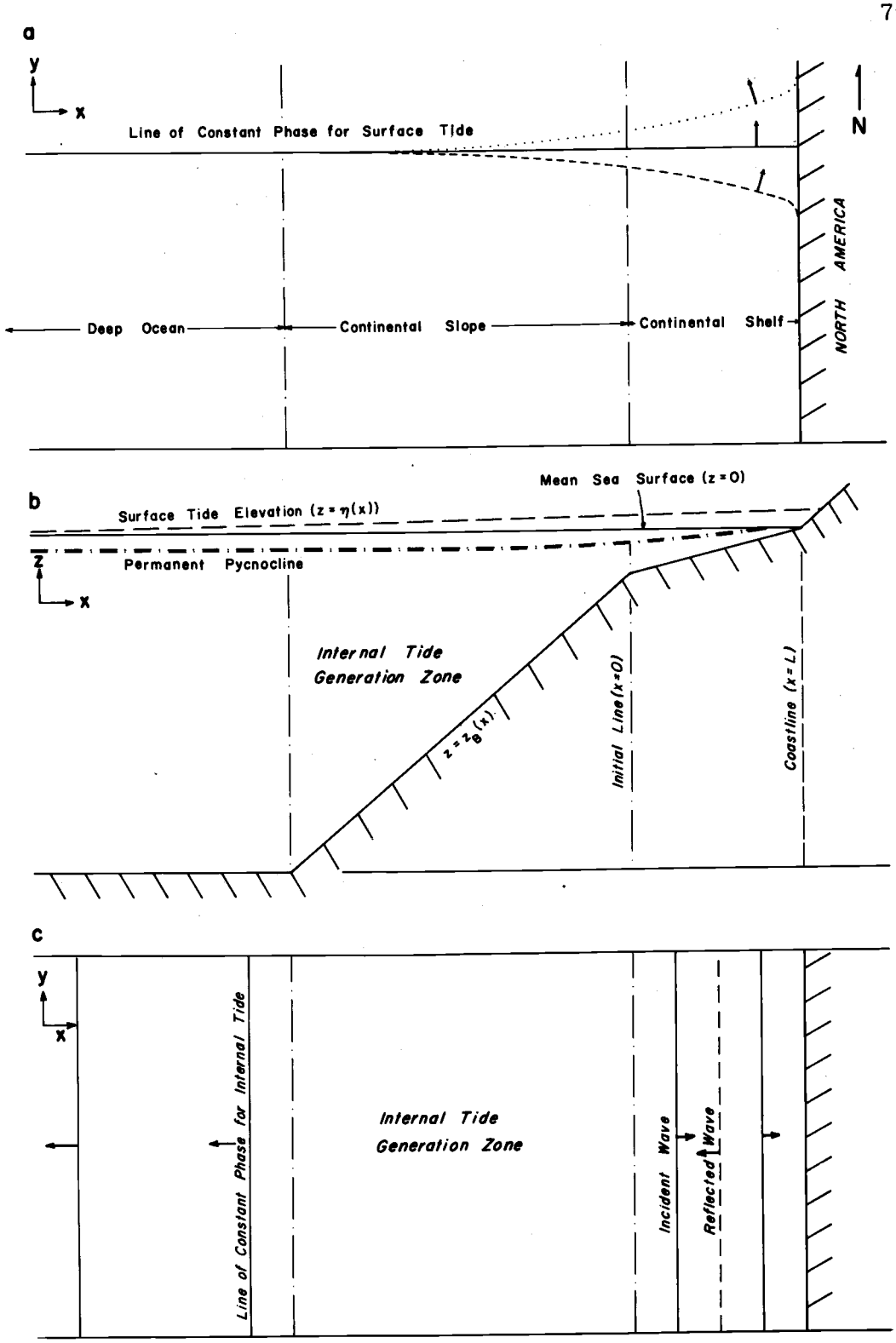

Figure 2. Simple model of the propagation of the surface (barotropic) tide along a coastal boundary and of the generation of the internal (baroclinic) tide in a coastal region.

C. Theoretical Analysis

A complete theoretical analysis of the interaction of an internal tide with a frontal zone is beyond the limits of the present understanding of the processes involved. Theoretical analysis is used to study key features of this interaction problem and to lay the foundations for more general studies. Observations are used to motivate the theoretical development. Both the mean flow of the coastal upwelling frontal zone and the propagation of the internal tide in such a region are governed by the hydrodynamics of rotating, continuously stratified, weakly viscid, incompressible fluids with variable bottom topography and a free surface. A mixture of observations, of approximate hydrodynamical theory, and of exact mathematical theory is used to develop the plausibility of the physical model of the interaction.

A detailed derivation is given for the governing equation, GE, of the interaction. The interaction is taken to be linear. The interaction GE is similar to the customary GE for inertial-internal waves, but it contains new terms. The new terms in the GE enter through "Coriolis coupling" of the inertial-internal waves to the mean flow. The GE governs inertial-internal waves propagating transverse to the axis of a frontal zone. Thus, the GE may be valid for other frontal zones in the Ocean and Atmosphere.

A general solution theory is outlined for inertial-internal waves propagating into a wedge-shaped region with variable stratification. Several wave problems are examined, including two analytical models of frontal regions. The theory is based on the method of characteristics applied to a mixed initial-boundary value problem. Because this method is based on the fundamental mathematical properties of the hyperbolic GE, it is appropriate for the study of waves whose GE has constant or variable coefficients and of waves propagating in regions with uniform or variable depth. Solutions are constructed for the continental shelf region assuming that the continental slope region can be treated as the source region for the semidiurnal internal tide.

The physical model is based on the roles which the permanent pycnocline plays for coastal upwelling and for the propagation of inertial-internal waves. Since a pycnocline is a waveguide for inertial-internal waves, the vertical displacement amplitudes and the vertical shears of the horizontal velocity of the wave motion are expected to be greatest in the pycnocline, or at its base. The hypothesis is made that the semidiurnal internal tide produces critically low dynamic stability at the base of the inclined frontal layer, inducing turbulent mixing. Thus, the interaction has the character of a negative feedback process. As coastal upwelling develops, the inclined frontal layer steepens and intensifies, becoming a more effective

waveguide for inertial-internal waves. But, as an effective waveguide, the dynamic stability of the frontal layer is reduced, causing the turbulent breakdown of the pycnocline.

D. Field Observations

The data introduced are principally field observations taken from 15 August to 24 September 1966 on the Oregon continental shelf and slope. Other data from this region are included to corroborate some of the general contentions. The principal observations are from a set of two to six-week time series of direct horizontal velocity and temperature measurements and from a set of hydrographic stations. The field observations were designed to define the principal properties of both the mean and the time-dependent flows in the upwelling season. The direct current and temperature measurements were made with moored, recording meters installed in a linear, three-point array, Figure 3. The array elements were implanted at 10-kilometer increments normal to the bottom contours. The array extended 30 kilometers offshore to the edge of the continental shelf. The installations at 10, 20, and 30 kilometers offshore were installed in water depths of 80, 140, and 200 meters, respectively, and they are designated DB5, DB10, and DB15, respectively. At each site, current meters were installed at depths of 20 and 60 meters, and thermographs at a depth of 20 meters. Four current meters and two

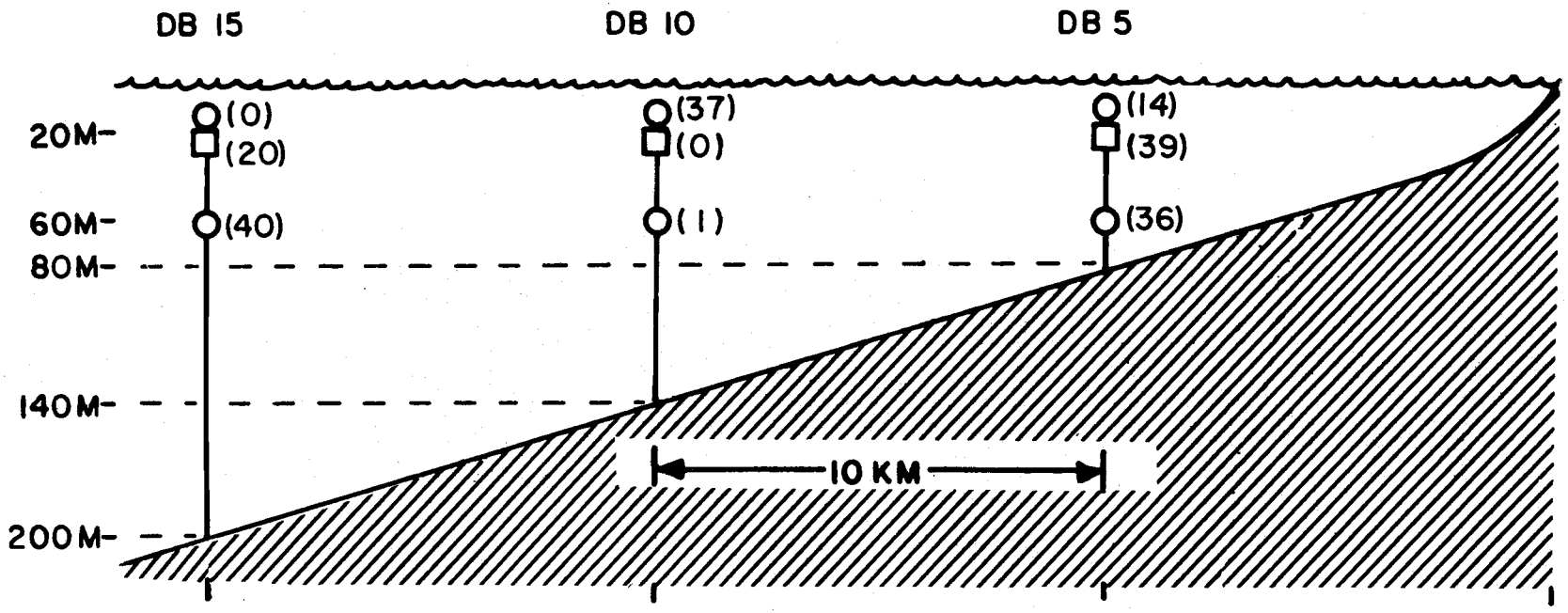

( ) Duration of useful data in days.

O Current meter

□ Thermograph

Figure 3. Vertical section of array configuration and sample duration. Depths are given in meters.

thermographs ran sufficiently long to be of use to this study.

The vertical locations of the current meters were chosen to sample above and at the base of the permanent pycnocline; the thermographs were placed near the base of the seasonal thermocline, and thus the seasonal pycnocline.[6] The horizontal locations were selected with the expectations that:

i) The semidiurnal internal tide propagates essentially normal to the bottom contours.

ii) The onshore-offshore horizontal wavelength of the semidiurnal internal tide is of the order of 20 to 40 kilometers over the continental shelf.

Thus, as installed, the array should have one-half-wavelength-spacing and should be aligned normal to the bottom contours. The sampling procedure consisted of forming ten-minute, integrated measurements. Least squares harmonic and auto and cross spectrum analyses were made of four current velocity and two thermograph

---

[6] The seasonal pycnocline is found at the base of the "surface layer" and is not to be confused with the weaker, deeper, permanent pycnocline, which forms the inclined frontal layer of prime interest to the present study. The seasonal pycnocline is formed in the summer season by the seasonal halocline derived from the Columbia River plume water and by the seasonal thermocline formed by summer heating. The permanent pycnocline is formed by the permanent halocline and is usually weakened by a temperature inversion; the permanent pycnocline is inclined upwards in the shoreward direction during the summer season.

records. Least squares harmonic analysis was also made of a single sea level record.

The observations along the hydrographic line off Depoe Bay, Oregon, were taken at the array stations and seaward along the normal to the bottom contours, Figure 4. At an anchor station, current velocity profiles were taken under sufficiently controlled conditions to make calculations of the dynamic stability. The profiles provided information about the vertical structure of the flow, while the moored, recording sensors provided time series which were sufficiently long to resolve the principal periodic structure in the diurnal and semidiurnal tidal bands of the spectrum.

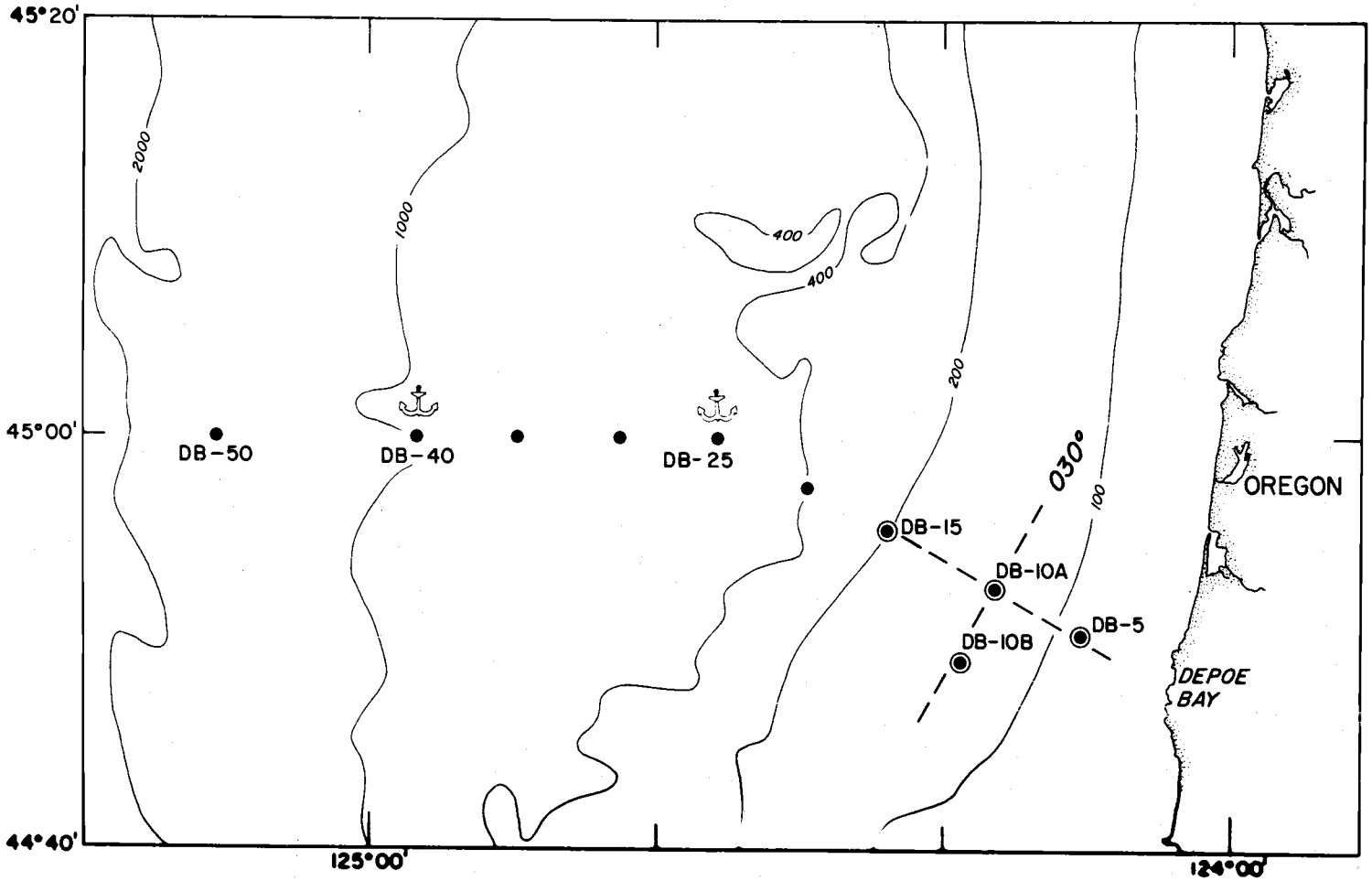

Figure 4. Locations of array and hydrographic stations off Depoe Bay, Oregon, August-September 1966. Depth contours are in meters.
Legend: • Hydrographic station ⚓ Anchor station
⊙ Instrument installation DB Depoe Bay

II. DERIVATION OF THE GOVERNING EQUATION FOR THE INERTIAL-INTERNAL WAVE FRONTAL INTERACTION

A. Introduction

The interaction of an inertial-internal wave propagating transverse to a frontal zone is formulated from first principles to make the physics clear. A general statement of the complete problem is made; the rationale is then given for each simplification necessary to achieve a reduction to a tractable and valid problem. The specific interaction problem considered relates to a central problem of geophysical fluid dynamics, viz., the interactions of wave-type motions with mean flows which lead to turbulent mixing and momentum transfers, either up or down the mass and momentum gradients.

B. Reduction of the Equations of Hydrodynamics for a Rotating and Continuously Stratified Fluid to a System of Equations for the Frontal Interaction

The fluid is considered to be weakly viscid, to be density stratified, to be under the influence of gravity, and to be on a rotating sphere. The effects of stresses on the free surface and the solid boundaries and of variable fluid depth are also of significance. Several of these phenomena are selectively disregarded in the derivation of the GE for the interaction. The Boussinesq approximation (Boussinesq, 1903, p. 172-176; Phillips, 1966) is adopted; i.e.,

variations in density are neglected in the inertia terms of the vector equation of motion but are included in the buoyancy term of the vertical component of the equation. This approximation is generally adequate except when finite amplitude effects are significant, e. g., in internal solitary waves (Long, 1965).

The pointwise conservation of fluid mass requires that

$$\frac{\partial \rho}{\partial t} + \vec{\nabla} \cdot \rho \vec{U} = 0 \tag{1}$$

or

$$\frac{d\rho}{dt} + \rho \vec{\nabla} \cdot \vec{U} = 0,$$

where ρ is the mass per unit volume, t is the time variable, $\vec{U}$ is the three-dimensional particle velocity vector, $\frac{\partial}{\partial t}( )$ is the partial derivative with respect to time, $\frac{d}{dt}( ) = \frac{\partial}{\partial t}( ) + \vec{U} \cdot \vec{\nabla}( )$ is the total derivative with respect to time, and $\vec{\nabla}$ is the three-dimensional grad operator. Assuming that the motions of interest are essentially isentropic, and using the thermodynamic relationship for the speed of sound, c_s,

$$c_s^2 = \left(\frac{dp}{d\rho}\right)_{\text{adiabatic}},$$

where p is the pressure, then

$$\frac{d\rho}{dt} = \frac{1}{c_s^2} \frac{dp}{dt}. \tag{2}$$

Assuming that the fluid is in hydrostatic balance,

$$dp = -\rho g dz, \tag{3}$$

where z is the vertical coordinate, which is positive in the upward direction. In terms of non-dimensionalized variables, (2) is

$$\frac{d\rho}{dt} = \left(\frac{c}{c_s}\right)^2 \frac{dp}{dt},$$

where $c = (gz_o)^{1/2}$ is the phase speed of a gravity wave, g is the gravitational acceleration, and z_o is the scale depth. For inertial-internal waves, the class of gravity waves of interest to this study, $z_o \sim \frac{\Delta\rho}{\rho_o} H$, where $\Delta\rho$ is the total density variation in a water column and H is the mean height of the column. In the Ocean, $c_s \sim 1.5 \times 10^5$ cm/sec and $c \sim 10^2$ cm/sec; thus, $\left(\frac{c}{c_s}\right)^2 \sim 10^{-6}$, thus (2) becomes:

$$\frac{d\rho}{dt} \approx 0.$$

Therefore, the Ocean can be treated as an incompressible fluid for the study of inertial-internal waves.[7] The incompressibility condition analytically filters acoustic waves from hydrodynamical flows.

[7] The adiabatic density gradient, $\rho_o g/c_s^2$, must be considered when computing the static stability; the static stability is the key parameter governing the propagation of inertial-internal waves and is discussed in Sections III. B and X. D.

It yields the equation of continuity, EOC:

(4) (EOC): $$\vec{\nabla} \cdot \vec{U} = 0,$$

which holds for the mean and fluctuating components of the flow separately, and it also yields the reduced conservation of mass equation, COM:

(5) (COM): $$\frac{d\rho}{dt} = \frac{\partial \rho}{\partial t} + \vec{U} \cdot \vec{\nabla} \rho = 0.$$

The COM is equivalent to the conservation of entropy relation because surfaces of constant density are approximately surfaces of constant entropy under the assumption of isentropic motions.

The three-dimensional Navier-Stokes equation of motion, EOM, for a rotating, density stratified, incompressible fluid, is adapted from Phillips (1966):

(6) (EOM): $$\frac{d\vec{U}}{dt} + \vec{f} \times \vec{U} = -\vec{\nabla} \pi - g \frac{(\rho - \rho_o)}{\rho_o} \hat{k} + \nu \nabla^2 \vec{U},$$

where $\vec{f}$ is the Coriolis parameter, $\hat{k}$ is the vertical unit vector, and ν is the kinematic molecular viscosity. The $\vec{U}$, π, and ρ variables are functions of space and time:[8]

---

[8]The overbar denotes an ensemble average, i. e., the "mean motion," (which may be space-and time-dependent). The prime denotes a fluctuating component, i. e., the turbulence, inertial-internal waves, or both. ρ_o is the space-and time-averaged density. (The

i) $\vec{U} = \vec{\bar{u}} + u'$

ii) $p = p_o + \bar{p} + p'$, where p' and $\bar{p} \ll p_o$.

iii) $\pi = \bar{\pi} + \pi'$

$= \frac{p}{\rho_o} + gz$, which incorporates the Boussinesq approximation.

iv) $\rho = \rho_o + \bar{\rho} + \rho'$, where ρ' and $\bar{\rho} \ll \rho_o$.

Expanding $\frac{d\vec{U}}{dt}$ for use in the next step,

$$\frac{d\vec{U}}{dt} = \frac{\partial(\vec{\bar{u}}+\vec{u'})}{\partial t} + (\vec{\bar{u}}+\vec{u'}) \cdot \nabla(\vec{\bar{u}}+\vec{u'}).$$

The ensemble average of (6) is then:

$$(7) \qquad \frac{\partial \vec{\bar{u}}}{\partial t} + \vec{\bar{u}} \cdot \nabla \vec{\bar{u}} + \vec{f} \times \vec{\bar{u}} = -\nabla \bar{\pi} - g \frac{\bar{\rho}}{\rho_o} \hat{k} + \vec{\Phi} + \nu \nabla^2 \vec{\bar{u}},$$

where, using the Einstein summation convention, the components of $\vec{\Phi}$ are

$$\Phi_i = -\overline{u_j' \frac{\partial u_i'}{\partial x_j}}.$$

---

zero-order state is assumed to be hydrostatic and barotropic so that $(p_o)_z = -\rho_o g$.) Then, $\overline{(\ )'} = 0$. Invoking the ergodic hypothesis, the "mean motion," or ensemble average, depends on the choice of space and time scales. The ensemble average serves as an analytical filter to separate flow components of commensurate time and space scales for individual study.

Using the EOC,

$$\Phi_i = -\frac{\partial}{\partial x_j}\overline{u_i' u_j'},$$

$$= \frac{1}{\rho_o}\frac{\partial}{\partial x_j}\tau_{ij}, \quad (i,j = 1, 2, 3),$$

where τ_{ij} is the Reynolds stress tensor, which can be produced by turbulence or irregular inertial-internal waves. It is customary to introduce an eddy viscosity function in a form analogous to the molecular viscosity, viz., $\Phi_i = (\vec{\nabla} \cdot \vec{A})\bar{u}_i'$ where the components of operator $\vec{A}$ are

$$A_j = N_j \frac{\partial}{\partial x_j}, \quad (j = 1, 2, 3)$$

and $\vec{N}$ is the eddy viscosity function.

The momentum equation for the mean motion, (7), is subtracted from (6) to obtain the equation for the fluctuating flow:

$$(8) \quad \frac{\partial \vec{u}'}{\partial t} + \vec{\bar{u}} \cdot \nabla \vec{u}' + \vec{u}' \cdot \nabla \vec{\bar{u}} + \vec{u}' \cdot \nabla \vec{u}' + \vec{f} \times \vec{u}' = -\vec{\nabla} \pi' - \frac{\rho' g}{\bar{\rho}} \hat{k} + \nu \nabla^2 \vec{u}' - \vec{\Phi},$$

which includes interaction terms. The term $\vec{\Phi}$ is common to (7) and (8) and provides for the momentum exchange between the mean and the fluctuating flows. The sign of $\vec{\Phi}$ indicates whether momentum is delivered to or derived from the mean flow: if $\vec{\Phi}$ is negative, it is a driving force for the mean flow; if it is positve, $\vec{\Phi}$ is a

driving force for the fluctuating flow. The eddy viscosity concept is usually formulated only for positive values of $\vec{N}$; i. e., the eddy viscosity is arbitrarily constrained to act as a viscous drag force on the mean flow. So-called "red shifts," due to negative eddy viscosity, are observed in geophysical fluids, as well as commonsensical "blue shifts," due to positive eddy viscosity (Starr, 1968). Therefore, there is no substitute for computing empirically (cf. Webster, 1965) or calculating theoretically (cf. Orlanski, 1968a, b), the Reynolds stresses. Eventually, the present interaction problem may require an analysis of $\vec{\Phi}$ by theory or observation.

Equation (5) is expanded for the analysis of the conservation of mass for the mean and the fluctuating flows:

$$\frac{\partial}{\partial t}(\bar{\rho}+\rho') + (\vec{\bar{u}}+\vec{u'}) \cdot \vec{\nabla}(\bar{\rho}+\rho') = 0. \tag{9}$$

Taking the ensemble average of (9), the equation for the mean density field follows:

$$\frac{\partial \bar{\rho}}{\partial t} + \vec{\bar{u}} \cdot \nabla \bar{\rho} = \overline{-u' \cdot \nabla \rho'} = -\vec{\nabla} \cdot \vec{M}, \tag{10}$$

where

$$\vec{M} = \overline{\vec{u'} \rho'}$$

is the mass flux vector and where the EOC has been used. The divergence of the mass flux vector is often replaced by the eddy diffusivity concept, viz.,

$$-\vec{\nabla} \cdot \vec{M} = (\vec{\nabla} \cdot \vec{B})\rho_o,$$

where

$$B_j = K_j \frac{\partial}{\partial x_j}, \quad (j = 1, 2, 3)$$

and $\vec{K}$ is the eddy diffusivity function. The concept of eddy diffusivity suffers the same deficiencies that the eddy viscosity concept does. Subtracting (10) from (9), the equation for the flucutating component of the density field is:

$$(11) \qquad \frac{\partial \rho'}{\partial t} + \vec{u'} \cdot \vec{\nabla} \bar{\rho} + \vec{\bar{u}} \cdot \vec{\nabla} \rho' + \vec{u'} \cdot \vec{\nabla} \rho' = \vec{\nabla} \cdot \vec{M}.$$

Two other dynamical aspects of the general problem are examined: the energy equation and the vorticity equation. Introducing the relative vorticity, $\vec{\nabla} \times \vec{U} = \vec{\omega}$, (6) is rewritten as:

$$(12) \qquad \frac{\partial \vec{U}}{\partial t} + (\vec{f} \times \vec{\omega}) \times \vec{U} + \vec{\nabla}(\pi + \frac{U^2}{2}) = -\frac{g(\rho - \rho_o)}{\rho_o} \hat{k} + \nu \nabla^2 \vec{U}.$$

The scalar product of (12) with $\vec{U}$ yields the energy equation, EE,

$$(13) \quad (EE): \quad \frac{\partial}{\partial t}(\frac{U^2}{2}) + \vec{U} \cdot \vec{\nabla} \pi + \vec{U} \cdot \vec{\nabla} \frac{U^2}{2} = -g\frac{(\rho - \rho_o)}{\rho_o} W + \nu \vec{U} \cdot \nabla^2 \vec{U},$$

where W is the vertical component of velocity.

Taking $W = \frac{d\zeta}{dt}$, where ζ is the vertical displacement,

multiplying (13) by ρ_o, and using the EOC, the EE is

$$\frac{\partial E}{\partial t} + \nabla \cdot \vec{F} = D,$$

where

$E = KE + PE$ is the total energy per unit volume,

$KE = \rho_o \frac{U^2}{2}$ is the kinetic energy per unit volume,

$PE = \zeta g(\rho - \rho_o)$ is the potential energy per unit volume,

$\vec{F} = \vec{U}(\rho_o \frac{U^2}{2} + \zeta g(\rho - \rho_o) + p + \rho_o g z)$ is the energy flux vector per unit volume,

and

$D = \mu \vec{U} \cdot \nabla^2 \vec{U}$ is the frictional dissipation per unit volume and μ is the molecular dynamic viscosity $(\mu = \rho_o \nu)$.

Taking the curl of (12), the vorticity equation, VE, is obtained:

(14) (VE):
$$\frac{d}{dt}\vec{\omega}_A = \vec{\omega}_A \cdot \nabla \vec{u} - \overbrace{\frac{g}{\rho_o}\left(\frac{\partial \rho_i}{\partial y} - \frac{\partial \rho_j}{\partial x}\right)}^{B} + \nu \nabla^2 \vec{\omega},$$

where $\vec{\omega}_A = \vec{f} + \vec{\omega}$ is the absolute vorticity, and since

$$\frac{\partial \vec{f}}{\partial t} = 0, \quad \nabla \cdot \vec{f} = 0, \quad \text{and} \quad \vec{\nabla} \cdot \vec{\omega} = \vec{\nabla} \cdot \vec{U} = 0,$$

The buoyancy term, B, indicates that, even if $\vec{\omega}_A = \vec{U} = 0$

initially and the fluid is inviscid, horizontal density gradients generate vorticity. Since a frontal zone is characterized by the existence of strong horizontal density gradients, the VE states that vorticity must be considered in the dynamics of a frontal zone. The EE and VE can be separated into their mean and fluctuating components to examine the interaction in terms of energy and vorticity exchange, but that separation is not essential to the development of the present problem.

The general formulation for the interaction of a mean flow with a fluctuating flow has been stated in terms of the EOM, EOC, COM, EE, and VE. The first simplifications necessary to derive the GE are:

i) A "locally" valid solution is sought, thus the Earth's sphericity can be neglected. The restriction to a "local" solution permits the use of Cartesian vice spherical coordinates and the neglect of the beta effect, i.e., $\beta = \frac{df}{dy}$ is set equal to zero. The neglect of the beta effect analytically filters planetary waves from the problem.

ii) The inviscid approximation is made, which is valid for strictly laminar flow where viscous effects are restricted to boundary layers. Viscous boundary layers have a thickness of the order of $\delta = (\frac{\nu}{\sigma})^{1/2}$. For seawater, $\nu \sim 0.01 \frac{cm^2}{sec}$ and for the semidiurnal tide $\sigma \sim 10^{-4}$, so $\delta \sim 10$ cm. The

depth scale under consideration is $H \sim 10^4$ cm, so $\delta \ll H$. The neglect of viscous effects is invalid for large-amplitude motions or in the presence of sufficiently intense turbulence.

iii) It is assumed that both the mean and the fluctuating flows are of sufficiently small amplitude to permit linearization. This assumption is reasonable for the alongshore component of the mean motion in the frontal zone. The validity of the assumption is less clear for the cross-stream flow, but the cross-stream flow is neglected in the final analysis. The fluctuating component occasionally appears to assume an asymmetrical, finite amplitude form indicative of nonlinear effects, hence future studies may have to consider nonlinear effects. The linearization does not entail neglect of the first-order interaction terms with the mean flow in the equations for the fluctuating component; it does analytically filter turbulent motions from the fluctuating component of the flow.

At this stage, for the mean flow, (7) becomes

$$\frac{\partial \vec{\bar{u}}}{\partial t} + \vec{f} \times \vec{\bar{u}} = -\vec{\nabla} \bar{\pi} - \frac{\bar{\rho}}{\rho_o} g\hat{k} + \frac{1}{\rho_o} \frac{\partial}{\partial x_j} \tau_{kj} . \tag{15}$$

For the fluctuating flow, (8) becomes

$$(16) \qquad \frac{d}{dt}\vec{u}' + \vec{u}' \cdot \nabla \vec{\bar{u}} + \vec{f} \times \vec{u}' = -\vec{\nabla}\pi' - \frac{\rho' g}{\rho_o}\hat{k} - \frac{1}{\rho_o}\frac{\partial}{\partial x_j}\tau_{kj},$$

where now

$$\frac{d}{dt}(\,) = \frac{\partial}{\partial t}(\,) + \vec{\bar{u}} \cdot \vec{\nabla}(\,).$$

Similarly, (11) becomes

$$(17) \qquad \frac{d}{dt}\rho' + \vec{u}' \cdot \nabla \bar{\rho} = \nabla \cdot \vec{M}.$$

The EOC, (4), continues to apply for each flow component.

Finally, the Reynolds stress and mass flux terms are neglected in the analysis of inertial-internal waves, assuming that (i) these terms in (15) are due to the effect of the turbulent flow and (ii) these terms in (16) are not significant for the inertial-internal wave motion. The Reynolds stress and mass flux terms due to the inertial-internal waves vanish as a consequence of assuming simple harmonic motion, SHM, for the time dependence. A restriction to SHM may eventually be found undesirable in the present problem. If the turbulent field in the frontal zone is sufficiently intense, the effect of Reynolds stress and mass flux terms on inertial-internal waves must be reconsidered. With the neglect of the Reynolds stress and mass flux terms, the mean flow and the fluctuating flow are uncoupled as far as momentum and mass transfers are concerned. The mean flow continues to modify the fluctuating flow, and the fluctuating flow can still affect the

dynamic stability of the mean flow.

C. The Governing Equation for Inertial-Internal Waves Propagating Transverse to a Frontal Zone

Since the flux terms are neglected, the system of equations (16), (17), and (4) are reduced to:

(18) (EOM): $$\frac{d\vec{u}}{dt} + \vec{f} \times \vec{u} + \vec{u} \cdot \nabla \vec{u} = - \vec{\nabla} \pi - \frac{\rho}{\rho_o} \hat{k},$$

(19) (COM): $$\frac{d\rho}{dt} + \vec{u} \cdot \nabla \bar{\rho} = 0,$$

and

(20) (EOC): $$\nabla \cdot \vec{u} = 0,$$

where the primes, but not the overbars, have been dropped. The geometry of the problem is established and further simplifications are applied to reduce the system of equations:

i) The coastline, the bottom contours, and the longitudinal axis of the frontal zone are considered to be parallel to the y-axis.

ii) The semidiurnal surface tide propagates northward, parallel to the positive y-axis, as a very long wave.

iii) The surface tide generates an internal tide which propagates shoreward, parallel to the positive x-axis, with a much shorter wavelength than that of the surface tide. Hence the partial derivatives in the x- and z-directions of the internal

tide are appreciable while those in the y-direction are assumed negligible. Due to the Coriolis effect, the y-component of the inertial-internal wave's particle velocity is not negligible.

iv) The mean flow and the mean density fields are considered homogeneous in the y-direction. Due to the Coriolis effect, the y-component of the mean flow is not neglected.

To further reduce the system of equations, scale analysis is used to justify the neglect of the cross-stream flow. The cross-stream flow enters the system of equations in the advective acceleration and shear-interaction terms. The scales are based on the observations reported in Chapter X. Henceforth, partial differentiation is denoted by subscripts.

The observations indicate that

$$\bar{u}_x \approx -3 \times 10^{-6} \text{ sec}^{-1}$$

$$\bar{u}_z \approx +1 \times 10^{-3} \text{ sec}^{-1}$$

$$\bar{v}_x \approx -1 \times 10^{-5} \text{ sec}^{-1},$$

and

$$\bar{v}_z \approx -5 \times 10^{-3} \text{ sec}^{-1},$$

where the shears are given in the poleward-onshore coordinate system. Since

$$\frac{\bar{u}_x}{\bar{u}_z} = -3 \times 10^{-3} \quad \text{and} \quad \frac{\bar{v}_x}{\bar{v}_z} = 2 \times 10^{-3},$$

then the ratio of the vertical to the horizontal scale of the mean motion is $r \sim 2 \times 10^{-3}$. The slope of the isopycnals, s, is of the order of 3×10^{-3}, so $r \sim s$. This result is consistent with the isentropic hypothesis for the mean flow. From the EOC, $O(\bar{u}_x) = O(\bar{w}_z)$. Thus, $O(\frac{\bar{w}}{\bar{u}}) = r \sim s$. Based on the observations, the scale of the x-component of the mean velocity is taken to be $u_o \sim 10$ cm/sec.

The ratio of the vertical to the horizontal scale of the fluctuating flow is taken to be equal to the order of magnitude of the slope of the characteristics, λ, and $\lambda \sim s$. From the EOC, $O(u_x) = O(w_z)$. Then, since $O(\frac{u_x}{u_z}) = \lambda$, $O(\frac{w}{u}) = \lambda \sim s$. The ratio of the horizontal to the time scale of the fluctuating flow is taken to be the horizontal phase speed, c_h. For the semidiurnal internal tide off Oregon, $c_h \sim 10^2$ cm/sec. The time scale, T, of the fluctuating flow is taken to be the period of the semidiurnal tide, so $T \approx 5 \times 10^4$ sec.

With the above scale estimates,

$$O(\frac{\bar{w}u_z}{\bar{u}u_x}) = \frac{s}{\lambda} \sim 1 \quad \text{and} \quad O(\frac{\bar{u}u_x}{u_t}) = \frac{u_o}{c_h} \sim 10^{-1}.$$

Analogous results follow for the other fluctuating components. Thus, the advective acceleration terms can be neglected, i. e., henceforth,

$$\frac{d}{dt}(\,) = (\,)_t.$$

Also from the above, $O(\frac{w\bar{u}_z}{u\bar{u}_x}) = \frac{\lambda}{r} \sim 1$; analogous results follow for $u\bar{w}_x$ and $w\bar{w}_z$. Since

$$O(\frac{w\bar{w}_z}{w_t}) = O(\frac{u\bar{u}_x}{u_t}) = T|\bar{u}_x| \sim 10^{-1},$$

the terms involving the shears of the mean cross-stream flow can be neglected.

Consequently, the mean cross-stream flow is completely neglected in the system of equations for the interaction. The above arguments are tenuous. There may be frontal zones elsewhere in the Ocean, or occasions for the coastal frontal zone off Oregon, when the neglect of the cross-stream flow can not be justified. Since $O(u) = O(v)$, then

$$O(\frac{w\bar{v}_z}{u\bar{v}_x}) = \frac{\lambda}{r} \sim 1,$$

Also

$$O(\frac{u\bar{v}_x}{v_t}) = T|\bar{v}_x| \sim 1.$$

Thus, the terms involving the shears of the mean alongshore flow can not be neglected. This statement is also based on a tenuous argument, but it is shown below that the retention of $u\bar{v}_x + w\bar{v}_z$ in the y-component momentum equation is necessary to be consistent with

the inclusion of the mean horizontal density gradient in the equation for ρ.

In component form, the reduced system of equations for the fluctuating flow is:

$$u_t - f_v v + f_h w = -\pi_x, \tag{21}$$

$$v_t + f_v u + u\bar{v}_x + w\bar{v}_z = 0, \tag{22}$$

$$w_t - f_h u = -\pi_z - \frac{\rho g}{\rho_o}, \tag{23}$$

$$\rho_t + u\bar{\rho}_x + w\bar{\rho}_z = 0, \quad \text{and} \tag{24}$$

$$u_x + w_z = 0, \tag{25}$$

where f_h and f_v are the horizontal and vertical components of the Coriolis force,[9] respectively. To simplify the following steps, two functions are introduced:

$$N^2 = -g\frac{\bar{\rho}_z}{\rho_o} \quad \text{and} \quad M^2 = -g\frac{\bar{\rho}_x}{\rho_o},$$

[9] Usually, the horizontal component of the Coriolis force is neglected. Since $f_h = f_v$ at latitude 45° N, the latitude of the field observations, f_h is not neglected at this stage. Whenever f_h is set equal to zero in this dissertation, it is understood that the so-called traditional approximation is made. Since (f_h, f_v) does not enter the energy equation, setting $f_h = 0$ does not affect the energetics, and it does simplify the analysis especially in the three-dimensional case, where complex-valued solutions arise. It is fair to say that it is not known whether any feature in the Ocean has been undetected or misinterpreted as a consequence of neglecting f_h. Some of the consequences of neglecting f_h are considered in Appendix II.

where N is the familiar Väisälä-Brunt frequency and M is its horizontal analogue. Eliminating v between (21) and (22), (26) follows:

$$(26) \qquad [(\,)_{tt} + f_v^2 + f_v \bar{v}_x](u) + [f_h(\,)_t + f_v \bar{v}_z](w) = -\pi_{xt} ;$$

similarly, eliminating ρ between (23) and (24), (27) follows:

$$(27) \qquad [(\,)_{tt} + N^2](w) + [-f_h(\,)_t + M^2](u) = -\pi_{zt}.$$

The EOC permits the introduction of a stream function, ψ, such that $u = -\psi_z$ and $w = \psi_x$. Cross-differentiating (26) and (27) and subtracting to eliminate π, the GE expressed in terms of ψ is obtained:

$$(28) \qquad [(\,)_{tt} + f_v(f_v + \bar{v}_x)]\psi_{zz} + [(\,)_{tt} + N^2]\psi_{xx} - [f_v \bar{v}_z + M^2]\psi_{xz}$$
$$+ [f_v \bar{v}_{xz} - (M^2)_x]\psi_z + [(N^2)_x - f_v \bar{v}_{zz}]\psi_x = 0.$$

The terms involving the horizontal component of the Coriolis force have cancelled. With variable coefficients, the GE is simpler in terms of ψ rather than π; with constant coefficients, there is no preference.

The neglect of the cross-stream component of the mean flow in the GE allows assuming the first-order equations for the frontal zone to be simply the geostrophic equation for the alongshore flow:

(29) $$-f_v \bar{v} = -\bar{\pi}_x$$

and the hydrostatic relation:

(30) $$0 = -\bar{\pi}_z - \frac{\bar{\rho}}{\rho_o} g.$$

Eliminating $\bar{\pi}$ from (29) and (30) by cross-differentiation and subtraction, the thermal wind equation is obtained:

(31) $$f_v \bar{v}_z = -\frac{\bar{\rho}_x}{\rho_o} g,$$

or

$$f_v \bar{v}_z = M^2.$$

Upon substitution of (31) into (28), the GE reduces to:

(32) $$[(\,)_{tt} + f_v^2 + f_v \bar{v}_x]\psi_{zz} + [(\,)_{tt} + N^2]\psi_{xx} - 2M^2\psi_{xz} = 0,$$

or, equivalently,

$$([(\,)_{tt} + f_v^2 + f_v \bar{v}_x]\psi_z - M^2\psi_x)_z + ([(\,)_{tt} + N^2]\psi_x - M^2\psi_z)_x = 0,$$

because $(N^2)_x = (M^2)_z$ and $(M^2)_x = (f_v \bar{v}_x)_z$. Therefore, the GE, (32), has the important property of self-adjointness.

SHM can be assumed for the time dependence of ψ, i.e., $\psi \propto e^{i\sigma t}$. Then, the final form of the GE is

(33) (GE): $$(N^2 - \sigma^2)\psi_{xx} - 2M^2\psi_{xz} - (\sigma^2 - f_v^2 - f_v \bar{v}_x)\psi_{zz} = 0.$$

Since

$$i\sigma\pi_x = (\sigma^2 - f_v(f_v + \bar{v}_x))u - (M^2 + i\sigma f_h)w$$

and

$$i\sigma\pi_z = -(M^2 - i\sigma f_h)u - (N^2 - \sigma^2)w,$$

then

$$u = i\sigma \frac{[(N^2 - \sigma^2)\pi_x - (M^2 + i\sigma f_h)\pi_z]}{\Delta}$$

and

$$w = \frac{i\sigma\,[-(\sigma^2 - f_v(f_v + \bar{v}_x))\pi_z - (M^2 - i\sigma f_h)\pi_x]}{\Delta},$$

where

$$\Delta = (N^2 - \sigma^2)(\sigma^2 - f_v(f_v + \bar{v}_x)) + M^4 + \sigma^2 f_h^2.$$

Applying the EOC to u and w in their above forms, the equation for π is obtained:

$$\left(\frac{(N^2 - \sigma^2)\pi_x - (M^2 + i\sigma f_h)\pi_z}{\Delta}\right)_x - \left(\frac{(\sigma^2 - f_v(f_v + \bar{v}_x)\pi_z + (M^2 - i\sigma f_h)\pi_x}{\Delta}\right)_z = 0.$$

In the case of constant coefficients, this equation for π is identical to the GE for ψ.

With use of the reduced system of equations, (21) to (25), for the fluctuating flow, the EE can be formed. Multiplying (21), (22), and (23) by ρ_o and by u, v, and w, respectively, and adding the three equations, the EE follows:

(34) $$(KE)_t = -[(up)_x + (wp)_z] - \rho_o[uv\bar{v}_x + wv\bar{v}_z] - \rho wg,$$

where the EOC has been used and

$$KE = \rho_o\left(\frac{u^2+v^2+w^2}{2}\right).$$

Take $u = \xi_t$ and $w = \zeta_t$, where ξ and ζ are the horizontal particle displacements, respectively, then (24) yields:

$$(\rho + \xi\bar{\rho}_x + \zeta\bar{\rho}_z)_t = 0$$

or

$$\rho = -(\zeta\bar{\rho}_x + \zeta\bar{\rho}_z),$$

neglecting the constant of integration without loss of generality, WLOG. It follows that

$$-\rho wg = \xi w\bar{\rho}_x g + \left(\frac{\zeta^2}{2}\right)_t \bar{\rho}_z g$$

$$= \xi w\bar{\rho}_x g - (PE)_t,$$

where

$$PE = \rho_o \frac{N^2\zeta^2}{2}.$$

Then (34) is written as

(35) $$E_t = -[(up)_x + (wp)_z] + w\xi\bar{\rho}_x g - \rho_o[uv\bar{v}_x + wv\bar{v}_z],$$

where $w\xi\bar{\rho}_x g$ is a vertical flux of potential energy and

$-\rho_o[uv\bar{v}_x + wv\bar{v}_z]$ is the horizontal flux of kinetic energy. Assuming that a volume of fluid is bounded by rigid boundaries so that no flow work is performed at the boundaries, the spatial average of (35) yields

$$\bar{\bar{E}}_t = g\bar{\bar{\xi}}\bar{\bar{w}}\bar{\bar{\rho}}_x - \rho_o[\bar{\bar{u}}\bar{\bar{v}}\bar{\bar{v}}_x + \bar{\bar{w}}\bar{\bar{v}}\bar{\bar{v}}_z], \tag{36}$$

where $\bar{\bar{(\ )}}$ denotes the spatial average. Integrating (36) with respect to time from $t = 0$ to $t = T$,

$$\bar{\bar{E}}(T) - \bar{\bar{E}}(0) = g\bar{\bar{\xi}}^t\bar{\bar{w}}^t\bar{\bar{\rho}}_x - \rho_o[\bar{\bar{u}}^t\bar{\bar{v}}^t\bar{\bar{v}}_x + \bar{\bar{w}}^t\bar{\bar{v}}^t\bar{\bar{v}}_z]$$

where $\bar{(\ )}^t$ denotes the time average. The righthand side, RHS, vanishes for T equal to an integral multiple of the wave period because v is in time-quadrature with u and w and because ξ and w are in time-quadrature. Therefore, the total energy is conserved in a region bounded by rigid walls for the periodic motions described by the equations of the interaction. If there is an interaction of consequence to energy transfer, it must be due to dynamic instability caused by the wave motion. As part of a more general analysis in Chapter IV, with a re-definition of the energy, the conservation of energy is proved without restriction to SHM.

With the two-dimensional form of the problem, the principal component of the vorticity is the y component, $\omega^{(y)}$, where

$$\omega^{(y)} = u_z - w_x = -(\psi_{xx}+\psi_{zz})$$

$$= -\left(\frac{N^2\psi_{xx} - 2M^2\psi_{xz} + f_v(f_v+\bar{v}_x)\psi_{zz}}{\sigma^2}\right),$$

from the GE. The relation for $\omega^{(y)}$ establishes that inertial-internal waves are rotational. Since ψ is a function of time, as noted by Eckart (1961), vorticity is not constant. The Ocean's density stratification contributes the term $(\frac{N}{\sigma})^2\psi_{xx}$, while the Earth's rotation contributes the term $(\frac{f_v}{\sigma})^2\psi_{zz}$ to $\omega^{(y)}$. Together with the Ocean's density stratification, the frontal interaction contributes the term $-2(\frac{M}{\sigma})^2\psi_{xz}$; together with the Earth's rotation, it contributes the term $\frac{f_v\bar{v}_x}{\sigma^2}\psi_{zz}$.

In summary, the linear interaction equations can be derived on the basis of the following hypotheses: (i) A linear inertial-internal wave is assumed to interact with a frontal flow while propagating transverse to the frontal flow. (ii) The frontal flow is characterized by strong horizontal density gradients and geostrophic and hydrostatic balance. (iii) The phase velocity of the inertial-internal wave is large compared to the cross-stream velocity, allowing the neglect of the latter. Scale considerations require the inclusion of the terms $u\bar{\rho}_x + w\bar{\rho}_z$ in the basic system of equations. The terms $u\bar{\rho}_x$ and $w\bar{v}_z$ have an equivalent effect on the GE; inclusion of $w\bar{v}_z$ requires inclusion of $u\bar{v}_x$ by scale analysis. Finally, the inclusion of $u\bar{v}_x$,

and the assumed hydrostatic and geostrophic equilibria of the mean flow, assure the self-adjointness of the GE.

D. Classification of the Governing Equation

The GE can be written in the general form:

$$AF_{xx} + BF_{xz} + CF_{zz} = 0.$$

The classification is based on the discriminant, Δ, of the GE, where $\Delta = B^2 - 4AC$:

i) If $\Delta > 0$, the GE is hyperbolic,

ii) If $\Delta < 0$, the GE is elliptic, and

iii) If $\Delta = 0$, the GE is parabolic.

For the case of frontal interaction,

$$A = N^2 - \sigma^2$$

$$B = -2M^2,$$

and

$$C = -(\sigma^2 - f_v(f_v + \bar{v}_x)).$$

$$\Delta = 4[M^4 + (N^2 - \sigma^2)(\sigma^2 - f_v(f_v + \bar{v}_x))] .$$

The GE is hyperbolic if and only if

$$M^4 + (N^2-\sigma^2)(\sigma^2-f_v(f_v+\bar{v}_x)) > 0,$$

or

$$\frac{a-b}{2} < \sigma^2 < \frac{a+b}{2},$$

where

$$a = N^2 + f_v(f_v+\bar{v}_x)$$

and

$$b = ((N^2-f_v(f_v+\bar{v}_x))^2+4M^4)^{1/2}.$$

When the frontal interaction is neglected, $a = N^2 + f_v^2$ and $b = N^2 - f_v^2$, so $f_v < \sigma < N$ defines the domain of hyperbolicity.

The frontal interaction can either expand or contract the domain of hyperbolicity. For example, consistent with the observations reported in Chapter X for the frontal zone, take

$$f_v \approx 10^{-4}\,\text{sec}^{-1},$$

$$\bar{v}_x \approx -10^{-5}\,\text{sec}^{-1},$$

$$N^2 \approx 3 \times 10^{-4}\,\text{sec}^{-2},$$

and

$$s \approx 3 \times 10^{-3},$$

so

$$M^2 \approx -9 \times 10^{-7}.$$

Thus,

$$N^2 \gg f_v(f_v+\bar{v}_x) \quad \text{and} \quad N^2 \gg |2M^2|,$$

so

$$b \approx N^2 - f_v(f_v + \bar{v}_x) + 2s^2N^2.$$

Then

$$\frac{a+b}{2} \approx N^2(1+s^2) \approx N^2$$

and

$$\frac{a-b}{2} \approx f_v(f_v + \bar{v}_x) - s^2N^2.$$

With the above values, $\frac{a-b}{2} \approx 0.63 \times 10^{-8}$. The domain of hyperbolicity is approximately $0.8\, f_v \tilde{<} \sigma \tilde{<} N$. Since $\sigma \approx 0.7\, f_v$ for the dirunal tide at 45° N, the possibility exists that the dirunal tide, as well as the semidiurnal tide, can exist as a baroclinic tide in the frontal zone off Oregon. Since N^2, s, and $\bar{v}_x$ vary with space and time, then so does the domain of hyperbolicity.

E. Boundary Conditions

There are several boundary conditions, BC's, which are used in the following chapters. The BC's are formulated for the stream function. At a rigid boundary, $z = z(x)$, the stream function must be a constant, i.e.,

(RBC): $$\psi\big|_{z=z(x)} = \text{constant},$$

which is a principal or kinematic BC.

If the sea surface is treated as a free boundary, the BC must

satisfy the condition that the perturbation pressure be conserved at the sea surface, $z = \eta(x)$. The linearized statement of this condition is

$$\left.\frac{d\pi}{dt}\right|_{z=\eta} = \left[\pi_t + w\,\frac{(p_o)_z}{\rho_o}\right]\Bigg|_{z=\eta} = 0,$$

or

$$\pi_t = g\psi_x$$

$$= g\eta_t \quad \text{at} \quad z = \eta.$$

Since

$$\pi_{tx} = g\psi_{xx} \quad \text{at} \quad z = \eta$$

and, with the frontal interaction and the neglect of f_h,

$$\pi_{tx} = (\sigma^2 - f_v(f_v + \bar{v}_x))u - M^2 w$$

$$= -(\sigma^2 - f_v(f_v + \bar{v}_x))\psi_z - M^2\psi_x,$$

from the x-component EOM, then

$$\text{(FBC):} \quad \left[(\sigma^2 - f_v(f_v + \bar{v}_x))\psi_z + M^2\psi_x + g\psi_{xx}\right]\Big|_{z=\eta} = 0,$$

which is a natural or dynamic BC. In Chapter IV, the FBC is derived in the process of developing the variational principle for the GE.

The significance of the FBC to inertial-internal waves is an issue which is not thoroughly understood. Using L and D as the

horizontal and vertical scales of the wave motion, and neglecting the frontal interaction, the FBC is necessary when

$$O\left(\frac{\gamma\psi_z}{\psi_{xx}}\right) = \frac{\gamma L^2}{D} = 1,$$

where

$$\gamma = \left(\frac{\sigma^2 - f_v^2}{g}\right) .$$

For the semidiurnal internal tide, $\gamma \sim 10^{-11}$, $L \sim 10^6$ cm, and take D to be the water depth. Then, the FBC is necessary when $D \sim 10$ cm. Because the FBC appears significant only for shallow water, the RBC is commonly applied at the sea surface. For most of the cases in Chapters VI, the RBC is applied at the sea surface, but there are situations when the FBC is essential

When variables are separable, the FBC presents no analytical difficulties. Its chief effect is to modify the eigenvalues of the solution. However, when variables are not separable, the influence of the FBC is more subtle. Mechanical analogues for the GE are given in Appendix IV to illustrate the FBC's qualitative effects.

When the artifice of a vertical coastal barrier is adopted, the RBC is ordinarily applied. For purposes of illustration, a lossy boundary condition, LBC, is employed in some cases. The LBC admits non-zero normal velocity but requires no net mass flux across the coastline. Thus, the coastline is treated as a flexible barrier

which can absorb energy but not mass or momentum. In other words, the fluid can do flow work on the flexible coastal barrier when the LBC is invoked.

III. THE GENERAL PROPERTIES OF INERTIAL-INTERNAL WAVES, WITH APPLICATION TO THE FRONTAL INTERACTION PROBLEM OFF OREGON

A. Introduction

For over a century, inertial-internal waves have intrigued investigators for the following reasons:

i) The waves are ubiquitous in the Ocean and Atmosphere.

ii) The subtleties of the waves are challenging to detect, describe, and comprehend.

iii) The waves play essential roles in other dynamical processes.

iv) The waves affect the distribution of the physical, chemical, biological, and geological properties of the Ocean.

Numerous studies of inertial-internal waves have been conducted theoretically, experimentally, and observationally, yet these waves are not fully understood. However, several properties of these waves have been determined reasonably well. Since it is impossible to examine all of the properties in a single theoretical, experimental, or observational study, and since ignorance of a key aspect of the waves can cause misinterpretations, it is necessary to have a basic understanding of the physics of inertial-internal waves.

This chapter contains a discussion of the properties of inertial-internal waves rather than an annotated bibliography. Several bibliographies on inertial-internal waves have been prepared in the recent

past, e.g., Lee (1965).

Several of the basic studies of the theory of inertial-internal waves are cited here. Fjeldstad (1933, 1964) applied normal mode theory to cases of variable $N^2(z)$ and compared his results to observations in a fjord; his success stimulated the modern investigations. Eckart (1960) applied the techniques of quantum mechanics to the normal mode theory and initiated the study of inertial-internal waves by ray theory and Poincare phase diagrams. Tolstoy (1963) made a broad survey using a Lagrangian rather than an Eulerian formulation. Phillips (1966) analyzed inertial-internal waves within the theoretical framework of modern surface wave theory. Krauss (1966a) published a comprehensive text on inertial-internal waves, including material on the normal mode theory and the theory of characteristics. Krauss (1966b) reviewed the contemporary knowledge of inertial-internal waves.

B. General Properties of the Waves

Inertial-internal, internal, and inertial waves are distinguished by their respective domains of hyperbolicity. Free waves can exist at frequencies within the domain of hyperbolicity, thus the domain of hyperbolicity can be interpreted as a passband. In the case of constant coefficients, the three-dimensional GE, derived in Appendix II, for inertial-internal waves is:

$$(N^2-\sigma^2)\pi_{xx} + (N^2-\sigma^2+f_h^2)\pi_{yy} - 2f_v f_h \pi_{yz} - (\sigma^2-f_v^2)\pi_{zz} = 0,$$

where

$$\frac{(N^2-\sigma^2)f_v^2}{N^2-\sigma^2+f_h^2} < \sigma^2 < N^2, \quad \text{if} \quad f_v < N \text{ (the usual case)},$$

defines the passband which is of most interest. With the neglect of f_h[10] and coefficients assumed constant, the GE is:

$$(N^2-\sigma^2)(\pi_{xx}+\pi_{yy}) - (\sigma^2-f^2)\pi_{zz} = 0,$$

where, $\sigma = f$ and $\sigma = N$ are the low and high frequency limits, respectively, for the passband.

Internal waves can occur only when the Earth's rotation can be neglected; they depend only on the effect of buoyancy. The GE is:

$$(N^2-\sigma^2)(\pi_{xx}+\pi_{yy}) - \sigma^2\pi_{zz} = 0,$$

where $\sigma = 0$ and $\sigma = N$ are the low and high frequency limits, respectively, for the passband.

Inertial waves can occur only when the Ocean's density stratification can be neglected; they depend only on the effect of the Earth's

---

[10] For the remainder of the dissertation, f_h is neglected and the symbol f is used instead of f_v. In Appendix II, some of the consequences of neglecting f_h are considered.

rotation. The GE is:

$$\sigma^2(\pi_{xx}+\pi_{yy}) - (f^2-\sigma^2)\pi_{zz} = 0,$$

where $\sigma = 0$ and $\sigma = f$ are the low and high frequency limits, respectively, for the passband. The similarity of buoyancy and inertial effects allows the application of results from studies of either internal waves or inertial waves to the other, or to inertial-internal waves, by analogy.

The observations of Fofonoff (1968b) give graphic proof of the passband relation for inertial-internal waves; his temperature and velocity spectra fall off rapidly outside the limit frequencies of the passband. For a fixed frequency, there exists a critical latitude poleward of which an inertial-internal wave can not propagate as a free wave. Oregon is poleward of the critical latitude (about 30° N) for the diurnal tides but equatorward of the critical latitude (about 72° N) for the semidiurnal tides.

With the frontal interaction, the passband is

$$f(f+\bar{v}_x) - s^2N^2 \lesssim \sigma^2 \lesssim (1+s^2)N^2.$$

Since $\bar{v}_x$ can be either positive or negative, the frontal interaction can narrow or broaden the passband. The order of magnitude argument given in Section II. D. suggests that the frontal interaction off

Oregon broadens the passband. The observations discussed in Chapter X indicate that $\bar{v}_x$ and s vary as functions of time and space. Thus, the passband in the frontal zone of coastal upwelling varies with time and space.

Except for finite spectral peaks at tidal and inertial frequencies, there is a general tendency for the spectral slope of velocity spectra to decrease with a minus 5/3-power dependence on frequency in the passband, Ozmidov and Yampolskii (1965) and Fofonoff (1968b). A minus 5/3-power law is also the frequency dependence of the energy spectrum in the inertial sub-range of the equilibrium range for isotropic turbulence. However, the physical conditions of the Ocean for inertial-internal waves differ vastly from the ideal conditions for isotropic turbulence. When dispersion relations for finite depth are included in the analysis, power laws ranging from minus 1 to minus 2 are anticipated. Temperature spectra also tend to decrease with a minus 5/3-power law. From the inspection of many spectra, Fofonoff (1968b) advanced the idea that there is a tendency for the development of a saturation spectrum in the passband, at least in the deep ocean. He interpreted this to mean that there may be a universal equilibrium, involving coherent internal waves and incoherent turbulence, established by shear instabilities of internal waves.

The upper frequency limit of inertial-internal waves is N(z), the Väisälä-Brunt frequency, Väisälä (1925) and Brunt (1927). The

Väisälä-Brunt frequency is the frequency of free oscillation of a water parcel displaced from hydrostatic equilibrium in a stratified fluid. It takes into account the adiabatic compressibility of sea water:

$$N^2 = E = \frac{-g}{\rho_o}\left[\frac{\partial \rho}{\partial T}\left(\frac{\partial T}{\partial z} - \frac{d\theta}{dz}\right) + \frac{\partial \rho}{\partial s}\frac{\partial s}{\partial z}\right] = \frac{-g}{\rho_o}\left[\left(\frac{\partial \rho}{\partial z}\right)_{\text{in situ}} - \left(\frac{\partial \rho}{\partial z}\right)_{\text{adiabatic}}\right],$$

where $\frac{d\theta}{dz} = \frac{-1}{\rho_o}\left(\frac{\partial \rho}{\partial z}\right)_{\text{adiabatic}} = \frac{g}{c_s^2}$ is the adiabatic lapse rate, E is the static stability, and c_s is the speed of sound. Since, for the coastal region off Oregon, $10^{-5} \lesssim E(x, z) \lesssim 10^{-3}\,\text{sec}^{-3}$, and since $(g/c_s)^2 = 4.4 \times 10^{-5}\,\text{sec}^{-2}$, the effects of compressibility can not be neglected in the computation of N^2 without verification. In the upper layers of the Ocean, and in the coastal region off Oregon, an approximate formula can usually be used:

$$E = \frac{-g}{\rho_o}\frac{d\sigma_t}{dz} \times 10^{-3}$$

$$\approx \frac{-d\sigma_t}{dz},$$

where σ_t is sigma-t, the density anomaly without regard for adiabatic effects, and z is in units of centimeters.

Pure Väisälä-Brunt oscillations represent a strictly differential, or local, viewpoint. A kindred class of motion is that of internal cellular waves (Neumann, 1949), which admits finite depth and horizontal wavelength.

The characteristic relation,[11] CR, is

$$\sigma^2 = \frac{N^2(k^2+\ell^2)}{(k^2+\ell^2+m^2)},$$

assuming $\sigma^2 \gg f^2$. Replacing $k^2+\ell^2$ by $K^2 = (\frac{2\pi}{\lambda^{(h)}})^2$, where $\lambda^{(h)}$ is the horizontal wavelength and m^2 by $(\frac{n\pi}{H})^2$ for the nth vertical mode in finite depth, H, then

$$\sigma_n^2 = \frac{N^2}{1+(\frac{n\lambda^{(h)}}{2H})^2}.$$

Thus, when $\lambda^{(h)} \sim 2H$, there can exist free motions at a discrete set of frequencies less than N for a fixed $\lambda^{(h)}$. Waves at or near such frequencies have been associated with the occurrence of surface slicks in coastal regions and with temperature oscillations (LaFond, 1962 and Carsola, et al. 1965). In the shallow waters of Massachusetts Bay, Halpern (1968) has detected high frequency stability oscillations; the generation of the waves is correlated with the surface tide.

In a theoretical analysis of internal tides, Vapnyar (1964) gave

---

[11] The term characteristic relation, CR, is used repeatedly for the equation which results from the GE when SHM is assumed for the spatial dependence, i.e., $\psi \propto e^{i(kx+\ell y+mz)}$, where k, ℓ, and m are the x, y, and z wave numbers, respectively.

a physical theory linking the tides and Väisälä-Brunt oscillations. His view is that the passage of a surface tide excites Väisälä-Brunt oscillations. In turn, the Väisälä-Brunt oscillations excite the internal normal modes at the tidal frequency, each of which propagates at its own phase speed. Internal cellular waves could be present in the time series of the present study.

Layered models, with each layer homogeneous in density, have been extensively studied by Defant (1961), Rattray (1960), Ichiye (1963), and many others. There are analytical advantages to the study of layered models, which yield interfacial waves rather than true internal (body) waves. The relevance of interfacial waves as idealizations of inertial-internal waves remains uncertain. Some of the essential physics of the inertial-internal waves are missed by the study of the interfacial waves. For instance, interfacial waves concentrate all of the vertical shear in horizontal velocity, or vorticity, at the density discontinuity, while inertial-internal waves distribute the vorticity throughout the fluid. Interfacial waves can be treated analytically as irrotational, so a potential function can be defined in each layer. Inertial-internal waves are rotational (shear) waves, as established in Section II. C., so no potential function exists for them.

As an eigenvalue problem, the GE and its BC's admit an infinite number of solutions, or normal modes, when SOV is possible. Fjeldstad (1933) initiated such studies. Yanowitch (1962) proved that,

in the limit of an infinite number of layers, the eigenvalues for a layered system converge to those for a continuously stratified system. The eigenvalues lead to calculation of the modal phase speed if the horizontal wavelength is known; the modal phase speed is approximately inversely proportional to the modal number. The important deduction that the largest amplitude of the waves is expected to occur at the base of a pycnocline follows from the normal mode analysis made by Tareev (1963).

Gossard and Munk (1954) and Gossard (1962) developed the basic waveguide theory for fluid layers with N constant in each layer. This case is intermediate between interfacial waves with ρ discontinuous and inertial-internal waves with N continuous. They found it possible for leaky waves to transfer momentum across a waveguide, i.e., a layer in which N is a maximum. Eckart (1961) found that it was possible for momentum to be exchanged between waves trapped on two or more pycnoclines, or waveguides. Thus, momentum transfer may occur across and between the permanent and seasonal pycnoclines in the coastal upwelling region. The observations of the present study do not allow the examination of this possibility.

Eckart (1960) remarked the possibility of using the theory of characteristics to analyze inertial-internal waves, but he chose to

use the WKBJ[12] approximation to develop a ray theory. Magaard (1962) and Sandstrom (1966) were the first to use the theory of characteristics to construct solutions. Fofonoff (1966) applied the theory of characteristics to the design of field observations, plotting the characteristics seaward of an assumed source at the edge of the continental shelf. Longuet-Higgins (1969) has developed a theory for the scattering of internal waves by irregular surfaces using the theory of characteristics. Jones (1969) has initiated the study of the propagation of internal waves through a temporally and spatially dependent velocity field with the aid of ray theory. The theory of characteristics is used extensively in this dissertation rather than the normal mode or ray theories.

The technique for finding the equation of the characteristics from the GE is given in Section V. B. The characteristics have several mathematical and physical interpretations:

a) They delimit the domains of influence and dependence for initial value problems.

b) They define the trajectories along which discontinuities in the solution, or shocks, propagate; i. e., they are colinear with the group velocity and energy flux.

---

[12]The WKBJ approximation is the Wentzel, Kramers, Brillouin, and Jeffreys approximation which assumes that the amplitude of a wave varies slowly over a wavelength, allowing the development of a ray theory from an approximate wave function in the case of variable coefficients.

c) They are lines of constant phase; i. e., they are perpendicular to the phase velocity and the vector wave number.

d) In the two-dimensional case, they are coplanar with particle trajectories; i. e., they are the x-z plane projections of streamlines.

These properties are developed in this section and in Chapter V.

With the neglect of f_h, the horizontal asymmetry of the three-dimensional GE vanishes so it is sufficient to consider the two-dimensional case. For simplicity, neglect the frontal interaction. Then the equation for the characteristics, ζ, is

$$(N^2-\sigma^2)(\zeta_x)^2 - (\sigma^2-f^2)(\zeta_z)^2 = 0.$$

Assuming constant coefficients, then the solutions for ζ are

$$\zeta^+ = z - Rx$$

and

$$\zeta^- = z + Rx,$$

where

$$R = \left(\frac{\sigma^2-f^2}{N^2-\sigma^2}\right)^{1/2}$$

and ζ^+ and ζ^- are the upgoing and downgoing characteristics respectively. Let $\hat{\zeta}$ be a unit vector along ζ^+ constant, then

$$\hat{\zeta} = \frac{(1, R)}{(1+R^2)^{1/2}}.$$

A vector wave number, $\vec{k} = (k, m)$ is introduced; then the CR yields

$$k^2 - R^2 m^2 = 0,$$

so $\frac{k}{m} = \pm R$. The spatial phase of the solution corresponding to the positive root of $\frac{k}{m}$ is $\theta^+ = kx - mz$. Then the slope of a line of constant phase is $\left(\frac{dz}{dx}\right)_{\theta^+} = \frac{k}{m} = R$, or θ^+ constant is parallel to ζ^+. Let $\hat{\theta}^+$ be a unit vector along θ^+ constant, then

$$\hat{\theta}^+ = \frac{(1, \frac{k}{m})}{(1+(\frac{k}{m})^2)^{1/2}}$$

and, since $\vec{k}^+ = (k, -m)$, then $\hat{\theta}^+ \cdot \vec{k}^+ = 0$. Therefore, the plus vector wavenumbers are orthogonal to the upgoing characteristics, since $\zeta \| \theta$. Similarly, $\vec{k}^- = (k, m)$ and

$$\hat{\theta}^- = \frac{(1, -\frac{k}{m})}{(1+(\frac{k}{m})^2)^{1/2}},$$

so $\hat{\theta}^- \cdot \vec{k}^- = 0$.

The phase and group velocities are analyzed in this section without regard for the influence of boundaries. By definition, the phase velocity is

$$\vec{c}_p = \frac{\vec{k}\sigma}{|\vec{k}|^2}$$

and the group velocity is

$$\vec{c}_g = (\sigma_k, \sigma_m).$$

Using the CR,

$$\vec{c}_p = \frac{\sigma}{(1+R^2)m^2}(k, m).$$

Since

$$\vec{c}_g = \frac{1}{RR'm^2}(k, -R^2 m), \quad \text{where} \quad R' = \frac{dR}{d\sigma},$$

then

$$\vec{c}_g \cdot \vec{c}_p = 0.$$

Therefore, the phase and group velocities are orthogonal, which is then a general property of wave motions whose GE's dependence on σ can be placed in the coefficient of one second-order term.

As a familiar counter-example, consider the case of the two-dimensional Helmholtz equation whose spatial dependence is elliptic:

$$\pi_{xx} + \pi_{yy} + R^2(\sigma)\pi = 0,$$

where the CR is

$$(k^2+\ell^2) - R^2(\sigma) = 0.$$

Then

$$\vec{c}_p = \frac{\sigma}{R^2}(k, \ell)$$

and

$$\vec{c}_g = \frac{1}{RR'}(k, \ell) = \frac{R}{\sigma R'}\vec{c}_p.$$

Since

$$\vec{c}_p \times \vec{c}_g = 0,$$

the group and phase velocities are colinear, as for surface gravity waves.

For inertial-internal waves,

$$\vec{c}_p = \frac{\sigma}{m^2}\left(\frac{N^2-\sigma^2}{N^2-f^2}\right)(k, m), \quad \text{thus} \quad |\vec{c}_p| = \left(\frac{N^2-\sigma^2}{N^2-f^2}\right)^{1/2}\frac{\sigma}{m}$$

Since

$$RR' = \sigma\frac{(N^2-f^2)}{(N^2-\sigma^2)^2},$$

then

$$\vec{c}_g = \frac{(N^2-\sigma^2)^2}{\sigma m^2(N^2-f^2)}\left(k, -\frac{(\sigma^2-f^2)}{(N^2-\sigma^2)}m\right), \quad \text{thus} \quad |\vec{c}_g| = \left(\frac{\sigma^2-f^2}{N^2-f^2}\right)^{1/2}\frac{(N^2-\sigma^2)}{\sigma m}.$$

Thus, the propagation of inertial-internal waves is dispersive and anisotropic. Since $\hat{\zeta}$ is perpendicular to $\vec{k}$, then $\hat{\zeta}$ is parallel to $\vec{c}_g$ and orthogonal to $\vec{c}_p$. Therefore, $\vec{c}_g$ parallels the characteristics while $\vec{c}_p$ is orthogonal to the characteristics. Because discontinuities in the second and higher order derivatives do propagate along characteristics, it is clear why $\vec{c}_g$ is parallel to the characteristics. $\vec{c}_g$ tends to the horizontal as N increases or when σ tends to f; thus, a pycnocline serves as a waveguide, especially as σ tends to f. As a corollary, lines of constant

phase tend to parallel a pycnocline. The EOC implies that

$uk + wm = 0$, or

$$\vec{u} \cdot \vec{c}_p = 0,$$

where

$$\vec{u} = (u, w).$$

Thus, the particle velocity is orthogonal to $\vec{c}_p$ and $\hat{\theta}$ and co-planar with $\vec{c}_g$ and $\hat{\zeta}$.

For the frontal interaction, the CR is

$$(N^2-\sigma^2)k^2 - 2kmM^2 - (\sigma^2-f(f+\bar{v}_x))m^2 = 0.$$

Then

$$\frac{m^{\pm}}{k} = \frac{M^2 \pm (M^4+(N^2-\sigma^2)(\sigma^2-f(f+\bar{v}_x)))^{1/2}}{(\sigma^2-f(f+\bar{v}_x))},$$

which indicates the asymmetry of the upgoing and downgoing vertical wave numbers, for a fixed horizontal wave number. Since

$$k^2 + m^2 = m^2\Delta^{\pm},$$

where

$$\Delta^{\pm} = \frac{[(N^2-\sigma^2)(N^2-f(f+\bar{v}_x))+2M^4 \pm 2M^2(M^4+(N^2-\sigma^2)(\sigma^2-f(f+\bar{v}_x)))^{1/2}]}{(N^2-\sigma^2)^2}$$

then

$$(\vec{c}_p)^{\pm} = \frac{\sigma}{m^2\Delta^{\pm}}(k, m^{\pm}),$$

thus

$$|(\vec{c}_p)^{\pm}| = (\frac{1}{\Delta^{\pm}})^{1/2} \frac{\sigma}{m^{\pm}}.$$

Similarly,

$$(\vec{c}_g)^{\pm} = \frac{1}{\sigma} \frac{(m^{\pm}, -k)}{m^4 (\Delta^{\pm})^2} [(N^2 - f(f+\bar{v}_x))km^{\pm} + M^2(k^2 - m^2)].$$

Thus, there is also asymmetry in the phase and group velocities of the upgoing and downgoing waves.

C. Further Properties of Inertial-Internal Waves, with Application to the Coastal Region

The possible mechanisms for the generation of inertial-internal waves include:

i) Inertial-internal waves may be generated by a surface wave or an internal wave passing over a region of variable topography (Zeilon, 1934; Rattray, 1960; Cox and Sandstrom, 1962; Ichiye, 1963; and Sandstrom, 1966).

ii) Internal tides may be generated by gravitational forces (Petterson, 1934; and Krauss, 1966c), especially at the critical latitudes where resonance occurs.

iii) Internal waves may be generated by wave-wave interactions, or scattering (Ball, 1964; Thorpe, 1966; and Kenyon, 1968). The interactions could involve surface as well as internal waves and would involve the vertical modal numbers as well

as frequencies and horizontal wave numbers.

iv) Inertial-internal waves may be generated by perturbation of a mean flow from an equilibrium state (Fjeldstad, 1958), or by the winds (Pollard, 1968).

Mechanism i) is probably the most significant for the generation of the semidiurnal internal tide in the coastal region off Oregon.

Theories for layered models, such as those of Rattray (1960), Ichiye (1963), and Weigand (1964), show that barotropic and baroclinic waves are coupled by stepped bottom topography, thus barotropic waves can generate baroclinic waves with appreciable amplitudes. For continuous models, Sandstrom (1966) used the method of characteristics, the RBC, and experimental evidence, to develop the concept of a critical bottom slope: a wave sustains large amplification when incident on a bottom whose slope approximates that of the wave's upgoing characteristics.

The basic principle of inertial-internal wave reflection from a sloping rigid boundary is demonstrated by the simple case of a plane wave incident on a bottom surface with uniform slope at depth $z = -H_o - m_o x$, where $m_o > 0$ is the bottom slope. Take $\psi^- = c^- e^{i(\sigma t - k^- x + m^- z)}$ for the downgoing wave and

$$\psi^+ = c^+ e^{i(\sigma t - k^+ x - m^+ z)}$$

for the upgoing wave; then $\psi = \psi^+ + \psi^-$. The RBC requires that

$$\psi\big|_{z=-H_o-m_o x} = \text{constant for all } x;$$

a necessary condition is that

$$k^+ - m^+ m_o = k^- + m^- m_o .$$

Since

$$\frac{k^-}{m^-} = \frac{k^+}{m^+} = R > 0,$$

then

$$m^+ = m^- \left(\frac{R+m_o}{R-m_o}\right) .$$

Therefore, if the slope is subcritical, i.e., if $R > m_o$, then $m^+ > m^-$ and $k^+ > k^-$. Thus the absolute value of the wave number is amplified upon reflection of a wave progressing up a slope. (This relationship is investigated more generally in Chapter V.) Consequently, since $|\vec{c}_p|$ and $|\vec{c}_g|$ are inversely proportional to m, from Section B, then $|\vec{c}_p|$ and $|\vec{c}_g| \to 0$ as a wave sustains an infinite number of reflections from a subcritical, sloping rigid boundary. This property is analyzed further at the end of this section. It is observed that the reflection rule is based on the fact that the orientation of the characteristics and the wave numbers is fixed in space, i.e., they are not oriented symmetrically with respect to the normal to a sloping boundary as are wave number vectors for motions governed by an elliptic GE.

The condition for a critical bottom slope, m_c, is given for a

fixed frequency by

$$m_c = R = \left(\frac{\sigma^2 - f^2}{N^2 - \sigma^2}\right)^{1/2};$$

or, for a fixed bottom slope, m_o, the critical frequency, σ_c, is given by

$$\sigma_c = \left(\frac{m_o^2 N^2 + f^2}{m_o^2 + 1}\right)^{1/2} .$$

The concept of subcritical, critical, and supercritical bottom slopes is illustrated for a coastal region in Figure 5. The symbols η and ζ represent upgoing and downgoing characteristics, respectively, which is a convention maintained throughout the remainder of this dissertation.

With the frontal interaction,

$$m_c = \frac{-M^2 + (M^4 + (N^2 - \sigma^2)(\sigma^2 - f(f + \bar{v}_x)))^{1/2}}{(N^2 - \sigma^2)} .$$

Since $M^2 \leq 0$ in the case under consideration, and if $\bar{v}_x < 0$, as it is near the coastal boundary, then $m_c > R$; i.e., the frontal interaction exerts a stabilizing influence on bottom reflection. Wunsch (1968, 1969) found partially separated normal modes for a progressive wave in a wedge; he reproduced the qualitative feature of marked amplification for near-critical bottom slopes.

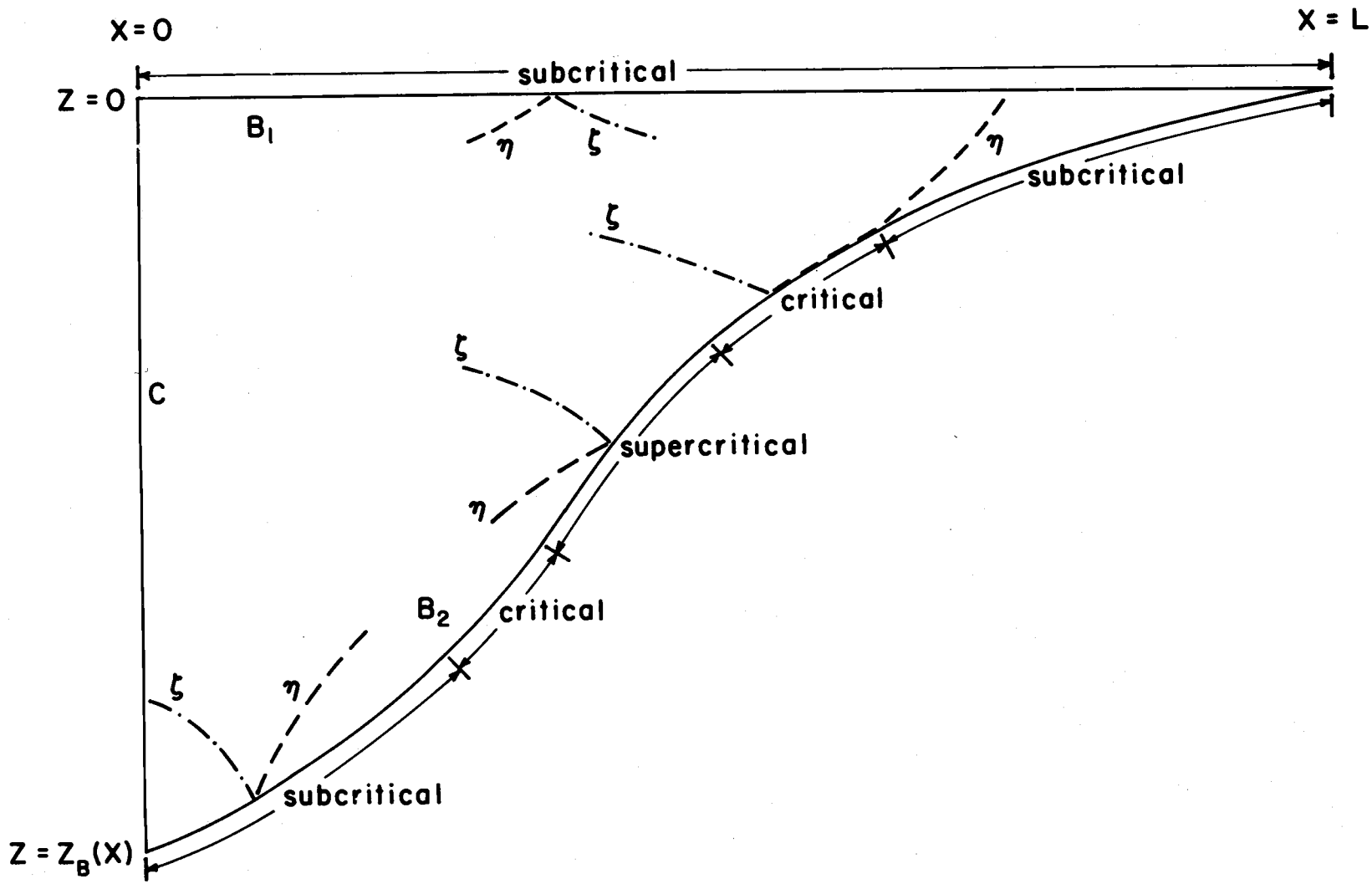

Figure 5. Illustration of the concept of subcritical, critical, and supercritical bottom slopes in a coastal region

Thus, critical bottom slopes are thought to play a crucial role in the generation of internal tides by surface tides.

In November 1966, Mesecar (1968) occupied a thermoprobe station on the continental slope off Depoe Bay, Oregon for 115 hours. The water depth was about 250 meters, and the distance offshore was about 33 kilometers. The thermoprobe site was close to the seaward sensor site of the present study, but it was occupied two months after the observations on the continental shelf were completed. The thermoprobe sampled the lower three meters of the water column and deeper than a meter into the sediments, once every hour.[13] Though there were no detectable temperature gradients in the lower three meters of the water column, he found large amplitude temperature oscillations, of the order of 0.2° C° to 0.5° C°. The oscillations occurred primarily at the semidiurnal frequency and its harmonics, and they extended at least 36 but less than 121 centimeters into the sediments. This is indirect evidence for strong semidiurnal bottom currents on the continental slope. Recently, Korgen (1969) has obtained direct evidence of semidiurnal tidal speeds close to the continental slope; they are an order of magnitude greater than those observed over the continental shelf. For the location and season of

[13] The sensors had a 15-second time constant. Samples were taken once every 10 seconds for the first twenty-four hours. No short period fluctuations were detected, hence a reduction in sampling rate was made.

Mesecar's observations, the best estimate of static stability is $E \approx 1$ to 2×10^{-5} sec^{-2}. At the semidiurnal frequency, the critical bottom slope, m_c, is then $m_c \approx 2$ to 3×10^{-2}, while the bottom slope, m, is $m \approx 2$ to 5×10^{-2}. Hence, the bottom slope is probably critical or supercritical for the semidiurnal internal tide, which is consistent with Mesecar's observations. Thorough time series observations of both bottom currents and static stability over the continental slope are necessary to verify this speculation. Since the static stability field over the continental shelf and slope is affected by coastal upwelling, then the criticality of the bottom slope may wax and wane with the state of coastal upwelling. If m_c does vary in such a manner, the generation process of internal tides may vary, and the internal tide over the continental shelf may have its character modulated too.

Because large horizontal velocities associated with inertial-internal waves can occur near the sea bottom, such motions can produce net sediment transports and sand ripples (LaFond, 1961a). These effects are expected to be most significant in shallow regions, e. g., coastal regions. Associated with the observations of this dissertation, there may be strong currents at the sea floor capable of modifying the distribution of sediments. Neudeck (1969) has found evidence for ripples in the sediments on the Oregon continental shelf which appear to be consistent with generation by internal waves

propagating onshore. Simultaneous measurements of both geological and physical properties near the bottom on the continental shelf have yet to be made and promise to be useful for the study of inertial-internal waves as well as geological processes.

The earlier observations of inertial-internal waves were based on temperature measurements. The observations of Haurwitz, Stommel, and Munk (1959) raised questions about the behavior of inertial-internal waves over sloping bottoms and the lack of coherence of tidal motions over relatively small spatial separations. The analysis of Radok et al. (1967) showed that, in mid-ocean, the lunar semidiurnal internal tide (M_2) was incoherent with respect to the lunar tide-producing forces. They attributed the random phase of the internal tide to the Ocean's variable temperature or current structure. They noted that the order of magnitude of the r. m. s. surface elevation associated with the M_2 internal tide is consistent with the observed r. m. s. incoherent M_2 surface elevations at coastal stations. (This is an example of where the FBC may play an essential role.) The measurements of Lee (1961), LaFond (1962), and Gaul (1961) pioneered the study of internal waves in very shallow water, the order of 20 meters deep; a fundamental lack of wave coherence was found (Cox, 1962).

Dowling (1966) used a linear array on the continental shelf off northwest Florida and found that high frequency internal waves obeyed

the dispersion law derived for the ambient stratification and finite depth; his measurements also suggested the existence of a continuum of wave motions. He advanced the hypothesis that breaking internal waves operate to establish a hyperbolic tangent density profile as an equilibrium configuration. The tendency for the density structure over the continental shelf off Oregon to have a hyperbolic tangent or an exponential depth dependence has influenced the choice of the frontal models employed in Chapter VII.

Summers and Emery (1963) found semidiurnal internal tides propagating onshore from the continental slope with phase speeds of 350 cm/sec over the continental slope and of 50 cm/sec over the continental shelf off southern California; the wave crests were aligned with the bottom contours and the wave amplitudes were of the order of 30 meters. (Their study served as early guidance for the design of the observations and the theory of this dissertation.) All but the measurements of Gaul (1961) were concentrated near 30° N, where it is difficult to resolve the inertial and diurnal motions.

Boston (1964) employed current meters in the geographic vicinity of Dowling's study; he found that the tidal motion was baroclinic and that it had a character suggestive of an internal edge wave. Mortimer (1963), using temperature measurements, in Lake Michigan, at a latitude similar to Oregon's, has detected a myriad of barotropic and baroclinic long wave motions under the influence of finite depth

and coastal boundaries, including baroclinic inertial motions. Using current data, Malone (1968) confirmed the occurrence of baroclinic inertial motions in Lake Michigan during the season of strong stratification. The studies in Lake Michigan are of special interest because a coastal jet and coastal upwelling occur there, as well as off Oregon. Recently, Warner (1968) made current measurements off the coast of Nova Scotia, also at 45° N. The observational techniques used were very similar to those reported in Chapters X and XI. The spatial coherence of internal tides was found to be generally lower than had been expected, a feature common to the observations off Oregon.

Haurwitz (1954) discussed the spasmodic, inconclusive evidence for the occurrence of internal tides in the deep ocean. Since the time of his study, the evidence has become more convincing for the existence of internal tides, though it indicates a general lack of spatial coherence (Webster, 1968a and Munk and Phillips, 1968).

Yasui (1961) advanced a theory for internal tides in the strong front in western boundary current regions; his objective was to explain the observed lack of internal tides in such regions. His model was based on a two-layered system with waves propagating along the axis of the front. He found that the front would tend to block waves attempting to cross it and would respond by tending to meander.

As this dissertation was in the final stages of revision, Healey

and LaBlond (1969) published an analysis of inertial-internal waves propagating transverse to a geostrophic current. They did not make the Boussinesq approximation in their theoretical analysis. (The GE without the Boussinesq approximation is derived in Appendix V.) As a consequence, though the principal part of their GE is equivalent to the GE of this dissertation, it includes terms with first-order partial derivatives of small consequence. Two of their qualitative conclusions are identical to deductions made in this dissertation, viz., an asymmetry in a wave's phase as a function of depth, which is $O(s)$, where s is the slope of an isopycnal, and an alteration of the passband, which is $O(s^2)$, are induced by the geostrophic current. Not having made the Boussinesq approximation, they were able to analyze the energy exchange of the interaction, which they found $O(s^3)$, i.e., very weak and negligible.

Most theoretical studies of internal waves in a shear flow, e.g., Phillips (1966) and Booker and Bretherton (1967), have been made at high frequencies so that the Coriolis parameter could be neglected. The concept of the critical level, i.e., the level at which the mean horizontal velocity and wave phase speed are equal, so $\sigma - u(z)k - v(z)\ell = 0$, has received recent attention. The significance of the critical level is that a transfer of momentum from a wave to a mean flow can occur there. Jones (1967) has included the effects of rotation and has found two additional critical levels

corresponding to $\sigma - u(z)k - v(z)\ell = \pm f$, where f is the vertical component of the Coriolis parameter. He also found that the solutions to the wave equation differ markedly from the case without rotation in the vicinity of the critical levels. In the two-dimensional case, the relation for the most likely critical level reduces to

$$\frac{\sigma}{f} = \frac{c_h(\sigma)}{c_h(\sigma)-\bar{u}(z)},$$

where c_h is the phase speed in the x-direction. Using the estimates of $c_h(\sigma)$ from Figure 32 and $\bar{u} \sim 10$ cm/sec from Chapter X, then $\sigma \approx 1.1f$ could have a critical level. Thus, it is possible that low frequency inertial-internal waves have critical levels in the coastal region off Oregon. Advective accelerations are not generally expected to be of significance for a wave propagating cross-stream in the frontal zone of coastal upwelling because $c_h \gg \bar{u}$. They could be significant for a wave attempting to propagate inshore of the surface front because c_h decreases as the depth decreases, or alongshore because $c_h \sim \bar{v}$. If the critical level existed for alongshore propagation in the frontal zone, it would be expected to be found near the surface front where the alongshore flow is the most intense, or in the pycnoclinic jet at the base of the inclined frontal layer.

Phillips (1968) has shown that vertical variations of N^2 and of vertical shear in the steady flow in a layer of finite thickness can

lead to nonlinear interactions with internal waves causing the internal waves to be trapped in the layer without a loss of energy or momentum from the steady fields.

Garrett (1968) has examined the theoretical formulation of the interaction between internal waves (without rotation) and a quite general shear flow. He derived and compared the radiation and interaction stress tensors, which were not identical.

Shen (1967) studied the propagation of long internal waves oriented at an arbitrary angle with respect to a mean wind with vertical shear. Neglecting the Coriolis force, he found that waves could propagate at any angle and that the cross-wind modifies the perturbation velocity to include a component of wave particle velocity perpendicular to the direction of wave propagation. Similarly, in the case of frontal interaction, if the Coriolis force is neglected, the alongshore component of wave particle velocity, v, is excited due to the effects of $\bar{v}_x$ and $\bar{v}_z$ on a wave propagating in the onshore-offshore direction.

Bowden (1965) investigated horizontal mixing due to a shear current, including the tidal as well as the steady component. Using theoretical flow models and observational material, he demonstrated that shear flows led to enhanced horizontal mixing, while density stratification suppressed vertical mixing. He attributed the turbulent mixing to tidal fluctuations, and he concluded that such effects are

likely to be significant in coastal waters.

In laboratory experiments with layered models, Zeilon (1934), Keulegan and Carpenter (1961), and Weigand (1962) have observed mixing associated with interfacial waves and the subsequent generation of secondary currents along the interface. Weigand's results are of particular interest because he included a stepped shelf; he found that water was mixed along the interface in shallow water and flowed into deep water. There is a possible analogy to be drawn here with the cross-stream flow at the base of the inclined frontal layer off Oregon. This seaward flow carries newly formed water, which is usually marked by a temperature inversion, as discussed in Chapter X.

The instability processes of internal waves are not fully understood. Woods (1968) made in situ photographs of evidence for internal wave instability. His evidence indicates that the vertical and horizontal scales of breaking internal waves are a few centimeters and tens of meters, respectively, which are much smaller scales than those of the observations in this dissertation.

A continental shelf is expected to manifest large amplitude inertial-internal waves, especially near the coastline where linear theory predicts the development of unbounded amplitudes. Griscom (1965) constructed a nonlinear theoretical model for interfacial waves which successfully reproduced observed waveforms in shallow water

on the continental shelf off southern California. In shallow water off southern California, LaFond (1961b) found that the character of the nonlinear internal waveform, and associated surface slicks, was dependent upon the position of the thermocline with respect to the sea surface and sea bottom. Recent experimental (Davis and Acrivos, 1967a) and theoretical (Benjamin, 1966), studies have found the existence of finite amplitude, solitary internal waves to be probable. Thus, it is necessary to be cautious about the validity of the linear theory and to be alert to the possible occurrence of finite amplitude effects in the observations over the continental shelf.

The most thorough study of the damping of inertial-internal waves is that of LeBlond (1966). He considered the case of continuous density stratification and of damping by eddy viscosity. LeBlond found that a long wave can not endure more than a few cycles as a free wave in depths commensurate with those of a continental shelf, though it can propagate to very large distances from the coast in the deep ocean. Thus, the internal tide is expected to be damped as it propagates shoreward over the continental shelf and to be amplified upon reflection from the sloping bottom. The process of damping may prevent the unbounded growth of inertial-internal waves by bottom reflection.

The theory of characteristics is used to estimate the effective horizontal wavelength, $\lambda^{(h)}$, and phase speed, c_h, taking into

account the influence of finite depth. Neglecting the frontal interaction, since the slope of a characteristic (a line of constant phase) is

$$\frac{dz}{dx})_{\pm} = \pm \left(\frac{\sigma^2 - f^2}{N^2 - \sigma^2}\right)^{1/2},$$

then

$$x^{\pm} - x_o = \pm \int_{z(x_o)}^{z(x)} \left(\frac{N^2 - \sigma^2}{\sigma^2 - f^2}\right)^{1/2} dz .$$

Taking the mean depth to be H, then $z_B = -H$, thus

$$\lambda^{(h)} = \int_{z_B(x_o)=-H}^{z_o(x_1)=0} \left(\frac{N^2 - \sigma^2}{\sigma^2 - f^2}\right)^{1/2} dz - \int_{z_o(x_1)=0}^{z_B(x_2)=-H} \left(\frac{N^2 - \sigma^2}{\sigma^2 - f^2}\right)^{1/2} dz,$$

where $z=z_o=0$ is the vertical coordinate of the sea surface and $x=x_1$ is the horizontal coordinate of the intersection of the sea surface with the characteristic originating on the bottom surface at $x=x_o$ and where $x=x_2$ is the horizontal coordinate of the intersection of the bottom surface with the characteristic originating on the sea surface at $x=x_1$. If the x-dependence of N^2 is neglected, then

$$\lambda^{(h)} \approx 2 \int_{z=-H}^{0} \left(\frac{N^2 - \sigma^2}{\sigma^2 - f^2}\right)^{1/2} dz;$$

if the z-dependence of N^2 is neglected, then

$$\lambda^{(h)} \simeq 2H\left(\frac{\overline{N^2}-\sigma^2}{\sigma^2-f^2}\right)^{1/2},$$

where $\overline{N^2}$ is the average value of N^2. For a wave of period $T = \frac{2\pi}{\sigma}$, the effective horizontal phase speed is

$$c_h \approx \frac{2H}{T}\left(\frac{\overline{N^2}-\sigma^2}{\sigma^2-f^2}\right)^{1/2}.$$

Thus, several qualitative remarks follow:

i) $c_h \xrightarrow[\sigma \to N]{} 0$, i.e., wavefronts do not propagate horizontally at the Väisälä-Brunt frequency;

ii) $c_h \xrightarrow[\sigma \to f]{} \infty$, i.e., wavefronts propagate horizontally at infinite speed for inertial motions;

and

iii) $c_h \xrightarrow[H \to 0]{} 0$, i.e., wavefronts never reach the coastline.

For the semidiurnal internal tide, $\sigma \approx \frac{3}{2}f$ and $f \approx 10^{-4}$ rad/sec, the following values are obtained for the continental shelf off Oregon:

	H (meters)	$\overline{N^2}\,((\frac{\text{rad}}{\text{sec}})^2)$	$\lambda^{(h)}$(m)	c_h(cm/sec)
DB15 to DB5	140	2×10^{-4}	35	78
DB10 to DB5	110	2×10^{-4}	28	62.

Then the estimated phase differences, $\Delta\theta$, are:

	Δx (KM)	$\Delta\theta$ (degrees)
DB15 to DB5	20	205
DB10 to DB5	10	130 .

Consistent with the above analysis, the effects of finite depth on $\vec{c}_p$ and $\vec{c}_g$ are investigated. With finite depth, $\vec{c}_p$ and $\vec{c}_g$ have, overall, only a horizontal component due to reflection of the waves from the free and bottom surfaces, or, equivalently, due to the influence of the BC's. In other words, the effect of finite depth is a waveguide effect; hence $\vec{c}_p$ and $\vec{c}_g$ have no net vertical component and are treated as scalars below. The vertical wave number is approximated by $m = \frac{\pi}{H}$, where H is the mean depth over a horizontal wavelength. Then, the CR yields

$$k = \frac{\pi}{H}\left(\frac{\sigma^2 - f^2}{N^2 - \sigma^2}\right)^{1/2},$$

Thus

$$c_p = \frac{\sigma}{k} = \frac{\sigma H}{\pi}\left(\frac{N^2 - \sigma^2}{\sigma^2 - f^2}\right)^{1/2},$$

which is equivalent to the results obtained above for the analysis by characteristics. From the CR,

$$\sigma^2 = \frac{N^2 k^2 + \left(\frac{\pi}{H}\right)^2 f^2}{k^2 + \left(\frac{\pi}{H}\right)^2},$$

then

$$c_g = \sigma_k$$

$$= \frac{1}{c_p} \left(\frac{H}{\pi}\right)^2 \frac{(N^2-\sigma^2)^2}{(N^2-f^2)}$$

$$= \left(\frac{H}{\sigma\pi}\right) \frac{(\sigma^2-f^2)^{1/2}(N^2-\sigma^2)^{3/2}}{(N^2-f^2)} .$$

Thus, several qualitative remarks follow:

i) $c_g \xrightarrow[\sigma \to N]{} 0$, i.e., wave energy does not propagate at the Väisälä-Brunt frequency;

ii) $c_g \xrightarrow[\sigma \to f]{} 0$, i.e., wave energy does not propagate at the inertial frequency;

and

iii) $c_g \xrightarrow[H \to 0]{} 0$, i.e., wave energy never reaches the coastline.

For $f^2 < \sigma^2 \ll N^2$, $c_g \approx \frac{1}{c_p} \left(\frac{HN}{\pi}\right)^2$ or $\frac{HN}{\pi} \approx (c_p c_g)^{1/2}$.

For the semidiurnal internal tide, and the previous estimates of the parameters,

	$c_p \left(\frac{cm}{sec}\right)$	$\frac{HN}{\pi}\left(\frac{cm}{sec}\right)$	$c_g \left(\frac{cm}{sec}\right)$
DB15 to DB5	78	63	51
DB10 to DB5	62	50	40 .

For a water depth of 140 meters, the phase speed of a surface tide is about 38 meters/sec; thus, the surface tide propagates fifty times

as rapidly as the internal tide. Then a surface tide of progressive wave type traverses the Depoe Bay array in a period of about 10 minutes, while the internal tide requires about 7 hours to make the traverse. Consequently, with a 10-minute sampling rate, the surface tide is essentially in-phase across the array, while the internal tide is essentially out-of-phase across the array.

The method of characteristics has been used to deduce the lines of constant phase for a progressive wave, as shown in Figures 6, 7, and 8. In Figure 6, the case of parallel boundaries and frontal interaction is illustrated. The figure demonstrates how the frontal interaction causes the wave to alternately accelerate and decelerate within an effective wavelength and as a function of depth. In Figure 7, the case of a wedge with subcritical bottom slope and no frontal interaction is illustrated. The figure demonstrates how the bottom slope retards a progressive wave within an effective wavelength as the wave propagates into a wedge. In Figure 8, the case of a wedge with subcritical bottom slope and with the frontal interaction is illustrated. Constant values for the parameters were chosen; they are consistent with the semidiurnal internal tide and the coastal region off Depoe Bay, Oregon, in August-September 1966:

$$E = 2.7 \times 10^{-4} \text{sec}^{-2},$$

$$s = 1 \times 10^{-3},$$

$$\bar{v}_x = -1 \times 10^{-5} \text{sec}^{-1},$$

$$\sigma = 1.5f,$$

and

$$f = 1 \times 10^{-4} \text{sec}^{-1}.$$

Both the frontal interaction and the bottom slope have a significant effect on the lines of constant phase.

a

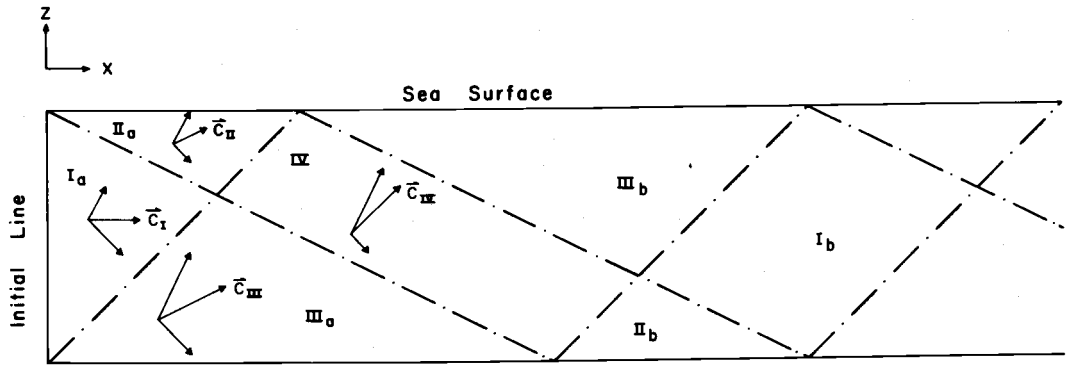

$(\lambda_1 = 1,\ \lambda_2 = -1/2)$

Regions	Wave Type	Phase Velocity
I_a, I_b	I	$\vec{C}_I = C\ (1,0)$
II_a, II_b	II	$\vec{C}_{II} = C\ (2/3, 1/3)$
III_a, III_b	III	$\vec{C}_{III} = C\ (4/3, 2/3)$
IV	IV	$\vec{C}_{IV} = C\ (1,1)$

b

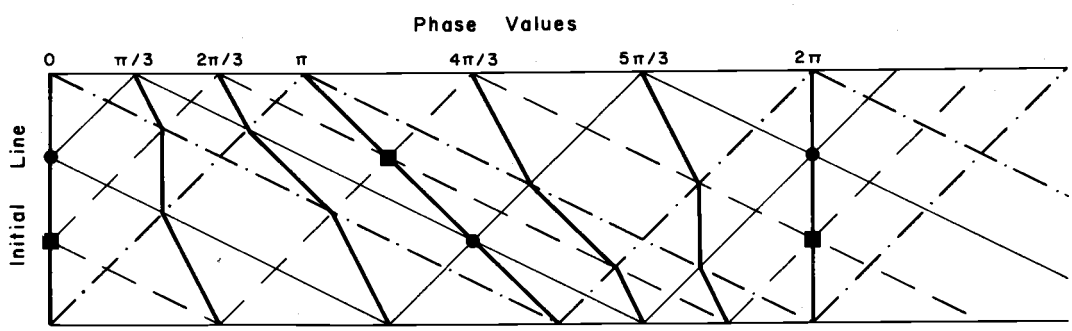

Lines of Constant Phase

Terminal Characteristics

Characteristics thru ●

Characteristics thru ■

Figure 6. Progressive wave model with parallel boundaries and with the frontal interaction.
a. Phase velocity
b. Lines of constant phase

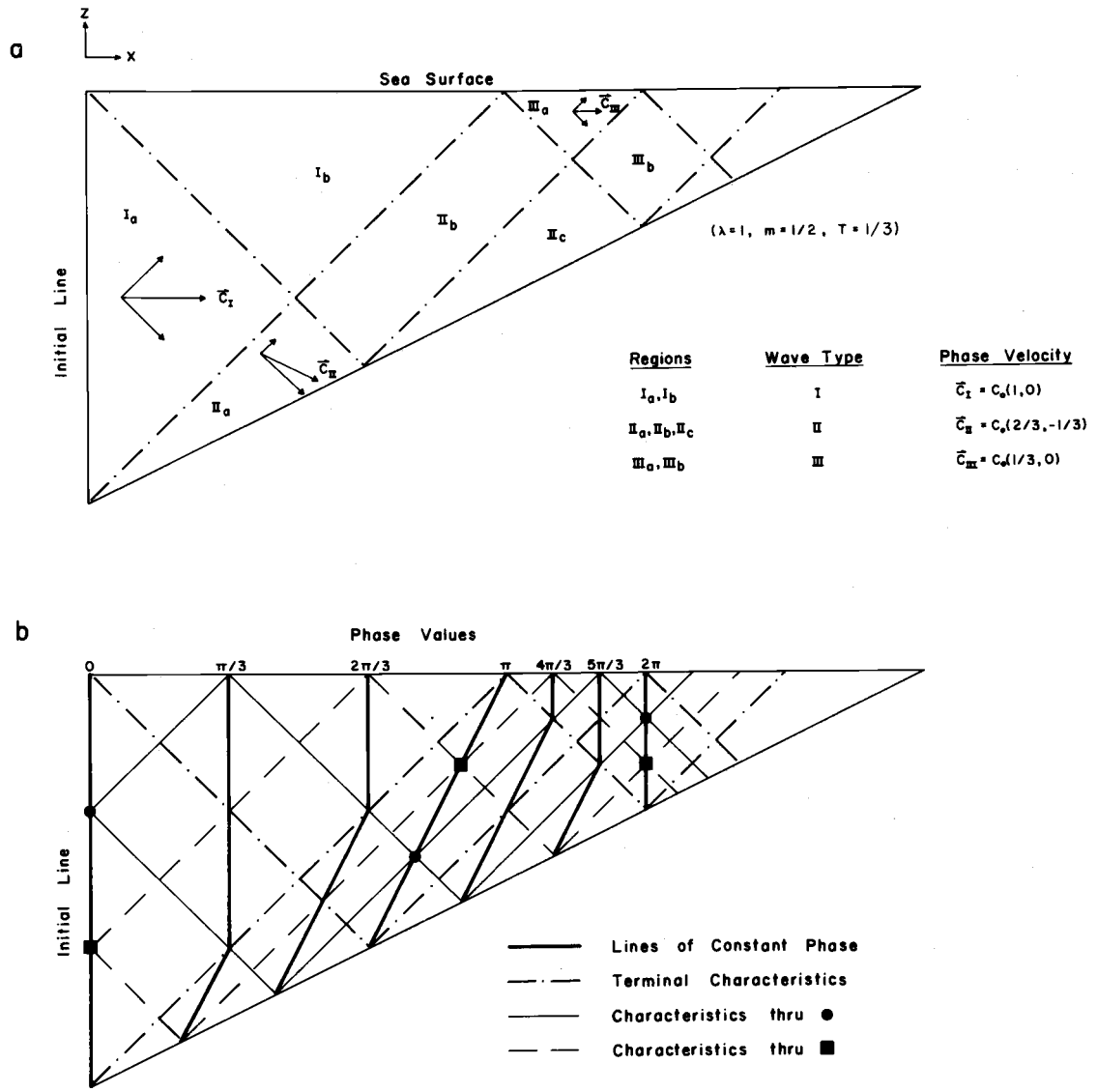

Figure 7. Progressive wave model in a coastal wedge and without the frontal interaction.
a. Phase velocity
b. Lines of constant phase

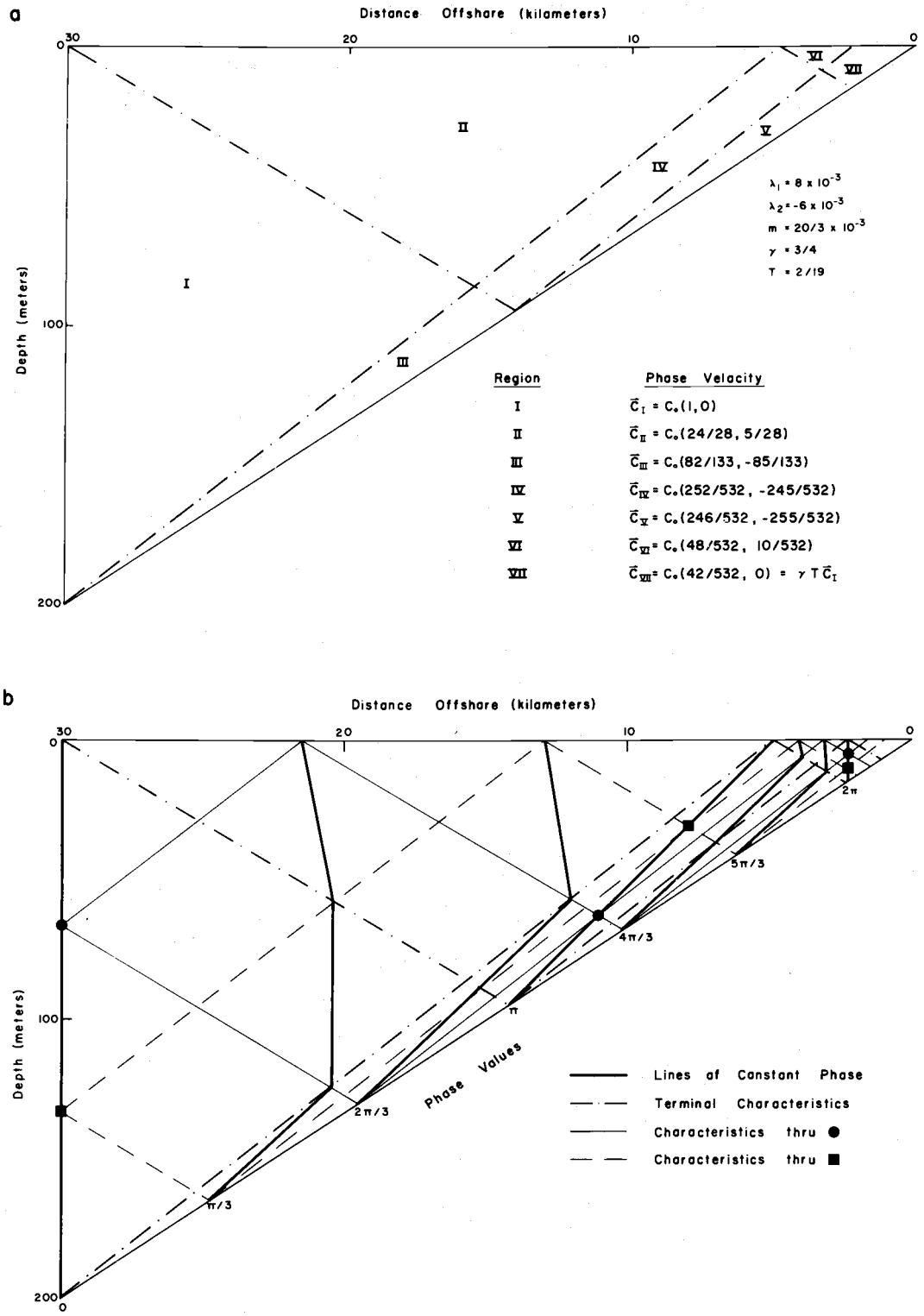

Figure 8. Progressive wave model in a coastal wedge and with the frontal interaction.
a. Phase velocity
b. Lines of constant phase

IV. THE PHYSICAL FORMULATION OF THE INERTIAL-INTERNAL WAVE PROBLEM IN A COASTAL REGION

A. Introduction

The problem of the propagation of inertial-internal waves into the coastal region off Oregon is conceived to be set in the following manner. As shown in Figure 2, the surface, or barotropic, tide propagates northward along the west coast of North America as a boundary wave something like a Kelvin wave.[14] A general discussion of permissible motions along a coastal boundary is given in Appendix I, where Figure 7 illustrates the Kelvin wave model of the semidiurnal surface tide. Under the proper conditions of density stratification and bottom slope, the semidiurnal surface tide generates an internal, or baroclinic, tide. With the values of static stability observed in the vicinity of the continental slope, the most likely region for the generation process is over the continental slope since the bottom slope there is approximately critical for the semidiurnal tide. Thus, the continental slope is considered the source region for the internal tide. Once generated, the internal tide propagates shoreward

[14] Professor Walter H. Munk (1969) has noted that the lunar semidiurnal tide propagates along the west coast of North America at a phase speed which is about 15% less than that of an ordinary Kelvin wave. He is also analyzing and interpreting recent observations of the offshore dependence of the tide. He thinks that the offshore dependence of the tide may have some of the trignometric character of the leaky modes mentioned in Appendix I.

and seaward from the continental slope. With the internal tide propagating essentially in the onshore-offshore-vertical plane, the problem is two-dimensionalized in the x-z-plane, but without neglect of the y-component of velocity. If there is perfect reflection at the coastline, a standing wave is established over the continental shelf. If the source for the internal tide is steady, and if any existent energy sinks are steady, a steady state motion occurs. With the presence of energy sinks, the motion over the continental shelf has the character of an incident and a partially reflected progressive wave.

Assuming a steady-state, ψ and its normal derivative, ψ_n, can be determined by measurements of the velocity field (u, v, w). The initial line, C, is taken as the boundary between the continental shelf and slope, $C = [(0,z): (z_B(0) \leq z \leq \eta(0))]$. Then $F(z) = \psi(0, z)$ and $G'(z) = \psi_n(0, z)$ serve as initial data, i.e., as Cauchy data, CD, for constructing the solution to the inertial-internal wave problem over the continental shelf. The measurement of $v(0, z)$ is not necessary for the determination of ψ, but $v(0, z)$ does provide information on the alongshore wave number. (In Chapters V, VI, and VII, the CD are assumed given.) The BC's are then applied at the sea surface and sea bottom to construct solutions over the continental shelf. There are two linearly independent solutions, one corresponding to each element of the CD pair. The solutions are individually of the form of standing waves. From the two standing wave

solutions, a progressive wave can be formed. The distinction between progressive and standing waves is made on the basis of the time-averaged horizontal energy flux across C. The energy flux across C is expressed in terms of the CD and their relative time phases. Other fundamental physical questions are examined viz., the reformulation of the energy conservation law, the variational principle from which the GE is derived, and the conservational law which the solution to the GE obeys as a function of the horizontal coordinate.

Several integrations are made over the coastal region and around its boundaries. As shown in Figure 9, the x-z plane cross section of the coastal region is defined by $D : [(x, z): (0 \leq x \leq L$ and $z_B(x) \leq z \leq \eta(x))]$, where $z_B(x)$ and $\eta(x)$ are the vertical coordinates of the sea bottom and the sea surface, respectively, and where 0 and L are the horizontal coordinates of the initial line and the coastline, respectively. The boundary of $R \subset D$ is

$$\Gamma = \Gamma_1 \cup \Gamma_2 \cup \Gamma_3 \cup \Gamma_4,$$

where

$$\Gamma_1 = [(x, z) : (0 \leq x \leq X \leq L \quad \text{and} \quad z = z_B(x))],$$

$$\Gamma_2 = C = [(0, z) : (z_B(0) \leq z \leq \eta(0))],$$

$$\Gamma_3 = [(x, z) : (0 \leq x \leq X \leq L \quad \text{and} \quad z = \eta(x))], \quad \text{and}$$

$$\Gamma_4 = [(X, z) : (z_B(X) \leq z \leq \eta(X))].$$

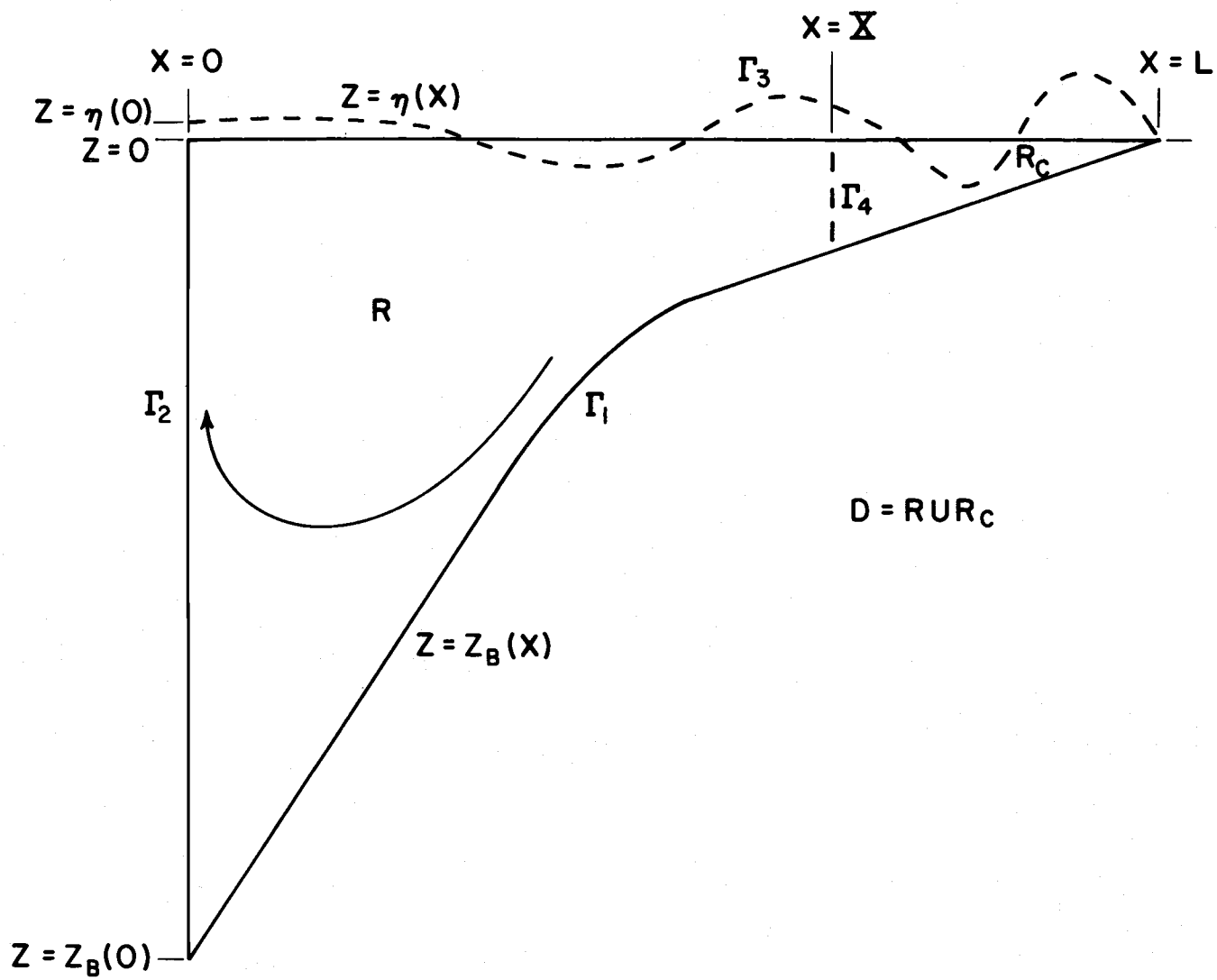

Figure 9. The domain $D = R \cup R_c$ and Γ, the boundary of R. $\Gamma = \Gamma_1 \cup \Gamma_2 \cup \Gamma_3 \cup \Gamma_4$.

when $X = L$, $R = D$ and Γ_4 vanishes, since $z_B(L) = \eta(L)$. The outward unit normals, $\hat{n}$, on Γ are:

i) For Γ_1, $\hat{n} = \frac{(m,-1)}{(1+m^2)^{1/2}}$, where $m = \frac{dz_B}{dx}$ is the bottom slope,

ii) For Γ_2, $\hat{n} = (-1, 0)$,

iii) For Γ_3, $\hat{n} = (0, 1)$, and

iv) For Γ_4, $\hat{n} = (1, 0)$.

The line integrals around Γ have the following limits of integration:

$$I_1 = \int_{\Gamma_1} (\,)ds = \int_{s=s(0)}^{s(X)} (\,)ds,$$

where $s = z_B(x)$ is the coordinate of the bottom surface;

$$I_2 = \int_{\Gamma_2} (\,)dz = \int_{z=z_B(0)}^{\eta(0)} (\,)dz,$$

where η is the coordinate of the sea surface;

$$I_3 = \int_{\Gamma_3} (\,)dx = \int_{x=0}^{X} (\,)dx;$$

and

$$I_4 = \int_{\Gamma_4} (\,)dz = \int_{z=z_B(X)}^{\eta(X)} (\,)dz.$$

The following symbols are used for certain integrals in this chapter:

$$\overline{(\,)} = \int_{z_B(x)}^{\eta(x)} (\,)dz$$

and

$$\overline{\overline{(\,)}} = \int\int_D (\,)dxdz.$$

Two integrals occur frequently in the following sections:

i) $$\rho_o \int_{\Gamma_3} w\pi dx = \rho_o \int_{\Gamma_3} \eta_t(g\eta)dx$$

$$= \frac{\partial}{\partial t} PE_s,$$

where

$$PE_s(X) = \int_{\Gamma_3} V_s dx$$

is the total potential energy of the free surface in R and

where

$$V_s(x) = \frac{\rho_o g \eta^2}{2},$$

and

ii) $$\rho_o \int_{\Gamma_2} u\pi dz = F^{(x)},$$

where $F^{(x)}$ is the horizontal energy flux across $C = \Gamma_2$.

Since $\overline{\eta}^t = 0$ for SHM, then $\overline{F^{(x)}}^t = \overline{F_1^{(x)}}^t + \overline{F_2^{(x)}}^t$, where

$$\overline{F_1^{(x)}}^t = \rho_o \int_{z=z_B(0)}^{0} \overline{u\pi}^t dz$$

is the time-averaged flow work across C and

$$\overline{F_2^{(x)}}^t \approx \rho_o \overline{u\pi\eta}^t \Big|_{\substack{x=0 \\ z=0}}$$

$$= 2\rho_o g \frac{\overline{u\eta^2}^t}{2} \Big|_{\substack{x=0 \\ z=0}}$$

is twice the time-averaged advection (flux) of potential energy of the sea surface across C.

B. The Time-Averaged Horizontal Energy Flux Across the Initial Line

For simplicity, the case of constant coefficients is considered, though the same results would follow for cases with variable coefficients.[15] From Section VI. C., the general solutions for ψ and π in the case of frontal interaction and constant coefficients are:

$$\psi = \frac{1}{(\lambda_1 - \lambda_2)} \{[\lambda_1 F(z-\lambda_2 x) - \lambda_2 F(z-\lambda_1 x)] + [G(z-\lambda_2 x) - G(z-\lambda_1 x)]\}$$

[15] The analysis would require evaluating π at the initial line from ψ expressed in terms of an integral involving the CD and the Riemann-Green function.

and

$$\pi = \frac{i(N^2-\sigma^2)}{2\sigma}\{[\lambda_1 F(z-\lambda_2 x)+\lambda_2 F(z-\lambda_1 x)] + [G(z-\lambda_2 x)+G(z-\lambda_1 x)]\},$$

where

$$F(z) = \psi|_{x=0} \quad \text{and} \quad G'(z) = \psi_n|_{x=0} = \psi_x|_{x=0}$$

are the CD and where λ_1 and λ_2 are the slopes of the upgoing and downgoing characteristics, respectively. Thus,

$$u|_{x=0} = -\psi_z|_{x=0} = -F'(z)$$

and

$$\pi|_{x=0} = \frac{i(N^2-\sigma^2)}{\sigma}\left[\frac{(\lambda_1+\lambda_2)}{2} F(z)+G(z)\right].$$

Since F and G linearly independent, and since the time dependence of F and G is only an implicit argument, a time phase may be arbitrarily assigned to F and G. Take

$$F(z;t) = e^{i\sigma t}F(z)$$

and

$$G(z;t) = e^{i(\sigma t+\phi(z))}G(z).$$

The time dependence is considered understood when not explicitly displayed.

The time-averaged horizontal energy flux, $\overline{F^{(x)}}^t$, across C is

$$\overline{F^{(x)}}^{t} = \frac{\rho_o}{4} \int_{\Gamma_2} [\pi^* u + \pi u^*] dz,$$

where $( )^*$ is complex conjugation

$$= \frac{-\rho_o}{4\sigma} \int_{\Gamma_2} (N^2 - \sigma^2) F'(z) G(z) [-ie^{-i\phi} + ie^{i\phi}] dz$$

$$= \frac{\rho_o}{2\sigma} (N^2 - \sigma^2) \int_{\Gamma_2} F'(z) G(z) \sin(\phi(z)) dz.$$

If F and G are in-phase, then $\phi = 0$ for all z and $\overline{F^{(x)}}^{t} = 0$. Therefore, the standing waves formed independently by F and G combine to form a single standing wave, or an internal seiche, shoreward of C. If $\phi \neq 0$ for all z, then $\overline{F^{(x)}}^{t} = 0$ only if $F'(z)$ and $G(z)$ are orthogonal on Γ_2 with respect to weight function $\sin(\phi(z))$. Otherwise, a progressive wave exists. If $\sigma = N$, $\overline{F^{(x)}}^{t} = 0$, as it must for the strictly vertical Väisälä-Brunt oscillations.

C. The Energy Integral

The energy integral is formulated in a more general way than in Chapter II. New definitions of energy components are necessary for the analysis in the following sections. The analysis is valid for the frontal interaction, variable coefficients, variable depth, and a free surface.

Rewrite the primitive equations:

(1) $$u_t - fv = -\pi_x,$$

(2) $$v_t + (f+\bar{v}_x)u + w\bar{v}_z = 0,$$

(3) $$w_t + \frac{\rho g}{\rho_o} = -\pi_z,$$

(4) $$\rho_t + u\bar{\rho}_x + w\bar{\rho}_z = 0,$$

and

(5) $$u_x + w_z = 0.$$

(1) and (3) are similar because there is a pressure term present, while (2) and (4) are similar because of the absence of a pressure term. This similarity of forms suggests treating u and w and v and ρ in an analogous manner when forming energy integrals. Take $(u, w) = (\xi_t, \zeta_t)$, then (2) and (4) become

(2)' $$(v + (f+\bar{v}_x)\xi + \bar{v}_z\zeta)_t = 0,$$

or

$$v + (f+\bar{v}_x)\xi + \bar{v}_z\zeta = 0, \quad \text{WLOG}$$

and

(4)' $$(\rho + \bar{\rho}_x\xi + \bar{\rho}_z\zeta)_t = 0,$$

or

$$\rho + \bar{\rho}_x\xi + \bar{\rho}_z\zeta = 0, \quad \text{WLOG.}$$

Eliminate v from (1) and ρ from (3) with the use of (2)' and (4)'; then

(1)' $$u_t + [f(f+\bar{v}_x)\xi + M^2\zeta] = -\pi_x$$

and

(3)' $$w_t + [M^2\xi + N^2\zeta] = -\pi_z.$$

Multiply (1)' by $u = \xi_t$ and (3)' by $w = \zeta_t$, then

(1)'' $$(\frac{u^2}{2})_t + f(f+\bar{v}_x)(\frac{\xi^2}{2})_t + M^2\zeta\xi_t = -u\pi_x$$

and

(3)'' $$(\frac{w^2}{2})_t + N^2(\frac{\zeta^2}{2})_t + M^2\zeta_t\xi = -w\pi_z.$$

Add (1)'' and (3)'' and multiply by ρ_o, then

(6) $$(\frac{\rho_o}{2})(u^2+w^2)_t + (\frac{\rho_o}{2})(f(f+\bar{v}_x)\xi^2 + 2M^2\zeta\xi + N^2\zeta^2))_t = -(up_x + wp_z)$$

$$= -(up)_x - (wp)_z,$$

by (5), the EOC. The LHS of (6) is taken to be the total energy per unit volume, E. Integrate (6) over D, then

$$\overline{\overline{E}}_t = \int_{\Gamma_1} \frac{\rho_o(um-w)ds}{\sqrt{1+m^2}} + \int_{\Gamma_2} updz - \int_{\Gamma_3} wpdx$$

$$= F^{(x)} - \frac{\partial}{\partial t}(PE_s),$$

since the RBC holds along Γ_1. Thus,

$$(\overline{\overline{E}} + PE_s)_t = F^{(x)}.$$

Therefore, if $\overline{F^{(x)}}^t = 0$, then $\overline{\overline{E}} + PE_s$ = constant, without assuming SHM as in Chapter II. Thus, from Section B, energy is conserved for a standing wave and not for a progressive wave.

The components of E are defined below:

$$T_H = \frac{\rho_o u^2}{2}, \qquad T_V = \frac{\rho_o w^2}{2},$$

$$V_H = \frac{\rho_o}{2}[f(f+\bar{v}_x)\xi^2 + M^2\zeta\xi],$$

and

$$V_V = \frac{\rho_o}{2}[N^2\zeta^2 + M^2\zeta\xi],$$

thus

$$E = T + V, \quad T = T_H + T_V, \quad \text{and} \quad V = V_H + V_V,$$

where T and V represent kinetic and potential energy, respectively, and the subscripts H and V represent horizontal and vertical components, respectively. With the introduction of ψ, and with the assumption of SHM,[16] then

---

[16] Having assumed SHM, then all of the energy terms implicitly involve the products of first partials of ψ and of ψ conjugate, or the cross products of the partials of ϕ and ψ and their conjugates in Section D. This point is essential in Section D where the sum $I_2 + I_3$ is shown to include the time-averaged horizontal energy flux across C.

$$T_H = \frac{\rho_o}{2}(\psi_z)^2, \qquad T_V = \frac{\rho_o}{2}(\psi_x)^2,$$

$$V_H = \frac{\rho_o}{2}\left[\frac{f(f+\bar{v}_x)}{\sigma^2}(\psi_z)^2 - \frac{M^2}{\sigma^2}\psi_x\psi_z\right],$$

and

$$V_V = \frac{\rho_o}{2}\left[\frac{N^2}{\sigma^2}(\psi_x)^2 - \frac{M^2}{\sigma^2}\psi_x\psi_z\right].$$

Without the frontal interaction,

$$V_H = \frac{\rho_o}{2}\,\frac{f^2}{\sigma^2}(\psi_z)^2,$$

thus V_H is the rotational potential energy. With the frontal interaction, both V_H and V_V are modified and V is not positive definite.

Similarly, the Lagrangian, Λ, is required in the following sections:

$$\Lambda = \Lambda_H + \Lambda_V,$$

where

$$\Lambda_H = T_H - V_H \quad \text{and} \quad \Lambda_V = T_V - V_V.$$

Taking into account the potential energy of the free surface,

$$\bar{\Lambda}_o = \bar{\Lambda} - V_s,$$

where $\bar{\Lambda}_o$ is then the Lagrangian for a vertical column.

D. The Variational Principle

The variational principle is discussed for three reasons:

i) The GE and BC's are placed on solid analytical and physical grounds once the variational principle is obtained,

ii) It is the analysis for the variational principle which has led to the proper identification of the components of E in Section C, and

iii) The variational principle also leads to the proper interpretation of the spatial conservation law in Section E.

The mechanical system analyzed is a continuous system in two independent variables; consequently, the variational principle involves double integrals (Gelfand and Fomin, 1963). The principle of least action is invoked and the action integral, J, is sought. Since x is constant on C, x is time-like, and then

$$J = \int_{x=0}^{L} \bar{\Lambda}_o dx$$

$$= \frac{\rho_o}{2} \iint_D \left[(1-(\frac{N}{\sigma})^2)(\psi_x)^2 + (1-\frac{f(f+\bar{v}_x)}{\sigma^2})(\psi_z)^2 + 2\frac{M^2}{\sigma^2}(\psi_x\psi_z) \right] dxdz$$

$$- \frac{g}{\sigma^2} \int_{\Gamma_3} (\psi_x)^2 dx$$

Let ψ be varied to $\tilde{\psi}$, where $\tilde{\psi} = \psi + \epsilon\phi + 0(\epsilon^2)$, ϵ is an arbitrarily small parameter, and $\phi \in \Phi$, the class of admissible functions. Φ is defined to be the class of all functions which are twice continuously differentiable in D and which vanish on Γ_1, consistent with the RBC along the bottom surface, and which equal $F(z)$ on Γ_2, consistent with the CD given on C. Vary J with respect to ϕ, then

$$\delta J = \epsilon \rho_o \{ \iint_D \left[(1-(\frac{N}{\sigma})^2)\psi_x\phi_x + (1-\frac{f(f+\bar{v}_x)}{\sigma^2})\psi_z\phi_z + \frac{M^2}{\sigma^2}(\psi_z\phi_x+\psi_x\phi_z) \right] dxdz$$

$$- \frac{g}{\sigma^2} \int_{\Gamma_3} \psi_x\phi_x dx \} + O(\epsilon^2).$$

The condition for the first variation of J to vanish is that

$$\iint_D \{ [(\sigma^2-N^2)\psi_x + M^2\psi_z]\phi_x$$

$$+ [(\sigma^2 f(f+\bar{v}_x))\psi_z + M^2\psi_x]\phi_z \} dxdz - g \int_{\Gamma_3} \psi_x\phi_x dx = 0.$$

Integrating by parts, this condition becomes

$$\sum_i I_i = I_o + I_1 + I_2 + I_3 = 0,$$

where

$$I_o = \iint_D \phi[(N^2-\sigma^2)\psi_{xx} - 2M^2\psi_{xz} - (\sigma^2-f(f+\bar{v}_x))\psi_{zz}]dxdz,$$

$$I_1 = \int_{\Gamma_1} \phi[m((\sigma^2-N^2)\psi_x+M^2\psi_z) - (M^2\psi_x+(\sigma^2-f(f+\bar{v}_x))\psi_z)]\frac{ds}{(1+m)^{1/2}}$$

$$= 0, \quad \text{because } \phi \text{ vanishes on } \Gamma_1,$$

$$I_2 = -\int_{\Gamma_2} \phi[(\sigma^2-N^2)\psi_x + M^2\psi_z]dz$$

$$= -\int_{\Gamma_2} \phi(i\sigma\pi_z)dz, \quad \text{from the z-component EOM,}$$

$$= i\sigma\int_{\Gamma_2} \phi_z\pi dz - i\sigma\phi\pi\Big|_{z=z_B(0)}^{\eta(0)}$$

and

$$I_3 = \int_{\Gamma_3} \phi[(\sigma^2-f(f+\bar{v}_x))\psi_z+M^2\psi_x+g\psi_{xx}]dx - g\phi\psi_x\Big|_{z=\eta(0)}^{\eta(L)}.$$

Then

$$I_2 + I_3 = i\sigma\int_{\Gamma_2} F'(z)\pi dz + \phi[-\pi_t+g\psi_x]\Big|_{z=\eta(0)}$$

$$+ \int_{\Gamma_3} \phi[(\sigma^2-f(f+\bar{v}_x))\psi_z + M^2\psi_x + g\psi_{xx}]dx,$$

since

$$\phi\Big|_{z=\eta(L)} = \phi\Big|_{z=z_B(0)} = 0.$$

Since $\sum_i I_i$ must vanish for any $\phi \in \Phi$, take $\phi = 0$ on Γ for a particular case, then $I_o = 0$. But ϕ is otherwise arbitrary,

thus

$$(N^2-\sigma^2)\psi_{xx} - 2M^2\psi_{xz} - (\sigma^2-f(f+\bar{v}_x))\psi_{zz} = 0,$$

which is the GE. Again, as a particular case, let $\phi = 0$ on Γ_3, then

$$I_2 + I_3 = 0.$$

Since

$$i\sigma \int_{\Gamma_2} F'(z)\pi dz = -\frac{i\sigma}{\rho_o} \overline{F^{(x)}}^t,$$

then J an extremum only if there is no time-averaged horizontal energy flux across C. Finally, with $\overline{F^{(x)}}^t = 0$, and for any non-zero ϕ on Γ_3, it is necessary that

$$\pi_t = g\psi_x = g\eta_t \quad \text{at} \quad z = \eta(0)$$

and

$$(\sigma^2-f(f+\bar{v}_x))\psi_z + M^2\psi_x + g\psi_{xx} = 0 \quad \text{on} \quad \Gamma_3,$$

which are both forms of the FBC.

The GE and the FBC have been derived by a variational principle, subject to the kinematic constraint along the bottom boundary and the constraint of $\overline{F^{(x)}}^t = 0$, or the conservation of energy in D. The identification of the component T's and V's in the previous section has been shown to be consistent.

For an alternative interpretation of J, Λ is examined in terms of the pressure, p:

$$\Lambda = \frac{\rho_o}{2\sigma^2}\{\psi_x[(\sigma^2-N^2)\psi_x+M^2\psi_z]+\psi_z[(\sigma^2-f(f+\bar{v}_x))\psi_z+M^2\psi_x]\}$$

$$= \frac{\rho_o}{2\sigma^2}[\psi_x(i\sigma\pi_x)-\psi_z(i\sigma\pi_x)],$$

then

$$J = \int_{x=0}^{L} \bar{\Lambda}\,dx - PE_s$$

$$= \frac{i}{2\sigma}\iint_D [(wp)_z+(up)_x]dxdz - PE_s$$

$$= \frac{i}{2\sigma}\left[\int_{\Gamma_3} wpdx - \int_{\Gamma_2} updz\right] - PE_s$$

$$= \frac{i}{2\sigma^2}\int_{\Gamma_3}\psi_x p_t dx - \frac{i}{2\sigma}\overline{F^{(x)}}^t - PE_s$$

$$= \frac{\rho_o g}{2}\int_{\Gamma_3}\eta^2 dx - \frac{i}{2\sigma}\overline{F^{(x)}}^t - PE_s$$

or,

$$J = -\frac{i}{2\sigma}\overline{F^{(x)}}^t.$$

Thus, if $\overline{F^{(x)}}^t = 0$, then

i) $J = 0$,

ii) $\delta J = 0$, and

iii) $\bar{\bar{E}}$ is conserved.

With $J = 0$, then

$$\overline{\overline{L}}_H + \overline{\overline{L}}_V - PE_s = 0$$

or

$$\overline{\overline{T}}_H + \overline{\overline{T}}_V = \overline{\overline{V}}_H + \overline{\overline{V}}_V + PE_s,$$

which proves the equipartition of the spatially averaged kinetic and potential energy.

E. The Spatial Conservation Law for the Mixed Initial-Boundary Value Problem

The GE is investigated to find the conservation law which the solution obeys as a function of space (Courant and Hilbert, 1962), in contradistinction to the conservation of energy as a function of time. The role of the FBC and RBC in determining the spatial distribution of the energy quantities for the mixed initial-boundary value problem, MIBVP, is determined. The condition of SHM in time continues to apply.

Since x is time-like for the MIBVP, the GE is multiplied by $\frac{\rho_o}{\sigma^2}\psi_x$ and rearranged:

$$\frac{\rho_o}{\sigma^2}\psi_x[(N^2-\sigma^2)\psi_{xx} - 2M^2\psi_{xz} - (\sigma^2-f(f+\bar{v}_x))\psi_{zz}] = 0$$

or,

$$\vec{\nabla}_2 \cdot \vec{q} + h = 0, \tag{7}$$

where

$$\vec{\nabla}_2 = (( )_x, ( )_z),$$

$$\vec{q} = \rho_o\{\frac{1}{2}[(\frac{N^2}{\sigma^2}-1)(\psi_x)^2 + (1-\frac{f(f+\bar{v}_x)}{\sigma^2})(\psi_z)^2],$$

$$- [\frac{M^2}{\sigma^2}(\psi_x)^2 + (1-\frac{f(f+\bar{v}_x)}{\sigma^2})(\psi_x\psi_z)]\},$$

and

$$h = \frac{\rho_o}{2\sigma^2}[(M^2)_z(\psi_x)^2 + f\bar{v}_{xx}(\psi_z)^2 - 2f\bar{v}_{xz}(\psi_x\psi_z)]$$

$$= \frac{\rho_o}{2\sigma^2}[(f\bar{v}_{zz}\psi_x - f\bar{v}_{xz}\psi_z)\psi_x + (f\bar{v}_{xx}\psi_z - f\bar{v}_{xz}\psi_x)\psi_z].$$

The divergence form of $\vec{q}$ prompts integration of (7) over R. The areal integral over R is reduced to line integrals along Γ to find the conservation law:

$$\iint_R [\nabla \cdot \vec{q} + h]dxdz = 0,$$

or

$$\int_\Gamma \vec{q} \cdot \hat{n}\, ds = H, \tag{8}$$

where

$$H = -\iint_R h dxdz.$$

Then

$$\int_\Gamma \vec{q} \cdot \hat{n}\, ds = I_1 + I_2 + I_3 + I_4,$$

where

$$I_1 = \frac{\rho_o}{\sigma^2}\int_{\Gamma_1}\{\frac{m}{2}[(N^2-\sigma^2)(\psi_x)^2+(\sigma^2-f(f+\bar{v}_x))(\psi_z)^2] + [M^2(\psi_x)^2+(\sigma^2-f(f+\bar{v}_x))(\psi_x\psi_z)]\}\frac{ds}{(1+m^2)^{1/2}},$$

$$I_2 = \frac{-\rho_o}{2}\int_{\Gamma_2}[(\frac{N^2}{\sigma^2}-1)(\psi_x)^2 + (1-\frac{f(f+\bar{v}_x)}{\sigma^2})(\psi_z)^2]\,dz,$$

$$I_3 = \frac{-\rho_o}{\sigma^2}\int_{\Gamma_3}[M^2(\psi_x)^2 + (\sigma^2-f(f+\bar{v}_x))(\psi_x\psi_z)]\,dx,$$

and

$$I_4 = \frac{-\rho_o}{2}\int_{\Gamma_4}[(\frac{N^2}{\sigma^2}-1)(\psi_x)^2 + (1-\frac{f(f+\bar{v}_x)}{\sigma^2})(\psi_z)^2]\,dz.$$

Take

$$\chi(x) = \frac{\rho_o}{2}\int_{z=z_B(x)}^{\eta(x)}[(\frac{N^2}{\sigma^2}-1)(\psi_x)^2 + (1-\frac{f(f+\bar{v}_x)}{\sigma^2})(\psi_z)^2]\,dz$$

$$= \bar{L}_H - \bar{L}_V,$$

from Section C; then

$$I_2 = -\chi(0)$$

and

$$I_4 = \chi(X).$$

From the FBC,

$$I_3 = \frac{\rho_o}{\sigma^2} \int_{\Gamma_3} \psi_x \psi_{xx} dx$$

$$= \frac{\rho_o}{2\sigma^2} g (\psi_x)^2 \Big|_{z=\eta(0)}^{\eta(X)}$$

$$= V_s(X) - V_s(0).$$

Since $\psi_x + m\psi_z = 0$ on Γ_1, then

$$I_1 = \frac{\rho_o}{2\sigma^2} \int_{\Gamma_1} \frac{m u_B^2}{(1+m^2)^{1/2}} \{m^2(N^2-\sigma^2) - (\sigma^2 - f(f+\bar{v}_x)) + 2M^2 m\} ds,$$

where

$$u_B = -\psi_z \Big|_{z=z_B(x)}.$$

The integrand of I_1 is reduced further by introducing the equations for the slopes of the characteristics derived in Section V. B.:

$$\lambda_1 = S + R$$

and

$$\lambda_2 = S - R,$$

where

$$S = \frac{-M^2}{(N^2-\sigma^2)}$$

and

$$R = \left(S^2 + \frac{(\sigma^2 - f(f+\bar{v}_x))}{(N^2-\sigma^2)}\right)^{1/2}.$$

Thus,

$$I_1 = \frac{-\rho_o}{2\sigma^2} \int_{\Gamma_1} \frac{mu_B^2}{(1+m^2)^{1/2}} (N^2-\sigma^2)(\lambda_1-m)(-\lambda_2+m)ds.$$

Take $B = -I_1$, then the spatial conservation law, (8), is reduced to:

$$\chi(X) + V_s(X) = \chi(0) + V_s(0) + B + H. \tag{9}$$

Several deductions can be made from the spatial conservation law:

i) The law governs the balance between $\overline{L}_H - \overline{L}_V + V_s$ as influenced by B and H.

ii) H contains the contribution of the frontal interaction; it can be considered to represent the effects of internal reflections.

iii) $\chi(0)$ can be written in terms of the CD:

$$\chi(0) = \frac{1}{2} \int_{\Gamma_2} [(\frac{N^2}{\sigma^2} - 1)(G'(z))^2 + (1 - \frac{f(f+\overline{v}_x)}{\sigma^2})(F'(z))^2] dz.$$

Thus, $\chi(0)$ is unrelated to the horizontal energy flux across C, and its time-average is not zero. For $f(f+\overline{v}_x) < \sigma^2 < N^2$, which excludes the anomalous, high and low frequency inertial-internal waves, then $\chi(x) \geq 0$ for all x.

iv) V_s contains the effect of the free surface; if the sea surface is rigid, $V_s = 0$ for all x.

v) B contains the contribution from the horizontal kinetic energy at the bottom. $B = 0$ for all x if $m = 0$ for all x or $\sigma = N$, i.e., for uniform depth or Väisälä-Brunt oscillations, B makes no contribution. For $f(f+\bar{v}_x) < \sigma^2 < N^2$, $\lambda_1 > 0$ and $\lambda_2 < 0$, thus $(\lambda_1 - m)$ is of arbitrary sign and $(-\lambda_2 + m) > 0$. If $\lambda_1 = m$ for all x, then B is again zero; i.e., for critical bottom slopes, B makes no contribution to $\chi + V_s - H$. If $\lambda_1 > m$ for all x, then $B > 0$; i.e., for subcritical bottom slopes, $\chi + V_s - H$ increases as x increases. Similarly, if $\lambda_1 < m$ for all x, then $B < 0$; i.e., for supercritical bottom slopes, $\chi + V_s - H$ decreases as x increases.

vi) As $X \to L$, then $R \to D$ and Γ_4 vanishes, hence $\chi(X) \to \delta\chi(L)$, where $\delta\chi(L) \neq 0$ only if $L_H - L_V$ becomes infinite in the limit. Thus,

$$\delta\chi(L) + V_s(L) = \chi(0) + V_s(0) + B(L) + H(L).$$

Neglecting the frontal interaction ($H(L) = 0$), and assuming the sea surface rigid ($V_s(L) = V_s(0) = 0$), in the case of subcritical bottom slope, $\delta\chi(L) = \chi(0) + B(L) > 0$. Therefore, $L_H - L_V$ and $\vec{\nabla}_2\psi$ become unbounded at the coastline for the case of subcritical bottom slope, no frontal interaction, and a rigid sea surface. If either the frontal

interaction or the free surface is included in the analysis, $\vec{\nabla}_2\psi$ need not become unbounded at the coastline. For the critical and supercritical cases, $\delta\chi(L)$ can vanish. For instance, in the supercritical case with a rigid sea surface and without the frontal interaction, there can be a balance between $\chi(0)$ and $B(L)$.

In particular, the analysis of the conservation law has proved the singular nature of the first order partial derivatives of ψ, and thus the velocity field, at the coastline in the case of a subcritical bottom slope, a rigid sea surface, and no frontal interaction. This feature of the solution is also demonstrated from an analysis of the characteristics in Section VI. D. for constant coefficients and a uniform bottom slope. The analysis of this section is valid for a more general bottom slope. The most important result is the demonstration that the free surface may play a crucial role in keeping the solution finite at the coastline.

V. THE MATHEMATICAL FORMULATION OF THE MIXED INITIAL-BOUNDARY VALUE PROBLEM FOR INERTIAL-INTERNAL WAVES

A. Introduction

In this and the two succeeding chapters, solution theories for a set of problems for inertial-internal waves in a coastal region are developed and applied. In this chapter, the foundations of the theory of the MIBVP for hyperbolic, second order partial differential equations in two indpendent variables are discussed. The GE derived in Chapter II for inertial-internal waves with the frontal interaction is used in the discussion. Chapter VI treats cases for which the GE has constant coefficients, and Chapter VII treats cases with variable coefficients.

B. Formulation in Terms of the Characteristic Coordinates

Since the GE is hyperbolic in the spatial variables for the frequencies of the inertial-internal wave passband, there exist characteristic surfaces in (x, z, ψ)-space associated with the solutions to the GE. For problems involving variable density stratification and variable bottom topography, a solution theory can be constructed based upon the properties of the characteristic surfaces. When finite amplitude effects become significant, the theory of characteristics for the linear problem can be extended to analyze the quasi-linear

equivalent to the GE. The two-dimensionalized problem can be examined in terms of its ordinary characteristics; for higher dimensional or higher order problems, bicharacteristics, and possibly higher order characteristics, must be used, about which there is only limited knowledge and experience. Campbell and Robinson (1955) present a discussion of the MIBVP, including a solution theory, for a wedge-shaped region. The discussion which follows is largely based on material to be found in Garabedian (1964), Courant and Hilbert (1962), and Abbott (1966).

There are three types of initial value problems:

i) The Cauchy problem, which occurs when the function and its normal derivative, i.e., the CD, are given along a non-characteristic ground curve, i.e., the initial line, C,

ii) The Goursat problem, which occurs when the CD are given along a characteristic ground curve, i.e., an ordinary characteristic, and the function, or its normal derivative, is specified along a non-characteristic ground curve which intersects the characteristic ground curve, and

iii) The characteristic initial value problem, which occurs when the function is given along each of two intersecting characteristics.

For the MIBVP, the CD are given on a non-characteristic initial line, C, and BC's are given on non-characteristic curves, B,

except where noted. $B \cup C = \Gamma$, the boundary of D, where D is the region for which the solution is sought. Consequently, the MIBVP is composed of problem types i) through iii). The solution is uniquely determined in the sub-region, R, the domain of influence, bounded by the intersecting characteristics drawn through the terminii of C.

If a characteristic is tangential to B, B is termed critical. If one of the two characteristics intersecting at any point on B has a segment in D in the positive direction of the time-like variable, and if the other characteristic has a segment in D in the negative direction, then B is termed subcritical. Otherwise, B is termed supercritical. The three cases for B are illustrated in Figure 6. If B is critical, the solution is over-determined in the sense that the CD and BC can not be independently specified. If B is supercritical, the solution is over-determined in the sense that both elements of the CD can not be independently specified. If B is subcritical, a BC can be used to extend each element of the CD pair from C to CE independently. CE is the extension of C which is necessary to enlarge the domain of influence to cover all of D. This construction is indicated in Figure 10f. CE has two components: CE^+, the extension of C above the sea surface, and CE^- the extension of C below the sea bottom.

The general linear GE is

(1) (GE): $$L(\psi) = A\psi_{xx} + B\psi_{xz} + C\psi_{zz} = 0$$

where A, B, and C are functions of x and z.

Through a change of variables, from (x, z) to (η, ζ) such that the Jacobian, $J(\eta, \zeta)$, of the transformation does not vanish, the GE is reduced to the canonical GE, the CGE: $\psi_{\eta\zeta} = G(\eta, \zeta, \psi_\eta, \psi_\zeta)$, where η and ζ are termed the characteristic coordinates. The family of curves η and ζ constant constitutes the family of characteristic ground curves of the problem. In the case of constant coefficients, the CGE becomes $\psi_{\eta\zeta} = 0$, the one-dimensional wave equation and the coordinate transformation is linear. When at least one of A, B, and C are variable, the general canonical form is usually the simplest reduction attainable since the coordinate transformation is nonlinear. Because the solution theory of the one-dimensional wave equation is well-known, it is relatively simple to solve a problem with constant coefficients, accounting for the BC's and boundary shapes. A significant difference is that the general theory of second-order linear hyperbolic equations in two independent variables is required to solve problems with variable coefficients.

The change of variables is performed in the usual manner, yielding:

(2) $$L(\psi) = Q(\eta,\eta)\psi_{\eta\eta} + 2Q(\eta,\zeta)\psi_{\eta\zeta} + Q(\zeta,\zeta)\psi_{\zeta\zeta} + L(\eta)\psi_\eta + L(\zeta)\psi_\zeta = 0,$$

where the operator $Q(r, s)$ is defined to be, with r and s as dummy variables:

$$Q(r, s) = A(r_x s_x) + \frac{1}{2}B(r_x s_z + r_z s_x) + C(r_z s_z).$$

To accomplish the coordinate transformation and reduction to canonical form, it must be true that

$$Q(\eta, \eta) = Q(\zeta, \zeta) = 0 \quad \text{and} \quad Q(\eta, \zeta) \neq 0.$$

For example,

$$Q(\eta, \eta) = 0$$

implies that

$$\left(\frac{dz}{dx}\right)_\eta = \frac{-\eta_x}{\eta_z} = (\lambda_1, \lambda_2) = \frac{+B \pm (B^2 - 4AC)^{1/2}}{2A},$$

where the discriminant, $B^2 - 4AC$, is greater than zero in the domain of hyperbolicity of the GE. λ_1 and λ_2 are the slopes of the characteristics. An identical relation follows for ζ, so the equation with the positive slope is assigned to η and the one with a negative slope to ζ. It is convenient to take

$$R = \frac{(B^2 - 4AC)^{1/2}}{2A} \quad \text{and} \quad S = \frac{B}{2A},$$

then

$$\lambda_1 = S + R \quad \text{and} \quad \lambda_2 = S - R.$$

When R and S are constants, the characteristics are given by $\eta = z - \lambda_1 x$ and $\zeta = z - \lambda_2 x$.

Again, in the domain of hyperbolicity of the GE, it follows that,

$$\frac{Q(\eta, \zeta)}{\eta_z \zeta_z} = A\left(\frac{\eta_x \zeta_x}{\eta_z \zeta_z}\right) + \frac{1}{2} B\left(\frac{\eta_x}{\eta_z} + \frac{\zeta_x}{\zeta_z}\right) + C = \frac{4AC - B^2}{2A} \neq 0.$$

This condition on $Q(\eta, \zeta)$ is equivalent to satisfying the requirement that $J(\eta, \zeta) \neq 0$, i. e.,

$$J = \eta_x \zeta_z - \eta_z \zeta_x = \left[\frac{(B^2 - 4AC)^{1/2}}{A}\right] \zeta_z \eta_z \neq 0.$$

Since $Q(\eta, \eta)$ and $Q(\zeta, \zeta) = 0$, and though $L(\psi)$ must be continuous, $\psi_{\eta\eta}$ and $\psi_{\zeta\zeta}$ may be discontinuous because they do not appear in the CGE. Thus ψ may have discontinuities in its second and higher order derivatives with respect to η and ζ, but only across characteristics η and ζ constant, respectively. Such discontinuities correspond to "shocks;" they are constrained to propagate along the characteristics. Finally, the CGE is:

(3) (CGE):
$$\psi_{\eta\zeta} = \frac{-L(\eta)\psi_\eta - L(\zeta)\psi_\zeta}{2Q(\eta, \zeta)}.$$

If A, B, and C are constant, the RHS of (3) is zero. In that case, the general solution of the CGE is that of D'Alembert:

$$(4) \qquad \psi = \frac{1}{(\lambda_1 - \lambda_2)}\{[\lambda_1 F(\zeta) - \lambda_2 F(\eta)] + [G(\zeta) - G(\eta)]\},$$

which is derived in detail in Section VI. C. The arbitrary CD given on C are

$$\psi(0, z) = F(z)$$

and

$$\psi_x(0, z) = G'(z), \quad \text{where} \quad G'(z) = \frac{dG}{dz}.$$

It is possible to apply the BC's to (4) to extend the CD over CE; this technique of analytic extension is developed in the next chapter.

When the coefficients are not constant, a canonical form of the solution does not necessarily exist. One approach is to solve the adjoint problem to find the corresponding Riemann-Green function. Then Riemann's method is used to reduce the problem to quadratures to be carried out along C and the bounding characteristics; this subject is pursued in Section F. Alternatively, the problem can be treated as a first-order hyperbolic system of two equations; this approach is discussed in the next section.

C. Reduction to Hyperbolic Systems

The GE,

$$\psi_{xx} + (\lambda_1 + \lambda_2)\psi_{xz} + \lambda_1\lambda_2\psi_{zz} = 0,$$

can be written as

(5) $$(w_x+\lambda_2 w_z) - \lambda_1(u_x+\lambda_2 u_z) = 0$$

or

(6) $$(w_x+\lambda_1 w_z) - \lambda_2(u_x+\lambda_1 w_z) = 0.$$

Because (5) and (6) have the form of directional derivatives along the characteristics, they are a pair of coupled, first-order ordinary differential equations equivalent to the GE.

Since

$$(\ )_x + \lambda_1(\ )_z = \frac{1}{x_\eta}(\ )_\eta$$

and

$$(\ )_x + \lambda_2(\ )_z = \frac{1}{x_\zeta}(\ )_\zeta,$$

then (5) and (6) become

(7) $$w_\zeta - \lambda_1 u_\zeta = 0,$$

an integration to be carried out along η constant, and

(8) $$w_\eta - \lambda_2 u_\eta = 0,$$

an integration to be carried out along ζ constant.

Because λ_1 and λ_2 are functions of η and ζ, the integrations can not usually be accomplished in closed form. Formulas (7) and (8) are readily adaptable to numerical solution, Section VII. E.

Though more formal procedures are generally necessary, in this case, the Riemann invariants of the GE are found directly from

(7) and (8). Integrating (7) along η constant and (8) along ζ constant, then

$$J_1 = w - \int_{\eta \text{ constant}} \lambda_1 du$$

and

$$J_2 = w - \int_{\zeta \text{ constant}} \lambda_2 du$$

are the Riemann invariants along η and ζ constant, respectively. Since λ_1 and λ_2 generally depend on both η and ζ, J_1 and J_2 can not always be explicitly evaluated, yet they can be used as conservation laws to check the solution. If λ_1 and λ_2 are constant,

$$J_1 = w - \lambda_1 u \quad \text{on} \quad \eta,$$

and

$$J_2 = w - \lambda_2 u \quad \text{on} \quad \zeta.$$

Formulas (7) and (8) constitute a non-symmetric system of equations. For analytical purposes, it is desirable to have a symmetric system of equations. There are formal procedures for transforming (5) and (6) to a symmetric system, but, in this case, it is simpler to rewrite (7) and (8):

$$(7)' \qquad (w-\lambda_1 u)_x + \lambda_2 (w-\lambda_1 u)_z = -[(\lambda_1)_x u + \lambda_2 (\lambda_1)_z u]$$

and

$$(8)' \qquad (w-\lambda_2 u)_x + \lambda_1 (w-\lambda_2 u)_z = -[(\lambda_2)_x u + \lambda_1 (\lambda_2)_z u].$$

The form of (7)' and (8)' suggests defining canonical variables U_1 and U_2 as

$$U_1 = w - \lambda_1 u$$

and

$$U_2 = w - \lambda_2 u.$$

Then (7)' and (8)' reduce to

$$(9) \qquad (U_1)_\zeta = R_1(U_1 - U_2)x_\zeta$$

and

$$(10) \qquad (U_2)_\eta = R_2(U_1 - U_2)x_\eta,$$

where

$$R_1 = \frac{[(\lambda_1)_x + \lambda_2(\lambda_1)_z]}{(\lambda_1 - \lambda_2)}$$

and

$$R_2 = \frac{[(\lambda_2)_x + \lambda_1(\lambda_2)_z]}{(\lambda_1 - \lambda_2)}.$$

The symmetric system of equations, (9) and (10), is awkward to solve, but several deductions can be made:

i) If λ_1 and λ_2 are constant, $R_1 = R_2 = 0$. Thus, $U_1 = J_1$ on η constant and $U_2 = J_2$ on ζ constant.

ii) If λ_1 and λ_2 are variables, then x_ζ and x_η may be difficult to evaluate explicitly. In general, (9) and (10) must be solved together with the equations for η and ζ.

iii) Since the system of equations is Lipschitzian, the Cauchy-Picard

Theorem can be applied to the first integrals of (9) and (10) to prove formally the uniqueness and existence of the solution. The first integrals can be used as the basis of an iterative procedure for the construction of a solution.

iv) In principle, (9) and (10) are integrated along η and ζ constant, respectively. At the intersection of η and ζ, u and w are obtained from U_1 and U_2. This procedure continues until one of the characteristics strikes a boundary, where the BC's are applied to switch from the "incoming" characteristic to the "outgoing" one. The RBC on a sloping boundary yields

$$U_1 = \frac{(\lambda_2 - m)}{(\lambda_1 - m)} U_2.$$

The FBC yields

$$e^{\rho x}\left[e^{-\rho x}\left(\frac{\lambda_1 U_1}{\lambda_1 - \lambda_2}\right)\right]_x = e^{-\rho x}\left[e^{\rho x}\left(\frac{\lambda_2 U_2}{\lambda_1 - \lambda_2}\right)\right]_x,$$

where

$$\rho = \frac{(\lambda_1 - \lambda_2)(N^2 - \sigma^2)}{2g}.$$

This differential equation reduces to quadratures which must be carried out along the sea surface from the initial line.

D. The Mixed Initial-Boundary Value Problem

The structure of the MIBVP is examined to understand how CGE's with variable coefficients can be solved in bounded domains. The linear, inhomogeneous CGE is discussed:

$$L(\psi) = \psi_{\eta\zeta} - f = 0,$$

where

$$f = \frac{-L(\eta)\psi_{\eta} - L(\zeta)\psi_{\zeta}}{2Q(\eta, \zeta)}.$$

The first step is to reduce the full problem to a succession of problems, each of which falls into one of three categories: a Cauchy problem, CP; a Goursat problem, GP; or a characteristic initial value problem, CIVP. In Figure 10a, the domain of interest is shown, together with the field of limiting characteristics dividing the domain into sub-domains where the problem is indicated to be one of the three categories listed above. In Figure 10e, the domain of interest is shown in the corresponding plane of characteristics.

A CP governs the solution in only one sub-domain, D_o, the curvilinear triangle bounded by C and the two intersecting characteristics emanating from the extremities of C. For any point $R_o \in {}_oD_o \subset D_o$, Figure 10b, the solution of the CP is

$$\psi(R_o) = \iint_{{}_oD_o} f d\eta d\zeta.$$

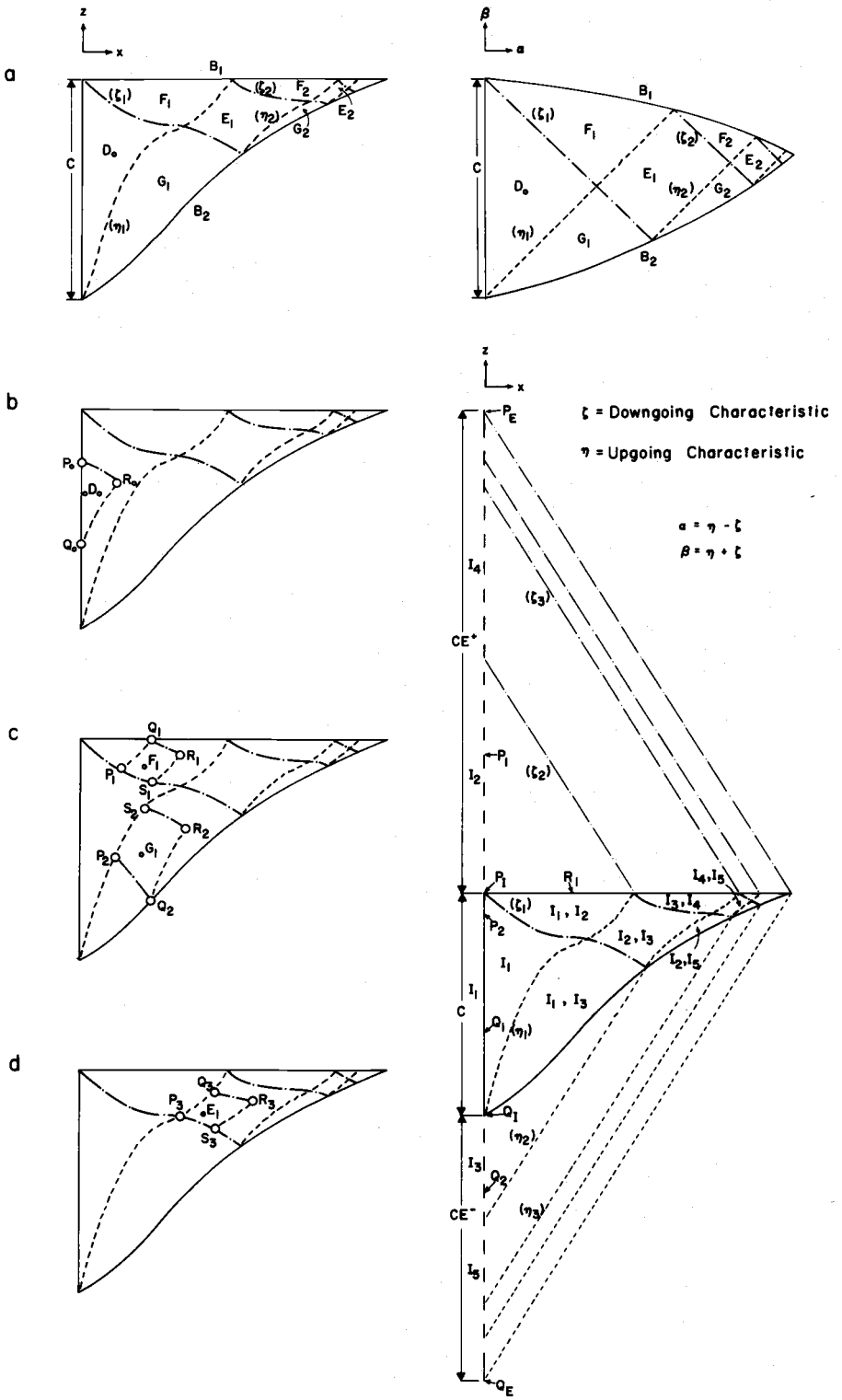

Figure 10. The mixed initial-boundary value problem. (A CP occurs in D_o; GP's occur in F_i's and G_i's, and CIVP's occur in E_i's.)

The GP's govern the solution in the sub-domains F_i and G_i, which have a segment of either the sea surface, B_1, or sea bottom, B_2, respectively, as one side of their curvilinear, triangular boundaries. For F_1 and G_1, with the CP solved in D_o, the solution and its normal derivative are given along the characteristics ζ_1 and η_1. Boundary conditions are also specified along B_1 and B_2. For any point $R_1 \in {}_oF_1 \subset F_1$, Figure 10c, the solution of the GP is

$$\psi(R_1) = \psi(P_1) - \psi(S_1) + \psi(Q_1) + \iint_{{}_oF_1} f d\eta d\zeta.$$

The solution is found in an analogous fashion for $R_2 \in {}_oG_1 \subset G_1$.

The CIVP's are located in the sub-domains E_i; which are interior, curvilinear rectangles bounded by characteristics. After two GP's contiguous to E_i have been solved, the solution is then known along two of the bounding characteristics of E_i. For example, the solution is given along η_1 separating F_1 and E_1 and ζ_1 separating G_1 and E_1. For any point $R_3 \in {}_oE_1 \subset E_1$, Figure 10d, the solution of the CIVP is

$$\psi(R_3) = \psi(P_3) - \psi(S_3) + \psi(Q_3) + \iint_{{}_oE_1} f d\eta d\zeta.$$

Thus, GP's and CIVP's continue to be solved alternately until the solution has been obtained for all of D. Each problem type involves an integro-differential equation which could be solved by Picard's method of successive approximation. The necessity to solve many component problems and to use an iterative scheme is inefficient. The next two sections are devoted to removing these deficiencies.

E. The Riemann-Green Function

The necessity to solve the above integro-differential equations can be circumvented by employing the Riemann-Green function, W, for the CGE. W is the solution to the adjoint GE, the AGE, and certain auxiliary conditions:

i) (AGE): $M(W) = W_{\eta\zeta} - g = 0,$

where

$$g = \frac{[L(\eta)W_{\eta} + L(\zeta)W_{\zeta}]}{Q(\eta, \zeta)} + [(\frac{L(\eta)}{Q(\eta, \zeta)})_{\eta} + (\frac{L(\zeta)}{Q(\eta, \zeta)})_{\zeta}]W,$$

ii) $W_{\zeta} = -\frac{L(\eta)}{Q(\eta, \zeta)} W, \quad \text{for} \quad \eta = \eta_o,$

iii) $W_{\eta} = -\frac{L(\zeta)}{Q(\eta, \zeta)} W, \quad \text{for} \quad \zeta = \zeta_o, \quad \text{and}$

iv) $W = 1 \quad \text{at} \quad \eta = \eta_o, \quad \zeta = \zeta_o.$

Thus, a CIVP must be solved for W. Together, the last three conditions define a pair of ordinary differential equations and a boundary condition common to each equation. This pair of equations can be

solved at least implicitly. W has the property that $L(W) = 0$ when W is considered a function of η_o and ζ_o. When W can be found, the solution for ψ can be written in terms of integrals along C of products involving W and the CD.

Taking the CP in Figure 10b as an explicit example, then

$$(11) \qquad \psi(R_o) = \frac{1}{2}[\psi(P_o)W(P_o; R_o) + \psi(Q_o)W(Q_o; R_o)]$$

$$- \int_{P_o}^{Q_o} W(P; R_o)\psi(P)\left[\frac{L(\eta)d\zeta - L(\zeta)d\eta}{Q(\eta, \zeta)}\right]$$

$$- \frac{1}{2}\int_{P_o}^{Q_o} W(P; R_o)[\psi_\zeta(P)d\zeta - \psi_\eta(P)d\eta]$$

$$- \frac{1}{2}\int_{P_o}^{Q_o} \psi(P)[W_\eta(P; R_o)d\eta - W_\zeta(P; R_o)d\zeta],$$

where

$$P = (\eta, \zeta).$$

Analogous formulae exist for the GP's and CIVP's. Since, if the Riemann-Green function is known, surface integro-differential equations are replaced by line integrals, there is motivation for seeking Riemann-Green functions. Specific cases are discussed in Chapter VII and in Appendix I. Even when W can not be found in explicit form, it generally can be reduced to quadratures. With W expressed in integral form, it can be substituted into the above formulae.

By use of an asymptotic expansion for the integrand of the integral representation of W, a bound for the solution to ψ can be evaluated in the limit of large argument.[17]

F. Solution of Mixed Initial-Boundary Value Problems With the Use of the Riemann-Green Function

In a MIBVP, the BC's can be introduced into the formal solution of a CP to find the rules for extension of the CD from C to all of CE. In other words, by extending the CD from C to CE, the MIBVP is converted into a "super" CP, Figure 10f. The termini of C are P_I and Q_I. The solution is sought in the triangle whose domain of dependence is bounded by the characteristics emanating from the termini, P_E and Q_E, of CE.

For conveneience, both boundaries, $B_1 = B_1(\eta, \zeta)$ and $B_2 = B_2(\eta, \zeta)$, are assumed rigid so that $\psi(B_i) = 0$, $(i = 1, 2)$, WLOG. Write the integrals of (11) in the following form:

$$I(P_o, Q_o; R_o) = I(P_o, S_o; R_o) + I(S_o, Q_o; R_o),$$

where S_o is any point between the P_o and Q_o on the CE. Let R_1 be the parameter of B_1, then

---

[17] This use of the Riemann-Green function was brought to the attention of the author by Dr. R. B. Guenther, Department of Mathematics, Oregon State University.

$$\psi(R_1) = 0 = \psi(P_1)W(P_1;R_1) + \psi(Q_1)W(Q_1;R_1) + I(P_1, Q_1;R_1),$$

or

$$(12)\quad [\psi(P_1)W(P_1;R_1) + I(P_1, S_1;R_1)] = -[\psi(Q_1)W(Q_1;R_1) + I(S_1, Q_1;R_1)],$$

where the characteristics which intersect at R_1 emanate from P_1 and Q_1. Let $S_1 = P_I$, then the RHS of (12) is known while the LHS contains the unknown functions $\psi(P) = F(P)$ and $\psi_n(P) = G'(P)$ for $P_I \leq P \leq P_1$ and $Q_1 \geq Q_I$. Since P_1 and Q_1 are determined as functions of R_1, then the problem of extending the CD from I_1 to I_2 has been reduced to solving a pair of independent Volterra integral equations of the third kind for $F(P)$ and $G(P)$.

Similarly, application of the boundary condition on B_2 yields another pair of independent Volterra integral equations of the third kind for $F(Q)$ and $G(Q)$, $Q_2 \leq Q \leq Q_I$ and $P_2 \leq P_I$, allowing the extension of the CD from I_1 to I_3. Proceeding in a stepwise fashion, F and G can be extended to all of CE by alternate use of the integral equations.

Thus, the MIBVP can be solved in general if the Riemann-Green function can be found and if the resultant integral equations can be solved. More general boundary conditions could also be introduced. In the next chapter, the above stepwise or "leapfrog" extension technique is employed in cases of constant coefficients. Then the GE reduces to the one-dimensional wave equation, for which $W = 1$, so

$$\psi(R_o) = \frac{1}{2}[\psi(P_o)+\psi(Q_o)] - \frac{1}{2}\int_{P_o}^{Q_o}[\psi_\zeta(P)d\zeta-\psi_\eta(P)d\eta]$$

$$= \frac{1}{2}[\psi(P_o)+\psi(Q_o)] + \frac{1}{2}\int_{Q_o}^{P_o}\frac{\partial\psi}{\partial n}(P(S))dS,$$

which is D'Alembert's solution. In that case the integration can be performed and there is no necessity to solve integral equations.

VI. SOLUTIONS FOR FRONTAL MODELS WITH CONSTANT COEFFICIENTS BY THE METHOD OF CHARACTERISTICS AND THE EXTENSION OF THE CAUCHY DATA

A. Introduction

The solution theory for frontal models with constant coefficients is developed and applied. The cases of parallel and sloping boundaries and of symmetrical (without frontal interaction) and asymmetrical (with frontal interaction) characteristics are considered. The solution theory is based upon utilization of the BC's to derive reflection rules for the extension of the CD as outlined in Section V. F. The equivalence of normal mode solutions to solutions given by characteristic theory is first demonstrated to illustrate the technique. The general reflection rules are then derived and applied in a series of cases.

The problem with constant coefficients can be formulated and solved in terms of the stream function, ψ, or the u and w velocity components with equal facility. Use of the stream function yields the most concise representation of the solution, while the use of the velocity components yields the quantities actually sought. The stream function has been chosen for the analysis.

In Sections B through F, a succession of cases with subcritical bottom slopes $(0 \leq m < \lambda_1)$ are considered. The basic solution technique is extended to supercritical $(0 < \lambda_1 < m)$ and critical

($m = \lambda_1$) bottom slopes in Sections G and H, respectively.

In all cases, it is considered that the solution is sought in a coastal region, i. e., shoreward of the initial line, C, located at $x = 0$. It is understood that the CD would in principle be matched to the deep ocean normal modes at C once the issue of net horizontal energy flux across C was settled. The matching problem is discussed in Appendix I.

B. Equivalence of Normal Mode Solutions to Solutions by the Method of Characteristics when the Boundaries are Parallel and when there is no Frontal Interaction

The case studied is elementary because the upper and lower boundaries are assumed parallel. A similar discussion has been given by Sandstrom (1966) but with different objectives and logical context.

The GE is:

$$\psi_{xx} - \lambda^2 \psi_{zz} = 0,$$

where

$$\lambda^2 = R^2 = \frac{\sigma^2 - f^2}{N^2 - \sigma^2}$$

and ψ is the stream function. N^2 is assumed constant so that λ^2 is constant. The domain of interest is $D : \{(x, z) : (0 \leq x \leq L, -H \leq z \leq \eta)\}$. The bottom BC is

RBC: $\psi = C_B$: constant at $z = -H$.

The surface BC is either

RBC: $\psi = C_S$: constant at $z = 0$

or

FBC: $\psi_{xx} + \frac{(\sigma^2 - f^2)}{g}\psi_z = 0$ at $z = 0$.

The BC at the vertical coastal barrier is either

RBC: $\psi = C_V$: constant at $x = L$

or

LBC: $\psi = S(z;t)$ at $x = L$.

The relations between C_B, C_S, and C_V are left open for the present; they are established successively to illustrate the imposition of constraints on the solution. The CD are

CD: $\psi = F(z)$

and

$\psi_x = G'(z)$ at $x = 0$, i.e., on C.

Normal Mode Solution

Normal mode theory is based on SOV, so $\psi = X(\lambda x)Z(z)$ and the BC's in x and z are satisfied by the forms chosen for X and Z. The solutions for X and Z are of the form:

$$X = A \cos(K\lambda x) + B \sin(K\lambda x)$$

and

$$Z = C \cos (K(z+\theta)) + D \sin (K(z+\theta)),$$

which are then subjected to the BC's. A and B are proportional to $e^{i\sigma t}$ but with an arbitrary relative phase at this stage.

Treating first the BC's in z, for $C_B = 0$, the RBC is satisfied if $\theta = H$, so $Z = \sin (K(z+H))$. D has been absorbed by A and B. If the condition of no net mass flux thru a vertical column is imposed, $C_S = C_B$. Then the RBC implies that $K_n H = n\pi$, n : integer. Alternatively, the FBC implies that

$$\tan (K_n H) = \frac{(N^2 - \sigma^2)}{K_n g}, \quad n : \text{integer}.$$

In either the FBC or RBC case, the eigenvalues, $\{K_n\}$, are determined, with little quantitative difference between the two sets of eigenvalues. It suffices to treat each normal mode individually.

The BC's in x are next applied. First, the BC at $x = L$ is examined. The LBC implies that

$$S(z;t) = D[A \cos (K\lambda L) + B \sin (K\lambda L)] \sin (K(z+H)).$$

Take

$$S(z, t) = S(z)e^{i\sigma t}$$

and

$$S(z) = S_o \sin (K(z+H)),$$

where

$$S_o = D[\mathbf{A} \cos (K\lambda L) + B \sin (K\lambda L)].$$

The RBC applied at $x = L$ corresponds to $S_o = 0$, i.e., $C_v = S_o = C_B = C_S = 0$ for continuity of ψ along the boundary. If $S_o \neq 0$, there is still no net mass or momentum flux through the coastal boundary; as an artifice for this discussion, the coastal boundary is conceived to be a soft barrier which can absorb energy, but not mass or momentum.

In either the LBC or RBC case, the values for $\mathbf{A}$ and B are made dependent by the coastal BC. Their relation depends upon the parameters S_o, K, λ, and L. Take $\mathbf{A} = \mathbf{A}_o e^{i\sigma t}$ and $B = B_o e^{(i\sigma t+\phi)}$, where $\mathbf{A}_o$ and B_o are constants.

The CD are examined:

$$\psi|_{x=0} = F(z) = \mathbf{A} \sin (K(x+H))$$

and

$$\psi_x|_{x=0} = G'(z) = K\lambda B \sin (K(z+H)).$$

Thus, once the coastal BC is fixed, there are no degrees of freedom remaining in the problem, and the CD are constrained to obey the above relations. The time-averaged horizontal energy flux, $\overline{F^{(x)}}^t$, is used to clarify the coastal BC. Since

$$u = -\psi_z = -K \cos (K(z+H))[\mathbf{A} \cos (K\lambda x)+B \sin (K\lambda x)]$$

and

$$\pi_z = \frac{i(N^2-\sigma^2)}{\sigma}\psi_x,$$

or

$$\pi = -\frac{i(N^2-\sigma^2)\lambda}{\sigma}\cos(K(z+H))[-A\sin(K\lambda x)+B\cos(K\lambda x)],$$

then

$$\overline{F^{(x)}}^t = \mathrm{Re}\left[\frac{\rho_o}{H}\int_{z=-H}^{0}(\overline{u\pi}^t)dz\right]$$

$$= \rho_o A_o B_o \frac{(N^2-\sigma^2)\lambda K\sin(\phi)}{4\sigma},$$

where Re means the real part. Thus, if $\phi = 0$, $\overline{F^{(x)}}^t = 0$ for all x. If $S_o = 0$, $\phi \overset{(must)}{=} 0$, and $B_o \overset{(must)}{=} -A_o\cot(K\lambda L)$. Then, re-examining the CD,

$$F(z) = A\sin(K(z+H))$$

and

$$G'(z) = \lambda KB\sin(K(z+H))$$

$$= -\lambda KA\cot(K\lambda L)\sin(K(z+H))$$

$$= -\lambda K\cot(K\lambda L)F(z).$$

The solution for X is then

$$X = A\frac{\sin(K\lambda(L-x))}{\sin(K\lambda L)},$$

thus

$$\psi = A\sin(K(z+H))\frac{\sin(K\lambda(L-x))}{\sin(K\lambda L)}.$$

If $\phi \neq 0$, $\overline{F^{(x)}}^t$ is a uniform function of x. Given $\overline{F^{(x)}}^t \neq 0$, then A_o and B_o are related, and S_o is determined as a complex-valued function by $\overline{F^{(x)}}^t$ = constant.

The demonstration of the lack of arbitrariness in the setting of the CD in the case of a vertical coastal barrier illustrates a key feature of the MIBVP. The loss of arbitrariness in the CD is a general property of regions with supercritical bottom slopes.

Mixed Initial-Boundary Value Problem Solution

The objectives are to recover the preceding solution by the method of characteristics and to demonstrate the technique as a prototype for subsequent sections. The GE is treated as a hyperbolic equation in the spatial variables, and the BC's are investigated to determine how they constrain the most general solutions so that the CD can be extended to cover the CE in the region D.

The general solution to the GE has the form

$$\psi(x, z) = \frac{1}{2}[F(z+\lambda x) + F(z-\lambda x)] + \frac{1}{2\lambda}[G(z+\lambda x)-G(z-\lambda x)],$$

where the CD are

$$\text{CD:} \qquad F(z) = \psi(0, z)$$

and

$$G'(z) = \psi_x(0, z),$$

as before.

The lines $\eta = z-\lambda x$ constant and $\zeta = z+\lambda x$ constant are the upgoing and downgoing characteristics, respectively. The solution can be expressed in terms of its Riemann invariants, $I_U(\eta)$ and $I_D(\zeta)$, i.e.,

$$\psi(x, z) = I_U(\eta) + I_D(\zeta),$$

where

$$I_U = \frac{1}{2}\left[F(\eta) - \frac{1}{\lambda} G(\zeta)\right]$$

and

$$I_D = \frac{1}{2}\left[F(\zeta) + \frac{1}{\lambda} G(\eta)\right]$$

are invariant along the upgoing and downgoing characteristics, respectively. If the CD can be extended over CE, the solution for ψ can be written for any point in D. After computing η and ζ at $(x, z) \in D$ and computing the corresponding values for I_U and I_D from the CD at $z = \eta$ and $z = \zeta$ on CE, respectively, $\psi(x, z)$ is found from $I_U(\eta)$ and $I_D(\zeta)$.

The CE is formed by determining the limiting characteristics; Figure 11 represents the problem statement graphically. The extreme-valued ζ intersects D at $(L, 0)$, i.e., $\zeta = 0 + \lambda L$, which emanates from $(0, \lambda L)$. Likewise, the extreme-valued η intersects D at $(L, -H)$, i.e., $\eta = -H - \lambda L$, which emanates from $(0, -H-\lambda L)$. Therefore, the CE has been determined to be:

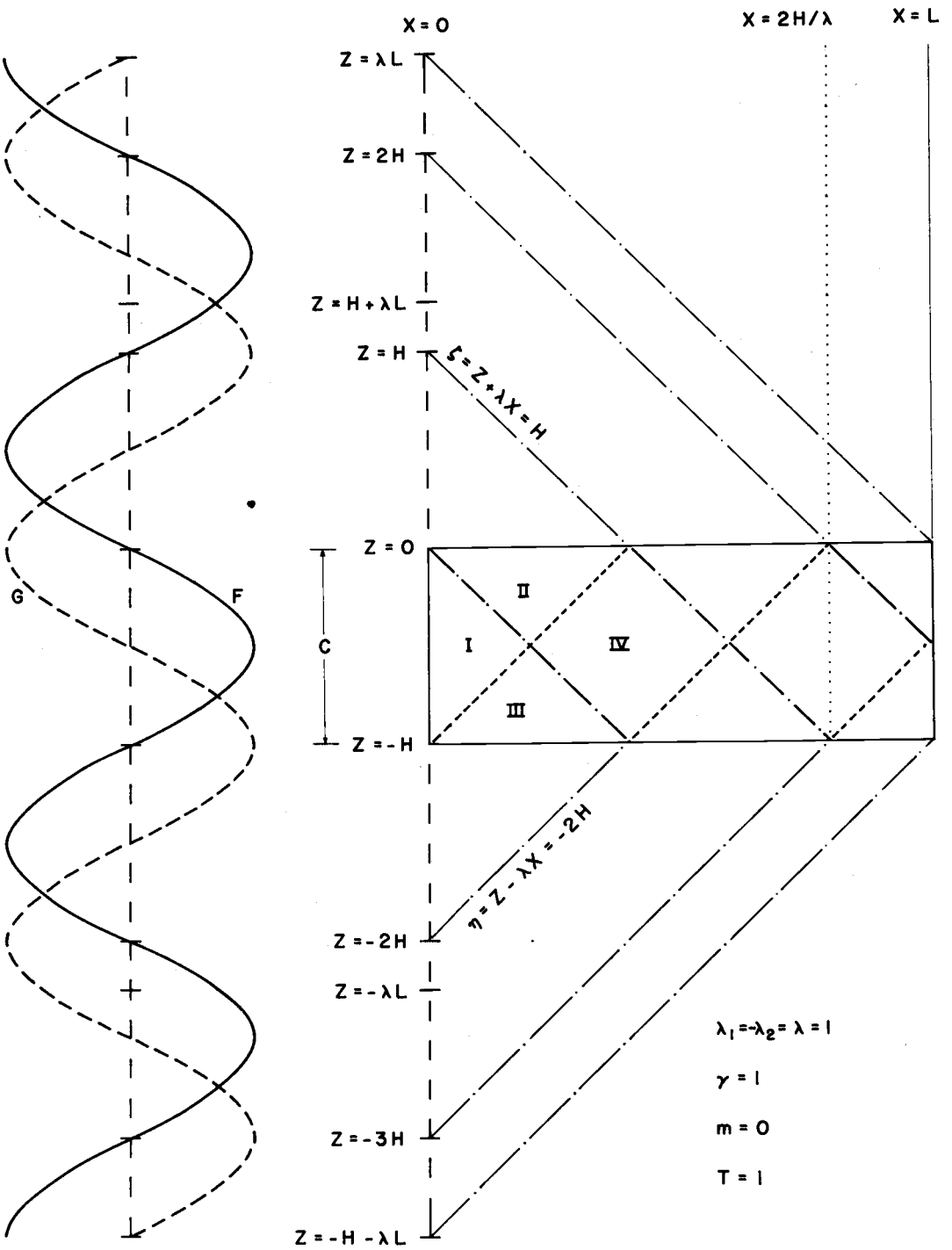

Figure 11. Graphical solution for a case with parallel boundaries and without frontal interaction.

a. Extended CD

b. Domain D and limiting characteristics

CE: $\{(0, z) : (-H - \lambda L \leq z \leq \lambda L)\}$.

The BC's are used to extend the CD to cover CE. Analytically, this problem is essentially that of finding a mapping of $\psi(D)$ onto $\psi(CE)$, i. e., all the information about the solution in D can be found from the CD on CE. The BC's are used to find reflection rules, RR1 and RR2, for extending the CD with respect to the sea surface and the sea bottom, respectively. It is convenient to define LE to be the lower segment of CE^- over which the CD are not influenced by RR1; similarly, UE is the upper segment of CE^+ over which the CD are not influenced by RR2.

The RBC is used to find the symmetry relation with respect to $z = 0$:

$$\psi(x, 0) = 0 = \frac{1}{2}[F(\lambda x)+F(-\lambda x)] + \frac{1}{2\lambda}[G(\lambda x)-G(-\lambda x)], \quad \text{for all } x \in D.$$

Since F and G are assumed independent, RR1 follows

RR1: $$F(z) = -F(-z)$$

and

$$G(z) = G(-z), \quad \text{for all } z \in CE \sim LE,$$

where

$$LE = \{(0, z) : -H - \lambda \leq z \leq -\lambda L\}.$$

Thus, F and G are odd and even functions, respectively, with

respect to the origin. The RBC is again used to find the symmetry relation with respect to $z = -H$:

$$\psi(x, -H) = 0 = \frac{1}{2}[F(-H+\lambda x)+F(-H-\lambda x)] + \frac{1}{2\lambda}[G(-H+\lambda x)-G(-H-\lambda x)],$$

for all $x \in D$. F and G are still assumed independent, therefore RR2 follows

RR2: $$F(-H+z) = -F(-H-z)$$

and $$G(-H+z) = G(-H-z),$$

for all $z \in CE \sim UE$, where $UE = \{(0, z) : \lambda L - H \leq z \leq \lambda L\}$. Thus, F and G are odd and even functions, respectively, with respect to $z = -H$.

For RR1 and RR2 to be compatible, it is straightforward to show that F and G must be periodic, with a period which is an integer multiple of $2H$. There is now enough information to extend the CD to cover CE in a "leapfrog" fashion, yet there is another BC to satisfy.

The RBC applied at $x = L$ implies

$$\psi(L, z) = 0 = \frac{1}{2}[F(z+\lambda L)+F(z-\lambda L)] + \frac{1}{2\lambda}[G(z+\lambda L)-G(z-\lambda L)],$$

for all $z \in D$. This relation must impose a further restriction on the solution. There are now only two degrees of freedom remaining:

the relation of L to H and the independence of F and G. Since the analysis must be valid for arbitrary L and H, the restriction imposed by the coastal BC must involve the coupling of F and G. Then reflection rule three, RR3, follows

$$\text{RR3:} \quad [F(z+\lambda L)+F(z-\lambda L)] + \frac{1}{\lambda}[G(z+\lambda L)-G(z-\lambda L)] = 0.$$

The most direct way of demonstrating the necessity for this coupling is to substitute forms for F(z) and G(z). The choice of

$$F(z) = A \sin (Kz)$$

and

$$G(z) = B \cos (Kz),$$

where

$$K = \frac{n\pi}{H},$$

is compatible with the RR1 and RR2. Then

$$F(z+\lambda L) + F(z-\lambda L) = 2A \sin (Kz) \cos (K\lambda L)$$

and

$$G(z+\lambda L) - G(z-\lambda L) = -2B \sin (Kz) \sin (K\lambda L),$$

so that RR3 requires

$$B = \lambda A \cot (K\lambda L).$$

Thus, the CD have been constrained to be:

$$\psi_x\big|_{x=0} = F(z) = A \sin (Kz)$$

and

$$\psi_x\big|_{x=0} = G'(z) = -BK \sin(Kz)$$
$$= -\lambda K \cot(K\lambda L)A \sin(Kz)$$
$$= -\lambda K \cot(K\lambda L)F(z),$$

which are equivalent to the results determined by normal mode theory. Therefore, the imposition of the coastal BC represents a condition for back reflection, which removes the last element of arbitrariness in the CD. The coupling of the CD does not occur in the case of subcritical bottom slope in a wedge, but it does occur in the case of supercritical bottom slope; the case of critical bottom slope is a degenerate case in this regard.

A sample solution can now be constructed for any point $(x_1, z_1) \in D$. The first step is to evaluate the upgoing and downgoing characteristics which intersect there, i.e.,

$$\eta_1 = z_1 - \lambda x_1$$

and

$$\zeta_1 = z_1 + \lambda x_1.$$

The second step is to evaluate the Riemann invariants at the points on CE from which η_1 and ζ_1 emanate, i.e., at $x = 0$, $z = \eta_1 = z_1 - \lambda x_1$ and $z = \zeta_1 = z_1 + \lambda x_1$, respectively:

$$I_D = \frac{1}{2}[F(\zeta_1) + \frac{1}{\lambda} G(\zeta_1)]$$

$$= \frac{A}{2}[\sin(K\zeta_1) + \cot(K\lambda L) \cos(K\zeta_1)]$$

and

$$I_U = \frac{1}{2}[F(\eta_1) - \frac{1}{\lambda} G(\eta_1)]$$

$$= \frac{A}{2}[\sin(K\eta_1) - \cot(K\lambda L) \cos(K\eta_1)].$$

The third step is to form ψ from the Riemann invariants:

$$\psi = I_U + I_D$$

$$= \frac{A}{2}\{[\sin(K\eta_1) + \sin(K\zeta_1)] - \cot(K\lambda L)[\cos(K\eta_1) - \cos(K\zeta_1)]\}$$

$$= \frac{A}{2}\{[\sin(K(z_1 - \lambda x_1)) + \sin(K(z_1 + \lambda x_1))]$$

$$- \cot(K\lambda L)[\cos(K(z_1 - \lambda x_1)) - \cos(K(z_1 + \lambda x_1))]\}$$

$$= A \sin(Kz_1)[\cos(K\lambda x_1) - \cot(K\lambda L) \sin(K\lambda x_1)]$$

$$= \frac{A \sin(Kz_1)}{\sin(K\lambda L)} \sin(K\lambda(L - x_1)).$$

By inspection, $\psi = 0$ when $z_1 = 0$, $z_1 = -H$, or $x_1 = L$. Also, at $x_1 = 0$, $\psi = A \sin(Kz_1)$ and $\psi_x = -\lambda KA \cot(K\lambda L) \sin(Kz_1)$. Therefore, ψ satisfies all of the BC's and the CD as well as the GE; it is also equivalent to the solution by normal mode theory. Now that the normal mode solution has been recovered by the method of characteristics, the latter method, which is more fundamental, is

extended to more general cases where normal modes do not apply.

Given the constraints on the CD, any suitable CD could be expanded in an infinite series of normal modes. With the method of characteristics, the solution can be given as a single composite waveform.

C. Derivation of the Reflection Rules for Extension of the Cauchy Data in the General Case

The reflection rules for extension of the CD are established under general conditions for the case of constant coefficients in the GE. The CGE, $\psi_{\eta\zeta} = 0$, is solved subject to the CD. The upgoing and downgoing characteristics are given by

$$\eta = z - \lambda_1 x$$

and

$$\zeta = z - \lambda_2 x,$$

respectively, where

$$\lambda_1 = S + R,$$

$$\lambda_2 = S - R,$$

$$S = -M^2/(N^2 - \sigma^2),$$

and

$$R = (M^4 + (N^2 - \sigma^2)(\sigma^2 - f(f + \bar{v}_x)))^{1/2}/(N^2 - \sigma^2).$$

Since $M^2 = -sN^2$, $N^2 > 0$, and $s \geq 0$ in an average sense for the Oregon coastal region, then $S \geq 0$. Then $\lambda_1 > 0$ and

$\lambda_2 < 0$, except for the anomalously high and low frequencies in the inertial-internal wave passband.

$$\psi|_{x=0} = F(z)$$

and

$$\psi_x|_{x=0} = G'(z),$$

where $z \in CE$, and it is assumed that the CD have been extended. The actual extension of the CD is developed at a later stage.

The alongshore flow and density fields implied by the assumption of constant coefficients for the GE are, for $(x, z) \in D$:

$$\bar{v} = ax - bz$$

and

$$\bar{\rho} = \rho_o(cx-dz),$$

where $a, b, c,$ and $d \geq 0$. With the fields for $\bar{v}$ and $\bar{\rho}$ given above, then

$$N^2 = dg,$$

$$M^2 = -cg,$$

$$s = \frac{-\bar{\rho}_x}{\bar{\rho}_z} = c/d,$$

$$\bar{v}_z = -b,$$

$$\bar{v}_x = a,$$

and

$$r = \frac{-\bar{v}_x}{\bar{v}_z} = a/b,$$

where r is the slope of an isotach. With the assumption of geostrophic equilibrium, $f\bar{v}_z = M^2$ or $fb = cg$. For the computation of the slopes of the characteristics, the quantities S and R are needed:

$$S = \frac{cg}{(dg-\sigma^2)},$$

and

$$R = \left[S^2 + \frac{(\sigma^2-f^2-fa)}{(dg-\sigma^2)}\right]^{1/2}.$$

In the low frequency limit, $\sigma^2 \ll N^2 = dg$, $S = s$ and

$$R = \left[s^2+t^2 - \frac{fa}{dg}\right]^{1/2},$$

where

$$t^2 = \frac{\sigma^2-f^2}{dg}.$$

Since

$$\frac{fa}{dg} = rs,$$

if $r = s$, i.e., if the slope of the isotachs equals that of the isopycnals, then $R = t$. In this case, the slopes of the characteristics are

$$\left(\frac{dz}{dx}\right)_\eta = \lambda_1 = s + t$$

and

$$\left(\frac{dz}{dz}\right)_\zeta = \lambda_2 = s - t.$$

Since $\psi_n|_{x=0} = \vec{\nabla}\psi \cdot \hat{n}|_{x=0}$, where $\vec{\nabla}\psi = (\psi_\eta, \psi_\zeta)$, and, since $\eta = \zeta$ at $x=0$, then $\hat{n} = \frac{(-1,+1)}{\sqrt{2}}$ is the unit normal directed out of D and $\psi_n|_{x=0} = (\psi_\zeta - \psi_\eta)/\sqrt{2}\,|_{\eta=\zeta}$. Because

$$\psi_\eta = \psi_x x_\eta + \psi_z z_\eta$$

and

$$\psi_\zeta = \psi_x x_\zeta + \psi_z z_\zeta ,$$

then

$$\psi_n|_{x=0} = \frac{-1}{\sqrt{2}}[\psi_x(x_\eta - x_\zeta) + \psi_z(z_\eta - z_\zeta)]|_{x=0}.$$

Since

$$x = \frac{(\zeta-\eta)}{(\lambda_1-\lambda_2)} \qquad \text{and} \qquad z = \frac{-\lambda_2\eta+\lambda_1\zeta}{(\lambda_1-\lambda_2)} ,$$

then

$$x_\eta = -1/(\lambda_1-\lambda_2)$$

$$x_\zeta = 1/(\lambda_1-\lambda_2)$$

$$z_\eta = -\lambda_2/(\lambda_1-\lambda_2),$$

and

$$z_\zeta = \lambda_1/(\lambda_1-\lambda_2).$$

Hence

$$\psi_n|_{x=0} = \frac{-1}{\sqrt{2}(\lambda_1-\lambda_2)}[-2\psi_x - (\lambda_2+\lambda_1)\psi_z]|_{x=0}$$

$$= \frac{1}{\sqrt{2}(\lambda_1-\lambda_2)}[2G'(z)+(\lambda_1+\lambda_2)F'(z)].$$

By D'Alembert's solution to the one-dimensional wave equation,

$$\psi(x, z) = \frac{1}{2}[F(\zeta)+F(\eta)] + \frac{1}{2}\int_{\eta}^{\zeta} \psi_n|_{x=0} dt,$$

where dt is the differential arc length along $\eta = \zeta$ and $dt = ((d\eta)^2+(d\zeta)^2)^{1/2} = \sqrt{2}\, dz$. Consequently,

$$\psi(x, z) = \frac{1}{2}[F(\zeta)+F(\eta)] + \frac{1}{2}\frac{1}{(\lambda_1-\lambda_2)}\{2[G(\zeta)-G(\eta)] + (\lambda_1+\lambda_2)[F(\zeta)-F(\eta)]\}$$

$$= \frac{1}{(\lambda_1-\lambda_2)}\{[\lambda_1 F(\zeta)-\lambda_2 F(\eta)] + [G(\zeta)-G(\eta)]\}.$$

The solution for all the other field variables can be found from ψ. In particular,

$$\pi = \frac{i(N^2-\sigma^2)}{2\sigma}\{[\lambda_1 F(\zeta)+\lambda_2 F(\eta)] + [G(\zeta)+G(\eta)]\},$$

from ψ and the x- or z-EOM.

The solution can be recast in terms of its Riemann invariants:

$$\psi(x, z) = I_U(\eta) + I_D(\zeta),$$

where

$$I_U(\eta) = \frac{-1}{(\lambda_1-\lambda_2)}[\lambda_2 F(\eta) + G(\eta)]$$

and

$$I_D(\zeta) = \frac{1}{(\lambda_1-\lambda_2)}[\lambda_1 F(\zeta) + G(\zeta)].$$

Thus, as in the preceding section, the technique of triangulation in

characteristic space can be used to find ψ at any point in D from the Riemann invariants constructed on CE, once it is determined how to extend the CD to cover CE.

Again the CD are extended by successively applying the BC's. Initially it is assumed that all the boundaries are rigid so that the RBC applies; later, the sea surface is allowed to be a free surface and the FBC is applied. First, the RBC is applied at $z = 0$:

$$\psi|_{z=0} = 0 = \frac{1}{(\lambda_1-\lambda_2)}\{[\lambda_1 F(-\lambda_2 x)-\lambda_2 F(-\lambda_1 x)]+[G(-\lambda_2 x)-G(-\lambda_1 x)]\}.$$

Since F and G are independent, it follows that RR1 is:

RR1:
$$F(\gamma r) = -\gamma F(-r)$$
and
$$G(\gamma r) = G(-r),$$

where

$$\gamma = \frac{-\lambda_2}{\lambda_1}.$$

The LHS of RR1 represents the extension of F and G onto CE^+, while the argument of the RHS sweeps out values of $r \in CE \sim LE$, where r is the parameter of CE.

Second, the RBC is applied along $z = z_b(x) = -H(x)$:

$$\psi|_{z=-H(x)} = 0 = \frac{1}{(\lambda_1-\lambda_2)}\{[\lambda_1 F(-H(x)-\lambda_2 x)-\lambda_2 F(-H(x)-\lambda_1 x)] + [G(-H(x)-\lambda_2 x)-G(-H(x)-\lambda_1 x)]\}$$

Since F and G are still independent, it follows that RR2 is

$$\text{RR2:} \qquad F(-H(x)-\lambda_1 x) = -\frac{1}{\gamma}F(-H(x)-\lambda_2 x)$$

and

$$G(-H(x)-\lambda_1 x) = G(-H(x)-\lambda_2 x), \quad \text{for all} \quad x \in D.$$

For no ambiguity in RR2, a necessary condition is that $H(x)$ be a monotonic function of x. For the physical case of interest, the bottom slope $m(x) = \frac{dz_b}{dx} = -\frac{dH(x)}{dx} \geq 0$. For the present purpose, it is sufficient to take m equal to a constant, then $z_b(x) = -H(x) = -[H_o - mx] = -H_o + mx$, where $m = H_o/L$. The RR2 becomes for $z \in CE \sim UE$,

$$\text{RR2:} \qquad F(-H_o - Tr) = -\frac{1}{\gamma}F(-H_o + r)$$

and

$$G(-H_o - Tr) = G(-H_o + r),$$

where

$$T = \frac{(\lambda_1 - m)}{(-\lambda_2 + m)} = \frac{R+S-m}{R-S+m}.$$

For $\sigma^2 \ll N^2$,

$$T \simeq \frac{t+s-m}{t-s+m}.$$

For the physically interesting case of $s \approx m$, i.e., isopycnals paralleling the bottom slope, $T \approx 1$. Since, as shown below, strong wave amplification is produced as $T \to 0$, then the inclined frontal layer exerts a stabilizing influence on inertial-internal waves in this regard. The LHS of RR2 represents the extension of F and G

onto CE^-, while the argument of the RHS sweeps out values above $r = -H_o$, where r is the parameter of CE. When there is no bottom slope, $m = 0$ and $T = \frac{1}{\gamma}$. When the slope of the upgoing characteristic equals the bottom slope, $\lambda_1 = m$ and $T = 0$, which is the degenerate, critical case for $m > 0$. When the slope of the downgoing characteristic equals the bottom slope, $\lambda_2 = m$ and $T = \infty$, which is the degenerate, critical case for $m < 0$. In the subcritical case, $\lambda_2 < m < \lambda_1$, there is no ambiguity in the extension of the CD. The degenerate supercritical $(m > \lambda_1)$ and critical $(m = \lambda_1)$ cases are treated in Sections G and H, respectively. In the subcritical case, and where $m > S$, then $T < 1$.

The general FBC requires:

$$g\psi_{xx} - (N^2-\sigma^2)[\lambda_1\lambda_2\psi_z + \frac{(\lambda_1+\lambda_2)}{2}\psi_x] = 0, \qquad \text{at} \quad z = 0.$$

RR1 becomes

$$\text{RR1:} \quad \frac{g}{(\lambda_1-\lambda_2)}[\lambda_2 F(-\lambda_2 x)+\lambda_1 F''(-\lambda_1 x)]+\frac{(N^2-\sigma^2)}{2}[F'(-\lambda_2 x)+F'(-\lambda_1 x)] = 0$$

and

$$\frac{g}{(\lambda_1-\lambda_2)}[\lambda_2^2 G''(-\lambda_2 x)-\lambda_1^2 G''(-\lambda_1 x)]+\frac{(N^2-\sigma^2)}{2}[\lambda_2 G'(-\lambda_2 x)-\lambda_1 G'(-\lambda_1 x)] = 0,$$

for all $x \in D$, and since F and G are independent. It follows that RR1 can be re-written in more compact form:

$$\text{RR1:} \qquad e^{-qx}(e^{qx}F'(\lambda_2 x))' = e^{qx}(e^{-qx}F'(\lambda_1 x))'$$

and

$$\lambda_2 e^{-qx}(e^{qx}G'(\lambda_2 x))' = -\lambda_1 e^{qx}(d^{-qx}G'(-\lambda_1 x))',$$

where

$$q = \frac{(N^2-\sigma^2)(\lambda_1-\lambda_2)}{2g} .$$

These expressions can be reduced to quadratures to be carried out along the sea surface from $x = 0$. Thus, the more subtle reflection rule involving the FBC is now known.

With the reflection rules known, the process of "leapfrog" extension can be used to extend the CD:

i) $F(z)$ and $G(z)$ are given for $-H_o \leq z \leq 0$.

ii) $F(z)$ and $G(z)$ are extended from $-H_o \leq z \leq 0$ to $0 \leq z \leq \gamma H_o$, by RR1.

iii) $F(z)$ and $G(z)$ are extended from $-H_o \leq z \leq 0$ to $-(1+T)H_o \leq z \leq -H_o$, by RR2.

iv) $F(z)$ and $G(z)$ are extended from $-(1+T)H_o \leq z \leq -H_o$ to $\gamma H_o \leq z \leq (1+T)\gamma H_o$, by RR1.

v) $F(z)$ and $G(z)$ are extended from $0 \leq z \leq \gamma H_o$ to $-(1+T(1+\gamma))H_o \leq z \leq -(1+T)H_o$, by RR2.

vi) This procedure is repeated until F and G are extended to all of CE.

Hence, there exist systematic reflection rules by which the CD can be extended for cases of asymmetrical characteristics, variable

depth, and a free or rigid sea surface. Consequently, solutions can be systematically constructed using the extended CD, the characteristics, and the Riemann invariants. In the following sections, RR1 and RR2 are employed to construct solutions for a succession of cases to illustrate the essential physics.

Having determined the extension of the CD to CE, the solutions for u and w can be determined by operating on the Riemann invariants. Since

$$\psi = I_U(\eta) + I_D(\zeta),$$

then

$$u = -\psi_z = -I_U'\eta_z - I_D'\zeta_z$$

$$= -[I_U' + I_D']$$

and

$$w = \psi_x = I_U'\eta_x + I_D'\zeta_x$$

$$= -[\lambda_2 I_U' + \lambda_1 I_D'].$$

Clearly, once I_U and I_D are known, then I_U' and I_D' can be determined, and, since they too are invariant, then the solutions for u or w can be constructed directly.

The question of net horizontal energy flux has not been discussed in this section, nor shall it be in the subsequent sections. From the analysis in Chapter IV, it is considered understood that the individual contributions of F and G to ψ have the character of standing waves. Whether the two portions of the solution combine to

form a single standing, a single progressive, or a mixed wave can be settled on the basis of the relative time phase between F and G, as before.

D. The Solution for Inertial-Internal Waves in a Wedge Without Frontal Interaction

The problem of inertial-internal wave propagation in a wedge is solved without the frontal interaction. The wedge is defined to be the domain D, where $D: \{(x, z) : (0 \leq x \leq L, -H_o + mx \leq z \leq 0)\}$, m constant and positive. A normal mode approach is not possible because the sloping bottom does not permit SOV. Aspects of this problem have been studied recently by Magaard (1962), Sandstrom (1966), and Wunsch (1968a, 1969); similar qualitative results are achieved in the present analysis.

This is a case with symmetric characteristics, i. e., $\lambda_1 = -\lambda_2 = \lambda$. The general form of the solution for ψ reduces to:

$$\psi(x, z) = \frac{1}{2}[F(z+\lambda x)+ F(z-\lambda x)] + \frac{1}{2\lambda}[G(z+\lambda x)-G(z-\lambda x)],$$

and the Riemann invariants are

$$I_U = \frac{1}{2}[F(z-\lambda x) - \frac{1}{\lambda} G(z-\lambda x)]$$

and

$$I_D = \frac{1}{2}[F(z+\lambda x) + \frac{1}{\lambda} G(z+\lambda x)].$$

Here, $\gamma = 1$ and $T = (\frac{\lambda - m}{\lambda + m}) < 1$. The reflection rules become

RR1:
$$F(r) = -F(-r)$$
$$G(r) = G(-r)$$

and

RR2:
$$F(-H_o - Tr) = -F(-H_o + r)$$
$$G(-H_o - Tr) = G(-H_o + r),$$

where r is a dummy variable whose range is to be determined. The geometry of the problem is given in Figure 12, where the case of $m = 2/5$, $\lambda = 1$, and $T = 3/7$ is illustrated. A few of the characteristics are traced; the ones chosen are the limiting characteristics for several intervals of extension on CE. The terminii of CE are determined by the characteristics which intersect at $(L, 0)$, thus CE : $\{(0, z) : (-\lambda L \leq z \leq \lambda L)\}$.

The extension of the CD proceeds in the following fashion:

i) The CD are given on $-H_o \leq z \leq 0$.

ii) They are extended from $-H_o \leq z \leq 0$ to $0 \leq z \leq H_o$, by RR1.

iii) They are extended from $-H_o \leq z \leq H_o$ to $-(1+2T)H_o \leq z \leq -H_o$, by RR2.

iv) They are extended from $-(1+2T)H_o \leq z \leq -H_o$ to $H_o \leq z \leq (1+2T)H_o$, by RR1.

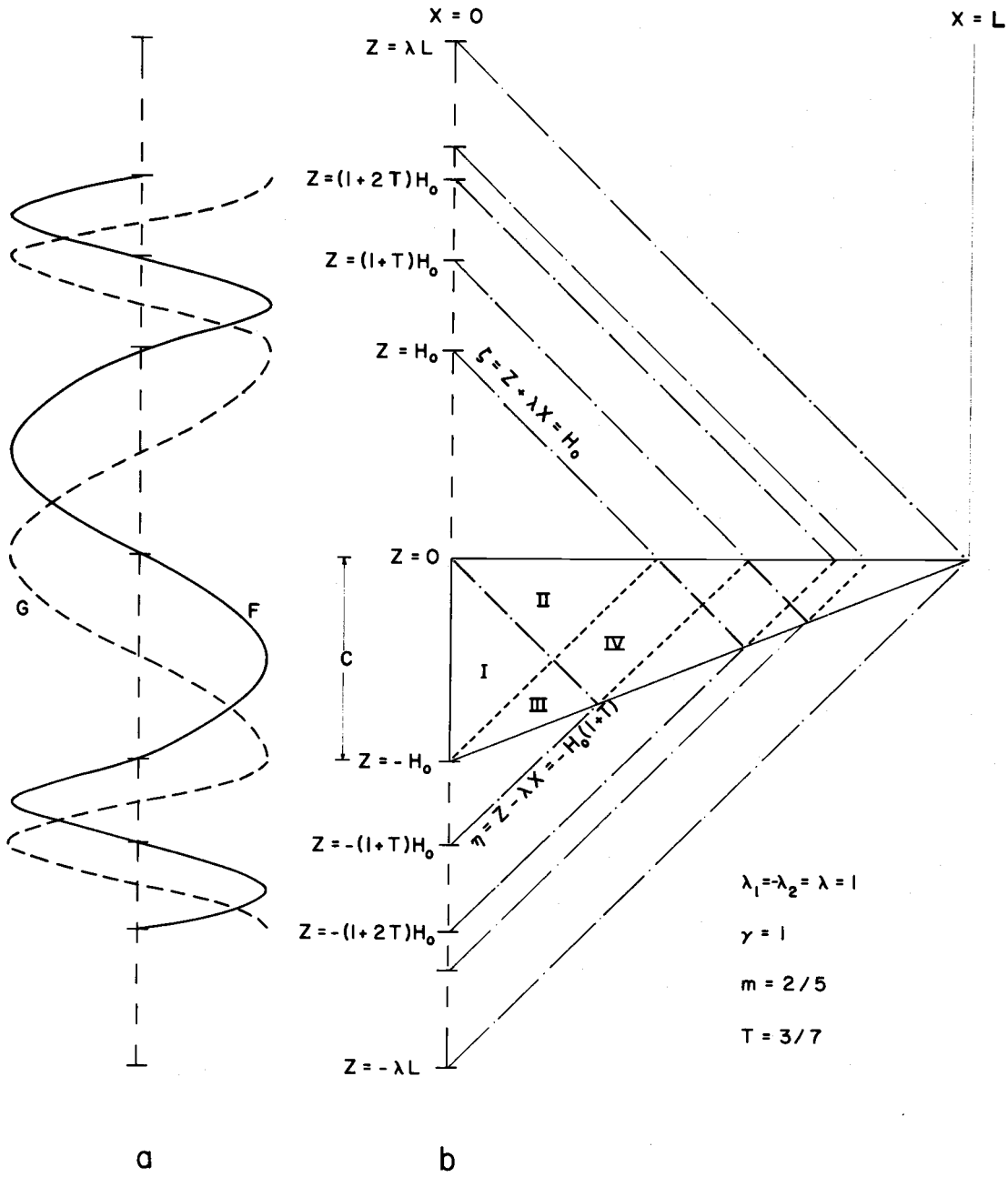

Figure 12. Graphical solution for a case in a wedge and without frontal interaction.
a. Extended CD
b. Domain D and limiting characteristics

v) They are extended from $H_o \leq z \leq (1+2T)H_o$ to

$-(1+2T(1+T))H_o \leq z \leq -(1+2T)H_o$, by RR2.

vi) They are extended from $-(1+2(T+T^2))H_o \leq z \leq -(1+2T)H_o$

to $(1+2T)H_o \leq z \leq (1+2(T+T^2))H_o$, by RR1.

vii) They are extended from $(1+2T)H_o \leq z \leq (1+2(T+T^2))H_o$

to $-(1+2(T+T^2+T^3)) \leq z \leq -(1+2(T+T^2))H_o$, by RR2.

viii) They are extended to all of the CE in the same manner.

It is apparent that the extension of the CD is performed in a "leapfrog" fashion onto intervals bounded by the points $A(m)$, m : integer, where

$$A^{\pm}(0) = 0$$

$$A^{\pm}(1) = \pm H_o$$

$$A^{\pm}(2) = \pm H_o(1+2T)$$

$$A^{\pm}(3) = \pm H_o(1+2(T+T^2))$$

$$A^{\pm}(4) = \pm H_o(1+2(T+T^2+T^3))$$

$$\cdots \qquad \cdots \qquad \cdots$$

$$A^{\pm}(m) = \pm H_o\left(1+2\sum_{i=1}^{m-1} T^i\right).$$

The $A^{\pm}(m)$'s form a geometric progression and, since $T < 1$, they have two limit points, $\pm A$:

$$A^{\pm}(m) \xrightarrow[m\to\infty]{} \pm H_o(1+2\sum_{i=1}^{\infty} T^i)$$

$$= \pm H_o(1+2(\frac{T}{1-T}))$$

$$= \pm H_o(\frac{1+T}{1-T})$$

$$= \pm H_o(\frac{\lambda}{m})$$

$$= \pm \lambda L = \pm A,$$

thus $\pm A$ are the termini of CE. Therefore, an infinite number of extensions of the CD, or reflections of the wave from the boundaries, are required to reach the vertex of D. This fact raises an important physical-philosophical point, though it presents no mathematical difficulties. The troublesome point is that the infinite number of wave reflections required to reach the vertex of the wedge is not consistent with the steady-state assumption of $\psi \sim e^{i\sigma t}$. This difficulty with the problem takes diminished significance when the singular nature of the solution in the vertex is recognized in subsequent steps. The singularity in the vertex indicates a breakdown of the linear, inviscid theory and admits the possibility of an energy sink.

The $A^{\pm}(m)$'s form a partition of CE. It is convenient to define

$$B(m) = B^{+}(m) \cup B^{-}(m),$$

where

$$B^+(m): \{z:(A^+(m-1) \leq z \leq A^+(m))\}$$

and

$$B^-(m): \{z:(A^-(m) \leq z \leq A^-(m-1))\}, \quad m = 1, 2, \ldots, \infty.$$

Then

$$C = B^-(1), \quad CE^+ = \bigcup_{m=1}^{\infty} B^+(m), \quad \text{and} \quad CE^- = \bigcup_{m=2}^{\infty} B^-(m).$$

Thus, RR1 is used to extend CD from $B^-(m)$ to $B^+(m)$, and RR2 is used to extend CD from $B^-(1) \cup B^+(1)$ to $B^-(2)$ initially and then from $B^+(m)$ to $B^-(m+1)$ for all m.

The iterative nature of the "leapfrog" extension, and the analysis of the $A^{\pm}(m)$'s, suggests seeking the rule for directly finding the CD on $B(m)$, m arbitrary, after the CD are set on $B^-(1)$. F and G are designated $F^{\pm}(z;m)$ and $G^{\pm}(z;m)$, respectively, on $B^{\pm}(m)$. The general rule is derived by induction.

The problem of extending F is considered. Let

$$F_o(z) = \begin{cases} F^-(z;1), & -H_o \leq z \leq 0 \\ F^+(z;1) = -F^-(-z;1), & 0 \leq z \leq H_o, \quad \text{by RR1,} \end{cases}$$

then

i) $$F^-(z;2) = -F_o(-H_o(1+\frac{1}{T})-\frac{z}{T}), \quad \text{by RR2}$$

$$= -F_o(-H_o+T^{-1}A^-(1)-T^{-1}z),$$

$$A^-(2) = -H_o(1+2T) \leq z \leq -H_o = A^-(1)$$

ii) $F^+(z;2) = -F^-(z;2)$, by RR1

$$= F_o(-H_o(1+\frac{1}{T})+\frac{z}{T})$$

$$= F_o(-H_o-T^{-1}A^+(1)+T^{-1}z),$$

$$A^+(1) = H_o \leq z \leq H_o(1+2T) = A^+(2)$$

iii) $F^-(z;3) = -F^+(-H_o(1+\frac{1}{T})-\frac{z}{T};2)$, by RR2

$$= -F_o(-H_o(1+\frac{1}{T})-H_o(\frac{1}{T}+\frac{1}{T^2})-\frac{z}{T^2})$$

$$= -F_o(-H_o(1+\frac{2}{T}+\frac{1}{T^2})-\frac{z}{T^2})$$

$$= -F_o(-H_o-\frac{H_o}{T^2}(1+2T)-\frac{z}{T^2})$$

$$= -F_o(-H_o+T^{-2}A^-(2)-T^{-2}z),$$

$$A^-(3) = -H_o(1+2(T+T^2)) \leq z \leq -H_o(1+2T) = A^-(2)$$

iv) $F^+(z;3) = F_o(-H_o-T^{-2}A^+(2)+T^{-2}z),$

$$A^+(2) = H_o(1+2T) \leq z \leq H_o(1+2(T+T^2)) = A^+(3)$$

v) then by induction,

$$F^+(z;m+1) = F_o(-H_o-T^{-m}A^+(m)+T^{-m}z),\ A^+(m) \leq z \leq A^+(m+1)$$

and

$$F^-(z;m+1) = -F_o(-H_o+T^{-m}A^-(m)-T^{-m}z),\ A^-(m+1) \leq z < A^-(m).$$

With

$$G_o(z) = \begin{cases} G^-(z;1), & -H_o \leq z \leq 0 \\ G^+(z;1) = G^-(z;1), & 0 \leq z \leq H_o, \end{cases}$$

then by analogy

$$G^{+}(z;m+1) = G_o(-H_o - T^{-m}A^{+}(m) + T^{-m}z),$$

$$A^{+}(m) \leq z \leq A^{+}(m+1)$$

and

$$G^{-}(z;m+1) = G_o(-H_o + T^{-m}A^{-}(m) - T^{-m}z),$$

$$A^{-}(m+1) \leq z \leq A^{-}(m).$$

The extended CD can be evaluated at the $A(m)$'s:

$$F^{\pm}(A^{\pm}(m), m+1) = \pm F_o(-H_o),$$

$$G^{\pm}(A^{+}(m), m+1) = G_o(-H_o),$$

$$F^{\pm}(A^{+}(m+1), m+1) = \pm F_o(H_o),$$

and

$$G^{\pm}(A^{\pm}(m+1), m+1) = G_o(H_o),$$

where the relation

$$-H_o \pm T^{-m}A^{\mp}(m) = +H_o \pm T^{-m}A^{\mp}(m+1)$$

has been employed for the last two relations. Thus, the full range of the CD extended to $-H_o \leq z \leq H_o$ is mapped onto each of the successively smaller $B(m)$'s. As a consequence, F and G "wiggle" at an ever increasing rate, thus the partial derivatives of ψ in D grow without bound as $T \rightarrow 0$ with $\lambda_1 \rightarrow m$. The result is consistent with the concept of the bounded beam phenomenon

(Sandstrom, 1966), i. e., large currents occur along a nearly critical bottom slope. The increased rate of "wiggle" of F and G is an intuitive way of expressing the fact that the effective wave number increases after each reflection from the bottom boundary. In essence, the incident wave "beats with the bottom slope" upon each reflection, causing a shift to ever-increasing wave numbers.

In sub-domain $D_{n,n} = \{(x, z) : (z_U \in B^-(n) \text{ and } z_D \in B^+(n))\}$, the downgoing and upgoing waves have the same wave numbers, which allows a simple analysis of the phase and group speeds. Take the incident wave number to be (k_o, m_o) at the initial line; then, in $D_{n,n'}$ the wave number is $(k_n, m_n) = \frac{1}{T^n}(k_o, m_o) \xrightarrow[n\to\infty]{} \infty$. Thus, the phase speed, $(c_p)_n$, for the wave in $D_{n,n}$ is

$$(c_p)_n = \frac{\sigma}{k} = T^n\left(\frac{\sigma}{k_o}\right) = T^n (c_p)_o \xrightarrow[n\to\infty]{} 0,$$

where $(c_p)_o$ is the phase speed of the incident wave. Similarly, the group speed, $(c_g)_n$, for the wave in $D_{n,n}$ is

$$(c_g)_n = \frac{k}{\sigma}\left[\frac{(N^2-f^2)m^2}{(k^2+m^2)^2}\right] = T^n (c_g)_o \xrightarrow[n\to\infty]{} 0,$$

where $(c_g)_o$ is the group speed of the incident wave. These results are consistent with the qualitative remarks of Section III. C. and are rigorously correct. In sub-domains $D_{m,n} (m \neq n)$, the wave

number, phase speed, and group speed of the downgoing and upgoing waves are not equal.

For any point (x_1, z_1) in D, $z_U = \eta = z - \lambda x$ and $z_D = \zeta = z + \lambda x$ are computed; then $z_U \in B^-(m)$ and $z_D \in B^+(n)$ for some m and n, where $m \neq n$ except in regions contiguous with the sea surface. Once m and n are determined, then F and G can be computed, the Riemann invariants formed, ψ at (x_1, z_1) formed, and $u(x_1, z_1)$ and $w(x_1, z_1)$ computed from ψ. Actually, the solution need not be computed point-by-point but rather for sub-domains $D_{m,n} = \{(x, z) : (z_U \in B^-(m) \text{ and } z_D \in B^+(n))\}$.

Several remarks are made:

i) Because $F(^{\pm}A(n)) = 0$ and $G(^{+}A(n)) = G(^{-}A(n))$ for all n, then $F(A) = F(-A) = 0$ and $G(A) = G(-A)$, therefore $\psi(L, 0) = \frac{1}{2}[F(A)+F(-A)] + \frac{1}{2\lambda}[G(A)-G(-A)] = 0$. Thus, the solution in the vertex of the wedge is zero, though the amplitudes of the u and w fields increase without bound as the vertex is approached.

ii) The linear theory is a small amplitude theory. The small amplitude criterion is typically $w_x \ll \sigma$, the wave frequency, where $w_x = \psi_{xx}$. If the initial value for w_x is kA where k is the incident horizontal wave number and A is the initial wave amplitude, then, after n reflections, $w_x = T^{-2n}(kA)$. Thus $w_x \sim \sigma$, when $n \approx \frac{1}{2}\frac{\ln (kA/\sigma)}{\ln (T)}$ and

a finite amplitude theory becomes mandatory. For example, for the semidiurnal internal tide, $\sigma \approx 10^{-4}\,\mathrm{sec}^{-1}$, take $k \approx 1/3 \times 10^{-5}\,\mathrm{cm}^{-1}$ and $A \approx 10^{-1}\,\mathrm{cm/sec}$, so $\frac{kA}{\sigma} \approx 1/4 \times 10^{-2} \ll 1$. Since T has been taken to be $3/7$ in Figure 12, then

$$n \approx 4.$$

Thus, after four reflections a finite amplitude theory may be necessary.

iii) The number of surface reflections which occur in a specified percentage, P, of the distance from the initial line to the vertex of the wedge can be determined:

$$\frac{A(n)}{\lambda L} \leq P \leq \frac{A(n+1)}{\lambda L}$$

or

$$(\frac{m}{\lambda})(1+2\sum_{i=1}^{n-1} T^i) \leq P \leq (\frac{m}{\lambda})(1+2\sum_{i=1}^{n} T^i)$$

so

$$(\frac{m}{\lambda})[1+2(T\,\frac{(1-T^{n-1})}{1-T})] \leq P \leq (\frac{m}{\lambda})[1+2(T\,\frac{(1-T^{n})}{1-T})]$$

or

$$T^{n+1} \leq \frac{[(1+T)-(1-T)(\frac{\lambda}{m})P]}{2} \leq T^{n}.$$

Since

$$1 + T = \frac{2\lambda}{\lambda+m}$$

and

$$1 - T = \frac{2m}{\lambda+m},$$

then

$$T^{n+1} \leq (1-P)\left(\frac{\lambda}{\lambda+m}\right) \leq T^{n}.$$

Since $0 \leq T \leq 1$, then

$$n \leq \frac{\ln (1-P) + \ln \left(\frac{\lambda}{\lambda+m}\right)}{\ln T} \leq n + 1.$$

For example, in the case chosen, $\ln T \approx -0.85$ and $\ln \left(\frac{\lambda}{\lambda+m}\right) \approx 0.34$. Take P_n and P_{n+1} to be the values of P when the equalities on the left and on the right hold, respectively. Then $\ln (1-P_3) \approx -2.21$ or $P_3 \approx 8/9$, and $\ln (1-P_4) \approx -3.06$ or $P_4 \approx 20/21$. Therefore, on the basis of the above and the calculation in ii), small amplitude theory would breakdown for the hypothesized wave at about (56 to 60/63's) of the distance from the seaward edge of the continental shelf to the coastline.

E. The Solution for Inertial-Internal Waves with Frontal Interaction when Boundaries are Parallel

A normal mode approach is not possible for cases with frontal interaction, since the presence of the ψ_{xz} term in the GE does not permit SOV in x and z. The GE does separate in η and ζ, but, of course, the BC's do not. The asymmetry introduced by the ψ_{xz} term induces the asymmetry of the characteristics η and ζ. Naturally, this same asymmetry haunts the solution as well as the problem. From Section C, the general solution for ψ has the form:

$$\psi(x, z) = \frac{1}{(\lambda_1 - \lambda_2)}\{[\lambda_1 F(z-\lambda_2 x) - \lambda_2 F(z-\lambda_1 x)] + [G(z-\lambda_2 x) - G(z-\lambda_1)]\}.$$

The reflection rules for extending the CD are

RR1:
$$F(\gamma r) = -\gamma F(-r)$$
$$G(\gamma r) = G(-r)$$

and, since $m = 0$, then $T = \frac{1}{\gamma}$ and

RR2:
$$F(-H_o - \frac{r}{\gamma}) = -\frac{1}{\gamma} F(-H_o + r)$$
$$G(-H_o - \frac{r}{\gamma}) = G(-H_o + r),$$

where, again, r is the parameter of CE.

The character of the solution can be discerned by extending the CD a few steps:

i) The CD are given on $-H_o \leq z \leq 0$.

ii) They are extended from $-H_o \leq z \leq 0$ to $0 \leq z \leq \gamma H_o$, by RR1.

iii) They are extended from $-H_o \leq z \leq 0$ to $-H_o(1+\frac{1}{\gamma}) \leq z \leq -H_o$ and from $0 \leq z \leq \gamma H_o$ to $-H_o(2+\frac{1}{\gamma}) \leq z \leq -H_o(1+\frac{1}{\gamma})$, by RR2.

iv) They are extended from $-H_o(1+\frac{1}{\gamma}) \leq z \leq -H_o$ to $\gamma H_o \leq z \leq H_o(1+\gamma)$ and from $-H_o(2+\frac{1}{\gamma}) \leq z \leq -H_o(1+\frac{1}{\gamma})$ to

$H_o(1+\gamma) \leq z \leq H_o(1+2\gamma)$, by RR 1.

v) They are extended to all of CE in the same manner.

Figure 13 illustrates the pattern of the extension of the CD on CE and the consequent solution types in D. The pattern can be summarized by saying that the given CD are continued over intervals alternating in length (γH_o and H_o) and ($\frac{1}{\gamma}H_o$ and H_o) over $z \geq 0$ and $z \leq -H_o$, respectively. There are three basic source types:

i) A, from a segment of CE H_o in length,

ii) B, from a segment of CE γH_o in length,

and

iii) C, from a segment of CE $\frac{H_o}{\gamma}$ in length.

When the prefixes U or D are added to the source type, it is indicated whether the source type is supplied by upgoing or downgoing characteristics, respectively. Four solution types emerge; they are categorized by the length of the segments of CE from which their characteristics emerge:

Solution type	CE segment lengths	Source type
I:	both segments H_o in length	UA and DA
II:	segments H_o and γH_o in length	UA and DB
III:	segments $\frac{H_o}{\gamma}$ and H_o in length	UC and DA
IV:	segments $\frac{H_o}{\gamma}$ and γH_o in length	UC and DB.

Types I and IV occur in the interior; types II and III occur contiguous with the upper and lower boundaries, respectively.

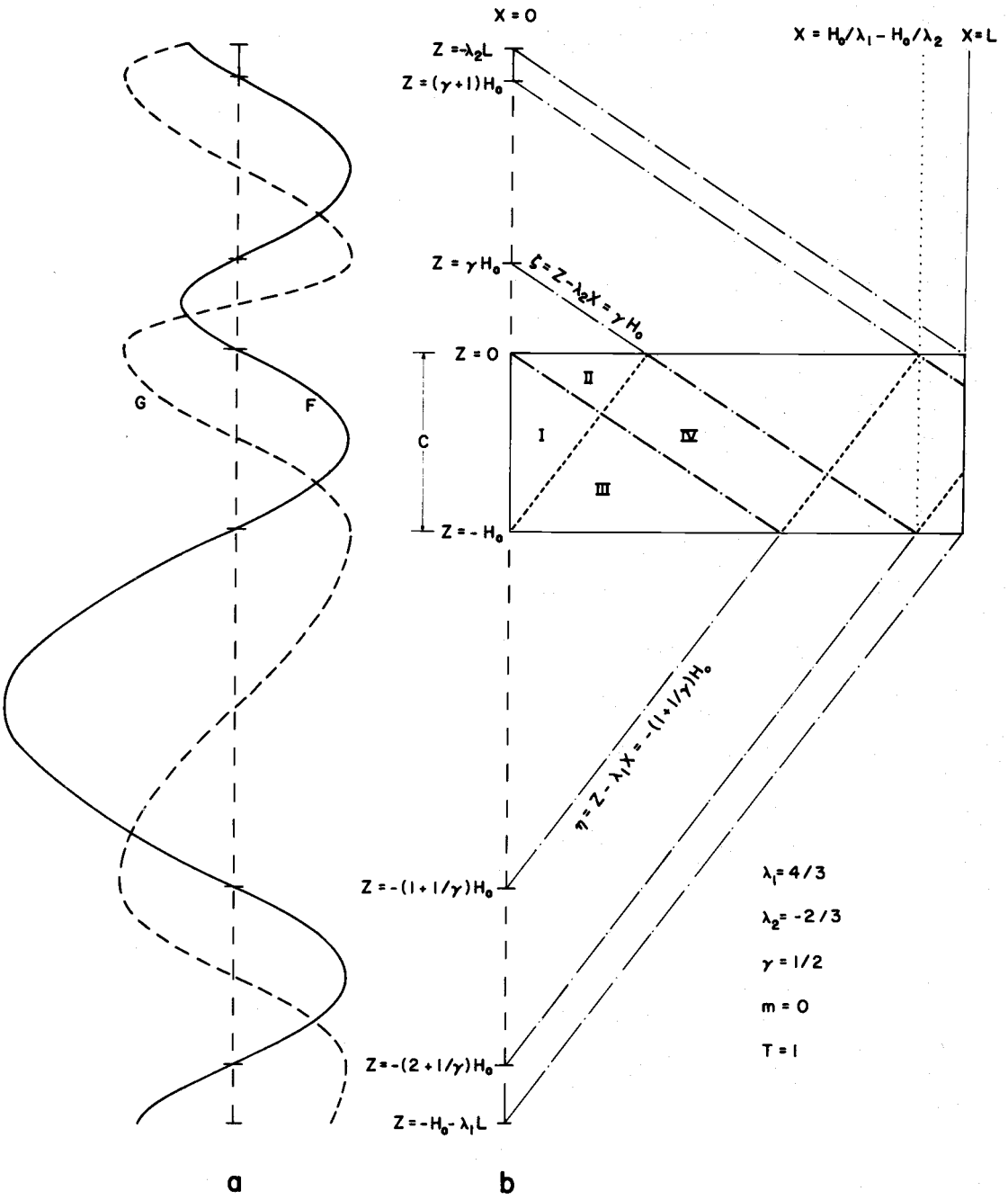

Figure 13. Graphical solution for a case with parallel boundaries and with frontal interaction.
a. Extended CD
b. Domain D and limiting characteristics

For a convenient example, take

$$F(z) = A \sin (Kz)$$

and

$$G(z) = B \cos (Kz), \quad \text{for} \quad -H_o \leq z \leq 0,$$

where $KH_o = n\pi$ for some n : integer; this is a type A source.

Then the following extensions are made for $n = 1$:

i) $F(z) = -\gamma A \sin (K(-\frac{z}{\gamma}))$

$= \gamma A \sin (K\frac{z}{\gamma})$, and

$G(z) = B \cos (K\frac{z}{\gamma}), \quad (0 \leq z \leq \gamma H_o)$;

this is a type B source.

ii) $F(z) = -\frac{1}{\gamma} A \sin (K(-(1+\gamma)H_o - z\gamma))$

$= \frac{-1}{\gamma} A \sin (K\gamma(H_o+z))$, and

$G(z) = B \cos (K(-(1+\gamma)H_o - z\gamma)$

$= -B \cos (\gamma(H_o+z)), \quad (-H_o(1+\frac{1}{\gamma}) \leq z \leq -H_o)$;

this is a type C source.

iii) $F(z) = -\frac{1}{\gamma}(\gamma A) \sin (\frac{K}{\gamma}(-(1+\gamma)H_o - z\gamma))$

$= A \sin (K(\frac{1}{\gamma}+1)H_o + z)$

$= -A \sin (K(\frac{H_o}{\gamma}+z)$, and

$G(z) = B \cos (\frac{K}{\gamma}(-(1+\gamma)H_o - z\gamma))$

$= -B \cos (K(\frac{H_o}{\gamma}+z)), \quad (-H_o(2+\frac{1}{\gamma}) \leq z \leq -H_o(1+\frac{1}{\gamma}))$;

this is a type A source.

iv) $F(z) = -\gamma(-\frac{A}{\gamma}) \sin (K\gamma(H_o - \frac{z}{\gamma}))$

$= -A \sin (K(z-\gamma H_o))$, and

$G(z) = -B \cos (K(z-\gamma H_o))$, $(\gamma H_o \leq z \leq (1+\gamma)H_o)$;

this is a type A source.

v) $F(z) = -\gamma(-A) \sin (K(\frac{H_o}{\gamma} - \frac{z}{\gamma}))$

$= \gamma A \sin (\frac{K}{\gamma}(H_o - z))$, and

$G(z) = -B \cos (\frac{K}{\gamma}(H_o - z))$, $((1+\gamma)H_o \leq z \leq (1+2\gamma)H_o)$;

this is a type A source.

The pattern of the extension of the CD continues to repeat itself to cover all of CE. The Riemann invariants are formed for each source type:

i) For source type A, both I_{UA} and I_{DA} are necessary:

$$I_{UA}(\eta) = \frac{-1}{(\lambda_1 - \lambda_2)}[\lambda_1 F(\eta) + G(\eta)]$$

$$= \frac{1}{(\lambda_1 - \lambda_2)}[\lambda_2 A \sin (K\eta) + B \cos (K\eta)]$$

and

$$I_{DA}(\zeta) = \frac{1}{(\lambda_1 - \lambda_2)}[\lambda_1 F(\zeta) + G(\zeta)]$$

$$= \frac{1}{(\lambda_1 - \lambda_2)}[\lambda_1 A \sin (K\zeta) + B \cos (K\zeta)].$$

ii) For source type B, only I_{DB} is necessary:

$$I_{DB}(\zeta) = \frac{1}{(\lambda_1-\lambda_2)}\left[-\lambda_2 A \sin\left(\frac{K\zeta}{\gamma}\right) + B \cos\left(\frac{K\zeta}{\gamma}\right)\right].$$

iii) For source type C, only I_{UC} is necessary:

$$I_{UC}(\eta) = \frac{1}{(\lambda_1-\lambda_2)}\left[-\lambda_1 A \sin(\gamma(H_o+\eta)) + B \cos(\gamma(H_o+\eta))\right].$$

The four solution types are then computed:

i) Type I,

$$\psi_I = I_{UA}(\eta) + I_{DA}(\zeta)$$

$$= \left(\frac{1}{\lambda_1-\lambda_2}\right)\{[\lambda_2 A \sin(K(z-\lambda_1 x)) - B \cos(K(z-\lambda_1 x))]$$

$$+ [\lambda_1 A \sin(K(z-\lambda_2 x)) + B \cos(K(z-\lambda_2 x))]\}.$$

ii) Type II,

$$\psi_{II} = I_{UA}(\eta) + I_{DB}(\zeta)$$

$$= \left(\frac{1}{\lambda_1-\lambda_2}\right)\{[\lambda_2 A \sin(K(z-\lambda_1 x)) - B \cos(K(z-\lambda_1 x))]$$

$$+ \left[-\lambda_2 A \sin\left(\frac{K}{\gamma}(z-\lambda_2 x)\right) + B \cos\left(\frac{K}{\gamma}(z-\lambda_2 x)\right)\right]\}.$$

iii) Type III,

$$\psi_{III} = I_{UC}(\eta) + I_{DA}(\zeta)$$

$$= \left(\frac{1}{\lambda_1-\lambda_2}\right)\{[-\lambda_1 A \sin(\gamma(H_o+z-\lambda_1 x)) + B \cos(\gamma(H_o+z-\lambda_1 x))]$$

$$+ [\lambda_1 A \sin(K(z-\lambda_2 x)) + B \cos(K(z-\lambda_2 x))]\}.$$

iv) Type IV,

$$\psi_{IV} = I_{UC}(\eta) + I_{DB}(\zeta)$$

$$= \left(\frac{1}{\lambda_1 - \lambda_2}\right)\{[-\lambda_1 A \sin(\gamma(H_o + z - \lambda_1 x)) + B\cos(\gamma(H_o + z - \lambda_1 x))]$$

$$+ [\lambda_2 A \sin\left(\frac{K}{\gamma}(z - \lambda_2 x)\right) + B \cos\left(\frac{K}{\gamma}(z - \lambda_2 x)\right)]\}.$$

The most important qualitative feature of the solution is that the asymmetry of the characteristics, due to the existence of the frontal zone, has induced alternating zones of increased, decreased, normal, and anormal (i. e., mixed increased and decreased) wave numbers. In other words, there are spatial zones where the wave "wiggles" more or less than usual; therefore there are zones of relatively high and low shear in the velocity of the wave. Another consequence is that lines of constant phase are tilted with respect to the vertical, i. e., the waves tend to be "tipped over," within an effective wavelength. After two reflections from each boundary, the wave is restored to its original form. The wave is characterized by an effective horizontal wavelength, $\lambda^{(h)} = \left(\frac{H}{\lambda_1} - \frac{H}{\lambda_2}\right)$, which is different than the horizontal wavelength, $\lambda^{(h)} = \left(\frac{2H}{\lambda}\right)$, without the frontal interaction.

The coastal BC is more difficult to apply in this case than in the case of Section B. Because the geometry of the problem is constrained by the asymmetrical characteristics, A and B must

satisfy two conditions to satisfy a coastal BC. Equivalently, the CD can not be assumed to be Type I. The best procedure is to solve the problem "backwards" from the coastline, where the solution must be Type I, to the initial line and then discover what solution type the CD are required to be. Because of these complications, the essential properties of the solution are illustrated in Figure 13 with the coast treated as an open boundary.

F. The Solution for Inertial-Internal Waves with Frontal Interaction in a Wedge

A slight extension of the analyses in Sections D and E is required to obtain the solution for inertial-internal waves with frontal interaction in a wedge. Because the solution in a wedge is sought, it is known from Section D that an infinite number of extensions of the CD are required. Because the solution sought involves the frontal interaction, it is known from Section E that there are four basic solution types. Thus, the solution exhibits the properties of the solutions of both Section D and E. In particular, the intervals of extension, $B^{\pm}(m)$, both tend to decrease in length as m increases, as in Section D, and tend to alternate in length by factors of γ and $\frac{1}{\gamma}$ on CE^{+} and CE^{-}, respectively, as in Section E.

From Section C, the general solution for ψ has the form:

$$\psi(x, z) = \frac{1}{(\lambda_1 - \lambda_2)} \{[\lambda_1 F(z-\lambda_2 x) - \lambda_2 F(z-\lambda_1 x)] + [G(z-\lambda_2 x) - G(z-\lambda_1 x)]\}$$

and the reflection rules for extending the CD are

RR1:
$$F(\gamma r) = -\gamma F(-r)$$
$$G(\gamma r) = G(-r)$$

and, assuming the bottom slope uniform,

RR2:
$$F(-H_o - Tr) = -\frac{1}{\gamma} F(-H_o + r)$$
$$G(-H_o - Tr) = G(-H_o + r),$$

where, again, r is the parameter of CE. Since the general solution was examined in detail in Sections D and F, it suffices to write the first Type IV solution and to examine it in detail. Figure 14 illustrates the pattern of extension of the CD on CE. The region, $D_1^{(4)}$, where the first Type IV solution occurs is indicated.

Take the CD to be given as

$$F(z) = A \sin (Kz)$$

and

$$G(z) = B \cos (Kz), \quad (-H_o \leq z \leq 0),$$

where $H_o K = n\pi$, n : integer. The first Type IV solution has its $I_D(\zeta)$'s coming from $0 \leq z \leq \gamma H_o$ on CE^+ and its $I_U(\eta)$'s

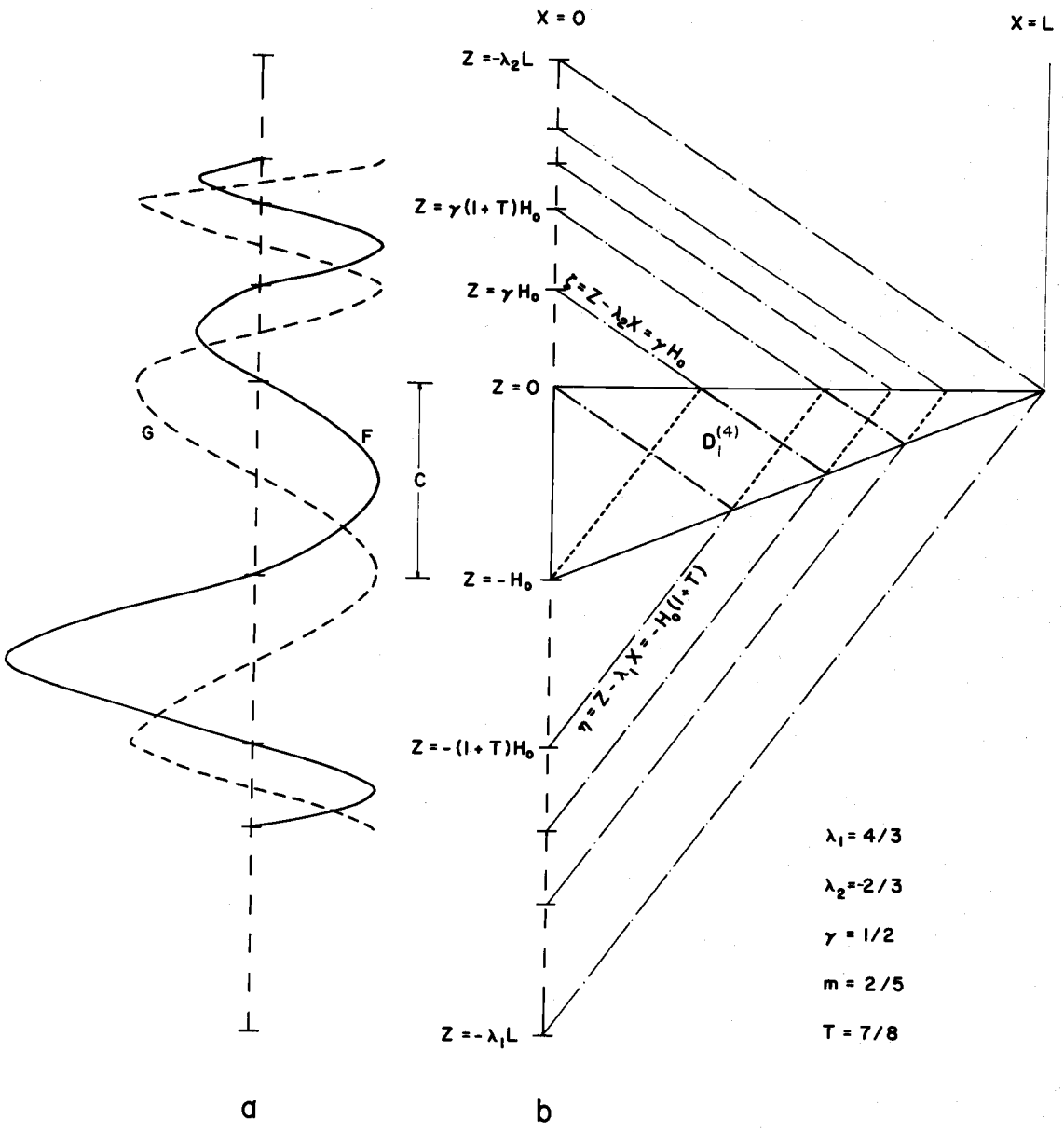

Figure 14. Graphical solution for a case in a wedge and with frontal interaction.

a. Extended CD

b. Domain D and limiting characteristics

coming from $-H_o(1+T) \leq z \leq -H_o$ on CE^-. The CD are extended and the relevant Riemann invariants written in a single step:

$$I_D(\zeta) = \frac{1}{(\lambda_1-\lambda_2)}[\lambda_1 F(\zeta) + G(\zeta)]$$

$$= \frac{1}{(\lambda_1-\lambda_2)}[-\gamma\lambda_1 A \sin(K\frac{-\zeta}{\gamma}) + B\cos(K\frac{-\zeta}{\gamma})]$$

$$= \frac{1}{(\lambda_1-\lambda_2)}[-\lambda_2 A \sin(K\frac{\zeta}{\gamma}) + B\cos(K\frac{\zeta}{\gamma})] \qquad (0 \leq \zeta \leq \gamma H_o)$$

and

$$I_U(\eta) = \frac{1}{(\lambda_1-\lambda_2)}[-\lambda_2 F(\eta) - G(\eta)]$$

$$= \frac{1}{(\lambda_1-\lambda_2)}[\frac{\lambda_2 A}{\gamma}\sin(K(-H_o(1+\frac{1}{T}) - \frac{\eta}{T})) - B\cos(K(-H_o(1+\frac{1}{T}) - \frac{\eta}{T}))]$$

$$= \frac{1}{(\lambda_1-\lambda_2)}[-\lambda_1 A \sin(K(\frac{\eta+H_o}{T})) + B\cos(K(\frac{\eta+H_o}{T}))],$$

$$(-H_o(1+T) \leq \eta \leq -H_o).$$

Then for any point (x, z) in $D_1^{(4)}$,

$$\psi(x, z) = \frac{1}{(\lambda_1-\lambda_2)}\{[-\lambda_2 A \sin(K\frac{(z-\lambda_2 x)}{\gamma}) + B\cos(K\frac{(z-\lambda_2 x)}{\gamma})]$$

$$+ [-\lambda_1 A \sin(K\frac{(z+H_o-\lambda_1 x)}{T}) + B\cos(K\frac{(z+H_o-\lambda_1 x)}{T})]\}.$$

The subregion $D_1^{(4)}$ has a vertex on the surface boundary at

$$\zeta = -\lambda_2 x = \gamma H_o \quad \text{or} \quad x = \frac{H_o}{\lambda_1} \quad \text{and} \quad z = 0,$$

and one on the bottom boundary at

$$\eta = -H_o + mx - \lambda_1 x = -H_o(1+T)$$

or

$$x = \frac{H_o T}{(\lambda_1 - m)}$$

$$= \frac{H_o}{(-\lambda_2 + m)}$$

and

$$z = \frac{\lambda_2 H_o}{(-\lambda_2 + m)} \quad .$$

Since

$$\left(\frac{z-\lambda_2 x}{\gamma}\right)\Bigg|_{\substack{x=\frac{H_o}{\lambda_1} \\ z=0}} = H_o \quad \text{and} \quad \left(\frac{z+H_o-\lambda_1 x}{T}\right)\Bigg|_{\substack{x=\frac{H_o}{\lambda_1} \\ z=0}} = 0,$$

$$\psi\left(\frac{H_o}{\lambda_1}, 0\right) = \frac{1}{(\lambda_1-\lambda_2)}\{[-\lambda_2 A \sin(KH_o) + B\cos(KH_o)]$$

$$+ [-\lambda_1 A \sin(K(0)) + B\cos(K(0))]\} = 0.$$

Since

$$\left(\frac{z-\lambda_2 x}{\gamma}\right)\Bigg|_{\substack{x=\frac{H_o}{(-\lambda_2+m)} \\ z=\frac{\lambda_2 H_o}{(-\lambda_2+m)}}} = 0$$

and

$$\left.\frac{(z+H_o-\lambda_1 x)}{\gamma}\right|_{\substack{x=\frac{H_o}{(-\lambda_2+m)} \\ z=\frac{\lambda_2 H_o}{(-\lambda_2+m)}}} = -H_o,$$

$$\psi\left(\frac{H_o}{(-\lambda_2+m)}, \frac{\lambda_2 H_o}{(-\lambda_2+m)}\right) = \frac{1}{(\lambda_1-\lambda_2)}\{[-\lambda_2 A \sin(0) + B\cos(0)]$$

$$+ [-\lambda_1 A \sin(-KH_o) + B\cos(-KH_o)]\}$$

$$= 0.$$

Thus, ψ in $D_1^{(4)}$ satisfies the BC's where it must.

To verify that the ψ in $D_1^{(4)}$ satisfies the GE, the second order partial derivatives of ψ are evaluated:

$$\psi_{xx} = -(\lambda_2)^2(\frac{K}{\gamma})^2 I_D(\zeta) - (\lambda_1)^2(\frac{K}{T})^2 I_U(\eta),$$

$$\psi_{zz} = -(\frac{K}{\gamma})^2 I_D(\zeta) - (\frac{K}{T})^2 I_U(\eta),$$

and

$$\psi_{xz} = +\lambda_2(\frac{K}{\gamma})^2 I_D(\zeta) + \lambda_1(\frac{K}{T})^2 I_U(\eta).$$

The GE is written as

$$\psi_{xx} + (\lambda_1+\lambda_2)\psi_{xz} + \lambda_1\lambda_2\psi_{zz} = 0.$$

Substituting into the GE, and considering the factors of $-(\frac{K}{\gamma})^2 I_D(\zeta)$, then

$$(\lambda_2)^2 + (\lambda_1+\lambda_2)(-\lambda_2) + \lambda_1\lambda_2 = 0,$$

and, considering the factors of $-(\frac{K}{T})^2 I_U$, then

$$(\lambda_1)^2 + (\lambda_1+\lambda_2)(-\lambda_1) + \lambda_1\lambda_2 = 0.$$

Thus, the solution in $D_1^{(4)}$ is valid in all respects.

G. The Solution for Supercritical Bottom Slope

To elucidate the essential physics of the solution for supercritical bottom slopes, it is sufficient to consider the case of no frontal interaction and a uniform bottom slope.

The general solution for ψ has the form

$$\psi = \frac{1}{2}[F(z+\lambda x) + F(z-\lambda x)] + \frac{1}{2\lambda}[G(z+\lambda x) - G(z-\lambda x)].$$

The reflection rules are given in their coupled forms until it becomes clear where F and G are independent:

RR1: $$[F(r)+F(-r)] + \frac{1}{\lambda}[G(r)-G(-r)] = 0$$

and

$$[F(-H_o+s)+F(-H_o-Ts)] + \frac{1}{\lambda}[G(-H_o+s)-G(-H_o-Ts)] = 0,$$

or

RR2: $$[F(r)+F(-(\frac{2\lambda H_o+(\lambda-m)r}{\lambda+m}))] + \frac{1}{\lambda}[G(r)-G(-(\frac{2\lambda H_o+(\lambda-m)r}{\lambda+m}))] = 0,$$

where r and s are parameters of CE.

The geometry of the problem is shown in Figure 15a. It is recognized that CE is $(-H_o \leq -\lambda L \leq r \leq \lambda L)$. RR1 provides the rule for the extension of the CD from $-\lambda L \leq r \leq 0$ to $0 \leq r \leq \lambda L$. It can be employed in its uncoupled form; i. e., F and G can be treated as independent over those intervals without ambiguity, thus

RR1: $$F(r) = -F(-r)$$

$$G(r) = G(-r), \quad (-\lambda L \leq r \leq \lambda L).$$

Examination of the arguments in RR2 indicates that RR2 provides the rule for the extension of the CD from $-H_o \leq r \leq \lambda L$ to $-H_o \leq r \leq -\lambda L$, hence there is an overlapping or ambiguity. Therefore, either F or G can be arbitrarily specified on $-H_o \leq r \leq -\lambda L$; the other is determined on that interval by RR2. For example let F be specified on $-H_o \leq r \leq -\lambda L$; then

$$G\left(-\left(\frac{2\lambda H_o + (\lambda - m)r}{\lambda + m}\right)\right) = G(r) + \lambda\left[F(r) + F\left(-\left(\frac{2\lambda H_o + (\lambda - m)r}{\lambda + m}\right)\right)\right]$$

Thus, there is a subtle "overmapping" of G onto itself in the interval $-H_o \leq r \leq -\lambda L$.

In summary, there are two types of solutions in D:

i) Type I occurs in the sub-domain above $z - \lambda x = -\lambda L$. This solution type can be either a progressive or standing wave

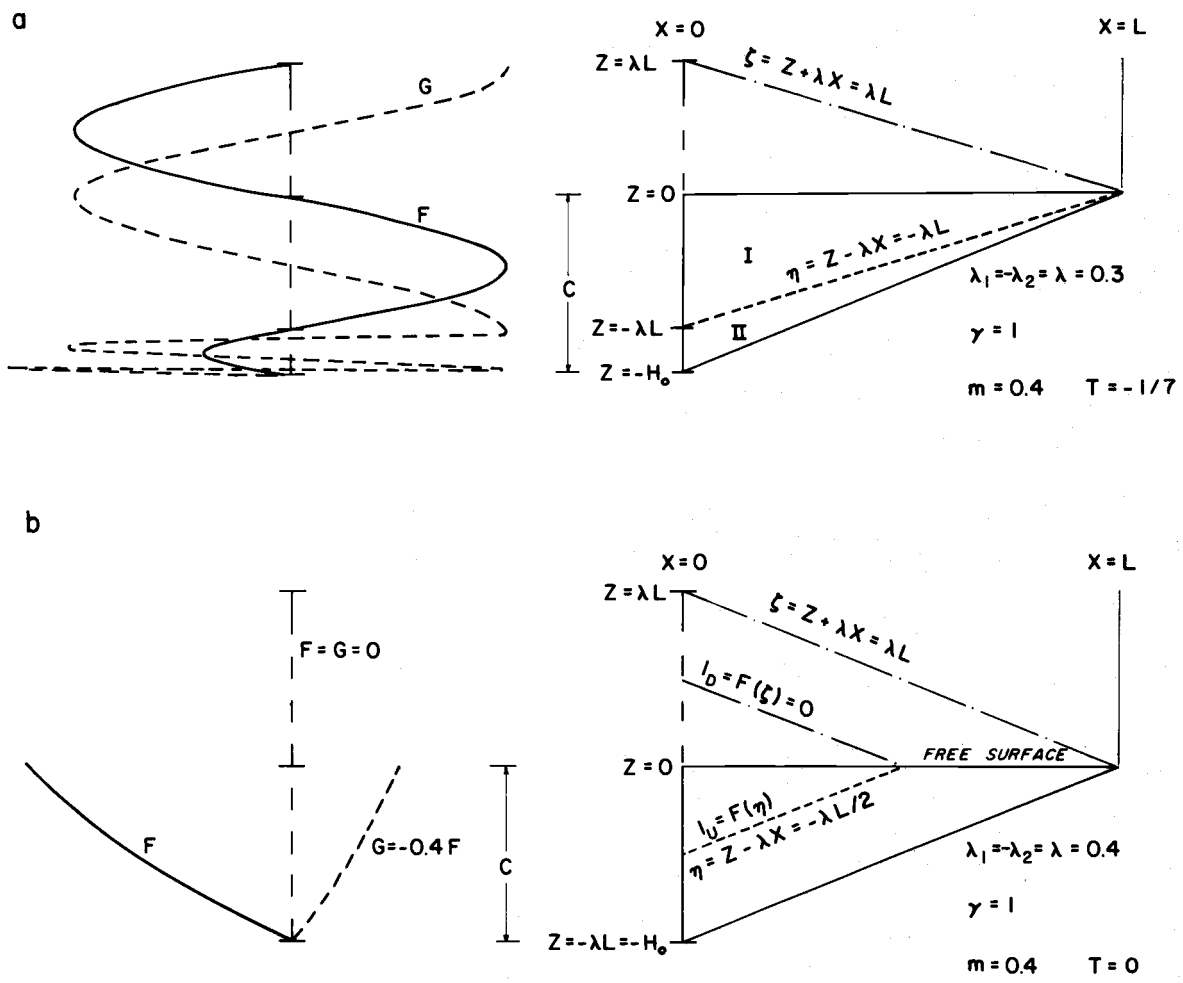

Figure 15. Graphical solution for a case without frontal interaction in a wedge.
a. Supercritical bottom slope
b. Critical bottom slope

depending on the time phase between F and G.

ii) Type II occurs in the sub-domain below $z - \lambda x = -\lambda L$. The nature of this solution type is controlled by the Type I solution. For example, if Type I is a standing wave, so is Type II, and, if Type I is a progressive wave, Type II is a mixture of standing and progressive waves.

A sample extension of the CD is given in Figure 15a; there are actually more wiggles in G near $r = -\lambda L$ than the resolution of the figure can convey.

The result follows that, since $-\lambda L \rightarrow -H_o$, as $\lambda \rightarrow m$, then G in $-H_o \leq r \leq -\lambda L$ has increasingly large derivatives. This result is consistent with the "bounded beam" concept, which has now been derived from the perspective of a supercritical bottom slope as well as from the perspective of a subcritical bottom slope.

H. The Solution for Critical Bottom Slopes ($m = \lambda$)

The degeneracy induced by a critical bottom slope is established for the case of a rigid sea surface, and then the solution is obtained for the case of a free sea surface. It is sufficient to treat the case without frontal interaction and with a uniform bottom slope.

The form of the general solution is the same as in the previous section. The reflection rules for the extension of the CD are written in their coupled forms:

RR1: $\lambda[F(r)+F(-r)] + [G(r)-G(-r)] = 0, \quad (-\lambda L \leq r \leq \lambda L),$

where $\lambda L = H_o$ and

RR2: $\lambda[F(-H_o+2s)+F(-H_o)]+[G(-H_o+2s)-G(-H_o)] = 0, \quad (0 \leq s \leq 2\lambda L),$

where r and s are the parameters of CE. Several deductions can be made:

i) RR1 requires that $F(0) = 0$

ii) RR2 requires that $F(-H_o) = 0$

iii) Take $-H_o + 2s = -r$, then RR2 requires that

$$\lambda F(-r) + G(-r) = G(-H_o).$$

Similarly, let $-H_o + 2s = r$, then

$$\lambda F(r) + G(r) = G(-H_o),$$

thus

$$\lambda[F(r)+F(-r)] + [G(r)+G(-r)] = 2G(-H_o).$$

iv) Substituting the results of iii) into RR1, it follows that

$$G(-r) = G(-H_o),$$

i.e., G is a constant for all r. Then, from RR2, it follows that F is zero for all r. Therefore, $\psi = 0$ throughout D. This result can be achieved from first principles by applying the RBC and treating the resultant

Goursat problem or by applying the RBC and treating the resultant extended Cauchy problem.

Allow the sea surface to be a free surface. Apply the RBC at the sea bottom to ψ in the following form:

$$\psi = \frac{1}{2}[F((z+mx)+F(z-mx)] + \frac{1}{2\lambda}[G(z+mx)-G(z-mx)].$$

Then at $z = -H_o + mx$, the RBC yields

$$-F(-H_o) = F(-H_0+2mx) + \frac{1}{\lambda}[G(-H_o+2mx)-G(-H_o)],$$

or,

$$F(-H_o) = 0$$

and

$$G(-H_o+2mx) = G(-H_o) - \lambda F(-H_o+2mx), \quad \text{for all } x \in D.$$

Thus,

$$G(r) = G(-H_o) - \lambda F(r),$$

and

$$\psi = F(z-mx).$$

The form for ψ is consistent with the facts that the CD are projected onto the sea surface along $z - mx = \text{constant}$ and that the downgoing wave must be perfectly reflected from the bottom surface. Then the FBC requires that

$$m^2F''(-mx) + (\frac{\sigma^2-f^2}{g})F'(-mx) = 0$$

Taking $-mx = r$ and $K = \frac{(\sigma^2 - f^2)}{gm^2}$, then

$$F = F_o e^{-Kr} - F_1$$

or

$$\psi = F_o [e^{-A(z-mx)} - e^{+AH_o}],$$

where $F_1 = F_o e^{AH_o}$ so that $\psi|_{z=-H_o+mx} = 0$ along the bottom.

Thus, assuming $\psi \propto \cos(\sigma t)$, the velocity fields are

$$u(x, z;t) = AF_o e^{-A(z-mx)} \cos(\sigma t),$$

and

$$w(x, z;t) = mAF_o e^{-A(z-mx)} \cos(\sigma t).$$

Then the vertical particle displacement is

$$\zeta(x, z;t) = \frac{mAF_o}{\sigma} e^{-A(z-mx)} \sin(\sigma t),$$

and the displacement of the sea surface is

$$\eta(x; t) = \zeta(x, 0; t) = \frac{mAF_o}{\sigma} e^{mx} \sin(\sigma t).$$

For a numerical example, let the surface tide have an amplitude of 1 meter at the coastline, then

$$\eta(L) = \frac{mAF_o}{\sigma} e^{AH_o} \sin(\sigma t) = 10^2 \sin(\sigma t) \text{ cm},$$

thus

$$u(0, -H_o) = AF_o e^{AH_o} \cos(\sigma t)$$

$$= \frac{\sigma}{m} 10^2 \cos(\sigma t) \text{ cm/sec.}$$

For the semidiurnal tide, $\sigma \approx 3/2 \times 10^{-4} \text{sec}^{-1}$, and take $m = 2/3 \times 10^{-2}$, so the bottom current at the at the seaward edge of the shelf is

$$u(0, -H_o) \approx \frac{9}{4} \cos(\sigma t) \text{ cm/sec,}$$

which is a reasonable value. Since $AH_o = \frac{(\sigma^2 - f^2)L}{gm}$, then, for $L = 30$ Km and $f = 10^{-4} \text{sec}^{-1}$,

$$AH_o \approx \frac{5/4 \times 10^{-8} \times 3 \times 10^6}{10^3 \times 2/3 \times 10^{-2}} = \frac{45}{8} \times 10^{-3} \approx 6 \times 10^{-3}.$$

Thus the surfacetide is amplified by a factor of $e^{0.006}$ from the seaward edge of the shelf to the coastline.

The role of the FBC is also investigated in the next section for a case with non-uniform bottom slope.

I. An Exact Solution for an Asymptotically Critical Bottom Slope

As observed in the previous section, the FBC admits exponential solutions in the case of uniform, critical bottom slopes. In this section, exponential CD are assumed for a case with subcritical

bottom slope, and the water depth is allowed to vary with x in a manner consistent with the solution for ψ. The permissible bottom shape is analyzed to determine how it is characterized.

The case of no frontal interaction is considered. The CD are assumed to be:

$$F(z) = Ae^{-Kz}$$

and

$$G(z) = 0, \quad \text{at} \quad x = 0;$$

then the solution is

$$\psi(x, z) = \frac{A}{2}\left[e^{-K(z+\lambda x)} + e^{-K(z-\lambda x)}\right]$$

$$= Ae^{-Kz} \cosh (K\lambda x).$$

The FBC requires that

$$K = \frac{(N^2 - \sigma^2)}{g}.$$

Since the bottom surface must be a streamline, set $\psi\big|_{z=z_b} = C$, thus

$$e^{Kz_b} = \frac{A}{C} \cosh (K\lambda x).$$

Alternatively, since $z_b(0) = -H_o$ and $\psi(0, -H_o) = Ae^{KH_o} = C$, then

$$z_b(x) = -H_o + \frac{1}{K} \ln (\cosh (K\lambda x)).$$

The coastline is at $x = L$ where $z_b(L) = 0$ or

$$L = \frac{1}{\lambda K} \cosh^{-1}(e^{KH_o}).$$

The bottom slope, m, is

$$m(x) = \frac{dz_b}{dx} = \lambda \tanh(K\lambda x),$$

thus

$$m(0) = 0$$

and

$$m(L) = \lambda \tanh(K\lambda L)$$

$$= \lambda (1 - \operatorname{sech}^2 (K\lambda L))^{1/2}$$

$$= \lambda (1 - e^{-2KH_o})^{1/2}.$$

For the semidiurnal tide in the coastal region, $\lambda \approx 1 \times 10^{-2}$ and $K \approx 10^{-7} \text{cm}^{-1}$. Take $H_o = 3 \times 10^5 \text{cm}$, then

$$(1 - e^{-2KH_o})^{1/2} = (1 - e^{-0.06})^{1/2} \approx 0.24$$

and $L \approx 2.4 \times 10^3$ km. Thus, $m(L) \approx 0.24\lambda \approx 2.4 \times 10^{-3}$, and the bottom slope is characterized as montonically increasing from zero at $x = 0$ to the critical value, $m = \lambda$, as $x \to \infty$.

The streamlines parallel the bottom topography and the strength of the flow increases exponentially downward along a vertical and shoreward along a horizontal. Other solutions which are variations

on the basic form can be constructed. The essential feature is that this is an additional case where the FBC plays a role in producing a flow which is strongest along the bottom.

VII. APPLICATION OF THE THEORY TO FRONTAL MODELS WITH VARIABLE COEFFICIENTS

A. Introduction

Two cases with coefficients varying in both independent variables are investigated as frontal models. The first step is to compute the explicit forms for the characteristics, if an integrating factor can be found; otherwise, there is the necessity of solving a pair of integral equations:

$$z(x) - z_o^{\pm} = \int_{x_o}^{x} \lambda^{\pm}(x, z)dx,$$

where, on the initial ine, $x = x_o$,

$$z(x_o) = z_o^{\pm} = \eta^{\pm}.$$

Picard's method of successive approximations can be employed to solve the integral equations. A sufficient condition for convergence of the approximation scheme is that $\lambda^{\pm}$ by Lipschtzian with rexpect to z, and a sufficient condition for that is for $\lambda^{\pm}$ to be continuously differentiable with respect to z, which is the case under most oceanographically realistic conditions.

The second step is to reduce the GE to its canonical form, CGE, which is generally not a wave equation. The CGE may have a

"functionally invariant solutions," if the characteristics satisfy the CGE, or the general solution may be found in terms of integrals of arbitrary functions (Koshlyakov, Smirnov, and Gliner, 1964). Then the general solution and the BC's can be used to extend the CD. Barring such good fortune, if the Riemann-Green function is known, then the solution can be found from the resultant integral involving the Riemann-Green function and the CD. An alternative approach is to convert the second-order CGE to the canonical form of a pair of first-order equations in either a symmetric or non-symmetric hyperbolic system and carry out the integration along characteristics, which usually involves a Picard scheme of successive approximations for a symmetric system or a finite difference scheme for a non-symmetric system. Another approach is to seek a finite difference solution of the GE itself, in either the original coordinates or in the characteristic coordinates. Solving the CGE is most compatible with theory, but it entails a mapping of the CD and the BC's from the (x, z) domain to the (η, ζ) domain and an inverse mapping of the solution. The characteristic variables may separate in the CGE, and, if the shape of the boundaries permits, which is unlikely, a pair of one-dimensional eigenvalue problems must be solved.

To illustrate the solution theories, two cases are considered which resemble actual frontal structures. In both cases, the examination is limited to low frequencies, such that $\sigma^2 \ll N^2$, and the

corresponding GE is:

$$\text{GE:}\quad N^2(x,z)\psi_{xx} - (f\bar{v}_z(x,z)+M^2(x,z))\psi_{xz} - (\sigma^2 - f(f+\bar{v}_x(x,z)))\psi_{zz} = 0.$$

The two analytical models advanced for the frontal region are of progressive complexity.

B. Model Frontal Regimes

Instead of providing a table of numbers for the two-dimensional fields of the variable coefficients and proceeding on a strictly numerical basis, an attempt is made to "probe the problem" with reasonable analytical models. From the outset, it is anticipated that a numerical method will eventually be required. There are several criteria which are sought in the models considered:

i) The self-adjoint nature of the GE should be preserved by the chosen analytical coefficients, i.e., attention is restricted to frontal regimes which are geostrophically balanced for the mean flow component, $\bar{v}$, parallel to the axis of the frontal regime.

ii) Model A should exhibit a monotonically increasing $N^2(x,z)$ as a function of both x and z. Such a model does not exhibit a subsurface frontal layer yet it does have an intensification of the key parameters as both the surface and the coastline are approached.

iii) In addition to exhibiting a monotonically increasing $N^2(x, z)$ as a function of both x and z, Model B should have an inclined frontal layer rising in the direction of increasing x. The frontal layer is characterized as coinciding with a maximum in $N^2(x, z)$ as a function of both x and z.

The frontal models are sketched in Figure 16.

For the mean density field in Model A, one which is both exponential in its x and z dependence is chosen:

$$\bar{\rho}(x, z) = \rho_o + \Delta\rho(1-e^{az-bx}), \quad \text{with} \quad a > 0 \quad \text{and} \quad b > 0,$$

thus

$$\bar{\rho}_z = -a\Delta\rho e^{az-bx} \quad \text{and} \quad \bar{\rho}_x = b\Delta\rho e^{az-bx};$$

then the slope of an isopycnal, s, is given by

$$s = \frac{dz}{dx}\Big)_{\bar{\rho}} = \frac{-\bar{\rho}_x}{\bar{\rho}_z} = \frac{b}{a} > 0.$$

Defining

$$E_o = \frac{a\Delta\rho g}{\rho_o} > 0,$$

then

$$N^2 = E = \frac{-\bar{\rho}_z g}{\rho_o} = E_o e^{az-bx},$$

$$f\bar{v}_z = \frac{-g\bar{\rho}_x}{\rho_o} = E_o e^{az-bx},$$

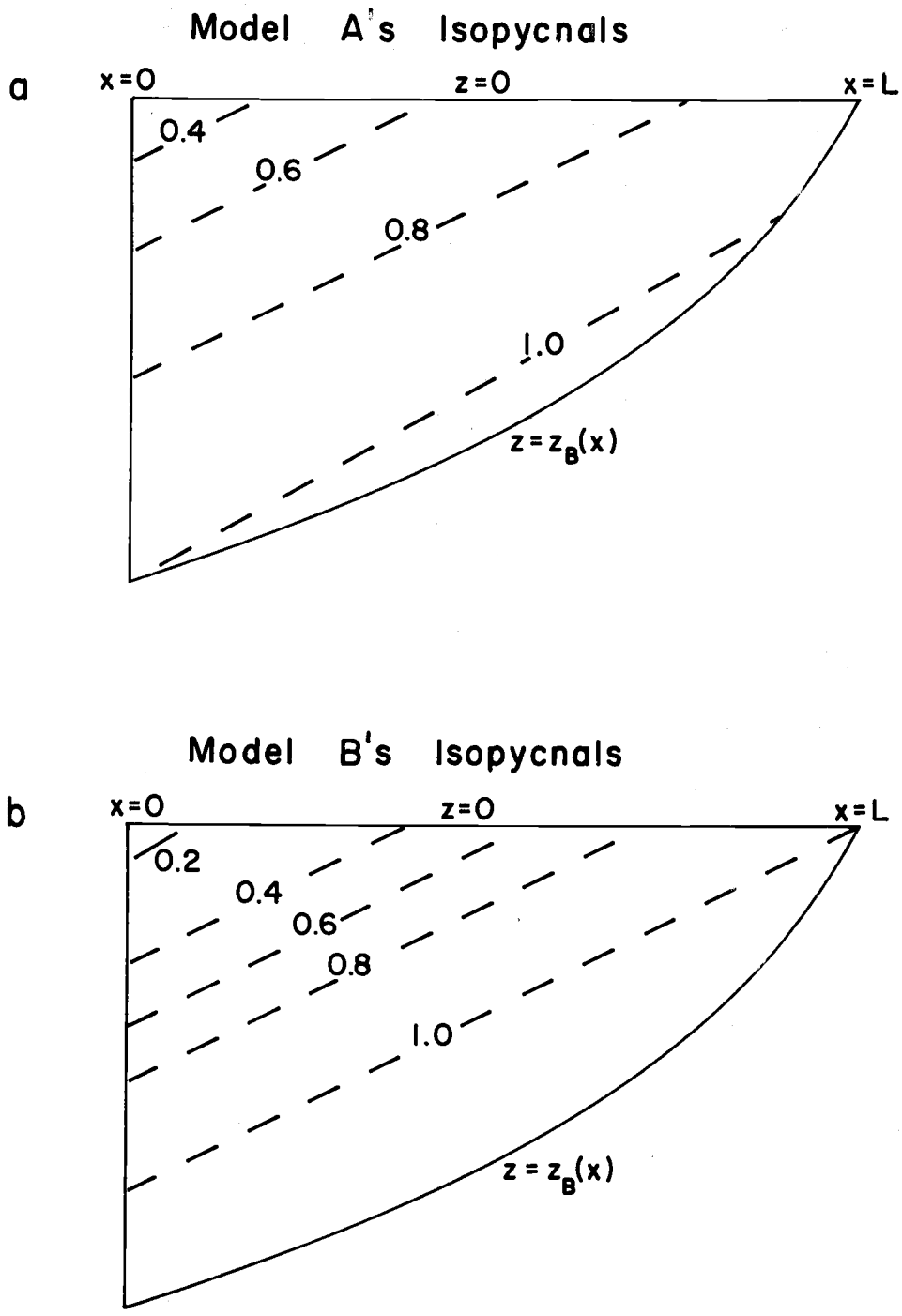

Figure 16. Sketch of the field of isopycnals for frontal models with variable coefficients.
a. Model A
b. Model B

$$f\bar{v} = -\frac{s}{a}E_o e^{az-bx}$$

and

$$f\bar{v}_x = s^2 E_o e^{az-bx},$$

without regard for functions of integration or boundary conditions, i.e., only internal consistency has been imposed on the mean fields.

The more complex model, Model B, is based on a hyperbolic tangent density dependence in both the x and z variables:

$$\bar{\rho} = \rho_o + \Delta\rho \tanh(-a(z+d)+bx),$$

with $a > 0$ and $b > 0$, again, and $0 \leq d \leq H_o$, where H_o is the water depth at $x = 0$. Since

$$\bar{\rho}_z = -a\Delta\rho \operatorname{sech}^2(-a(z+d)+bx)$$

and

$$\bar{\rho}_x = b\Delta\rho \operatorname{sech}^2(-a(z+d)+bx),$$

then

$$s = \left.\frac{dz}{dx}\right)_\rho = \frac{-\bar{\rho}_x}{\bar{\rho}_z} = \frac{b}{a} > 0$$

again. Taking

$$E_o = \frac{a\Delta\rho g}{\rho_o}$$

again, then

$$N^2 = E = \frac{-\bar{\rho}_z g}{\rho_o} = E_o \operatorname{sech}^2(-z(z+d)+bx),$$

$$f\bar{v}_x = \frac{-g\bar{\rho}_x}{\rho_o} = -sE_o \operatorname{sech}^2(-a(z+d)+bx),$$

$$f\bar{v} = \frac{sE_o}{a}\tanh(-a(z+d)+bx),$$

and

$$f\bar{v}_x = s^2E_o \operatorname{sech}^2(-a(z+d)+bx).$$

This model has a frontal surface, or center of the frontal layer; the intersection of the frontal surface with the (x, z) plane is given by $-a(z+d)+bx = 0$. Thus, the frontal surface rises from a depth of $z = -d$ at $x = 0$ to intersect the sea surface, forming a surface front, at $s = \frac{d}{s}$ if $\frac{d}{s} < L$; otherwise, it intersects the bottom. At the frontal surface, $\bar{v}$ has a zero crossing and $\bar{v}_z$ has an extremum.

C. Frontal Interaction with Model A

The problem is examined systematically for Model A; in the next section, it is studied in the same fashion for Model B. Using the functions computed for the coefficients of the GE in the preceding section, then:

GE:

$$L(\psi) = E_o e^{az-bx}\psi_{xx} + 2sE_o e^{az-bx}\psi_{xz} - (\sigma^2 - f_v^2 - s^2E_o e^{az-bx})\psi_{zz} = 0.$$

Take

$$K^2 = \frac{\sigma^2 - f_v^2}{s^2 E_o}$$

and change variables to

$$\mu = e^{\frac{b}{2}x} \quad \text{and} \quad \nu = e^{-\frac{a}{2}z},$$

then

$$\text{GE:} \qquad \mu^2\psi_{\mu\mu} - 2\mu\nu\psi_{\mu\nu} - \nu^2(K^2\mu^2\nu^2 - 1)\psi_{\nu\nu} + \mu\psi_{\mu} - (K^2\mu^2\nu^2 - 1)\nu\psi_{\nu} = 0.$$

The slopes of the characteristics are found to be

$$-\frac{d\nu}{d\mu})_{\eta} = \frac{\eta_{\mu}}{\eta_{\nu}} = \frac{\nu}{\mu}[1 + K\nu\mu]$$

and

$$-\frac{d\nu}{d\mu})_{\zeta} = \frac{\zeta_{\mu}}{\zeta_{\nu}} = \frac{\nu}{\mu}[1 - K\nu\mu].$$

Rewriting the equation for η,

$$\frac{d\nu}{\nu} + \frac{d\mu}{\mu} + K\nu d\mu = 0.$$

This equation has an integrating factor, $F = \frac{1}{\mu\nu}$. Then

$$K\frac{d\mu}{\mu} + \frac{\mu d\nu + \nu d\mu}{\mu^2\nu^2} = 0,$$

thus

$$\eta = \frac{1}{\mu\nu} - K \ln(\mu)$$

and, similarly,

$$\zeta = \frac{1}{\mu\nu} + K \ln(\mu).$$

η and ζ can be expressed in terms of x and z;

$$\eta = e^{\frac{a}{2}z - \frac{b}{2}x} - K\frac{b}{2}x$$

and

$$\zeta = e^{\frac{a}{2}z - \frac{b}{2}x} + K\frac{b}{2}x;$$

then

$$x = \frac{(\zeta - \eta)}{bK}$$

and

$$z = \frac{2}{a}\ln\left(\frac{\eta+\zeta}{2}\right) + \frac{(\zeta-\eta)}{aK}\ .$$

Thus, the mapping from the (x, z) plane to the (η, ζ) plane, and its inverse, are determined in closed form.

The reduction of the GE to the CGE follows after $L(\eta)$, $L(\zeta)$, and $Q(\eta, \zeta)$ have been evaluated from the set of first and second order partial derivatives for η and ζ:

$$\eta_\mu = -\frac{1}{\mu^2\nu} - K\frac{1}{\mu}, \qquad \zeta_\mu = -\frac{1}{\mu^2\nu} + K\frac{1}{\mu}$$

$$\eta_\nu = -\frac{1}{\mu\nu^2}, \qquad \zeta_\nu = \eta_\nu$$

$$\eta_{\mu\mu} = \frac{2}{\mu^3\nu} + K\frac{1}{\mu^2}, \qquad \zeta_{\mu\mu} = \frac{2}{\mu^3\nu} - K\frac{1}{\mu^2}$$

$$\eta_{\mu\nu} = \frac{1}{\mu^2\nu^2}, \qquad \zeta_{\mu\nu} = \eta_{\mu\nu}$$

$$\eta_{\nu\nu} = \frac{2}{\mu\nu^3}, \qquad \zeta_{\nu\nu} = \eta_{\nu\nu}.$$

Thus,

$$L(\eta) = L(\zeta) = -K^2\mu\nu \quad \text{and} \quad Q(\eta, \zeta) = -4K^2,$$

and

$$\frac{L(\eta)}{Q(\eta, \zeta)} = \frac{L)\zeta)}{Q(\eta, \zeta)} = \frac{1}{4}\mu\nu.$$

Then

CGE: $$L(\psi) = \psi_{\eta\zeta} + \frac{1}{4}\mu\nu[\psi_\eta + \psi_\zeta] = 0,$$

but

$$\frac{1}{\mu\nu} = \frac{(\eta+\zeta)}{2},$$

thus

CGE: $$L(\psi) = \psi_{\eta\zeta} + \frac{1}{2}\frac{1}{(\eta+\zeta)}[\psi_\eta + \psi_\zeta] = 0.$$

Alternatively, let $\alpha = \eta - \zeta$ and $\beta = \eta + \zeta$, then

CGE: $$L(\psi) = \psi_{\alpha\alpha} - \psi_{\beta\beta} - \frac{1}{\beta}\psi_\beta = 0.$$

The CGE is one for which the Riemann-Green function is known (Garabedian, p. 150, 1964). Formulating the adjoint problem, then

i) AGE: $M(W) = W_{\eta\zeta} - \frac{1}{2}\frac{1}{(\eta+\zeta)}[W_\eta + W_\zeta] + \frac{1}{(\eta+\zeta)^2} W = 0$

or

$$M(W) = W_{\alpha\alpha} - W_{\beta\beta} + \frac{1}{\beta} W_\beta - \frac{1}{\beta^2} W = 0$$

ii) $W_\eta = \frac{1}{2(\eta+\zeta)} W, \quad (\zeta = y)$

iii) $W_\zeta = \frac{1}{2(\eta+\zeta)} W, \quad (\eta = x)$

iv) $W = 1, \quad (\eta = z, \ \zeta = y).$

Together, ii) through iv) imply that

$$W \frac{(\eta+\zeta)}{(\eta+y)^{1/2}(x+\zeta)^{1/2}} \qquad \text{for} \quad \eta = x \quad \text{or} \quad \zeta = y;$$

to find W for all (η, ζ) it is necessary to change variables to

$$\sigma = \frac{(\eta - x)(\zeta - y)}{(\eta + x)(\zeta + y)} .$$

The details of the solution technique are not essential, and it is sufficient to know that

$$W(\eta, \zeta; x, y) = \frac{(\eta+\zeta)}{(\eta+y)^{1/2}(x+\zeta)^{1/2}} F(\tfrac{1}{2}, \tfrac{1}{2}; 1; \sigma),$$

where $F(a, b; c; d)$ is a hypergeometric function with arguments a, b, c, and d. W satisfies i) through iv) above and also $L_{(x, y)}(W) = 0$. The solution theory involving the Riemann-Green function, W, can be used directly to evaluate ψ, as outlined in Chapter V.

If the solution, ψ, can be separated in the (α, β) plane, then

$$\psi = \sum_n C_n A_n(\alpha) B_n(\beta),$$

where

$$A_n'' + \gamma_n^2 A_n = 0$$

and

$$B_n'' + \frac{1}{\alpha} B_n' + \gamma_n^2 B_n = 0.$$

γ_n^2 is the separation constant and C_n is a constant coefficient. Hence, the solution bases are:

$$A_n = (\sin(\gamma_n \alpha), \cos(\gamma_n \alpha))$$

and

$$B_n = (J_o(\gamma_n \beta), N_o(\gamma_n \beta))$$

where J_o and N_o are zero order Bessel and Neumann functions, respectively. In terms of x and z,

$$A_n = (\sin(\gamma_n Kbx), \cos(\gamma_n Kbx))$$

and

$$B_n = (J_o(\gamma_n^2 \exp(\frac{az}{2} - \frac{bx}{2})), N_o(\gamma_n^2 \exp(\frac{az}{2} - \frac{bx}{2}))).$$

The physical boundaries of the problem do not permit SOV, but these functional forms do give insight into the character of the solution. This set of separable solutions could be used in an approximation

scheme for obtaining a solution with boundary data given on boundaries not parallel in the (α, β) plane. The BC's can be readily applied along lines $az - bx = \text{constant}$, which would be satisfactory for a uniform bottom slope of $m = b/a$, but not for a surface boundary.

In the limit of a weak front, i.e., $s \to 0$ so $b \to 0$, then

$$\text{GE:} \qquad \psi_{xx} - \frac{(\sigma^2 - f^2)}{E_o} e^{-az} \psi_{zz} = 0.$$

With $\nu = e^{\frac{a}{2}z}$,

$$\psi_{xx} - \frac{K^2}{4}[\psi_{\nu\nu} + \frac{1}{\nu}\psi_{\nu}] = 0,$$

where

$$K^2 = (\frac{\sigma^2 - f_v^2}{E_o})a^2 > 0.$$

With SOV,

$$\psi = \sum_n X_n(x) Z_n(\nu),$$

then

$$X_n = (\sin(\gamma_n K x), \cos(\gamma_n K x))$$

and

$$Z_n = (J_o(2\gamma_n e^{\frac{a}{2}z}), N_o(2\gamma_n e^{\frac{a}{2}z})),$$

which are identical with the results obtained by taking the limit in the separable solution for a strong front. The BC's can be satisfied for parallel boundaries by solving the resultant eigenvalue problem,

involving the eigenvalues $\{\gamma_n\}$.

D. Frontal Interaction with Model B

Using the functions computed for the coefficients of the GE for Model B in Section B,

$$\text{GE:} \quad E_o \operatorname{sech}^2(-a(z+d)+bx)\psi_{xx} + 2sE_o \operatorname{sech}^2(-a(z+d)+bx)\psi_{xz} - (\sigma^2-f^2-s^2E_o \operatorname{sech}^2(-a(z+d)+bx))\psi_{zz} = 0.$$

Again, take

$$K^2 = \frac{\sigma^2-f^2}{s^2E_o} > 0,$$

and change variables to $\mu = bx$ and $\nu = -a(z+d)$, then the GE is reduced to

$$\text{GE:} \quad \psi_{\mu\mu} - 2\psi_{\mu\nu} - (K^2 \cosh^2(\mu+\nu)-1)\psi_{\nu\nu} = 0.$$

The slopes of the characteristics are found to be

$$-\frac{d\nu}{d\mu})_\eta = \frac{\eta_\mu}{\eta_\nu} = 1 + K \cosh(\mu+\nu)$$

and

$$-\frac{d\nu}{d\mu})_\zeta = \frac{\zeta_\mu}{\zeta_\nu} = 1 - K \cosh(\mu+\nu).$$

To find the equations of the characteristics, examine the equation for η rewritten as

$$d\nu + [1+\frac{K}{2}(e^{(\mu+\nu)} + e^{-(\mu+\nu)})]d\mu = 0.$$

Change variables to $r = e^{\mu}$ and $s = e^{\nu}$, then

(1) $$\frac{ds}{s} + [1+\frac{K}{2}(rs+\frac{1}{rs})]\frac{dr}{r} = 0.$$

Take $v = rs$ so that

(2) $$\frac{dv}{v} = \frac{ds}{s} + \frac{dr}{r}.$$

Subtracting (1) and (2) and separating variables,

$$\frac{dv}{\frac{K}{2}(v^2+1)} = -\frac{dr}{r},$$

which integrates to

$$\ln (r) + \frac{2}{K}\tan^{-1}(v) = \eta$$

or,

$$\mu + \frac{2}{K}\tan^{-1}(e^{(\mu+\nu)}) = \eta$$

or,

$$-bx + \frac{2}{K}\tan^{-1}[e^{-a(z+d)+bx}] = \eta.$$

Similarly,

$$-\ln (r) + \frac{2}{K}\tan^{-1}(v) = \zeta$$

or,

$$-\mu + \frac{2}{K}\tan^{-1}(e^{(\mu+\nu)}) = \zeta$$

or,

$$-bx + \frac{2}{K} \tan^{-1}[e^{-a(z+d)+bx}] = \zeta.$$

Since

$$x = \frac{(\eta - \zeta)}{2b}$$

and

$$z = -d + \frac{(\eta - \zeta)}{2a} - \frac{1}{a} \ln [\tan ((\frac{\eta+\zeta}{4})K)],$$

then the mapping from the (x, z) plane to the (η, ζ) plane and its inverse are known in closed form.

The reduction of the GE to the CGE follows after $L(\eta)$, $L(\zeta)$, and $Q(\eta, \zeta)$ have been evaluated from the set of first and second order partial derivatives for η and ζ:

$$\eta_\mu = 1 + \frac{1}{K} \text{ sech } (\mu+\nu), \qquad \zeta_\mu = -1 + \frac{1}{K} \text{ sech } (\mu+\nu)$$

$$\eta_\nu = \frac{1}{K} \text{ sech } (\mu+\nu), \qquad \zeta_\nu = \eta_\nu$$

$$\eta_{\mu\mu} = - \text{ sech } (\mu+\nu) \tanh (\mu+\nu), \qquad \zeta_{\mu\mu} = \eta_{\mu\mu}$$

$$\eta_{\nu\nu} = \eta_{\mu\mu}, \qquad \zeta_{\nu\nu} = \eta_{\mu\mu}$$

$$\eta_{\mu\nu} = \eta_{\mu\mu}, \qquad \zeta_{\mu\nu} = \eta_{\mu\nu}.$$

Thus,

$$L(\zeta) = L(\nu) = K^2 \sinh (\mu+\nu)$$

and

$$Q(\eta, \zeta) = -4,$$

Then

$$\frac{L(\eta)}{Q(\eta,\zeta)} = \frac{L(\zeta)}{Q(\eta,\zeta)} = -\frac{K^2}{4}\sinh(\mu+\nu),$$

thus

$$\psi_{\eta\zeta} - \frac{K^2}{4}\sinh(\mu+\nu)(\psi_\eta+\psi_\zeta) = 0;$$

but

$$\mu + \nu = \ln\left[\tan\left[\frac{K}{4}(\eta+\zeta)\right]\right],$$

thus

$$\text{CGE:}\quad \psi_{\eta\zeta} + \frac{K^2}{4}\left[\cot\left(\frac{K(\eta+\zeta)}{2}\right)\right](\psi_\eta+\psi_\zeta) = 0.$$

Take

$$p = \frac{K\eta}{2} \quad \text{and} \quad q = \frac{K\zeta}{2},$$

then

$$\psi_{pq} + \frac{K}{2}\cot(p+q)[\psi_p+\psi_q] = 0;$$

alternatively, let $\alpha = p - q$ and $\beta = p + q$, then

$$\text{CGE:}\qquad \psi_{\alpha\alpha} - \psi_{\beta\beta} - K\cot(\beta)\psi_\beta = 0.$$

Formulating the adjoint problem

i) $M(W) = W_{pq} - (\frac{K}{2})\cot(p+q)[W_p+W_q] + K\csc^2(p+q)W = 0$

or

$M(W) = W_{\alpha\alpha} - W_{\beta\beta} + K\cot(\beta)W_\beta - K\csc^2(\beta)W = 0$

ii) $W_p = (\frac{K}{2})\cot(p+q)W, \quad (q=y)$

iii) $W_q = (\frac{K}{2})\cot(p+q)W, \quad (p=x)$

iv) $W = 1, \quad (p=x, q=y).$

Together, ii) through iv) imply that

$$W = \frac{\sin (p+q)^K}{\sin^{K/2}(p+y)\, \sin^{K/2}(q+z)} \qquad \text{for} \quad p = x \quad \text{or} \quad q = y.$$

If it is assumed that the solution ψ can be separated in the (α, β) plane, then

$$\psi = \sum_n D_n A_n(\alpha) B_n(\beta),$$

where

$$A_n'' + \gamma_n^2 A_n = 0$$

and

$$B_n'' + K \cot(\beta) B_n' + \gamma_n^2 B_n = 0.$$

γ_n^2 is the separation constant, and D_n is a constant coefficient. The equation for B_n in normal form is, with

$$B_n = (\sin(\beta))^{-\frac{K}{2}} F_n(\beta),$$

$$F_n'' + [(\gamma_n^2 + \frac{K^2}{4}) + (\frac{K}{2} - \frac{K^2}{4})\csc^2(\beta)] F_n = 0.$$

With $\gamma_n^2 = a_n(a_n+K)$, then the solution bases for A are

$$A_n = (\sin((a_n(a_n+K))^{1/2}\alpha),\ \cos((a_n(a_n+K))^{1/2}\alpha));$$

for B, they are

$$B_n = (C_{a_n}^{\frac{K-1}{2}}(\cos(\beta)),\ D_{a_n}^{\frac{K-1}{2}}(\cos(\beta))),$$

where $C_\mu^\nu(z)$ and $D_\mu^\nu(z)$ are Gegenbauer, or ultraspherical functions of degree μ, of order ν, and of argument z (Bateman, 1953). When $a_n = n$, the Gegenbauer functions become the Gegenbauer polynomials. Expressed in the original variables,

$$\alpha = Kbx$$

and

$$\beta = 2\tan^{-1}[e^{-a(z+d)+bx}].$$

The forms for A and B could be used in an approximation scheme.

If the solution to the adjoint problem is assumed separable in the (α, β) plane, then

$$W = \sum_n E_n A_n(\alpha) B_n(\beta),$$

where

$$A_n'' + \gamma_n^2 A_n = 0$$

and

$$B_n'' - K\cot(\beta)B_n' + [\gamma_n^2 + K\csc^2(\beta)]B_n = 0.$$

γ_n^2 is a separation constant, and E_n is a constant coefficinet. The solution for B_n is

$$B_n = (\sin(\beta))^{K/2} F_n(\beta),$$

where F_n satisfies the same equation as F_n for the GE. Thus, A_n for W is the same as A_n for ψ and B_n for W is equal to B_n for ψ multiplied by $\sin^K(\beta)$.

The author has experimented with a host of techniques to find W. The most complete result entails the use of the solution bases as outlined in Copson (1958). Even then W can only be reduced to quadratures. Using the relations between the ultraspherical and associated Legendre functions, viz.

$$C_\mu^\nu(\cos(\beta)) = (-1)^{-\frac{\nu}{2}} (\sin(\beta))^{-\nu} P_{\mu+\nu}(\cos(\beta))$$

and

$$D_\mu^\nu(\cos(\beta)) = (-1)^{\frac{\nu}{2}} (\sin(\beta)^{-\nu} Q_{\mu+\nu}(\cos(\beta)),$$

then, with $\rho = \frac{K-1}{2}$,

$$W(\alpha, \beta; A, B) = \pm\pi\left(\frac{\sin(\beta)}{\sin(B)}\right)^\rho \sin^2(B) \frac{e^{i\rho\pi}}{\sin(\rho\pi)} \int_{-\infty}^{\infty} e^{i(\lambda(\lambda+K)^{1/2}(\alpha-A)}$$

$$[P_{\lambda+\rho}^{\rho}(\cos(B))P_{\lambda+\rho}^{-\rho}(\cos(\beta)) - P_{\lambda+\rho}^{-\rho}(\cos(B))P_{\lambda+\rho}^{\rho}(\cos(\beta))]d\lambda .$$

This form is not readily solvable, but it could be used to obtain

asymptotic limits on the solution as mentioned in Section V. E.

In the limit of a weak front, $s \rightarrow 0$ so $b \rightarrow 0$, then

$$\text{GE:} \qquad \psi_{xx} - \frac{(\sigma^2 - f^2)}{E_o} \cosh^2(-a(z+d))\psi_{zz} = 0,$$

or, with

$$\nu = -a(z+d),$$

$$\psi_{xx} - K^2 \cosh^2(\nu)\psi_{\nu\nu} = 0,$$

where

$$K^2 = \left(\frac{\sigma^2 - f^2}{E_o}\right) a^2 > 0.$$

Change variables to

$$p = 2 \tan^{-1}(e^{\nu})$$

and

$$q = Kx,$$

then the GE becomes

$$\psi_{qq} - \psi_{pp} - K \cot(p)\psi_p = 0.$$

Assuming SOV,

$$\psi = \sum_n X_n(x) Z_n(x),$$

then

$$X_n = (\sin(\gamma_n Kx), \cos(\gamma_n Kx))$$

and

$$Z_n = (C_{a_n}^{\frac{K-1}{2}}(\cos(p)),\ D_{a_n}^{\frac{K-1}{2}}(\cos(p))),$$

where

$$p = 2\tan^{-1}(e^{-a(z+d)})$$

and

$$\gamma_n^2 = a_n(a_n+K).$$

The expressions for X_n and Z_n are identical to those obtained by taking the limit $b \to 0$ in the separable solution for a strong front. Groen (1948) considered a case similar to the weak front.

E. Numerical Solution Techniques

The background for this section is found in Forsythe and Wasow (1960) and Garabedian (1964). In both Models A and B, the equations of the characteristics were found explicitly and the GE was reduced to a compact canonical form, viz.

(1) $$\psi_{\eta\zeta} + \frac{1}{2}f(\eta+\zeta)[\psi_\eta+\psi_\zeta] = 0$$

or

(2) $$\psi_{\alpha\alpha} - \psi_{\beta\beta} - f(\beta)\psi_\beta = 0, \quad (\alpha=\eta-\zeta \text{ and } \beta=\eta+\zeta)$$

where, for Model A,

$$f(\beta) = \frac{1}{\beta},$$

and for Model B,

$$f(\beta) = K \cot(\beta).$$

These forms are appreciably simpler than the original GE expressed in the (x, z) plane. It would be very tedious to attempt to solve the GE on a non-uniformly spaced, curvilinear grid commensurate with the field of characteristics in the (x, z) plane. Considerations of convenience and stability suggest carrying out the calculations in the (η, ζ) or (α, β) plane at the expense of a possible loss of accuracy through the inverse mapping of the solution. Because the objectives are only qualitative, accuracy is not of paramount importance. Since the characteristics tend to converge in the inclined frontal layer, a more detailed solution is achieved for computations in the characteristic plane than in the (x, z) plane precisely where the solution is expected to have the most structure and is of the most interest.

Method One

Form (2) is ideal for a finite difference scheme; it has the additional advantage that the coordinate α is directly proportional to the coordinate x, so that the initial line, $(x = 0)$, in the physical plane transforms into the β axis, $(\alpha = 0)$, in the characteristic plane. Since x is time-like, then α is also time-like. The central difference equivalents to the derivatives in (2) are:

$$f(\beta)\psi_\beta \cong f_j\left(\frac{1}{2\Delta\beta}\right)(\psi_{i,j+1}-\psi_{i,j-1}),$$

$$\psi_{\beta\beta} \cong \left(\frac{1}{\Delta\beta}\right)^2(\psi_{i,j+1}+\psi_{i,j-1}-2\psi_{i,j}),$$

and

$$\psi_{\alpha\alpha} \cong \left(\frac{1}{\Delta\alpha}\right)^2(\psi_{i+1,j}+\psi_{i-1,j}-2\psi_{i,j}),$$

where the indices i and j correspond to α and β, respectively. Then (2) becomes

$$\psi_{i+1,j} = -\psi_{i-1,j} + A\psi_{i,j} + B_j\psi_{i,j+1} + C_j\psi_{i,j-1}, \tag{3}$$

where

$$A = 2[1-\gamma^2], \quad B_j = [\gamma^2+\lambda f_j], \quad C_j = [\gamma^2-\lambda f_j],$$

$$\gamma = \left(\frac{\Delta\alpha}{\Delta\beta}\right), \quad \text{and} \quad \lambda = \gamma\frac{\Delta\alpha}{2}.$$

For stability and convergence, it is necessary that $\gamma \leq 1$. The CD are $\psi(0,\beta) = F(\beta)$ and $\psi_\alpha(0,\beta) = G(\beta)$. The initial values for the numerical calculations are

$$\psi_{1,j} = F(j)$$

and

$$\psi_{2,j} = F(j) + \Delta\alpha G(j) + \frac{(\Delta\alpha)^2}{2}F''(j), \quad (j = j_B(1), 1, j_T(1)),$$

where $j_B(1)$ and $j_T(1)$ are the coordinates of the sea bottom and surface, respectively, at $i = 1$, the initial line in the (α,β) plane. Both the upper and lower boundaries are assumed rigid so that the boundary values for ψ are given as

$$\psi_{i,\, j_B(i)} = 0 \quad \text{and} \quad \psi_{j,\, j_T(i)} = 0, \quad (i = 1, 2, \ldots, i_c),$$

where i_c is the coordinate of the coastline in the (α, β) plane. The calculation proceeds with the use of (3). The velocity components are found from ψ:

$$U_{i,j} = -\frac{\beta_z}{\Delta\beta}[\psi_{i,j+1} - \psi_{i,j-1}] \tag{4}$$

and

$$W_{i,j} = \frac{\alpha_x}{\Delta\alpha}[\psi_{i+1,j} - \psi_{i-1,j}] + \frac{\beta_x}{\Delta\beta}[\psi_{i,j+1} - \psi_{i,j-1}]. \tag{5}$$

No term including α_z enters (4) since $\alpha_z = 0$.

Method Two

From Equations (7) and (8) of Section V. C.,

$$w_\eta - \lambda_2 u_\eta = 0, \quad \text{along} \quad \zeta \text{ constant} \tag{6}$$

and

$$w_\zeta - \lambda_1 u_\zeta = 0, \quad \text{along} \quad \eta \text{ constant} \tag{7}$$

The following difference scheme is sufficient to approximate (6) and (7):

$$[w_{i,j} - w_{i-1,j}] - I(j)[u_{i,j} - u_{i-1,j}] = 0, \quad \text{along} \quad \zeta_j \tag{8}$$

and

$$[w_{i,j} - w_{i,j-1}] - J(i)[u_{i,j} - u_{i,j-1}] = 0, \quad \text{along} \quad \eta_i, \tag{9}$$

where

$$I(j) = \frac{1}{2}\left[\lambda^{(1)}_{i,j} + \lambda^{(1)}_{i-1,j}\right]$$

and

$$J(i) = \frac{1}{2}\left[\lambda^{(2)}_{i,j} + \lambda^{(2)}_{i,j-1}\right].$$

This pair of linear simultaneous equations can be solved for the unknowns, $u_{i,j}$ and $w_{i,j}$, then

$$u_{i,j} = \frac{1}{(J(i)-I(j))}\left[UI(i-1,j)-DI(i,j-1)\right] \tag{10}$$

$$w_{i,j} = \frac{1}{(J(i)-I(j))}\left[I(j)UI(i-1,j)-J(i)DI(i,j-1)\right], \tag{11}$$

where

$$UI(i-1,j) = J(i)u_{i,j-1} - w_{i,j-1}$$

and

$$DI(i,j-1) = I(j)u_{i-1,j} - w_{i-1,j}$$

are the discrete analogues of the Riemann invariants.

The expressions for λ_1 and λ_2 are evaluated in terms of η and ζ from the analytical expressions for both Model A and Model B. For Model A,

$$\lambda_1 = \left(\frac{dz}{dx}\right)_{\eta} = s\left[1+\frac{2K}{\eta+\zeta}\right]$$

and

$$\lambda_2 = \left(\frac{dz}{dx}\right)_{\zeta} = s\left[1-\frac{2K}{\eta+\zeta}\right];$$

and, for Model B,

$$\lambda_1 = \frac{dz}{dx})_{\eta} = s[1+(\frac{K}{2})(\tan(\frac{K(\eta+\zeta)}{4}) + \cot(\frac{K(\eta+\zeta)}{4}))]$$

and

$$\lambda_2 = \frac{dz}{dx})_{\zeta} = s[1-(\frac{K}{2})(\tan(\frac{K(\eta+\zeta)}{4}) + \cot(\frac{K(\eta+\zeta)}{4}))].$$

The BC's for this technique are applied through (8) and (9). Let characteristic η_i intersect the sea surface, which is assumed rigid, at (i, j), then $w_{i,j} = 0$, thus

$$u_{i,j} = u_{i,j-1} - \frac{w_{i,j-1}}{J(i)}.$$

Let the characteristic ζ_j intersect a sloping bottom boundary at (i, j), then $w_{i,j} = (m(j))u_{i,j}$. Thus

$$u_{i,j} = \frac{1}{(I(j)-m(j))}[I(j)u_{i-1,j} - w_{i-1,j}],$$

where there is one value of the bottom slope, $m(j)$, assigned for each ζ_j. The denominator does not equal zero for subcritical bottom slopes. It has been found most convenient to adapt the above equations to the grid and indices in the (α, β) plane which is used with Method One.

Methods One and Two have been computer programmed, as has the mapping from the physical plane to the characteristic plane and

the inverse mapping. Test calculations have been carried out by both methods for Model B in a wedge. Because there are some doubts about the results, though the phenomenon of bottom amplification of the wave does appear, the solutions are not plotted or discussed in this dissertation. The observations reported in Chapter X indicate that the case of variable coefficients is important, thus it is planned to continue this work in the future.

VIII. HYDRODYNAMIC STABILITY

A. Introduction

For hydrodynamic instability to occur, perturbations on a steady flow must overwhelm restoring forces. Then the perturbations can grow or decay. The restoring forces for inertial-internal waves are the Coriolis (rotational) force in the horizontal plane and the buoyancy (gravitational) force in the vertical plane. The former is related to geostrophic equilibrium while the latter is related to hydrostatic equilibrium. For each restoring force, there is an associated frequency of free oscillation. Associated with the Coriolis restoring force, there are free inertial oscillations at $\sigma = f$, while free Väisälä-Brunt oscillations at $\sigma = N$ are associated with the buoyancy restoring force. Without the frontal interaction, as $\sigma \to f$, the characteristics (and the group velocity) are cast into the horizontal plane; however, as $\sigma \to N$, the characteristics (and the group velocity) are cast into the vertical. Thus, inertial motions occur in the horizontal plane while stability oscillations occur in the vertical plane, as do their respective restoring forces.

With the frontal interaction, when $\sigma \to \sigma^{+} \approx N(1+s^2)^{1/2}$, then the slope of both of the characteristics becomes approximately $-\frac{1}{s}$; i.e., both characteristics are deflected downwards very steeply, but not vertically. Also, when $\sigma \to \sigma^{-} \approx [f(f+\bar{v}_x)-s^2N^2]^{1/2}$, then the

slope of both of the characteristics becomes approximately s; i.e., both characteristics are deflected upwards nearly parallel to the isopycnals. Further, when $\sigma \to N$, the upgoing characteristics become vertical, while the downgoing characteristics have a slope of approximately $-\frac{1}{2s}$. Similarly, when $\sigma \to (f(f+\bar{v}_x))^{1/2}$, the downgoing characteristics become horizontal, while the upgoing characteristics have a slope of about $2s$. The anomalous behavior of the characteristics, and of the group velocity as well, for $\sigma \sim N$ and $\sigma \sim f$ raises the question of whether or not baroclinic instability can occur for the frontal interaction.

The analytical properties of the GE are investigated to obtain information about the stability of the motion. The main effects on stability to be explored are those of finite depth and of the inclined frontal layer. In the final section, the observable Richardson numbers are introduced.

B. Baroclinic Stability

For an assumed mean flow, investigations of baroclinic stability are generally made for the conditions of the growth of a perturbation upon the mean flow. The GE for $\sigma < \sigma^-$, is elliptic, an analytical property which has been exploited to derive theorems for stability conditions (Stern, 1961 and Magaard, 1963). For the inertial-internal wave problem, an approach appropriate to the hyperbolic GE must

be employed.

If the perturbation motion paralleled the dominant mean flow, the relevant stability problem would be some form of the inviscid limit of the Orr-Sommerfeld equation (Lin, 1967), where the vertical curvature of the mean flow plays a crucial role. In the limit of a layered medium, such a problem reduces to the Kelvin-Helmholtz instability problem (Lamb, 1945), where the instability criterion is that the discrete analogue of the Richardson number be less than one. Huppert (1968) examined the influence of rotation on Kelvin-Helmholtz instability; he found that rotation plays a stabilizing role for long waves.

The problem of perturbation motion transverse to the mean flow apparently has not received a general treatment. A discussion of the stability effects of horizontal density gradients on the propagation of inertial-internal waves has been given by Rhines (1963). The GE derived in Chapter II for the frontal interaction is the two-dimensional version of the one Rhines considered, except that the effects of $\bar{v}_x$ and $\bar{v}_z$ have been considered in the present analysis. The question is: Can the effects of the horizontal density gradient and of the horizontal and vertical shears in the mean flow upset the stabilizing effects of the Coriolis force and of the vertical buoyancy force?

First the integral, or global, viewpoint is adopted, and then the

differential, or local, viewpoint is taken. Writing the GE in its divergence form, multiplying by ψ conjugate, and integrating over $D : [(x, z): (0 \leq x < L, -H(x) \leq z \leq \eta(x))]$, the resultant integral reduces to

$$\overline{\overline{T}} + \frac{i}{2\sigma}\overline{F^{(x)}}^{t} = \overline{\overline{V}} + PE_s,$$

as in Section IV. D. Thus, if $\overline{F^{(x)}}^{t} \neq 0$, then σ is imaginary; i.e., $\overline{\overline{E}}$ either grows or decays with time, unless there is a sink or source, respectively, in D not accounted for in the analysis. Since $\overline{\overline{T}} \geq 0$, when $PE_s + \overline{\overline{V}} \leq 0$, then $\overline{F^{(x)}}^{t} \neq 0$ and σ is imaginary. Since $PE_s \geq 0$, then $\overline{\overline{V}} \leq 0$ is a necessary condition for baroclinic instability. Because

$$\overline{\overline{V}} = \frac{\rho_o}{2\sigma^2}\iint_D [f(f+\bar{v}_x)(\psi_z)^2 + N^2(\psi_x)^2 - 2M^2\psi_x\psi_z]dxdz$$

$$= \frac{\rho_o}{2\sigma^2}\iint_D [N^2(\psi_x+s\psi_z)^2 + (\psi_z)^2(f(f+\bar{v}_x) - s^2N^2)]dxdz,$$

a necessary condition for $\overline{\overline{V}} < 0$ is that

$$s^2 > s_c^2 = \frac{f(f+\bar{v}_x)}{N^2} + \left[\frac{\psi_x}{\psi_z} + s\right]^2$$

for at least one point $(x, z) \in D$. Since the characteristics are lines

of constant phase, then

$$O(\frac{\psi_x}{\psi_z}) = \lambda .$$

And, since $\lambda \sim s$ for $\sigma \sim f$, then it is feasible that s can be greater than s_c for $\sigma \sim f$. Thus, an inclined frontal layer may induce baroclinic instability.

Adopt the differential, or local, viewpoint, neglect the BC's, and take $\psi \propto e^{i(kx+mz)}$. Then the CR yields

$$(N^2-\sigma^2)k^2 - 2M^2km - (\sigma^2-f(f+\bar{v}_x))m^2 = 0,$$

or, rearranging terms,

$$\sigma^2 = \frac{N^2(k+sm)^2 + (f(f+\bar{v}_x)-s^2N^2)m^2}{k^2+m^2} .$$

Let $(\frac{k}{m})_1$ and $(\frac{k}{m})_2$ correspond to the upgoing and downgoing waves, respectively. Since $\sigma^2 < 0$, if

$$s^2 > ((\frac{k}{m})+s)^2 + \frac{f(f+\bar{v}_x)}{N^2} ,$$

then, if

$$(\frac{k}{m})_1 \leq -s + (s^2 - \frac{f(f+\bar{v}_x)}{N^2})^{1/2} ,$$

or if

$$(\frac{k}{m})_2 \geq - s - (s^2 - \frac{f(f+\bar{v}_x)}{N^2})^{1/2} ,$$

baroclinic instability may occur.

Thus, an inclined frontal layer may cancel the stabilizing effects of gravity and of the Earth's rotation. The implicit view taken above is that a wave incident on a frontal zone has a fixed ratio of k to m and that the interaction acts to alter the frequency.

If the view is taken that frequency is fixed, then, since $\frac{k}{m} = -\lambda_1$ or $-\lambda_2$, λ_1 and λ_2 become complex if $\sigma^2 < f(f+\bar{v}_x) - s^2N^2$, or if $\sigma^2 > N^2(1+s^2)$, which means that the GE is elliptic. λ_1 and λ_2 are equal if equality holds in the above inequalities; then, a parabolic degeneracy exists for the GE.

A less degenerate situation occurs for $f(f+\bar{v}_x) - s^2N^2 < \sigma^2 < f(f+\bar{v}_x)$; then both λ_1 and λ_2 are positive. From the beam viewpoint, Figure 17, the downgoing beam is deflected upwards and the upgoing beam is inclined more steeply than the frontal layer. The upgoing beam strikes the sea surface and never crosses the frontal layer; instead, the wave is reflected from the sea surface and propagates in the $-x$ direction in the beam bounded by the dotted lines.

Similarly, if $N^2 < \sigma^2 < N^2(1+s^2)$, then λ_1 and λ_2 are both negative and the upgoing and downgoing beams are both deflected downwards by the inclined frontal layer. Thus, from the viewpoint of fixed frequency, the inclined frontal layer exerts a waveguide effect, or a wave-blocking effect, for both the anomalously low and

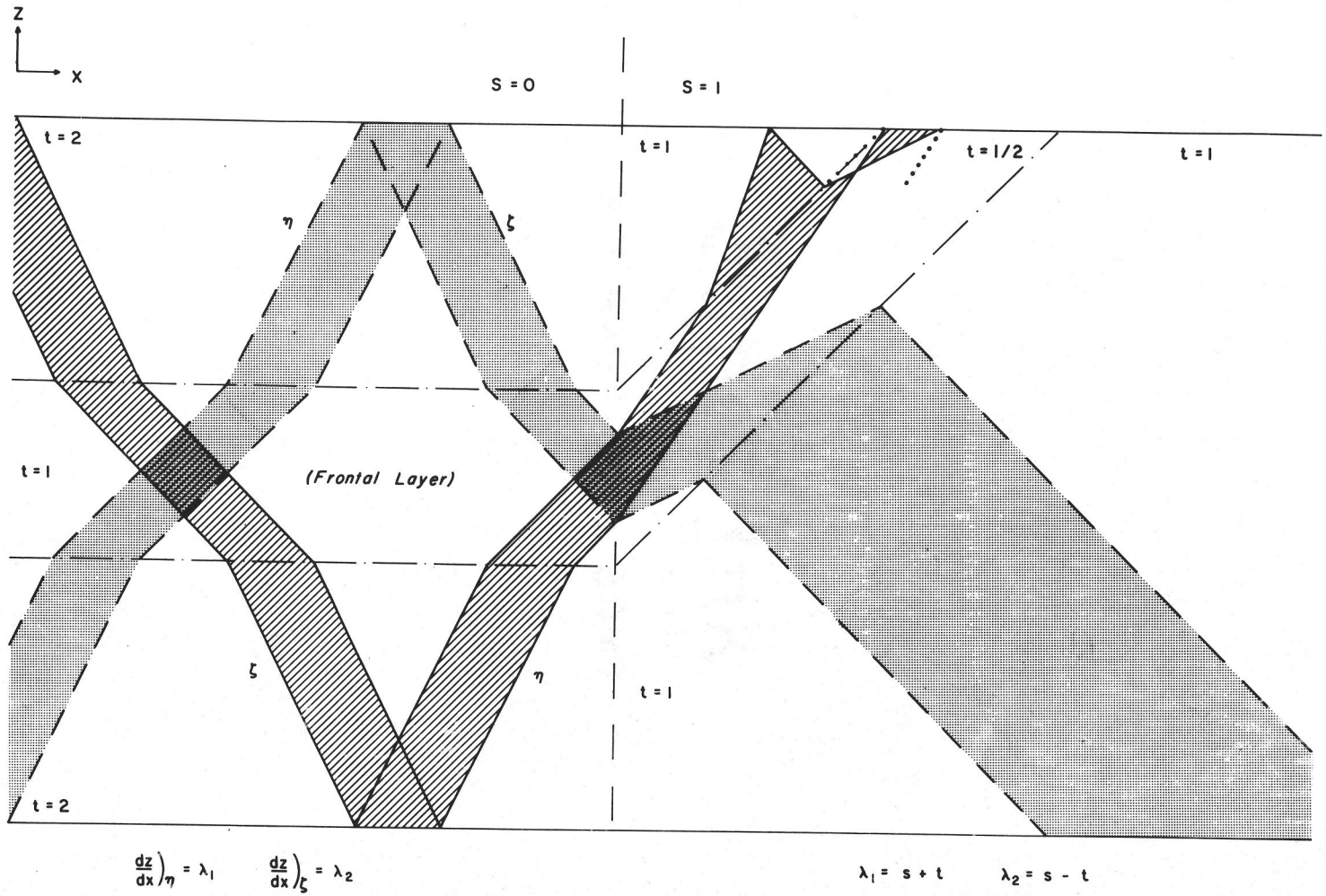

Figure 17. Hypothetical case of wave-blocking by a strong frontal zone.

high frequencies of the inertial-internal wave passband.

The present analysis of baroclinic instability has been cursory. An analysis of the time-dependent problem may prove to be more satisfactory. Perhaps the ray method of Jones (1969) will prove profitable.

C. Dynamic Stability

The details of destabilization require knowledge of the microscale of turbulent processes; the discussion in Section B is only adequate on a mesoscale. A compatible bridge between the microscales and mesoscales is the concept of dynamic stability. The Richardson number (Richardson, 1920), is the parameter most widely used in oceanography and meteorology as an indicator of dynamic stability. The vertical shear in the horizontal flow of a stratified fluid represents a mechanism for extracting kinetic energy from the mean flow, or from long waves, and increasing the potential energy of the fluid through mixing. The flux Richardson number, Rf, is the ratio between the buoyancy force and the destabilizing shear effect. Rf is equivalent to the ratio of the "time rate of increase of potential energy, PE_t, due to turbulent mixing" to the "time rate of vertical transfer of kinetic energy, KE_t, removed from the mean horizontal flow:"

$$Rf = \frac{(PE)_t}{(KE)_t} = \frac{g\,\overline{\rho' w'}}{-\bar{\rho}\,\overline{w'u'}\,\frac{d\bar{u}}{dz}} ,$$

where $g\,\overline{\rho' w'} = gK_v \frac{d\bar{\rho}}{dz}$ is the vertical buoyancy flux, $-\bar{\rho}\,\overline{w'u'} = \bar{\rho} N_v \frac{d\bar{u}}{dz}$ is the relevant component of Reynolds stress, K_v is the vertical eddy diffusivity coefficient, N_v is the vertical eddy viscosity coefficient, and Rf is the flux Richardson number. In an alternative form,

$$Rf = \frac{-g\frac{d\bar{\rho}}{dz}K}{\bar{\rho}N_v\left|\frac{d\bar{u}}{dz}\right|^2} = \frac{K_v}{N_v}\frac{E}{\left|\frac{d\bar{u}}{dz}\right|^2} = \frac{K_v}{N_v} R_i ,$$

where E is the static stability and $Ri = \frac{E}{\left|\frac{d\bar{u}}{dz}\right|^2}$ is the gradient Richardson number. Rf is determined by turbulence measurements, while Ri is determined by the vertical gradients of the mean properties. Frequently, it is desired to know Rf while only Ri can be computed; if N_v and K_v are known, Rf can be inferred. In the absence of accurate information, N_v is often assumed equal to K_v. A critical Rf, or Ri, is employed as a stability criterion. The critical value of Rf is unity, if the kinetic energy of the turbulence is constant. Then, if the eddy Prandtl number, (N_v/K_v), is equal to one, the critical value of Ri is also unity. For several cases of wave motion studied analytically (Miles, 1961; Yih, 1965; and Proudman, 1952), the critical value for wave

instability is $Ri = 1/4$.

The observations of this study do not permit calculation of Rf; the observations do permit the calculation of certain Ri's. In Sections D and E, inertial-internal wave theory is examined to determine what predictions can be made for Ri; then observable Ri's are discussed in Sections F and G. In Section XI. H, observed Ri's are reported for the field observations. The objective is to determine whether or not the vertical shear of the horizontal velocity of the semidiurnal internal tide is sufficiently large to make the frontal zone occasionally dynamically unstable.

D. Inertial-Internal Wave Richardson Number

Munk (1966) derived the Richardson number for inertial-internal waves, IGRN. His analysis is given a simple extension here to include the effect of finite depth. Neglecting the frontal interaction, since

$$u = (\sigma^2 - f^2)^{-1}(i\sigma\pi_x + f\pi_y)$$

and

$$v = (\sigma^2 - f^2)^{-1}(i\sigma\pi_y - f\pi_x),$$

then

$$u_z = (\sigma^2 - f^2)^{-1}(i\sigma\pi_{xz} + f\pi_{yz})$$

and

$$v_z = (\sigma^2 - f^2)^{-1}(i\sigma\pi_{yz} - f\pi_{xz}).$$

Assuming SOV, take $\pi = Z(z)e^{i(\sigma t - kx - \ell y)}$ and set $\sigma t - kx - \ell y = 0$ after differentiation. The CR is $(N^2-\sigma^2)(k^2+\ell^2) - (\sigma^2-f^2)m^2 = 0$, where m is the vertical wave number. π_z is expressed in terms of the vertical displacement, ζ; since $\zeta_t = w = \frac{-\pi_{zt}}{(N^2-\sigma^2)}$ then $Z' = -\zeta(N^2-\sigma^2)$. Rotate coordinates to the major and minor axes of the hodograph, i.e., from velocity coordinates (u, v) to (W_1, W_2), where W_1 and W_2 are the velocity components along $\theta_1 = \frac{\ell}{k}$ and $\theta_2 = -\frac{k}{\ell_1}$, respectively, and θ_1 and θ_2 are measured anticlockwise from east. Then

$$((W_1)_z)^2 = \sigma^2 \frac{(k^2+\ell^2)}{(\sigma^2-f^2)} (Z')^2$$

$$= \sigma^2 m^2 \zeta^2 \frac{(N^2-\sigma^2)}{(\sigma^2-f^2)},$$

by the CR and the relation for π_z; similarly,

$$(W_2)_z^2 = f^2 m^2 \zeta^2 \frac{(N^2-\sigma^2)}{(\sigma^2-f^2)}.$$

The component IGRN's are then

$$IGRNW_1 = \left(\frac{\sigma^2-f^2}{N^2-\sigma^2}\right) \frac{N^2}{\sigma^2(m\zeta)^2}$$

and

$$IGRNW_2 = \left(\frac{\sigma^2 - f^2}{N^2 - \sigma^2}\right) \frac{N^2}{f^2 (m\zeta)^2} .$$

Since $\sigma > f$, and since W_1 and W_2 are in-quadrature, then $IGRNW_1 \leq IGRN \leq IGRNW_2$ as a function of time. The wave motion is dynamically stable as $\sigma \rightarrow N^-$, and it is dynamically unstable as $\sigma \rightarrow f^+$, for fixed ζ.

Assuming $\sigma^2 \ll N^2$,

$$IGRNW_1 \approx \frac{(\sigma^2 - f^2)}{\sigma^2} \frac{1}{(\zeta m)^2}$$

and

$$IGRNW_2 \approx \frac{(\sigma^2 - f^2)}{f^2} \frac{1}{(\zeta m)^2} .$$

If the depth, H, is assumed uniform so that $m = \frac{n\pi}{H}$, where n is the vertical mode number; then

$$IGRNW_1 \approx \frac{(1 - r^{-2})}{(\zeta n\pi/H)^2}$$

and

$$IGRNW_2 \approx \frac{(r^2 - 1)}{(\zeta n\pi/H)^2} ,$$

where $r^2 = \left(\frac{\sigma}{f}\right)^2$. For the semidiurnal tide at latitude 45°, $r^2 \approx 9/4$, thus

$$IGRNW_1 \approx \frac{0.56}{(\zeta n\pi/H)^2}$$

and

$$IGRNW_2 \approx \frac{1.25}{(\zeta n\pi/H)^2}.$$

Let $n = 1$ and assume representative values for ζ and H: $\zeta \sim 10$ meters and $H \sim 100$ meters. Then $IGRNW_1 \approx 5$ and $IGRNW_2 \approx 11$, which are sufficiently close to dynamic instability to merit observational scrutiny. As $\ell \to 0$, $\theta_1 \to 0$ and $\theta_2 \to -\frac{\pi}{2}$, then $W_1 \to u$ and $W_2 \to -v$; thus, there is a slight tendency for the u component to be less stable than the v component.

Using the critical Ri criterion for waves of $Ri = 1/4$, for the W_1 component, when $(\zeta/H) > \frac{1.4}{n\pi}$, the motion becomes unstable; similarly, for the W_2 component, when $(\zeta/H) > \frac{2.2}{n\pi}$, the motion becomes unstable. For ζ and H fixed, there is a greater tendency for the higher modes than for the lower modes to be unstable. Considering the first mode only, when $\zeta \sim H$, the motion tends to be dynamically unstable. The order of magnitude estimate for ζ is 10 meters, then the semidiurnal tide should tend to become unstable in a water depth of 10 meters on this basis.

Without density stratification, the phenomenon of shear instability would not exist yet the stratification parameter, $E = N^2$, does not explicitly enter the final form for the stability criterion. N^2 does enter implicitly through influencing the value for $m(z)$; as N^2 increases, $m(z)$ tends to increase, restricting ζ to smaller

values for dynamic stability. Thus, the motions tend to be least stable in the pycnocline, where N^2 and ζ tend to be the greatest.

E. Inertial-Internal Wave Richardson Number for Frontal Interaction

The general problem of dynamic stability for the interaction is not readily tractable. For simplicity, it is assumed that coefficients are constant and simple waves are analyzed. Set

$$\psi^+ = Ae^{im(z-\lambda_1 x)} e^{i\sigma t}$$

and

$$\psi^- = Be^{im(z-\lambda_2 x)} e^{i\sigma t},$$

where ψ^+ and ψ^- are the stream functions of the upgoing and downgoing waves, respectively. Then,

$$u_z^+ = -\psi_{zz}^+ = m^2\psi^+$$

and

$$\zeta^+ = \frac{\psi_x^+}{i\sigma} = \frac{-m\lambda_1}{\sigma}\psi^+,$$

thus

$$u_z^+ = \frac{-\sigma m}{\lambda_1}\zeta^+;$$

similarly,

$$u_z^- = \frac{-\sigma m}{\lambda_2}\zeta^-.$$

Therefore,

$$IGRNU^{+} = \frac{\lambda_1^2 N^2}{(\sigma m \zeta^{+})^2}$$

and

$$IGRNU^{-} = \frac{\lambda_2^2 N^2}{(\sigma m \zeta^{-})^2} .$$

Since $\lambda_2 \to 0$ when $\sigma \to (f(f+\bar{v}_x))^{1/2}$, then so does $IGRNU^{-}$.

F. The Frontal Richardson Number

Consistent with the observations in the frontal zone off Oregon, the vertical shear of the mean alongshore flow is given by the thermal wind equation:

$$\bar{v}_z = \frac{-sE}{f} .$$

Then the frontal Richarson number, FRN, takes the heuristic form:

$$FRN = \frac{E}{(\bar{v}_z)^2} = \frac{f^2}{s^2 E} ;$$

i.e., the dynamic stability is inversely proportional to the static stability. The dynamic stability in a frontal zone assumes its smallest value in the inclined frontal layer where the product of E (frontal intensity) and s^2 (square of the frontal slope) takes its maximum value. A conservative estimate for the minimum FRN in the permanent pycnocline off Oregon, based on $f \approx 10^{-4} sec^{-1}$,

$E_{max} \approx 4 \times 10^{-4}\,sec^{-2}$, and $s_{max} \approx 3 \times 10^{-3}$, yields a value of minimum FRN ≈ 3. Though the minimum dynamic stability of the frontal zone may be rather low, the frontal zone is stable "in the large," as it must be to exist as a quasi-steady phenomenon. The estimate of minimum FRN, which is based on hydrographic data alone, is compared with results for the mean vertical shear based on direct measurements in Section X. C.

G. Observable Richardson Numbers

For each of the observable Ri's, the complex representation of the horizontal velocity is employed: $W = u + iv$. Then the magnitude of the shear vector, $|W_z|^2 = |u_z|^2 + |v_z|^2$, is invariant under coordinate rotation, and

$$RI = \frac{E}{|W_z|^2} = \frac{E}{|u_z|^2 + |v_z|^2}$$

is also invariant. RI takes into account shear due to directional twist with depth as well as vertical variation in the speed. Each RI can be written in component form:

$$RIU = \frac{E}{|u_z|^2} \quad \text{and} \quad RIV = \frac{E}{|v_z|^2},$$

then

$$RI = \frac{RIU \cdot RIV}{RIU + RIV}.$$

With time series measurements, a plethora of Ri's can be computed, including those related to the instantaneous, mean, variance, and spectral components of the flow. The other Ri's used are designated as follows:

i) From the shear of the mean flow,

$$RIM = \frac{E}{(\frac{d\bar{u}}{dz})^2 + (\frac{d\bar{v}}{dz})^2} .$$

ii) From the r.m.s. vertical shear of the flow,

$$RIVAR = \frac{E}{Var(u_z) + Var(v_z)} .$$

For peak values of shear, RIVAR is divided by 2 to obtain the average minimum RIVAR.

iii) From the r.m.s. shear of the flow in a measurement bandwidth, $\Delta\sigma$, centered at σ,

$$RIS(\sigma) = \frac{E}{[P_{u_z u_z}(\sigma) + P_{v_z v_z}(\sigma)]\,\Delta\sigma} .$$

iv) Alternatively, for the coherent portion of the motion at σ, least squares analysis yields amplitudes for the shear vector:

$$W_z = \tilde{A}_z \cos(\sigma t) + i\tilde{B}_z \sin(\sigma t)$$

and a time-dependent Ri is formed:

$$RIC(\sigma;t) = \frac{E}{|W_z(\sigma;t)|^2} .$$

v) A net Ri is formed from the mean shear $\overline{W}_z$ and the coherent shear at a fixed frequency $W_z(\sigma,t)$:

$$RIN(\sigma, t) = \frac{E}{|\overline{W}_z + W_z(\sigma, t)|^2}$$

In Section X. C., temporal minimum values of RIN are examined as a function of depth.

Within the limits of measurement error, all of the observable Ri's are upper bounds on the minimum values for the actual dynamic stability because the observed shears are lower bounds on the maximum shears due to the finite spacing of sensors and the discrete sampling in time.

IX. THE OBSERVATIONAL PLAN OF AUGUST-SEPTEMBER 1966

A. Introduction

The objectives and design of the August-September 1966 field observations are discussed. In Chapter X, the mean flow and hydrographic fields established by the observations are examined, as well as auxiliary properties of the oceanographic regime which are relevant to the inertial-internal wave problem. In Chapter XI, the time series of the velocity and temperature fields are analyzed to determine the evidence for and the properties of inertial-internal waves. Thus, this chapter provides the planning background for the two succeeding chapters.

B. The Observational Objectives

Because competing and variable phenomena occur simultaneously in the Ocean, especially in coastal regions, it is essential to have a measure of the spectrum of motions. There is also a necessity for an iterative approach to measurement. This philosophy is also espoused in Collins et al. (1968) and Fofonoff (1968a); its corollary is that it is unrealistic to expect to make definitive measurements on one or a few "outings." The most pessimistic view is that there are no repeatable or intelligible measurements to be made because the

flow regime is completely nonstationary and has no typical behavior. The optimistic view is that sensible patterns will eventually emerge from both the mean and fluctuating components of the flow. The iterative viewpoint has been chosen; it is an operational one in that each set of planned observations can adapt to prior results and because it embraces the possibility of disappointment in the realization of optimistic expectations. In other words, one learns what works and what does not work and proceeds accordingly along the same basic theme. It was considered poor procedure to attempt to study tidal and inertial motions in the coastal region without due regard for the effective mean flow of coastal upwelling, and vice versa. On the basis of time series measurements of currents and hydrography made in the coastal region in the summer of 1965 through the winter of 1966, analyzed and discussed by Collins (1968) and Collins et al. (1968), it was apparent that tidal and inertial motions were quite significant in the coastal upwelling region. The two-headed question, which provided the motivation for the thesis of this dissertation, presented itself: how does the frontal zone of coastal upwelling modify the semidiurnal internal tide and how does the semidiurnal internal tide, in turn, modify the frontal zone of coastal upwelling? In August-September 1966, the second iterative step was taken. The observational effort differed from that of 1965 to early 1966 primarily in the extension of single vertical arrays of moored, recording sensors to a horizontal

linear array, containing vertical array elements. In other words, an oceanographic antenna was established. An intensive set of complementary hydrographic data was also included. Hydrographic data have been sampled for the past century and moored, recording meters have been employed in the past decade; yet there had been few, if any, attempts to integrate the two measurement techniques to define a flow regime until the observations of August-September 1966.

Prior to the installation of the August-September 1966 array, a list of hypotheses was formulated. This list, given below with only minor editorial revisions, is divided into two components: one regarding the semidiurnal internal tides and the other the frontal zone of coastal upwelling.

The hypotheses regarding the semidiurnal internal tides off Oregon are:

i) They exist in the coastal region off Depoe Bay, Oregon.

ii) They are generated in the coastal region.

iii) They are composed of standing and progressive waves.

iv) They are refracted by bottom topography and are consequently aligned parallel to bottom contours.

v) They are long-crested; i.e., they are essentially uniform in the alongshore direction.

vi) They have measurable parameters, e.g., amplitude, period, wavelength, phase speed, and propagation direction.

vii) They can be described effectively by the first one or two vertical modes.

viii) They tend to become unstable as they approach shallow water and in the region of the inclined frontal layer.

ix) They coexist with inertial motions and may relate to the generation of the inertial motions.

The hypotheses regarding the frontal zone of coastal upwelling off Oregon are:

x) The inclined frontal layer is present 10 to 30 kilometers offshore in a water depth of 80 to 200 meters during the season of observations, mid August to late September.

xi) It is feasible to measure the mean and fluctuating components of the flow in the vicinity of the frontal layer.

xii) The seaward dissipation of the prevalent temperature inversion occurring at the base of the frontal layer is indicative of low dynamic stability and, thus, of mixing in the frontal layer.

xiii) The occurrence of critically low dynamic stability is associated with the vertical shear of the semidiurnal internal tide.

xiv) Estimates of horizontal eddy coefficients can be made from turbulent heat and momentum fluxes and mean flow calculations.

xv) The frontal flow field of coastal upwelling responds systematically to the atmospheric forcing functions.

Because of the sensor failures and inadequacies of the design of the field observations, not all of the hypotheses were satisfactorily tested. Hypothesis xiv) is tested in Mooers et al. (1969); it is not discussed here because its relevance to the present study is not sufficiently obvious. Hypothesis xv) is an entire topic in itself and is not discussed here; Collins (1968) has taken several steps in the investigation of this hypothesis.

C. The Design of the Observational Plan

The August-September 1966 observations were designed to test the previously stated hypotheses with the available instrumentation, the available data analysis techniques, the contemporary knowledge of the coastal upwelling flow regime, and the contemporary theoretical and observational understanding of inertial-internal waves. The available instrumentation consisted of (i) six recording current meters and four recording thermographs and (ii) standard shipboard hydrographic equipment, viz., Nansen bottles with reversing thermometers, bathythermographs, and a profiling current meter. The moored, recording sensors provided data which have been examined by standard statistical techniques for their gross features and by the statistical techniques of time series analysis for their spectral content. The hydrographic data have been analyzed through preparation of vertical profiles and sections to describe the oceanographic setting.

The tide gauge record sampled at the Marine Science Center, Newport, Oregon, had been intended to play a crucial role in testing the phase relation between the surface tide and the internal tide; it only functioned properly through a portion of the observations, but it has been incorporated in the present study in a limited fashion. Other data sets sampled include time series of atmospheric pressure and winds, but they are not employed in the present study, except for a summary of the wind field in Section X. C., see Mooers et al. (1968).

The successful experience of July 1965 to February 1966 demonstrated that it was feasible to moor the recording meters in a depth of water of 100 to 140 meters. With the shallowest sensor at a depth of 20 meters, there was little fear of data contamination from surface waves.[18]

To detect an inertial-internal wave, at least two sensors in the vertical and two in the horizontal are necessary. To define the frontal flow regime, at least one sensor near the top of the inclined frontal layer, at a depth of about 20 meters, and one near the base of it,

---

[18] Because swell data were available, the 1965 current speed data were inspected for episodes of weak winds and low swell which were followed by episodes of high swell and no appreciable increase in wind speed. The onset of high swell induced no apparent increase in current speed. The question of data contamination by swell needs further field verification. In the absence of full knowledge on this issue, it is consistent with the information available to assume that the sensor strings moved with the water column under the influence of swell so that the sensors were blind to the particle velocities associated with swell.

at a depth of about 60 meters, are necessary; similar measurements are needed at two or more locations in the onshore-offshore direction.

The horizontal locations of the sensors were selected on the basis of an estimate of the onshore-offshore location of the frontal zone of coastal upwelling. It was estimated that the inclined frontal layer tends to intersect the sea surface about 5 to 15 kilometers offshore and that the inclined frontal layer extends offshore to at least the seaward edge of the continental shelf.

The horizontal spacing of the sensors was selected on the basis of an estimate of the onshore-offshore wavelength of the semidiurnal internal tide. The order of magnitude estimate for the fundamental horizontal wavelength, $\lambda_{,}^{(h)}$ of the semidiurnal internal tide was $\lambda^{(h)} \sim$ 20 to 40 kilometers, Section III. C. Since it was desirable to observe a wave over a sizable fraction of a wavelength, a horizontal span of at least 20 kilometers for the sensor array was chosen.

The feasibility of extending the mooring scheme to depths greater than 140 meters was uncertain. Thus, a compromise was made by extending the array offshore only to a water depth of 200 meters, i. e., to the seaward edge of the continental shelf. The capability of the mooring scheme for holding in shallow water, and the ability of the sensors to recover data uncontaminated by surface wave motions in shallow water, were uncertain. Thus, a compromise

was made by extending the array inshore only to a water depth of 80 meters. With these decisions on the terminal depths of the array, the array span was then 20 kilometers, extending from 10 kilometers to 30 kilometers offshore, and from a water depth of 80 meters to that of 200 meters. Thus, the array spanned an appreciable fraction of both the frontal zone of coastal upwelling and a semidiurnal internal tidal wavelength.

The deployment of the six current meters involved a choice between placing two in the vertical at three horizontal points, placing three in the vertical at two horizontal points, or incorporating some redundancy in the array. The unwarranted assumption was made that the current meters could be depended upon for a high percentage of data recovery, and no significant redundancy was planned. With previous experience at placing two and three sensors in the vertical and none with horizontal spacing, it was thought wise to explore the horizontal structure at three positions and to be content with two samples in the vertical. The third horizontal position was selected to be the midpoint between the array termini. As shown in Figure 3, the array consisted of current meters at depths of 20 and 60 meters, and at distances 10, 20, and 30 kilometers offshore; these stations are termed DB5, DB10, and DB15, respectively.

The estimated positions and depths of the sensor strings were:

Sensor site	Latitude	Latitude	Distance offshore along array axis (oriented 120° to 300° T) (kilometers)	Water depth (meters)
DB5	44° 50. 2'N	124° 10. 7'W	10. 5	80
DB10	44° 53. 0'N	124° 17. 3'W	20. 5	140
DB15	44° 56. 0'N	124° 24. 1'W	30. 8	200 .

The ratio of the vertical to the horizontal scale of the array was

$$R = \frac{\Delta z}{\Delta x} = \frac{40m}{10 \times 10^{3} m} = 4 \times 10^{-3},$$

while the slope of the semidiurnal tidal characteristic was

$$|\lambda| \sim (\frac{f}{N}) \approx 1 \text{ to } 10 \times 10^{-3},$$

and the frontal slope was $s \approx 1$ to 4×10^{-3}. Since $R \sim \lambda$ and $R \sim s$, then the sensor spacing was reasonable for the study of both the internal tide and the frontal flow. The current meters at DB10, 60 meters, and at DB15, 20 meters, failed to give long records. For dynamic stability calculations, the presumably most important vertical pair, at DB5, operated sufficiently long. With the types and limited number of sensors available, it was not possible to test hypotheses ii) and vii); i. e., the generation and modal structure of internal tides could not be examined.

The deployment of the four thermographs was influenced by the

same considerations as the deployment of the current meters plus the fact that the thermocline off Oregon is quite shallow, extending to a depth of only 25 to 30 meters. It was decided to use a thermograph at a depth of 20 meters at each of the three horizontal array positions. The remaining thermograph was deployed on a separate mooring 10 kilometers southward of the linear onshore-offshore array and along the same depth contour as the DB10 meter string. With the fourth thermograph, it was hoped to test hypotheses iv) and v), i. e., the refraction and long-crestedness of the internal tide, but that thermograph failed to operate as did the other one at 20 kilometers offshore. The thermographs at DB5 and DB15 did operate successfully.

The sensor sampling rate was determined by two considerations: the highest frequency inertial-internal waves expected and the inherent limitations of the sensors. The highest frequencies anticipated were those associated with oscillations at the Väisälä-Brunt frequency. Since the static stability, $E = N^2$, ranges from 1×10^{-5} to $1 \times 10^{-3}\ sec^{-2}$, the period of Väisälä-Brunt oscillations, T_N, was expected to range from $T_N \sim 3$ to 30 min, where $T_N = \frac{2\pi}{N}$. To define Väisälä-Brunt oscillations, and to avoid aliasing of spectra at lower frequencies, it was necessary to sample at a rate of at least once per minute. Such a rapid sampling rate was not possible with the available sensors and the risk was taken of using a sampling rate of once per 10 minutes. A sampling rate as high as

once per 5 minutes was possible, but it was decided to double the record duration which would have been possible with the 5-minute sampling rate. Thus it is not possible to definitively discuss Väisälä-Brunt oscillations in conjunction with internal tidal motions. Since the tidal and inertial motions are of large amplitude, the risk of serious contamination by aliasing from the Väisälä-Brunt oscillations was thought to be small. The question of aliasing is examined by looking for anamalous peaks in the computed spectra of Chapter XI. With the sampling rate of once per 10 minutes, the Nyquist sampling frequency was 3 cph, and the total potential record duration was about 40 days, which was achieved within 10% for four of the ten sensors. Using the semidiurnal tide as a frame of reference, the sampling procedure chosen meant that the observations were made at about every 1/75 of a wave cycle for a total of about 75 wave cycles.

One of the subtle hazards in observations from a moored array is that there is a commitment to a spatially pointwise, temporally semicontinuous viewpoint. The most obvious way to acquire a compensating, semicontinuous spatial view is to use the hydrographic techniques in conjunction with a moored array. The hydrographic techniques were used in several fashions:

a) To compute vertical profiles of the density anomaly, detailed vertical profiles of temperature and salinity were made alongside each sensor string at the beginning, in the

middle, and at the end of the observation period.

b) To compute vertical sections of the density anomaly, detailed vertical sections of temperature and salinity were made along the axis of the array from 10 to about 100 kilometers offshore in the middle and at the end of the installation period.

c) Anchor stations were occupied for a lunar day at distances of 45 (twice), 75, and 100 kilometers offshore in order to detect tidal structure in the hydrographic fields; at one of the stations 45 kilometers offshore, good quality vertical profiles of current meter observations were made from the R/V Yaquina.

d) Several vertical profiles of current meter observations were also taken close to the moored sensor strings (Mooers et al., 1968).

X. THE OREGON COASTAL OCEANOGRAPHIC REGIME

A. Introduction

The oceanographic setting of the August-September 1966 observations and the properties of the Oregon coastal regime relevant to the propagation of inertial-internal waves are described. First, the general flow regime off Oregon and the specific flow regime of the frontal zone of coastal upwelling in August-September 1966 are discussed. Then, the seasonal fields of static stability off Oregon and the field of static stability in the coastal region in August-September 1966 are analyzed. Finally, the field of characteristics for the semidirunal internal tide in the coastal region in August-September 1966 is examined.

B. General Description

The oceanographic regime off Oregon is typical of the mid-latitude zone of the Ocean's eastern boundary regions (Wooster and Reid, 1963). There is a coastal regime consisting of the waters over the continental shelf and slope, which extend to about 100 kilometers offshore; a transition region about 100 kilometers wide; and an offshore regime seaward of 200 kilometers offshore. The mid-latitude zone of eastern boundary regions is characterized by a weak, broad, and shallow equatorward flow offshore. Because of the seasonal

reversal of the alongshore wind, and because the wind and pressure fields are highly variable on the time scale of days to weeks, the flow of the coastal regime is very time-dependent. In the offshore region off Oregon, the California Current flows equatorward on the average. In the coastal region, the prevailing northerly winds yield an equatorward and offshore flow in the surface layer in the summer, while prevailing southerly winds yield a poleward surface flow, the Davidson Inshore Current, in the winter. There are other, interrelated distinctions between summer and winter: in the summer, density stratification is intense, coastal upwelling predominates, and a coastal, poleward undercurrent occurs, while in the winter both the density and flow fields are more nearly uniform as a function of depth. These properties determine the seasonal state of the mean flow with which an internal tide interacts.

Smith (1964) and Smith, Pattullo, and Lane (1966) have made comprehensive studies of coastal upwelling off Oregon. In the former study, using hydrographic and atmospheric data, Smith tested models of coastal and open-ocean upwelling adapted for the Oregon coastal and offshore regions; his study encompassed the annual cycle. In the latter paper, hypotheses were tested regarding the inception of upwelling; the hydrographic and atmospheric data gave credence to the applicability of the basic physical concepts of coastal upwelling to the coastal regime off Oregon. Collins (1964) examined the annual march

of the permanent pycnocline and made deductions about the flow regime based on hydrographic data; he documented the onshore rise of the permanent pycnocline in the spring and its descent in the autumn. Collins (1968) analyzed time series of current velocity and temperature observations over the continental shelf off Oregon, representing all but the spring season. These and other studies have established the existence of coastal upwelling off Oregon and have contributed to the understanding of coastal upwelling in general. The studies of coastal upwelling off Oregon, and the more general studies of Yoshida (1967) and Smith (1968), form the observational and deductive basis for the mean flow upon which the present study is structured.

Pavlova (1966) has presented hydrographic evidence, based on data spanning a 35-year interval, for the seasonal structure of the California Current System south of the Oregon border. In particular, her work shows the existence of a poleward undercurrent near the coastal boundary during the upwelling season; the undercurrent becomes most intense late in the summer and early autumn. Munk (1950) has attributed the coastal countercurrent off southern California to a balance between the curl of the local wind stress and the advection of planetary vorticity. Yoshida (1967) has employed this balance in layered, baroclinic models.

Yoshida and Tsuchiya (1957) linked the existence of a coastal, poleward undercurrent to the occurrence of coastal upwelling. They

chose a vertical section of density sampled about 100 kilometers from the Depoe Bay hydrographic line to illustrate their contention. They employed the thermal wind concept, which is illustrated in Figure 18. A field of isopycnals is shown in Figure 18a which has upwarped isopycnals overlying downwarped isopycnals. This field of isopycnals is representative of the continental slope and shelf regions during coastal upwelling, with the downwarped isopycnals occurring beneath the permanent pycnocline. Vertical profiles of the thermal wind and the resultant alongshore velocity are shown in Figures 18b and 18c, respectively. Figure 18b is derived from Figure 18a and Figure 18c from Figure 18b. The downwarping of isopycnals beneath the permanent pycnocline during upwelling season and close to the continental slope was taken by Yoshida and Tsuchiya (1957) as evidence for the existence of a poleward undercurrent. Figures 18b and 18c illustrate how a poleward undercurrent follows from such a density structure. The direct current observations to be discussed shortly confirm their deduction.

The concept of frictional cross-stream flow is introduced for an aid to the interpretation of the observations in the next section. If the balance in the y-component momentum equation for the mean flow is $f\bar{u} = N_v \bar{v}_{zz}$, where N_v is the vertical coefficient of eddy viscosity, then a frictional cross-stream flow exists. Introducing the thermal wind relation into the frictional cross-stream flow relation,

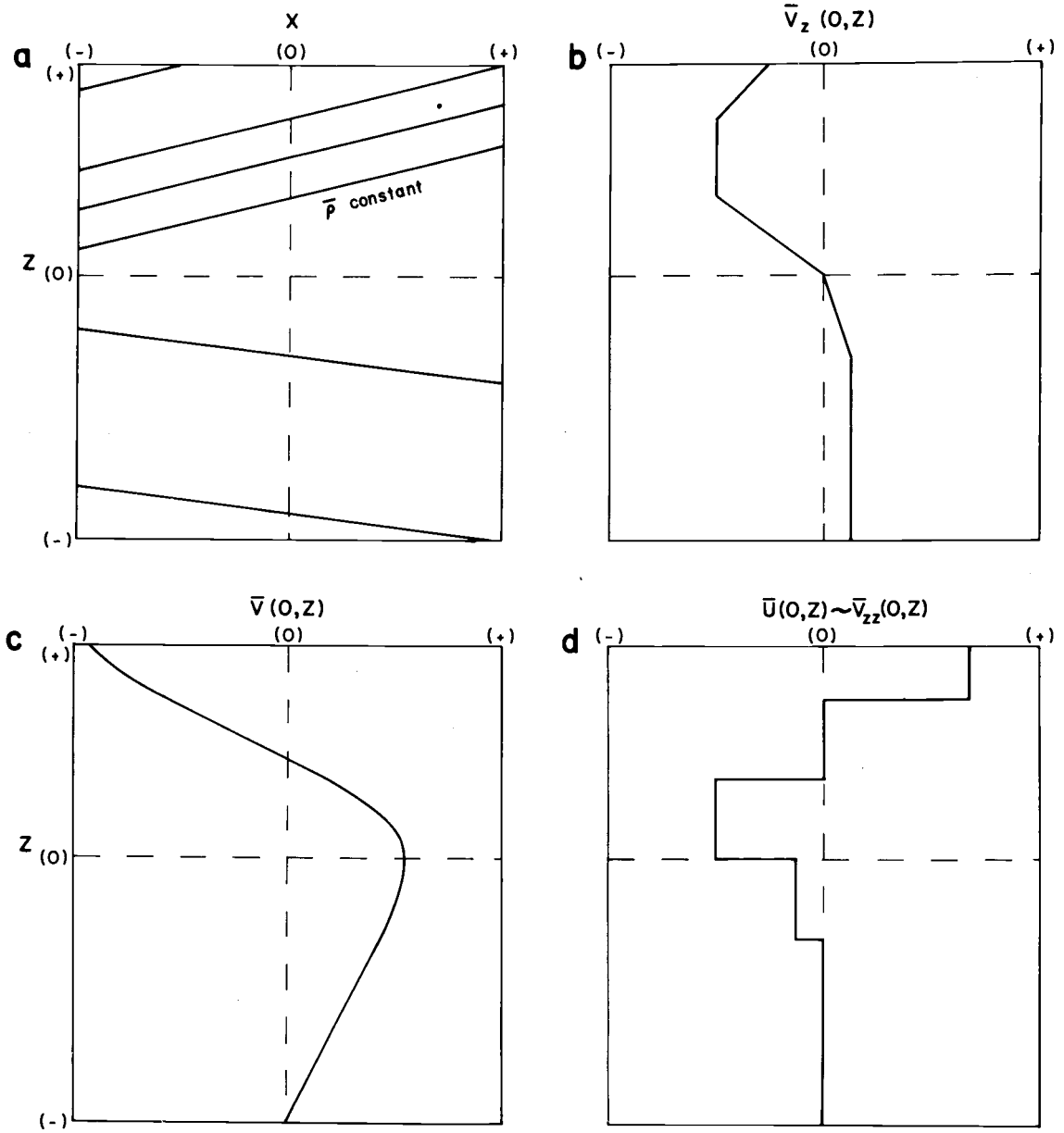

Figure 18. The thermal wind and frictional cross-stream flow concepts.
a. Field of isopycnals
b. Vertical profile of alongshore thermal wind
c. Vertical profile of alongshore flow
d. Vertical profile of frictional cross-stream flow

$$\bar{u} = \frac{+N_v}{f^2} g \frac{(\bar{\rho}_x)_z}{\rho_o} = \frac{-N_v}{f^2} (sE)_z .$$

A qualitative plot of $\bar{u} \propto (\bar{\rho}_x)_z$ is shown in Figure 18d; it is derived from Figure 18c. The frictional cross-stream flow relation predicts onshore flow above the center of the frontal layer and offshore flow beneath. Since the temperature inversion water was found below the center of the frontal layer, and since it moved offshore from its inshore source, the observed cross-stream flow of the temperature inversion water was consistent with the hypothesized frictional cross-stream flow.

A pictorial description of a simple model for the steady-state coastal upwelling process was given in Figure 1; a more complete schematic model is given in Figure 25, which is discussed in the next section. A verbal description of the coastal upwelling flow regime follows:

i) In the summer season, the mean north-northwesterly winds cause a net offshore transport of water in the surface Ekman layer,[19] which is of the order of 10 meters thick. They also cause a southward flow in the alongshore direction, which can be thought of as the barotropic component of the

[19] An Ekman layer is a boundary layer in which frictional effects predominate over other effects in the equations of motion.

alongshore flow.

ii) Mass compensation requires a net onshore transport of water in the bottom Ekman layer, which is also of the order of 10 meters thick.

iii) Since the water of the open ocean reservoir is density stratified with a permanent pycnocline at a depth of about 100 meters, the net offshore transport of light water near the surface and the net onshore transport of heavy water near the bottom cause the permanent pycnocline to rise inshore, forming an inclined frontal layer.

iv) The inclined frontal layer induces a "thermal wind." Thus, there is a baroclinic component to the alongshore flow such that the flow in the inclined frontal layer is increasingly poleward relative to the surface flow as the depth increases. To the extent that the barotropic and baroclinic flow components can be considered linearly superimposed, the barotropic flow induced by the wind, or inclination of the sea surface, either operates to reinforce or to cancel the baroclinic flow in the frontal layer. For instance, with the permanent pycnocline at a fixed intensity and inclination, if the barotropic flow is sufficiently southerly, the lower layer can come to a standstill or be reversed to equatorward flow, while the surface layer continues to flow equatorward. On

the other hand, if the barotropic component relaxes, or reverses, the upper layer can come to a standstill or be reversed to poleward flow, while the lower layer continues to flow poleward. Reversals similar to those described are observed to occur on a time scale of several days to weeks.

v) The seasonal pycnocline develops at the base of the surface Ekman layer. It is formed by the seasonal thermocline, which develops from summer heating, and by the seasonal halocline, which is derived from the mixing of surface layer water with the relatively fresh water of the Columbia River plume. The seasonal pycnocline breaks the sea surface to form a surface front, which tends to block the offshore flow of lower layer water that has been supplied to the surface Ekman layer inshore. The seasonal and permanent pycnoclines tend to merge beneath the surface front.

vi) The above remarks present only a steady-state model. When the winds accelerate sufficiently, the permanent pycnocline becomes more steeply inclined and breaks the surface, forming a surface front, while the surface front formed by the seasonal pycnocline propagates offshore, causing a strong surface divergence to develop. The acceleration process may be largely advective. When the winds decelerate, the response is less rapid because the process of developing

an inclined frontal layer is essentially irreversible, requiring mixing for cancellation.

In summary, the vertical structure to the horizontal flow in the frontal zone of coastal upwelling is divided as follows:

i) An Ekman layer at the sea surface, with the seasonal pycnocline at its base except in the vicinity of the surface front, where the seasonal pycnocline must penetrate the surface Ekman layer.

ii) An Ekman layer at the sloping bottom.

iii) A quasi-geostrophic interior where the effects of the inclined frontal layer predominate over frictional effects due to the stresses applied at the boundaries. The quasi-geostrophic interior can be viewed as subdivided into a thin layer above the frontal layer, the frontal layer per se, and a thick layer beneath. A cross-stream flow occurs in the quasi-geostrophic interior; it may be a purely frictional, purely inertial,[20] or a combination frictional-inertial flow.

The inclined frontal layer is a region where the processes of frontogenesis, necessary for the development and the sustenance of the frontal layer, and of frontolysis, necessary for the destruction of

---

[20]The term inertial is used here in connection with the advective acceleration terms in the equations of motion rather than as it has been used elsewhere in this dissertation in connection with the Coriolis terms.

the frontal layer, are of significance. Secondary, cross-stream flows in the vicinity of the frontal layer are anticipated. A dynamical discussion of the cross-stream flow will be found in Mooers et al. (1969) and a preliminary theoretical discussion of cross-stream flows is found in Mooers (1968). Appreciable mixing occurs in the frontal zone. If mixing is sufficiently intense, the isopycnals in the layer beneath the inclined frontal layer become downwarped, intensifying the tendency for northward flow there. Mixing warm, fresh waters derived from the surface layer with cold, saline waters from the lower layer near the surface front replenishes the water mass of the frontal layer. The freshly formed water mass of the frontal layer sinks to the lower half of the inclined frontal layer and below and then flows seaward, adding to the volume of the permanent pycnocline. The temperature inversion in the lower half of frontal layer is a key indicator of this flow pattern. The hydrological-optical investigation of Pak et al. (1969) supports the deduced cross-stream flow pattern.

C. The Frontal Zone of Coastal Upwelling in August-September 1966

In Figure 19, vertical sections of the density anomaly, sigma-t, are shown for August-September 1966; the positions of the moored, recording sensors are indicated by solid symbols. The section shown in Figure 19a was sampled two weeks after installation of the sensors,

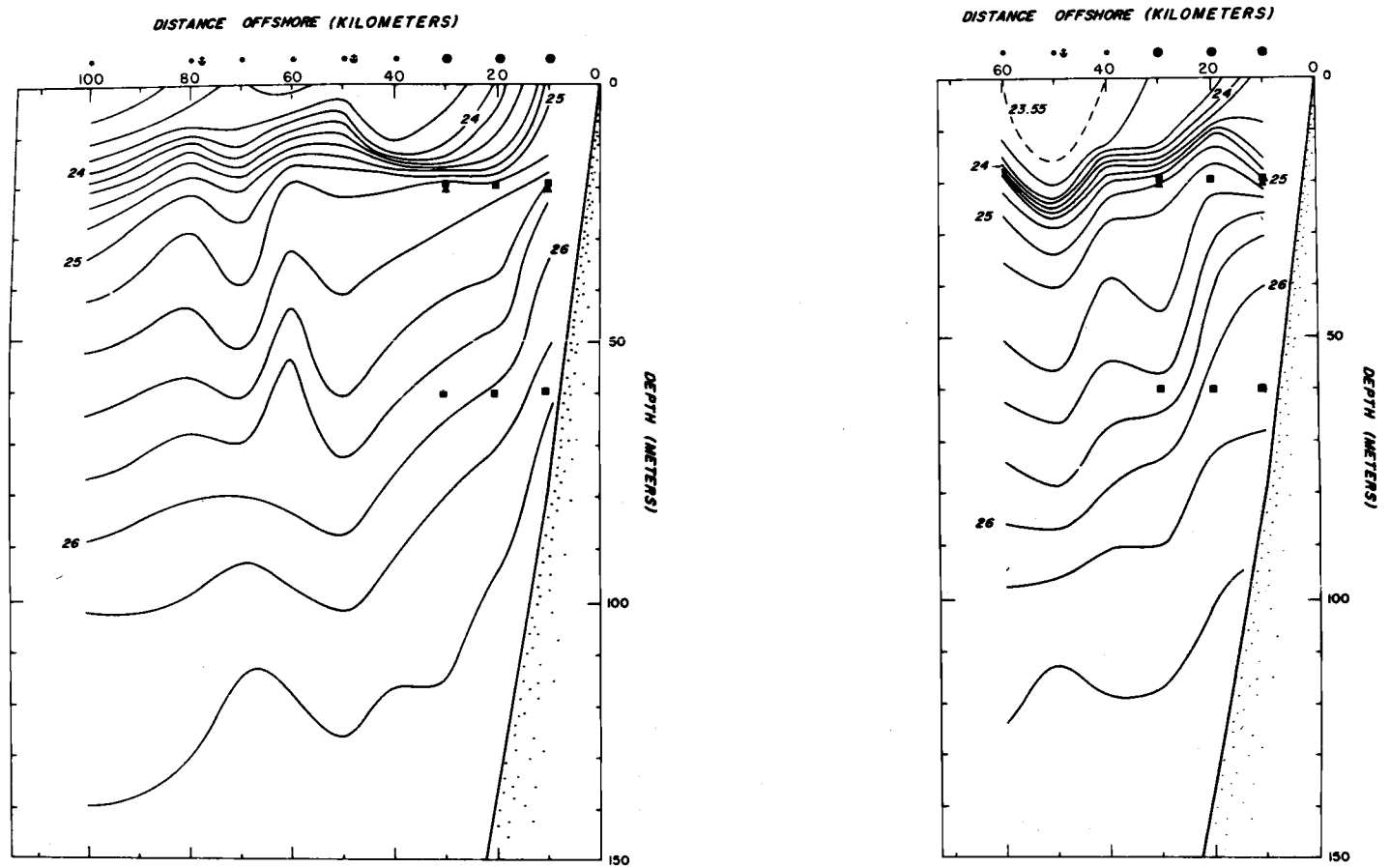

Figure 19. Vertical sections of sigma-t off Depoe Bay, Oregon.
a. Late August 1966
b. Late September 1966

▪ Current meter
• Hydrographic station
•⚓ Anchor station
▲ Thermograph
● Instrument installation

and the one shown in Figure 19b was sampled a month later, upon recovery of the sensors. The contoured fields of sigma-t are based on single casts taken at each station; the sections were each sampled during a two-day interval and the indicated vertical position of the isopycnals could differ from their daily mean vertical position by as much as ±10 meters, due to inertial-internal waves or other causes. The overall pattern was essentially the same in late August as it was in late September, with exceptions noted below. The 24.0 and 24.6 isopycnals delimit the seasonal pycnocline and the 25.4 and 26.0 isopycnals delimit the permanent pycnocline. Collins (1964) found the latter to be reliable indicators of the permanent pycnocline. The seasonal pycnocline has yet to be treated in similar detail. Thus, the moored, recording sensors bracketed the inclined frontal layer formed by the permanent pycnocline during the period of observation.

At 50 kilometers offshore, the seasonal pycnocline was found in the depth zone of 10 to 20 meters deep, while the permanent pycnocline was found in the depth zone of about 50 to 90 meters deep there. Both pycnoclines rose inshore; the seasonal pycnocline broke the surface about 10 to 20 kilometers offshore, while the permanent pycnocline rose to the depth zone of 20 to 40 meters deep about 10 kilometers offshore. What occurred inshore of 10 kilometers is uncertain, but the existent observations suggest that the region inshore of 10 kilometers offshore was quite variable, indicative of mixing. The

vertical density gradient or, equivalently, the static stability, is taken as the measure of frontal, or pycnocline, intensity. The seasonal pycnocline was about four times as intense as the permanent pycnocline at 50 kilometers offshore, while inshore the permanent pycnocline intensified by a factor of two. The slope of a pycnocline, or frontal layer, is given by the slope of its fiducial isopycnals. The overall frontal slope of the seasonal pycnocline was about $\frac{15 \text{ meters}}{30 \text{ kilometers}} = 0.5 \times 10^{-3}$ and that of the permanent pycnocline was about $\frac{40 \text{ meters}}{40 \text{ kilometers}} = 1 \times 10^{-3}$. The maximum frontal slope of the seasonal pycnocline was about $\frac{10 \text{ meters}}{10 \text{ kilometers}} = 1 \times 10^{-3}$ and that of the permanent pycnocline was about $\frac{30 \text{ meters}}{10 \text{ kilometers}} = 3 \times 10^{-3}$. The largest values of the frontal slope for both the seasonal and permanent pycnoclines were found at their inshore edges. The most significant changes from August to September indicated by the sigma-t sections were

i) The intensification of the seasonal pycnocline.

ii) The marked downwarping of the isopycnals beneath the inshore edge of the seasonal pycnocline.

iii) The reduction of the inclination of the isopycnals beneath the inshore edge of the permanent pycnocline.

The three notable changes are consistent with increased mixing occurring in the frontal zone as the decay phase of coastal upwelling progresses. They are also consistent with the thermal wind concept

and the observed increase of poleward flow in the lower layer 10 kilometers offshore from late August to late September.

In Figure 20, the vertical sections of temperature, salinity and sigma-t for mid August, late August, and late September 1966 are shown. Four points are noted:

i) The seasonal pycnocline was the result of both a seasonal halocline and a seasonal thermocline.

ii) The permanent pycnocline was the result of a halocline; in fact, the temperature inversion near its base weakened the effect of the halocline on the formation of the pycnocline.

iii) The temperature inversion was most intense inshore and followed the descent of the frontal layer offshore.

iv) The inclined frontal layer weakened and became less steep while the temperature inversion became more intense from mid August to late September.

Since the temperature inversion was formed near the surface front, and since it was subsequently advected offshore, it is used as an indicator of cross-stream flow. The existence and the frontal significance of the temperature inversion were first noted by Pattullo and McAlister (1962). Mooers et al. (1969) explore its dynamical interpretation further. The salinity and temperature structure is representative of the summer season off Oregon. For inertial-internal wave measurements, a recording salinograph would be more

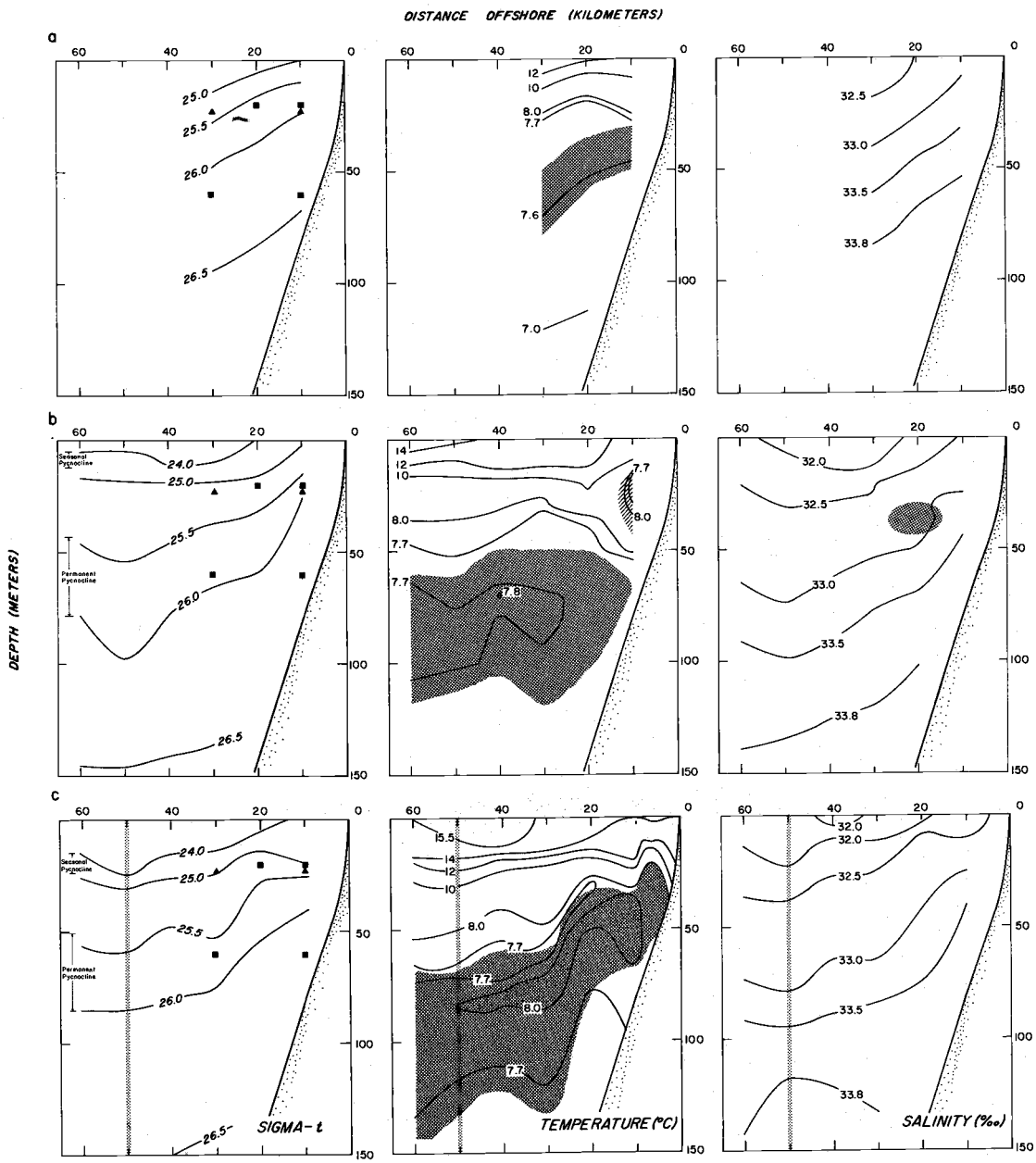

Figure 20. Vertical sections of sigma-t, temperature, and salinity off Depoe Bay, Oregon. (Hatched areas indicate temperature or salinity inversions.

a. Mid August 1966

b. Late August 1966

c. Late September 1966

useful than a recording thermograph because salinity is generally, though not always, a monotonic function of depth and has appreciable, nearly uniform, vertical gradients over a considerable range of depths, while temperature is a multiple-valued function of depth and has weak or non-uniform vertical gradients over much of the water column.

The temperatue inversion was related to the flow field. Figure 21 shows a vertical section of temperature as a function of time sampled at an anchor station 45 kilometers offshore. The instantaneous depth of the secondary maximum[21] in the instantaneous current speed is shown by solid circles superimposed on the temperature field. The most significant feature are:

i) The ±10 meter vertical displacements of the isotherms in the temperature inversion at a depth of about 100 meters had a semidiurnal character.

ii) The secondary maximum of instantaneous speed occurred in the upper half of the temperature inversion; its depth also had a semidiurnal character. Thus, appreciable vertical shears and variability in the horizontal flow appear to have occurred at the base of the pycnocline. These contentions are examined more thoroughly in the following discussion.

---

[21] The primary maximum in both the instantaneous and the mean current speed is found near the sea surface.

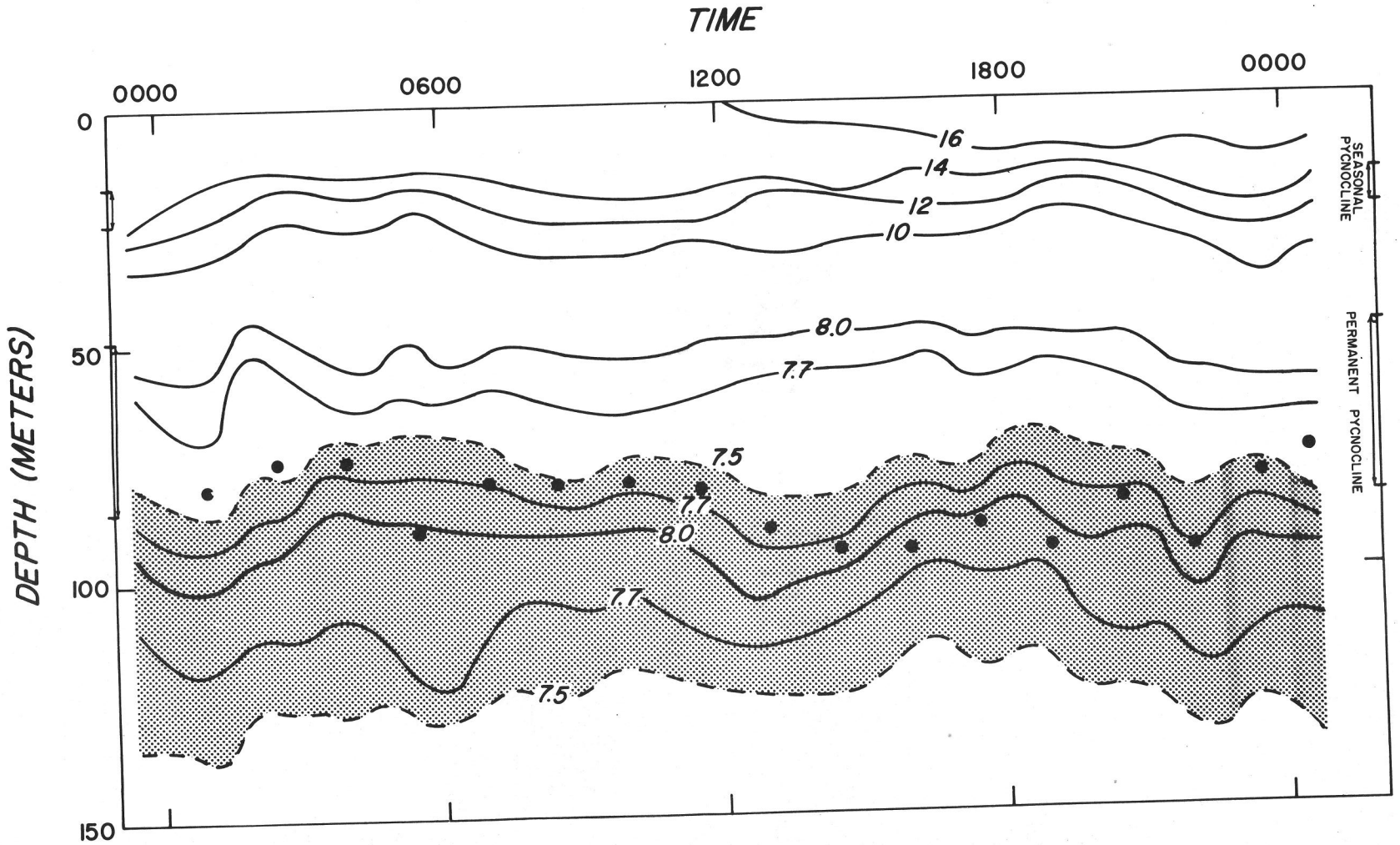

Figure 21. Vertical time section of the temperature field and the depth of the secondary maximum in the instantaneous current speed. (Anchor Station DB25, late September 1966.)

Figure 22 shows the vertical profiles of the mean of the scalar speed and of the speed of the vector mean for the data from which Figure 21 was derived. The ratio, I, of the two profiles, depth-for-depth, is a measure of the steadiness of the flow at each depth. The secondary maximum of the speed of the vector mean occurred at a depth of 105 to 120 meters; since $I \approx 4/3$ in that depth zone, the flow was quite steady there. The secondary maximum in the mean of the scalar speed occurred at a depth of 80 to 90 meters; since $I \approx 5$ in that depth zone, the flow was quite variable there.

Figure 23 displays vertical profiles of quantities computed from the time series used in compiling Figures 21 and 22. The profiles extend from the sea surface to a depth of only 100 meters. Because observations were made for only one-half the observation period below that depth, and because calculations were made for the semidiurnal component of the motion at each depth, it was safe to consider only the results for the observations made over two semidiurnal cycles. The vertical profiles of the lunar semidiurnal (M_2) velocity component magnitude and phase are shown in Figures 23a and 23b, respectively. The values for the tidal estimates were obtained by least squares analysis. The vertical profiles of the mean of the velocity components, also obtained in the least squares analysis, are shown in Figure 23c. The M_2 magnitude and phase and the mean of both velocity components vary smoothly with depth. The secondary maximum in

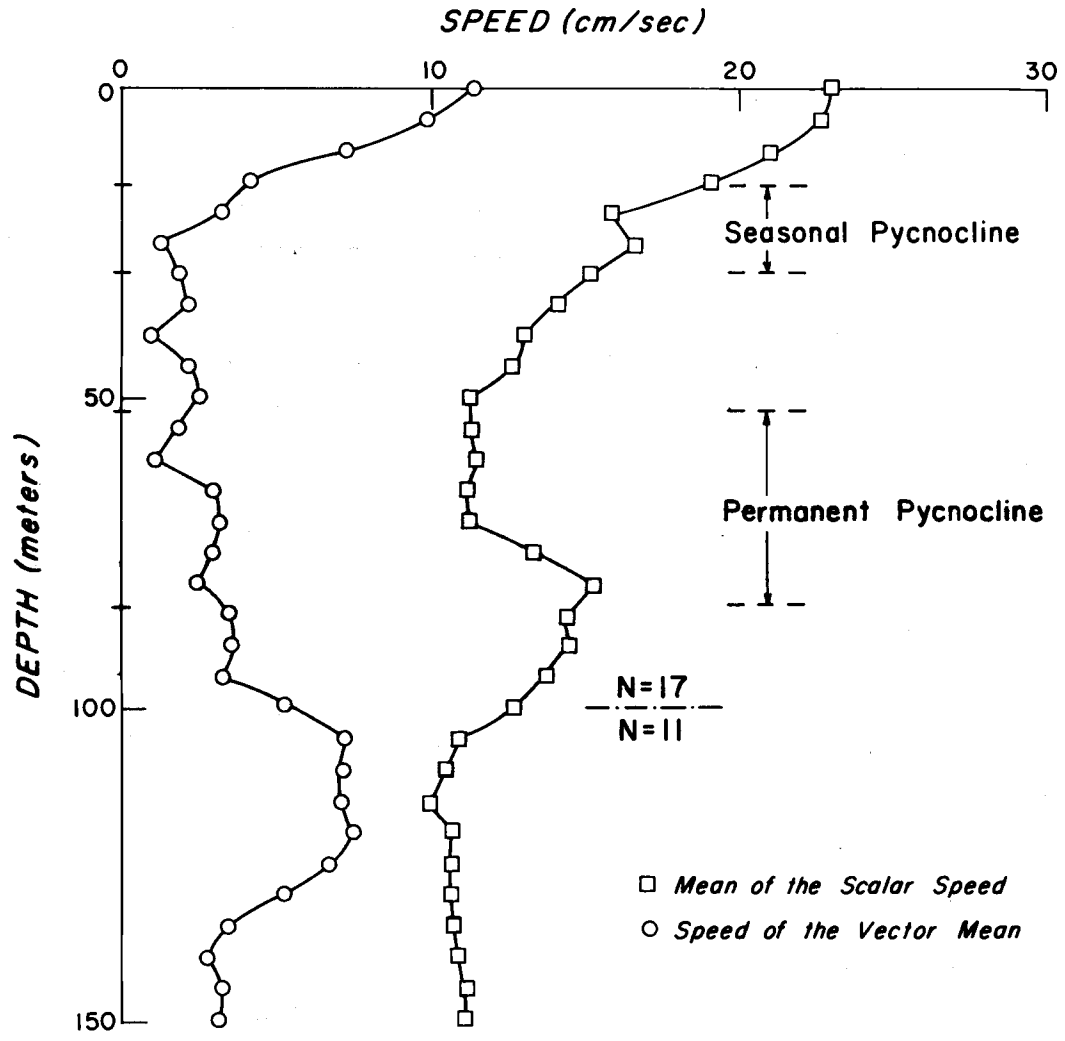

Figure 22. Vertical profiles of the mean of the scalar speed and of the speed of the vector mean. (Anchor Station DB25, late September 1966.) (N is the number of samples; sample duration was one lunar day.)

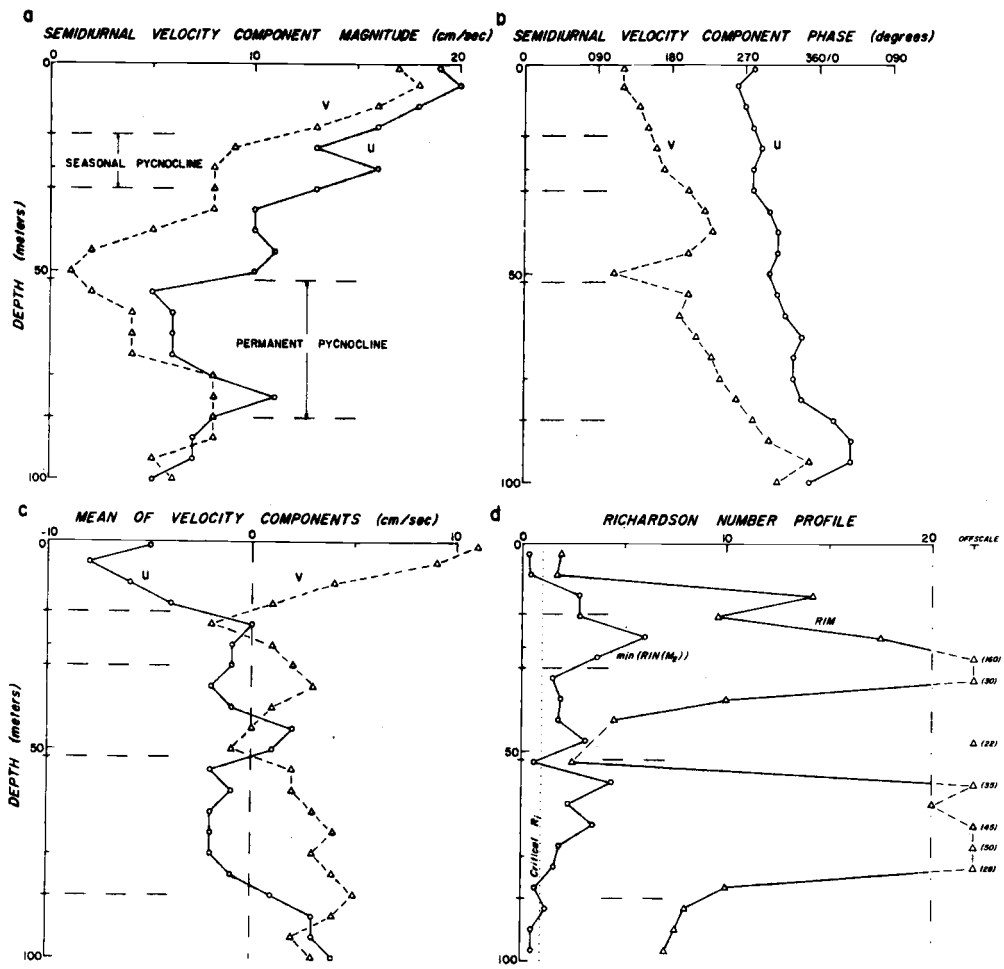

Figure 23. Vertical profiles of quantities derived from horizontal velocity observations. (Anchor Station DB25, late September 1966.)

a. Semidiurnal velocity component magnitude
b. Semidiurnal velocity component phase
c. Mean of velocity components
d. Richardson numbers

the M_2 velocity magnitude at the base of the permanent pycnocline is the most striking feature in Figure 23a. Appreciable vertical shears are associated with the secondary maximum. The M_2 phase sustained a 100° and a 180° variation from the surface to 100 meters deep in the onshore and poleward components, respectively. The variations in depth of the magnitude and phase of the M_2 tide are baroclinic effects, thus a semidiurnal internal tide was present in the observations.

The mean profiles of Figure 23c indicate that the flow in the permanent pycnocline was poleward and offshore, while it was poleward and onshore beneath the permanent pycnocline. These features of the mean flow are consistent with the previous discussion about the thermal wind and frictional cross-stream flow concepts upon careful analysis.

Vertical profiles of Richardson numbers for the mean flow, RIM, and for the temporal minimum of the combination of the mean flow and the M_2 amplitude, $\min(\mathrm{RIN}(M_2))$, are shown in Figure 23d. RIM indicates that the mean flow was dynamically stable and that it was most stable in the pycnoclines, while it was least stable at the top and at the base of each pycnocline. The vertical shear of the M_2 velocity reduced the minimum Ri. The occurrence of critically low values for $\min(\mathrm{RIN}(M_2))$ at the base and beneath the permanent pycnocline is the most striking and convincing pattern. This result is consistent with the thesis of this dissertation. (Instantaneous Ri's

yield even smaller values, but, due to inevitable sampling errors, the more conservative min ($RIN(M_2)$) has been displayed because it is based on the least squares analysis for the full time series.) Thus, there is evidence for the semidiurnal internal tide functioning as a destabilizing, or mixing, agent in the frontal layer over the continental slope. In Section XI. H., Ri's computed for the time series observed over the continental shelf at DB5, 10 kilometers offshore, are examined.

The directly measured and geostrophic winds (Mooers et al., 1968), both indicate the following qualitative patterns:

i) Strong winds from the north-northwest occurred during the first three weeks of August. This was a favorable condition for coastal upwelling.

ii) Weak and variable winds, generally from the southwest, occurred during the following week. This was an unfavorable condition for coastal upwelling.

iii) Moderate winds from the north-northwest occurred during the next week. This was a favorable condition for coastal upwelling.

iv) Weak and variable winds, generally from the southwest, occurred during the last three weeks of September. This was an unfavorable condition for coastal upwelling.

The wind patterns suggest that the observations were made during the

late stages of the coastal upwelling season and the initial stages of the seasonal transition to southerly winds and the cessation of coastal upwelling. The interval of common record durations, the last two weeks of August, is characterized as favorable for coastal upwelling in the first week and unfavorable in the second week. These comments must temper the interpretations placed on the mean calculations of the velocity and temperature fields.

In Tables 1, 2, and 3 the means and standard deviations of the observations from the moored, recording sensors of the August-September 1966 field observations are given.[22] Several of the mean flow features are noted from Table 1a:

i) The alongshore flow was southerly at a depth of 20 meters; it was more intense at 10 kilometers than at 20 kilometers offshore.

ii) The alongshore flow was northerly at a depth of 60 meters; it was more intense at 30 kilometers than at 10 kilometers

[22] For most of the discussion, Tables 1a, 2a, and 3a are used, In those tables, the velocity, temperature, and velocity differences are given for common record lengths, each 339 hours long. The velocity and velocity differences resolved into alongshore (normal to the array axis) and onshore (tangential to the array axis) components are used. The axis of the array was aligned along 300 to 120° True, while the bottom contours were aligned along 025 to 205° True, 030-120° True, and 035-125° True at the 10, 20, and 30 kilometers offshore sites, respectively. In other words, the normal to the array axis was oriented within ±5° of the bottom contours. The primed coordinates and velocities are in the alongshore-onshore coordinate system. The change of coordinates required a 30°, clockwise rotation.

Table 1. Statistics of the mean flow field.

Depoe Bay station	Distance offshore (kilometers)	Water depth (meters)	Sensor depth (meters)	Record duration (No. of hours)	Eastward component (u) (cm/sec) mean ± std. dev.	Northward component (v) (cm/sec) mean ± std. dev.	Scalar speed (cm/sec) mean ± std. dev.	Speed of vector mean (cm/sec)	Direction of vector mean (deg. true)	Onshore component (u') (cm/sec) mean	Poleward component (v') (cm/sec) mean
1a. Based on hourly averages for common record lengths											
5	10	80	20	339	-2.2 ± 11	-17.9 ± 12	23.4 ± 7	18.0	187°	+7.1	-16.6
5	10	80	60	339	+2.8 ± 6	+ 0.7 ± 9	11.0 ± 3	2.9	076°	+2.0	+ 2.0
10	20	140	20	339	+4.5 ± 10	-12.1 ± 9	18.1 ± 6	12.9	160°	+9.9	- 8.3
15	30	200	60	339	+6.0 ± 6	+ 7.9 ± 13	13.3 ± 7	9.9	043°	+1.2	+ 9.8
1b. Based on integrated 10-minute samples for full record lengths											
5	10	80	20	346	-2.1 ± 11	-17.9 ± 12	23.4 ± 7	18.0	187°	+7.2	-16.5
5	10		60	872	+2.7 ± 7	+ 5.1 ± 13	14.3 ± 6	5.8	028°	-0.3	+ 5.8
10	20	140	20	890	-0.8 ± 11	-13.6 ± 9	18.4 ± 6	13.6	183°	+6.1	-12.2
15	30	200	60	956	+4.8 ± 8	+ 3.9 ± 8	12.5 ± 3	6.2	051°	+2.2	+ 5.8

Table 2. Statistics of the mean temperature field.

Depoe Bay station	Distance offshore (kilometers)	Water depth (meters)	Sensor depth (meters)	Record duration (hours)	Temperature (°C) mean ± std. dev.
2a. Based on hourly averages for common record lengths					
5	10	80	20	339	8.44 ± 0.6
15	30	200	20	339	10.19 ± 1.2
2b. Based on integrated 10-minute samples for full record lengths					
5	10	80	20	938	8.86 ± 1.2
15	30	200	20	482	10.72 ± 1.6

offshore.[23]

iii) All sensors exhibited onshore flow. The flow was converging and diverging onshore at the 20 and 60 meter levels, respectively. The convergence at the 20 meter level was an order of magnitude greater than the divergence at the 60 meter level.

iv) The speed of the vector mean flow had values between 2.9 and 10 cm/sec, at a depth of 60 meters at 10 and 20 kilometers offshore; the mean of the scalar speed had values between 11 and 13 cm/sec at those stations, respectively. The flow was most variable at a depth of 60 meters, 10 kilometers offshore, where I was about 4. At the other sites, I was about 1.3.

While a much higher sensor density is necessary to make unequivocal statements about the pattern of the mean flow for the last two weeks in August 1966, the present observations allow some deductions.

Figure 24 aids in the interpretation of Table 1a, the flow field, and Table 2a, the temperature field. All sensors were located in the quasi-geostrophic interior. Further,

[23] From Table 1b, the situation changed when the full six weeks of data were used rather than the two weeks of common record length; i.e., the mean poleward flow intensified at 10 kilometers offshore and diminished at 30 kilometers to the same value. Thus, the poleward flow was greater at 10 kilometers than at 30 kilometers offshore in the latter portion of the observation period.

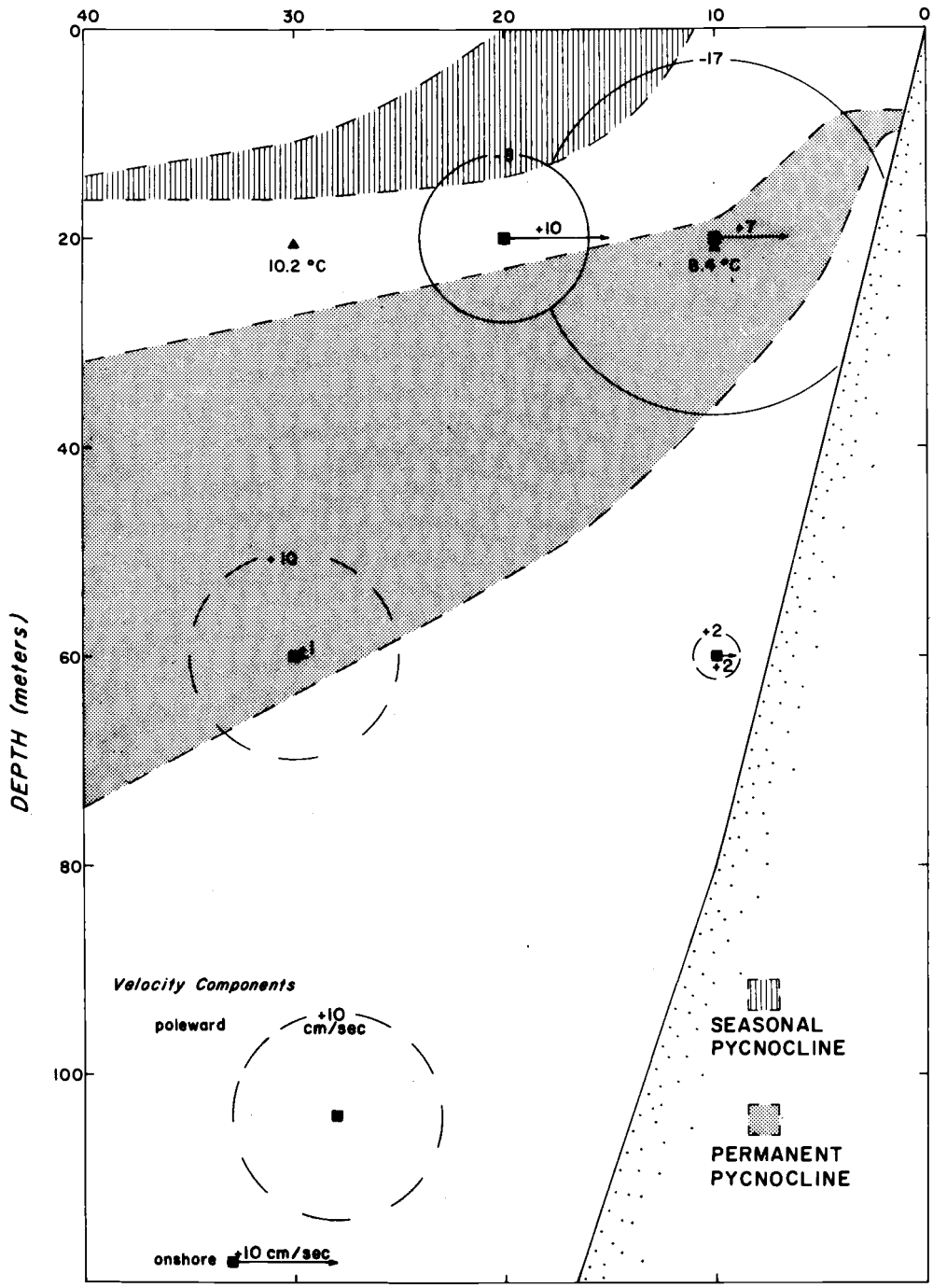

Figure 24. The observed frontal structure and mean flow field over the continental shelf off Depoe Bay, Oregon, 15 to 29 August 1966.

i) The sensor at a depth of 20 meters, 10 kilometers offshore was at the upper boundary of the inclined frontal layer. The flow had an onshore-component consistent with frictional cross-stream flow. The mean temperature, 8.4° C, indicates that interior water was present at the sensor.

ii) The sensor at a depth of 60 meters, 10 kilometers offshore was below the inclined frontal layer. The flow had an onshore component, which may indicate that the site was governed by the bottom Ekman layer at that time.

iii) The sensor at a depth of 20 meters, 20 kilometers offshore was at the upper boundary of the inclined frontal layer. The flow had an onshore component, again consistent with frictional cross-stream flow.

iv) The mean temperature, 10.2° C, indicates that surface layer water was present at a depth of 20 meters, 30 kilometers offshore.

v) The sensor at a depth of 60 meters, 30 kilometers offshore was near the center of the inclined frontal layer. Again, the flow had an onshore component consistent with frictional cross-stream flow.

vi) Under the hypothesis of frictional cross-stream flow, if the sensor at a depth of 60 meters, 20 kilometers offshore had operated, it would have indicated offshore flow because it

wat at the base of the inclined frontal layer and in the temperature inversion. In other words, the offshore flow associated with the temperature inversion "leaked" through the array. Also, the array was too deep to detect the offshore flow of the surface Ekman layer.

Figure 25 is a schematic of the cross-stream flow; it is based on the observations depicted in Figure 24 , the hydrographic sections of Figures 19 and 20, and the verbal model presented in Section B.

In Table 3, the mean velocity differences, and consequent shears are presented; they are based on the same data as Table 1. The principal properties of the mean shears and the mean temperature gradient are summarized below:

i) The value of $\overline{v}'_z$ computed at 10 kilometers offshore between the depths of 20 and 60 meters indicates a thermal wind of $-4.6 \times 10^{-3}\,\mathrm{sec}^{-1}$. The vertical section of sigma-t of Figure 19 indicates that $E \approx 2 \times 10^{-4}\,\mathrm{sec}^{-2}$ and $s \approx 2 \times 10^{-3}$, thus, with $f = 10^{-4}\,\mathrm{sec}^{-1}$, the thermal wind relation, $\overline{v}'_z = \frac{-sE}{f}$, predicts $\overline{v}'_z \approx -4 \times 10^{-3}\,\mathrm{sec}^{-1}$. Thus, it is established that the alongshore flow was essentially geostrophic in the interior. The value of $\overline{u}'_z$, $+1.2 \times 10^{-3}\,\mathrm{sec}^{-1}$, suggests that, in a complete theory for inertial-internal waves in a frontal zone, it may also have an appreciable effect for interactions. From the computed

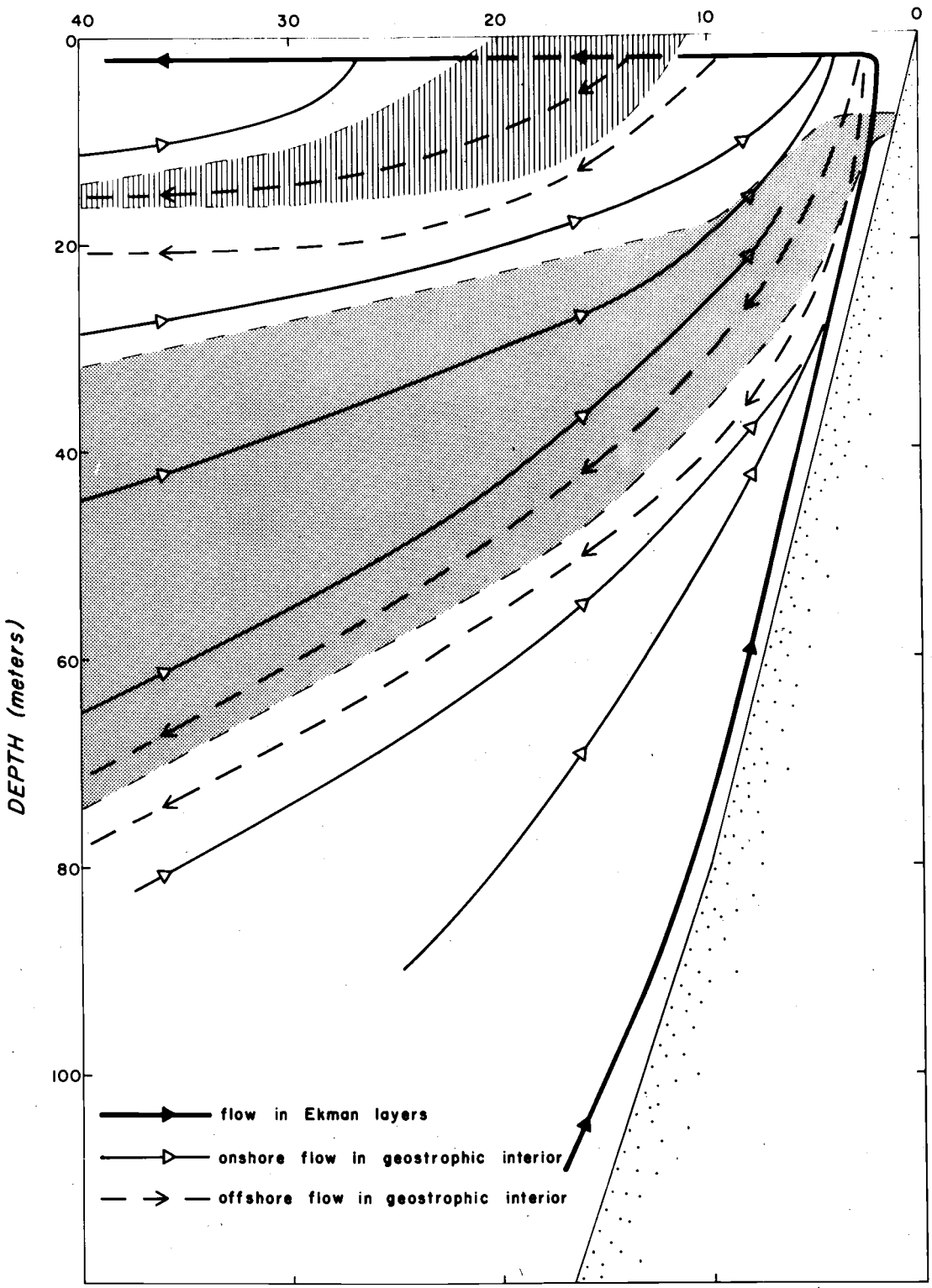

Figure 25. Inferred cross-stream flow field over the continental shelf off Depoe Bay, Oregon, 15 to 29 August 1966.

Table 3. Statistics of the mean shear field.

Depoe Bay Station/ sensor combination in difference	Record duration (No. of hours)	u-differences (cm/sec) mean±std. dev.	Shear term	Shear value mean (sec^{-1})	v-differences (dm/sec) mean±std. dev.	Shear term	Shear value mean (sec^{-1})	Mean shear vector magnitude (sec^{-1})	Mean shear vector direction (deg. true)	u'-differences (cm/sec) mean	Shear term	Shear value mean (sec^{-1})	v'-differences (cm/sec) mean	Shear term	Shear value mean (sec^{-1})
3a. Based on hourly averages for common record lengths															
DB5, 20-60 meters	339	-5.0 ± 13	$\bar{u}_z$	-1.2×10^{-3}	-18.6 ± 11	$\bar{v}_z$	-4.6×10^{-3}	4.8×10^{-3}	194	+5.0	$\bar{u'}_z$	$+1.2 \times 10^{-3}$	-18.6	$\bar{v'}_z$	-4.6×10^{-3}
DB5-DB10, 20 meters	339	-6.7 ± 15	$\bar{u}_x$	-7.7×10^{-6}	- 5.7 ± 11	$\bar{v}_x$	-6.6×10^{-6}	10.0×10^{-5}	229	-3.0	$\bar{u'}_{x'}$	-3.0×10^{-6}	- 8.3	$\bar{v'}_{x'}$	-8.3×10^{-6}
DB5-DB15, 60 meters	339	-3.4 ± 9	$\bar{u}_x$	-2.0×10^{-6}	- 7.4 ± 6	$\bar{v}_x$	-4.2×10^{-6}	4.6×10^{-5}	206	+0.8	$\bar{u'}_{x'}$	$+0.4 \times 10^{-6}$	- 8.1	$\bar{v'}_{x'}$	-4.0×10^{-6}
3b. Based on hourly averages for longest, common record lengths															
DB5, 20-60 meters	345	-5.0 ± 13	$\bar{u}_z$	-1.2×10^{-3}	-18.6 ± 11	$\bar{v}_z$	-4.6×10^{-3}	4.8×10^{-3}	194	+5.0	$\bar{u'}_z$	$+1.2 \times 10^{-3}$	-18.6	$\bar{v'}_z$	-4.6×10^{-3}
DB5-DB10, 20 meters	343	-6.8 ± 15	$\bar{u}_x$	-7.8×10^{-6}	- 5.7 ± 11	$\bar{v}_x$	-6.6×10^{-6}	10.0×10^{-6}	230	-3.1	$\bar{u'}_{x'}$	-3.1×10^{-6}	- 8.3	$\bar{v'}_{x'}$	-8.3×10^{-6}
DB5-DB15, 60 meters	860	-2.2 ± 10	$\bar{u}_x$	-1.3×10^{-6}	+1.5 ± 16	$\bar{v}_x$	$+0.9 \times 10^{-6}$	1.6×10^{-6}	305	-2.5	$\bar{u'}_{x'}$	-1.2×10^{-6}	+ 0.2	$\bar{v'}_{x'}$	$+0.1 \times 10^{-6}$

value of $\bar{v}'_z$ and the estimate of E, FRN ≈ 8, which is about three times the minimum value estimated in Section VIII. C.

ii) The values of $\bar{u}'_x$ at a depth of 20 and 60 meters between 10 and 20 kilometers and 10 and 30 kilometers offshore, respectively, reflect the onshore convergences and divergences noted earlier. The mean temperature gradient at a depth of 20 meters indicates that warm water converged onshore, consistent with frontogenesis. The corresponding values of $\bar{v}'_x$ are one order of magnitude less than the planetary vorticity, f. (The term $\bar{v}'_x$ was not dropped from the GE for the inertial-internal waves with frontal interaction in order to maintain the self-adjointness of the GE and because its maximum value may have been appreciably larger on smaller spatial scales than those of the observations.) Since $r = -\bar{v}'_{x'}/\bar{v}'_{z'}$ is about -1 to -2×10^{-3}, then $r \sim s$, i.e., the slopes of the mean alongshore isotachs and of the isopycnals were about equal but of opposite sign. The difference in the sign of r and s suggests that there was a significant tilt and curvature to the sea surface.

In summary, the geostrophy of the alongshore flow in the interior, the existence of the inclined frontal layer in conjunction with a temperature inversion at its base, and the existence of a poleward

undercurrent are well-established by direct observation in the fontal zone of coastal upwelling over the continental shelf off Oregon. The hypothesized frictional cross-stream flow is consistent with the observations but still must be considered tentative until more detailed observations are examined. Thus, hypotheses x) through xiii) of Section IX. B. have been substantiated by the observations reported in this section.

D. The Field of Static Stability

The hydrographic fields off Oregon have been under routine surveilance for the past decade. The most important property of the hydrographic fields for inertial-internal waves is the vertical density gradient, or, equivalently, the static stability. The mean vertical profiles of sigma-t, σ_t; static stability, E; and Väisälä-Brunt period, T_N, as a function of season and offshore position off Newport, Oregon, are introduced in Figure 26. The Newport hydrographic line is located about 75 kilometers to the south of the measurement site off Depoe Bay, Oregon. The calculations of E(z) have been made with and without the adiabatic correction; due primarily to the temperature inversion, the correction amounts to as much as a 10% difference between the two calculations. Since E(z) has a large range, this is a small discrepancy for most purposes.

The offshore dependence is delineated by three categories:

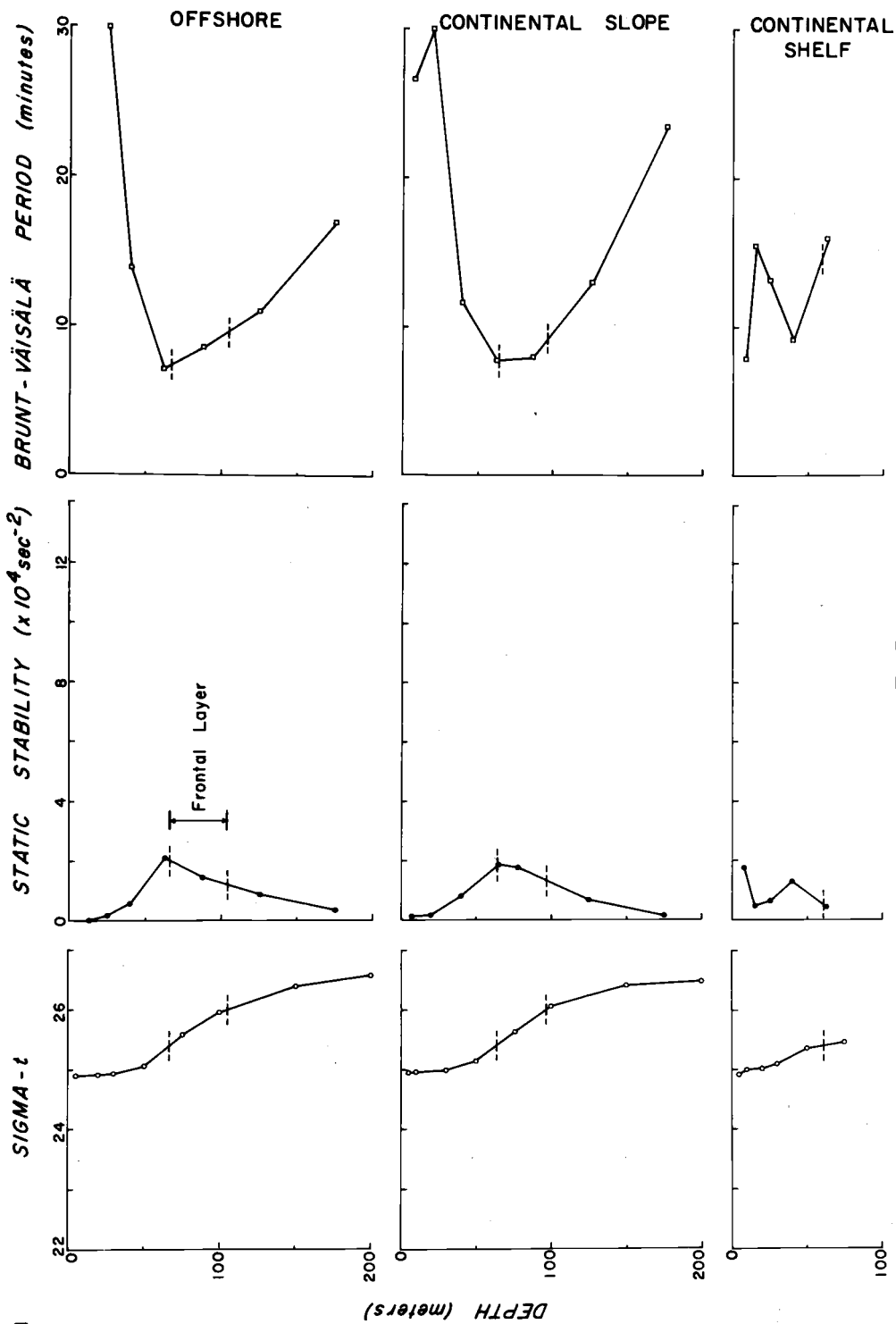

Figure 26a. Winter vertical profiles of sigma-t, static stability, and Väisälä-Brunt period off Newport, Oregon.

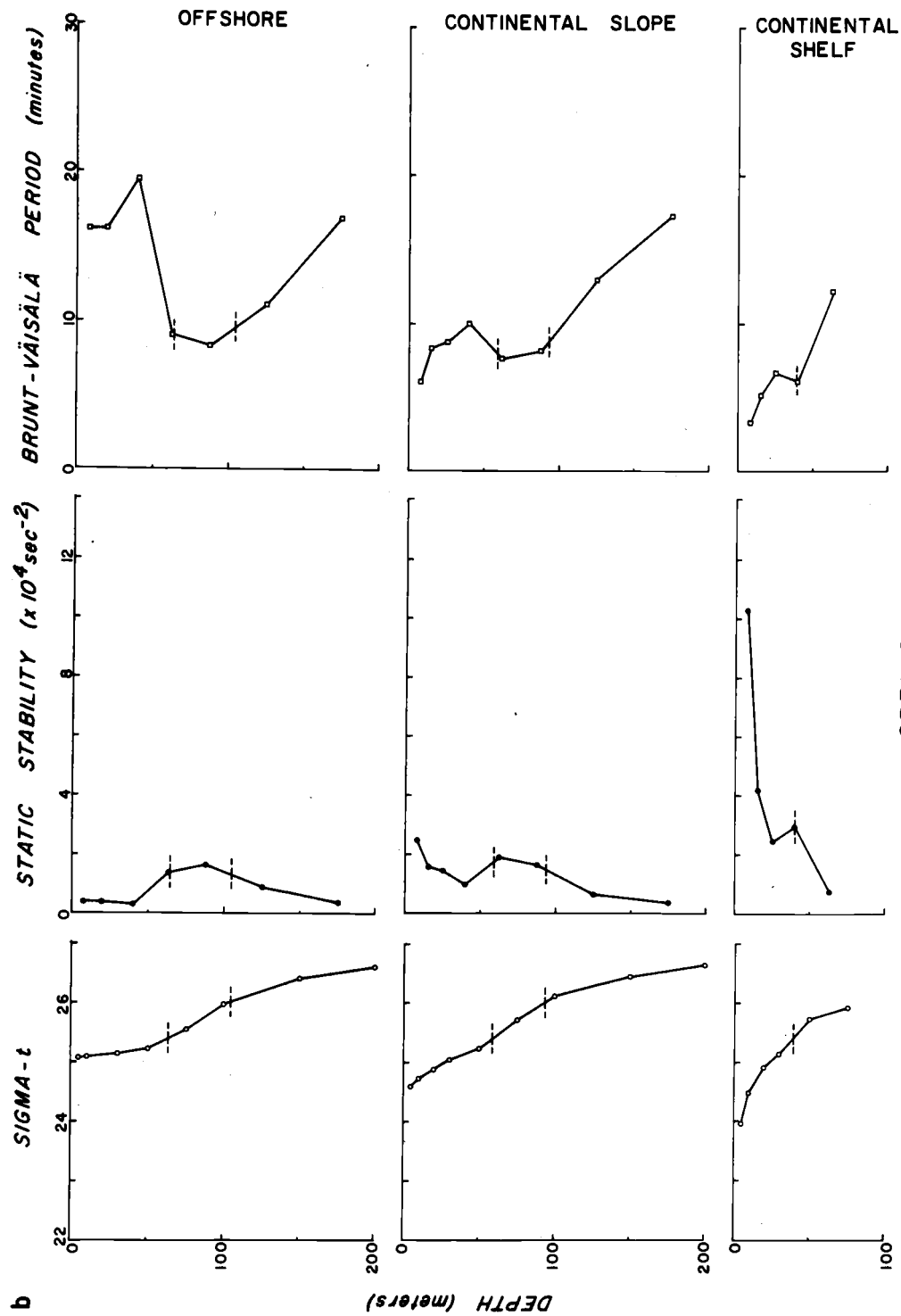

Figure 26b. Spring vertical profiles of sigma-t, static stability, and Väisälä-Brunt period off Newport, Oregon.

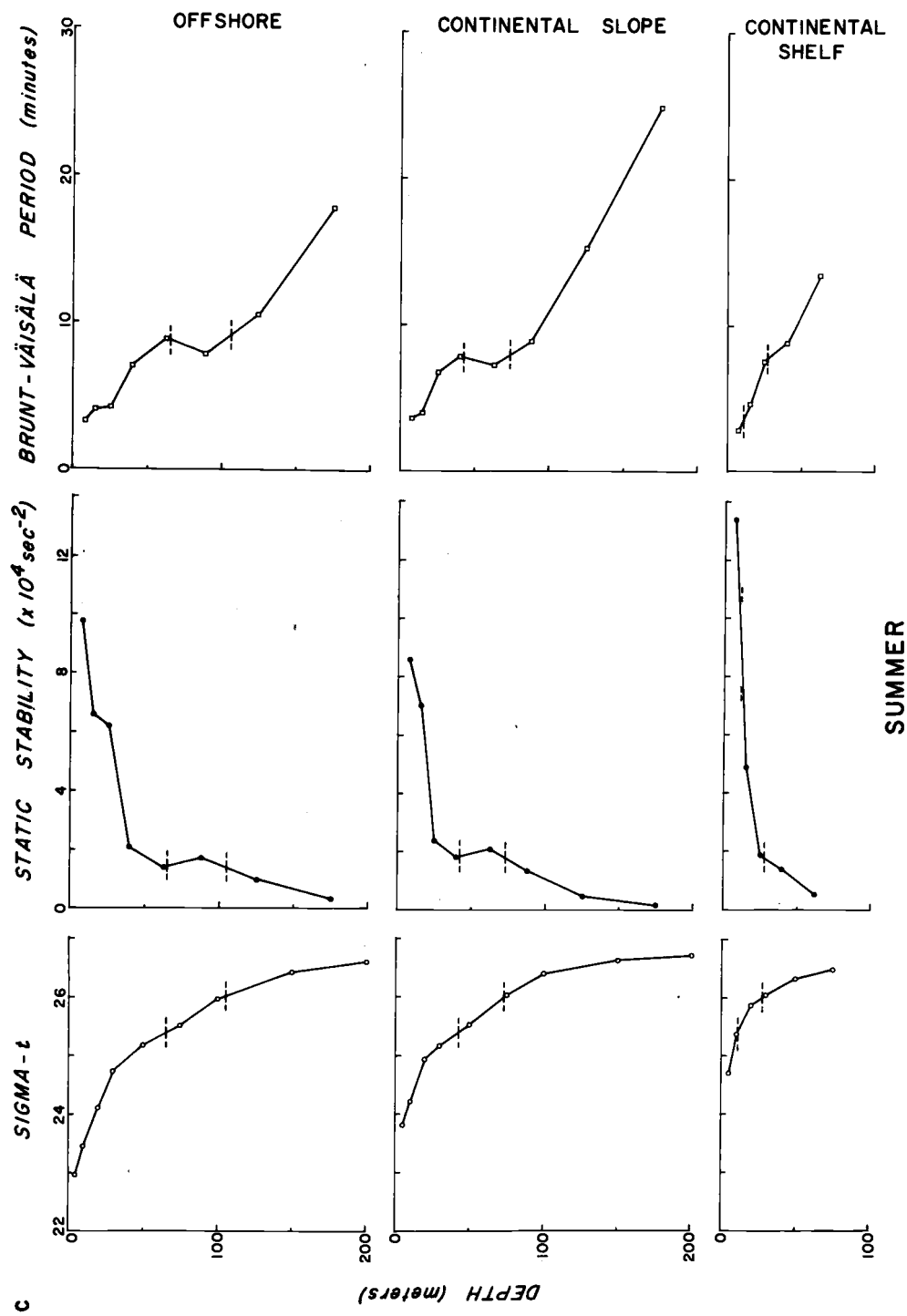

Figure 26c. Summer vertical profiles of sigma-t, static stability, and Väisälä-Brunt period off Newport, Oregon.

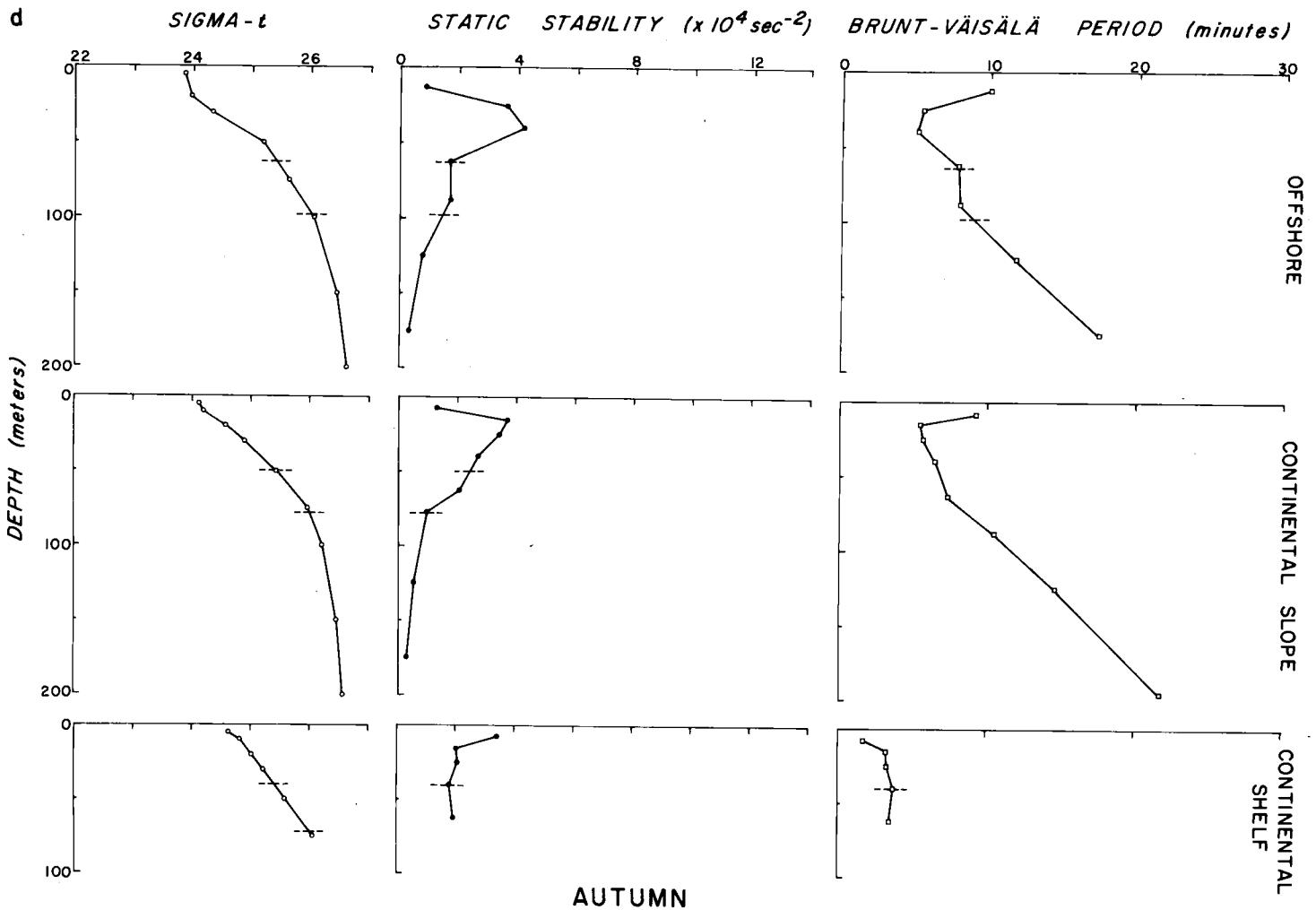

Figure 26d. Autumn vertical profiles of sigma-t, static stability, and Väisälä-Brunt period off Newport, Oregon.

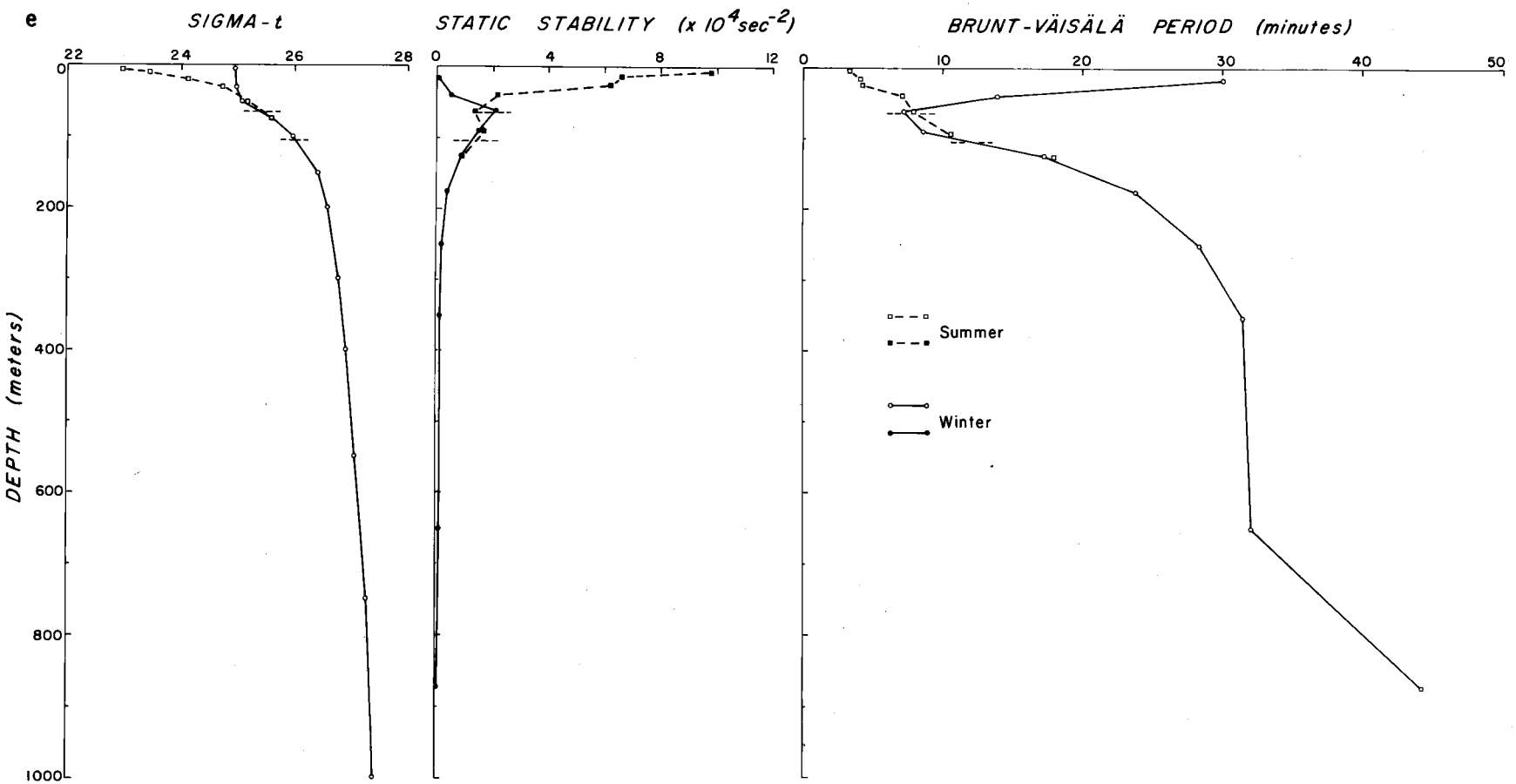

Figure 26e. Deep, offshore, vertical profiles of sigma-t, static stability, and Väisälä-Brunt period off Newport, Oregon.

i) Offshore: depth greater than 1000 meters and distance greater than 72 kilometers offshore.

ii) Continental slope: depth greater than 200 meters and less than 1000 meters and distance greater than 27 kilometers but less than 72 kilometers offshore.

iii) Continental shelf: depth less than 200 meters and distance less than 27 kilometers offshore.

The seasonal dependence is delineated by four categories:

i) Winter: December through February.

ii) Spring: March through May.

iii) Summer: June through August.

iv) Autumn: September through November.

These categories were chosen on the basis of information about the horizontal and seasonal structure of coastal upwelling; though the categories could be subdivided profitably, they are sufficient for the present purposes.

The profiles are based on six years of data, from 1961 through 1966. The range of the number of samples in individual depth categories are listed:

	Season							
	Winter		Spring		Summer		Autumn	
Offshore category	min	max	min	max	min	max	min	max
Offshore	16	66	16	39	21	79	23	55
Continental slope	6	21	5	6	28	39	11	15
Continental shelf	7	20	5	7	7	27	6	28

In Figures 26a to 26d vertical profiles of σ_t, E, and T_N in the upper 200 meters are shown for each season and each offshore category. The position of the frontal layer is denoted by the dashed lines at the depths of the fiducial isopycnals for the permanent pycnocline. The frontal layer is essentially level in the winter season. It rises and intensifies in the onshore direction in the summer season. In the spring and autumn seasons, the frontal layer occupies intermediate positions. In the upper 200 meters, E(z) varies from 10^{-3} to 10^{-5} sec^{-2}. Figure 26e shows the vertical profiles of σ_t, E, and T_N to a depth of 1000 meters in the offshore region for the summer and winter seasons. There is no difference in the summer and winter profiles at depths greater than 125 meters. Most of the variability is confined to the upper 60 meters, i.e., above the frontal layer. E(z) has a minimum of about 0.1×10^{-4} sec^{-2} at a depth of 900 meters. In the winter, the minimum value also occurs near the surface, where E(z) has a maximum of about 10×10^{-4} sec^{-2} in the summer.

In the winter season, E(z) generally has a maximum of 2×10^{-4} sec^{-2} in the frontal layer at a depth of about 60 meters. In the spring season, E(z) develops a maximum of 10×10^{-4} sec^{-2} and 2.5×10^{-4} sec^{-2} at a depth of 10 meters over the continental shelf and over the continental slope, respectively, corresponding to the development of the seasonal pycnocline. In the summer season,

the maximum of $E(z)$ continues to be associated with the seasonal pycnocline and extends to the offshore region. Over the continental shelf, the secondary maximum of $E(z)$, associated with the frontal layer, merges with the primary maximum associated with the seasonal pycnocline. In the autumn season, the primary maximum of $E(z)$ continues to be associated with the seasonal pycnocline, but it is only about $4 \times 10^{-4} sec^{-2}$ and tends to occur deeper than during the summer, at a depth of 20 to 40 meters, over the continental slope and offshore.

In Figures 27 and 28, $E(z)$ is displayed for the August-September 1966 observations. The conversion graph in the lower lefthand corner of Figures 27 and 28 can be used for computing T_N from E.

Figure 27 shows the mean vertical profiles of $E(z)$ for the four anchor stations of August-September 1966. They show the primary and secondary maxima in $E(z)$ associated with the seasonal and permanent pycnoclines, as noted in Figure 26. These curves differ from those of Figure 26 in the following ways:

i) They have about twice as much vertical detail.

ii) They are based on samples taken at a single spatial location.

iii) They are based on a dozen or more samples, as indicated, taken over a period of a lunar day.

The profiles of Figures 27a to 27c are from the continental slope region,

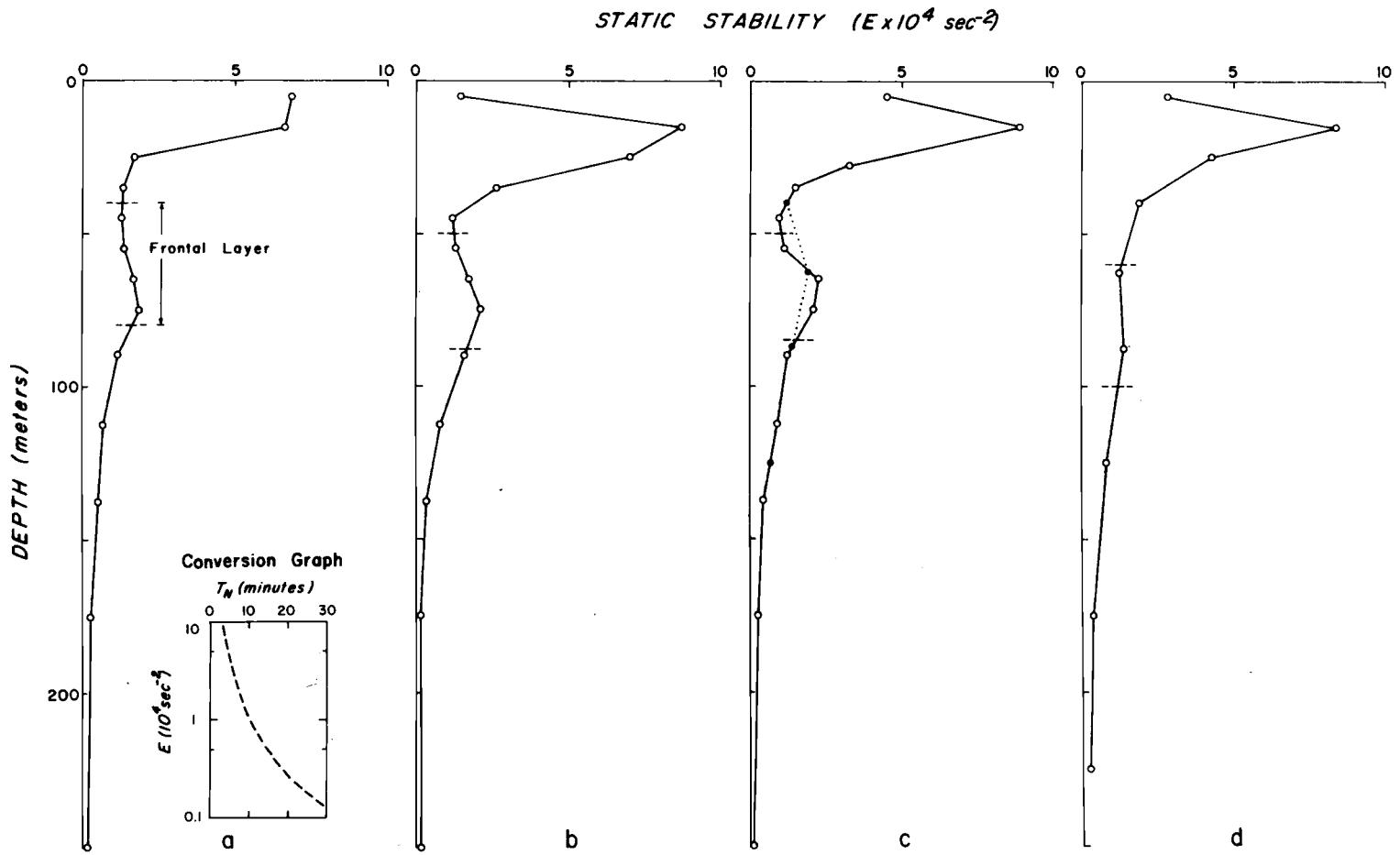

Figure 27. Vertical profiles of static stability for anchor stations off Depoe Bay (DB), and Newport (NH), Oregon.
a. DB25, late August 1966 (14 casts)
b. DB25, late September 1966 (18 casts)
c. DB40, late August 1966 (14 casts)
d. NH65, late September 1966 (12 casts)

while that of Figure 27d is from the offshore region. The essential features of Figure 27 are:

i) The primary maximum of $E(z)$ intensified and deepend from late August to late September over the continental slope.

ii) The primary maximum of $E(z)$ is more intense at the seaward edge of the continental slope and offshore than at the inshore edge, which is consistent with the Columbia River plume being more intense offshore than over the continental shelf.

iii) The secondary maximum in $E(z)$ is less distinct offshore than over the continental slope; this point is verified by the dashed curve of Figure 27c which shows $E(z)$ evaluated at the same depths as the less-densely sampled offshore profile of Figure 27d.

Figures 28a and b show $E(z)$ computed from single hydrographic profiles for three different times during the observation interval at the offshore and inshore termini of the sensor array. These profiles indicate some of the detailed variability of $E(z)$, in both space and time. Overall, their general form is consistent with previous remarks for this season and the continental shelf. An anomalous feature of importance was the minimum in $E(z)$ found at a depth of 40 to 60 meters in late September at the inshore terminus.

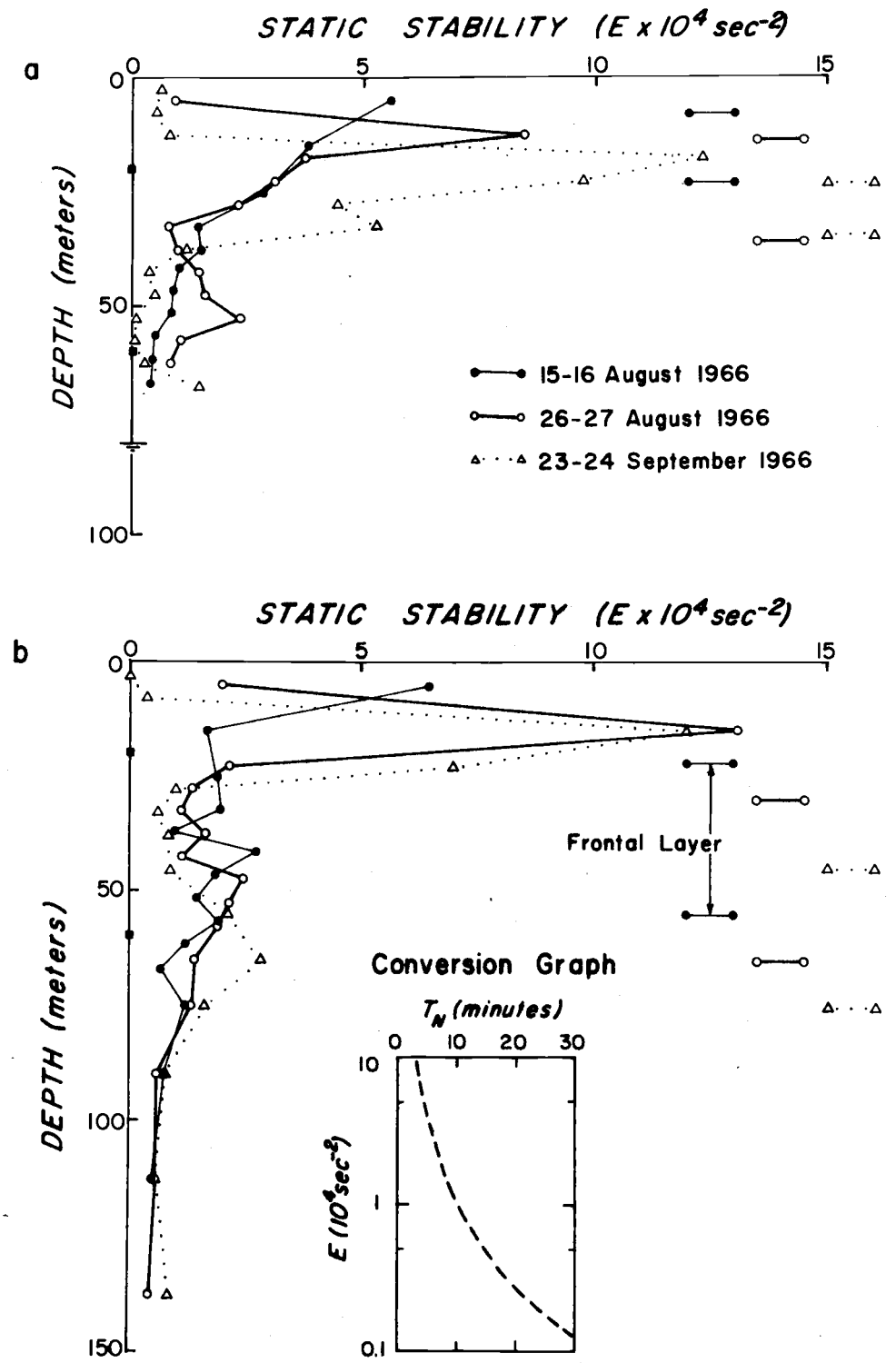

Figure 28. Vertical profiles of static stability at sensor sites off Depoe Bay, Oregon, August-September 1966.
a. DB5, 10 kilometers offshore
b. DB15, 30 kilometers offshore

This minimum was as small as $0.1 \times 10^{-4} sec^{-2}$, corresponding to $T_N = 33$ minutes at a depth of about 60 meters. At the same time, the primary maximum in $E(z)$ occurred at a depth of about 20 meters; it had a value of about $12 \times 10^{-4} sec^{-2}$, corresponding to $T_N = 3$ minutes. For the purpose of interpreting the possibility of $N(z)$ aliasing the spectra of Chapter XI, the following ranges of values are considered representative:

Depth	$E\ (sec^{-2})$	$N\ (sec^{-1})$	T_N (minutes)
20 meters	2 to 12×10^{-4}	1 to 4×10^{-2}	3 to 8
60 meters	0.1 to 3×10^{-4}	0.3 to 2×10^{-2}	6 to 33.

E. The Field of Characteristics for the Semidiurnal Internal Tide

On the basis of the hydrographic data sampled over the continental shelf in late August 1966 and the theory of Section V. B., the fields of characteristics for the semidiurnal tide are displayed in Figures 29 to 31. To determine the fields of $E(x, z)$ and of $s(x, z)$, the slope of the isopycnals, it would have been ideal to have made simultaneous anchor stations at 5 kilometer increments over the continental shelf for a lunar day once each week throughout the period of moored array observations. In practice, a smoothed version of the sigma-t field for late August was used to estimate the values of $E(x, z)$ and $s(x, z)$. The slopes of the characteristics were computed with and

without the frontal interaction. Without the frontal interaction,

$$\lambda_1 = \frac{dz}{dx})_{\eta} \approx + \frac{1.1}{N} \times 10^{-4} = \lambda$$

and

$$\lambda_2 = \frac{dz}{dx})_{\zeta} \approx -\lambda ,$$

where the relations $\sigma^2 \ll N^2$ and $\sigma \approx 1.5f$ have been used.

Similarly, with the frontal interaction,

$$\lambda_1 = \frac{dz}{dx})_{\eta} \approx s + \lambda$$

and

$$\lambda_2 = \frac{dz}{dx})_{\zeta} \approx s - \lambda .$$

In Figure 29 , the η and ζ characteristics are drawn seaward and shoreward from an origin at DB5, 60 meters. The characteristics for three representative values of E constant are illustrated for the case without the frontal interaction. For the most representative value of E, one beam, i.e., the domain of influence for an excitation between two characteristics, is indicated by the hatched area; it illustrates the effect of beam contraction, equivalent to a shift to higher wave numbers and to wave amplification, upon reflection from the sloping bottom. The beam originates from the depth zone of about 110 to 190 meters at the seaward edge of the

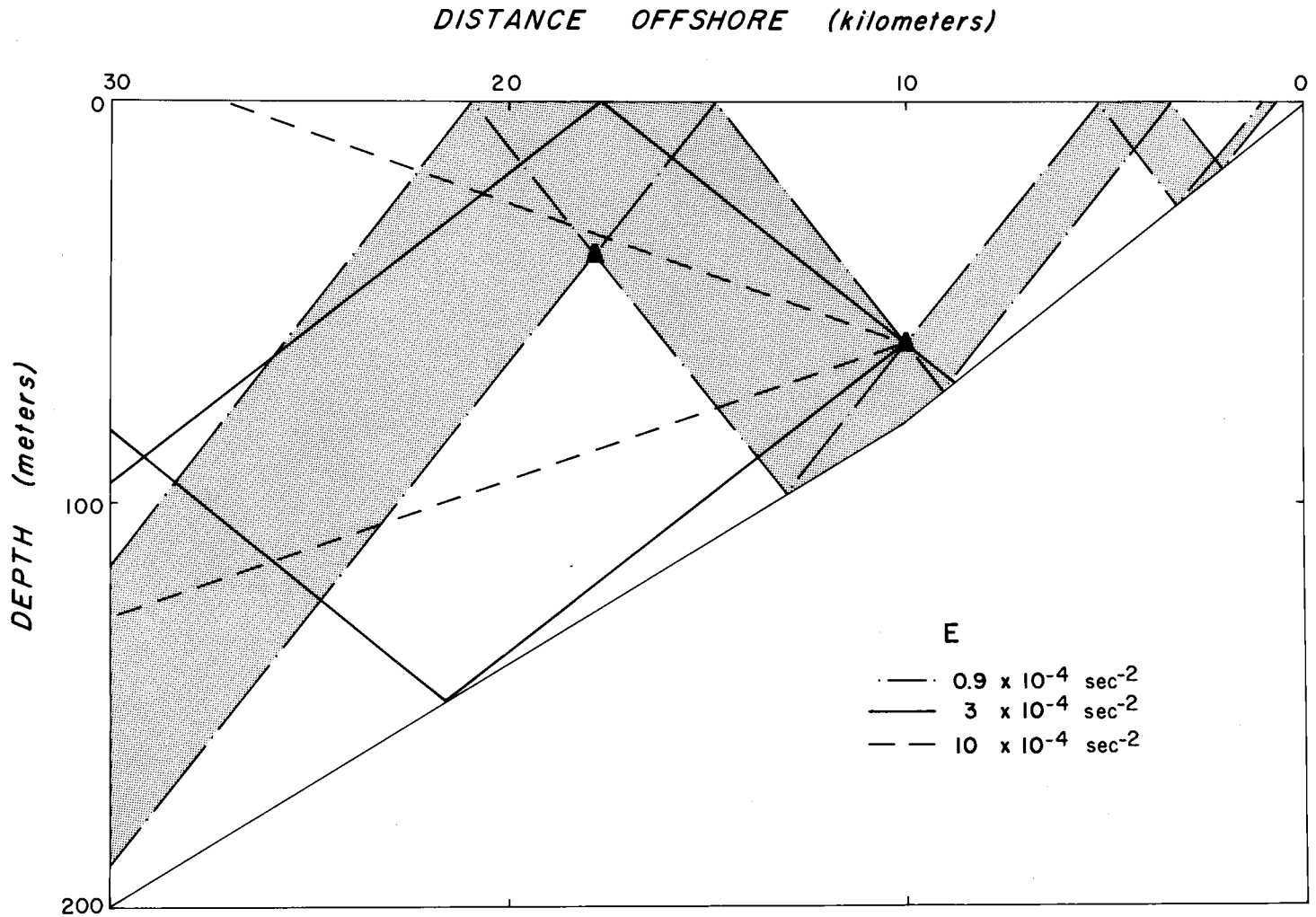

Figure 29. The field of characteristics for the semidiurnal internal tide over the continental shelf off Depoe Bay, Oregon. (Static stability is constant and there is no frontal interaction.)

continental shelf; it reaches DB5, 60 meters after one reflection from the sea surface. After two reflections from the bottom, and two further reflections from the surface, the beam has traversed 29 kilometers of the continental shelf, i.e., to within 1 kilometer of the coast. The vertical thickness of the beam is reduced from 80 meters at the shelf edge to 4 meters at 1 kilometer from the coast. Such a contraction corresponds to an amplification of the velocity field of the wave by a factor of 20.

In Figure 30 , the characteristics are plotted for a case with the frontal interaction. Both E and s are functions of x and z. The downgoing and upgoing beams originating at the seaward edge of the continental shelf between the depths of 22 and 45 meters are indicated by the hatched areas. The fiducial isopycnals of the inclined frontal layer are also portrayed. The beams exhibit the following features:

i) Beam contraction occurs upon reflection from the sloping bottom.

ii) When downgoing and upgoing, the beams experience expansion and contraction, respectively, as they pass through the inclined frontal layer.

iii) From 30 kilometers to 10 kilometers offshore, the width of the beam bounded by solid lines expands by 60%, while that of the beam bounded by dashed lines contracts by 80%. The

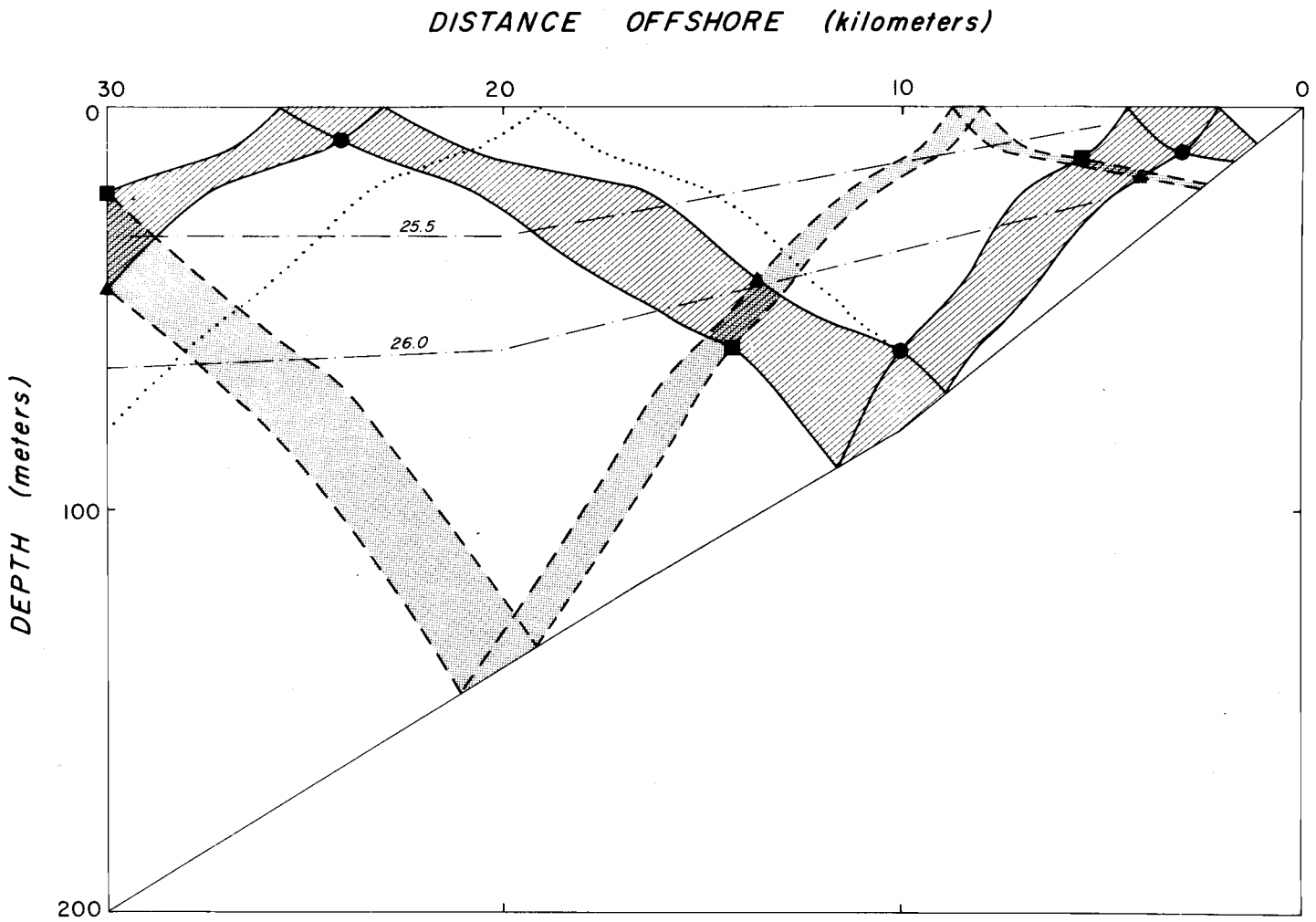

Figure 30. The field of characteristics for the semidiurnal internal tide over the continental shelf off Depoe Bay, Oregon. (Static stability varies with x and z and there is a frontal interaction.)

net effect is that the semidiurnal internal tide is expected to exhibit nearly uniform energy density over the sensor array.

iv) The beams tend to be deflected by the frontal layer.

v) Inshore of 10 kilometers offshore, the bottom slope is nearly critical.

vi) Points of common phase are shown on the figure. There is a 180 degree phase reversal between 30 and about 14 kilometers offshore and between about 14 and about 4 kilometers offshore. Hence, the effective wavelength between 30 and 10 kilometers offshore is about 26 kilometers.

A single characteristic for the case of no frontal interaction, but E a function of x and z, is shown by a dotted line terminating at DB5, 60 meters. This characteristic illustrates the fact that the frontal interaction does significantly modify the characteristics, consistent with the thesis of this dissertation.

The same values of $E(x, z)$ and $s(x, z)$ as used for Figure 30 were used in computing the more complete field of characteristics shown in Figure 31a. Figure 31b was determined from Figure 31a. Positions of the sensors which operated usefully long are shown in Figure 31. The realism of Figure 31 is limited by a lack of hydrographic data from near the bottom and inshore of 10 kilometers offshore. From Figure 31a, it can be seen that there is a concentration of characteristics, and thus energy associated with the seasonal

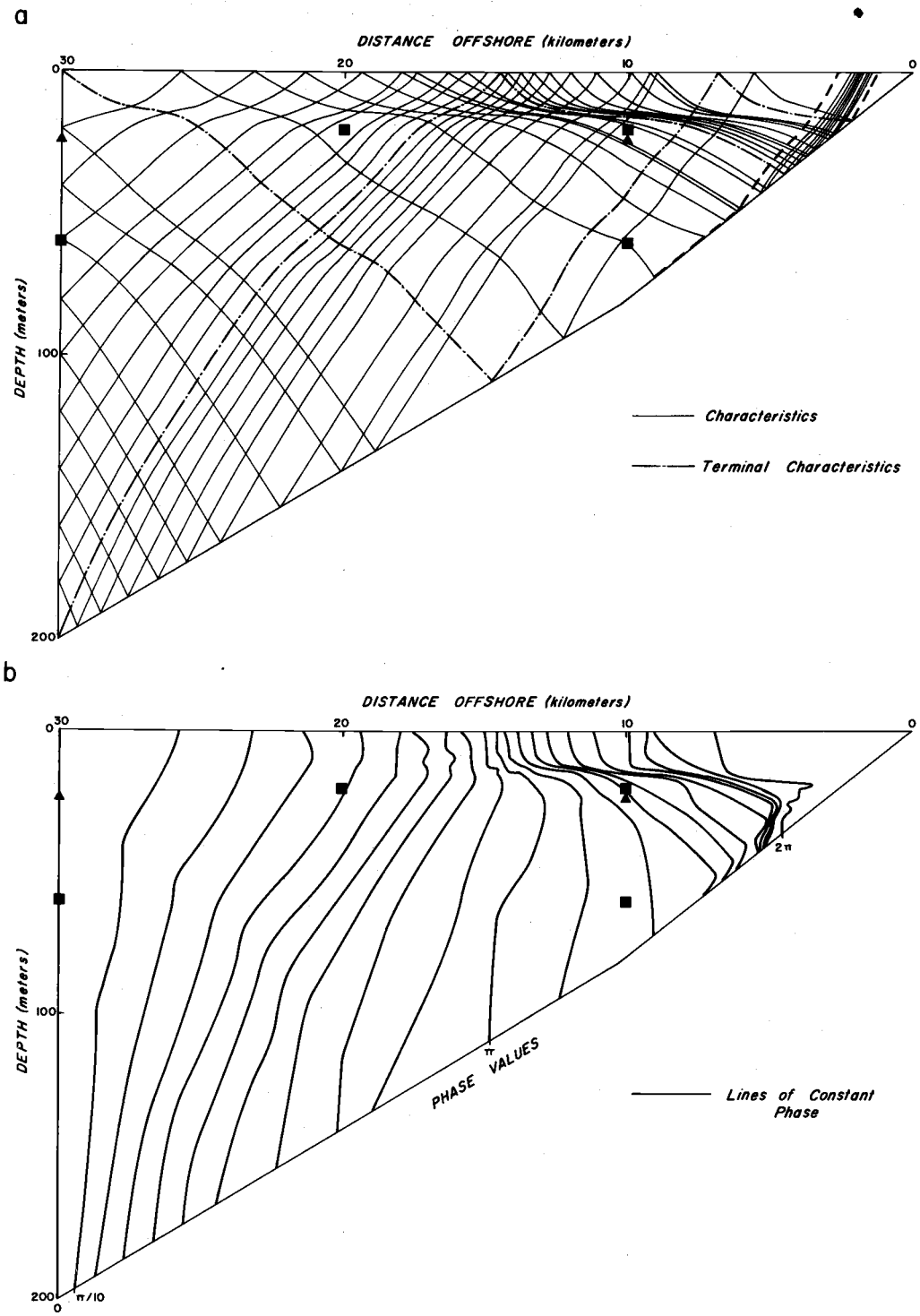

Figure 31. Characteristics for the semidiurnal internal tide over the continental shelf off Depoe Bay, Oregon.
a. Field of characteristics
b. Lines of constant phase

pycnocline and the surface front near the sensor site 10 kilometers offshore and at a depth of 20 meters. Again, the bottom slope is nearly critical inshore of 10 kilometers within the limits of the extrapolated hydrographic data. The lines of constant phase in Figure 31b are considerably distorted by the frontal zone. Figure 31b bears a resemblance to Figure 9; the differences between the two figures emphasizes the inadequacy of models with N^2 constant. For a progressive wave, phase differences between sensor sites can be obtained from Figure 31b.

In Figure 32, the theoretical horizontal phase speed versus frequency and the phase versus frequency functions are given for the Depoe Bay array. The simplest possible model has been assumed, i.e., a progressive wave onshore, uniform depth, constant N^2, and no frontal interaction. The curves are given for two representative values of N^2. The cases of DB15 versus DB5 and of DB10 versus DB are displayed. These curves are useful for comparison with the phase results obtained from cross spectrum analysis in the next chapter. They indicate that inertial-internal waves are essentially non-dispersive over the measurement band except near the inertial frequency, about 1.4 cpd.

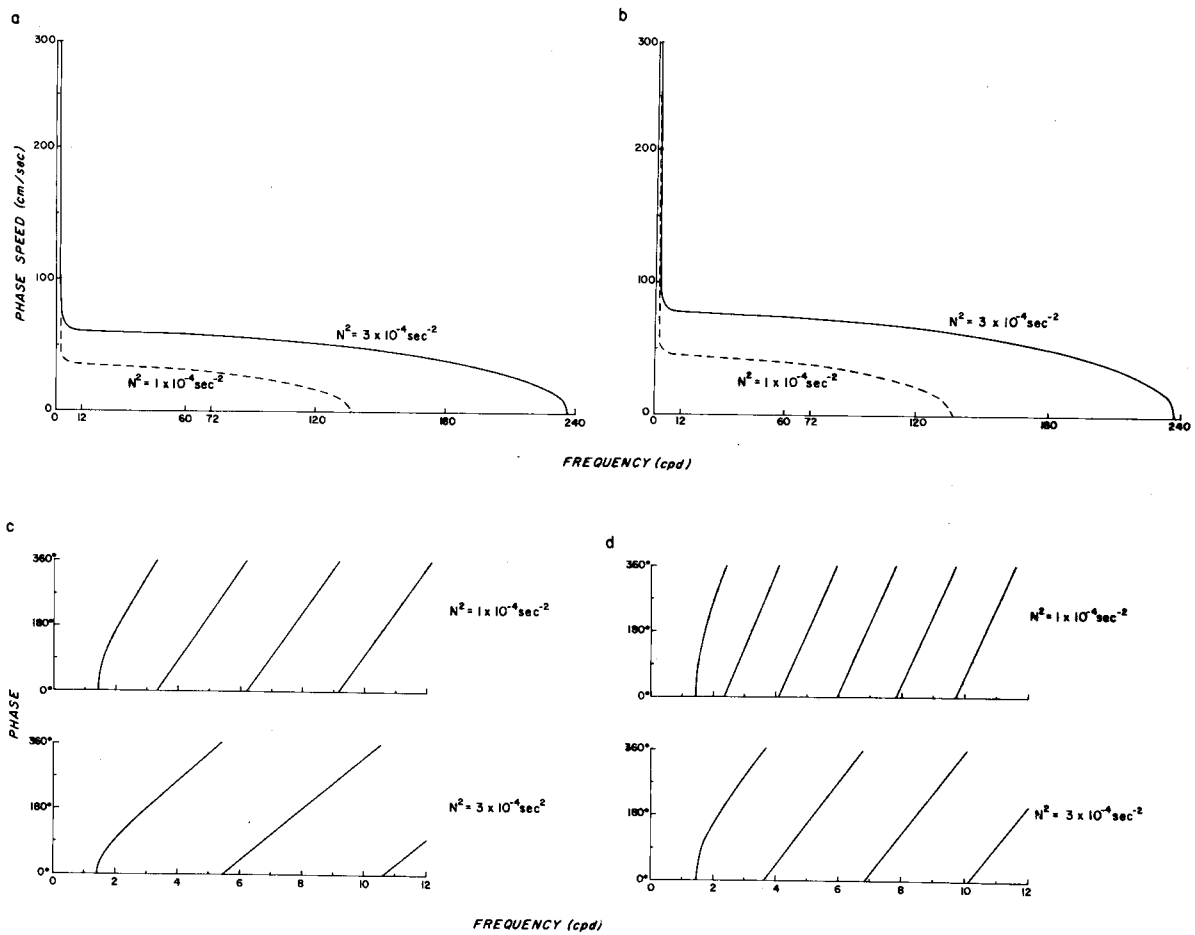

Figure 32. The theoretical horizontal phase speed versus frequency and the phase versus frequency functions for inertial-internal waves with constant coefficients and without frontal interaction.

a. Phase speed, DB15 to DB5
b. Phase speed, DB10 to DB5
c. Phase versus frequency function, DB15 vs DB5
d. Phase versus frequency function, DB10 vs DB5

XI. THE TIME SERIES ANALYSES OF THE OBSERVATIONS

A. Introduction

Four horizontal velocity, two temperature, and a sea level time series are analyzed. The resolvable, coherent tidal components have been removed from the original[24] series to produce residual series. Both the original and residual series are examined by spectrum analysis. The autospectra of the velocity and temperature time series are examined to determine the frequencies at which energy peaks occur and to characterize the spectra in general. The coherence squared, phase, and axis functions of velocity series observed at a single point are examined to identify coherent motion, the rotational sense of the hodograph, and the hodograph orientation, respectively. The coherence squared and phase functions of series observed at various spatial separations are examined to seek evidence for spatially coherent motions and to determine their direction and speed of propagation. The spectra of the difference series are used to make deductions about the presence of inertial-internal waves and the dynamic stability of the frontal zone.

---

[24] In this chapter, the expression original series is used for the hourly averages of the 10-minute samples.

B. The Time Series Analyses

A myriad of practical considerations arise when treating several time series with unequal record lengths. The most distressing concern is the necessity, due to cost and time considerations, to select from a host of options without full experimentation. Most of the options have been explored to a limited extent. The options available, and the rationale for the selection of those employed, are discussed. The practical limitations of the time series are also examined.

The data series were recorded continuously on photographic films in an analog format. The films advanced once every 10 minutes; thus, several discrete sets of analog records were created. Upon reduction, the films provided digital series, which determined the mode of the subsequent analyses. Each frame of the thermograph films was exposed throughout a 10-minute cycle, while those for the current meters were exposed for 9 minutes during each 10-minute cycle. The difference in recording intervals was due to the difference in film advance mechanisms; the difference in recording intervals was accounted for in data conversion. Additional details about the moored, recording meters, and their performance, can be found in Mooers et al. (1968).

The number of 10-minute samples per series range between

about 2100 and 5700. The series were numerically tapered[25] to separate them into low-passed (half-power point of about 40 hours), intermediate-passed (half-power points of about 6 and 40 hours), and high-passed (half-power point of about 6 hours) components (Mooers et al., 1968). The low-passed and high-passed records were examined in an exploratory fashion. The low-passed records contain large amplitude (~ 10 cm/sec) oscillations with periods of several days, but the record durations were insufficient to define their spectral structure. The high-passed records contain no large amplitude oscillations and very little spectral structure of interest other than at tidal harmonics and at what are probably frequencies of internal celluar waves. The intermediate-passed records could have been used for the analyses of the tidal frequencies; they have the advantage over hourly averages of having had low frequency trends removed. It was decided to use uniformly weighted hourly averages instead, which allows a broader band study than that which the analysis of intermediate-passed records permit. Because hourly averages were used, the original records were decimated by a factor of six. Since it was logistically impossible to install all of the sensors simultaneously, and since the majority of the sensors failed before their recovery, the time series have different start and stop times. For the

[25] A numerical taper is a weighted average applied in the time domain; its equivalent in the frequency domain is a digital filter.

maximum utilization of a time series, the entire time series is used in some analyses. For the comparison of records sampled at different spatial points or from different sensors at the same spatial point, it is necessary to use common record durations. In Table 4, the start and stop times, the common record durations, and the number of samples for the hourly averages are listed. Acceptable sea level data commenced at 1200// 8/24/66; 900 hourly values of this data were used only in the tidal analysis, which was referenced to the common start time of the other data series.

Timing errors are devastating for the calculation of spectra. The worst estimate of frame count uncertainty is four frames in 6000, which is twice the greatest clock error observed (Mooers et al., 1968). This error is equivalent to a one-half minute error during each semidiurnal cycle. Thus, timing errors are not likely to be significant in the time series of this study. An unequivocal statement can not be made because there is present the spectre of erratic film advance, which could give no apparent error in a long time series.

Excessive sensor string tilt would impair the performance of the current meters. In the worst case, only 14% of the 10-minute samples were recorded at a tilt in excess of 3°, corresponding to a horizontal displacement in excess of 3 meters (Mooers et al., 1968). Thus, sensor string tilt was well within the operating range of the current meters.

Table 4. Record durations (hourly averages).

Sensor	Sensor start time	Initial No. of samples	Common start time	No. of samples	Common end time	No. of samples	Common end time	No. of samples	Common end time	No. of samples	Common end time	Terminal No. of samples	Sensor end time	Total No. of samples
Common			1900// 8/15	339	2100// 8/29	482	2000// 9/4	568	1000// 9/8	865	1900// 9/20			
DB5, 20 meters														
Thermograph	1300// 8/15	6		+		+		+		+		67	1400// 9/23	938
Current meter	1300// 8/15	6		+		-		-		-		-	2100// 8/29	345
DB5, 60 meters														
Current meter	1300// 8/15	6		+		x		+		+		-	1900// 9/20	871
DB10, 20 meters														
Current meter	1500// 8/15	4		+		x		+		+		20	1500// 9/21	889
DB15, 20 meters														
Thermograph	1800// 8/15	1		+		+		-		-		-	0900// 9/8	568#
DB15, 60 meters														
Current meter	1900// 8/15	0		+		x		+		+		89	1200/ 9/24	954

The final 85 samples were rejected because the onset of erratic film advance was suspected.

+ Sensor operating and analysis performed for this record length.

- Sensor not operating.

x Sensor operating but no analysis performed for this record length.

The accuracy in vertical positioning of the sensors is estimated to be ±1 meter referenced to mean sea level (Mooers et al., 1968). It is possible for the moorings to drag along the bottom, and there are limitations to the accuracy in determining the geographic position of a mooring upon installation and recovery. The estimates of the navigational uncertainty and of the stability of a mooring's position yield a positional accuracy of ±0.5 Km (Mooers et al., 1968) or ±5% of the horizontal spacing of the array.

The standard concepts and techniques of variance and spectrum analyses (Blackman and Tukey, 1958; Bendat and Pierson, 1966; Granger, 1964; and Jenkins and Watts, 1968), have been the primary statistical tools used for analyzing the time series. The covariance function for time series $u(t)$ and $v(t)$ is $\text{Covar}_{uv}(\tau) = \overline{u(t)v(t+\tau)}^{t}$. Their cross spectrum is $\tilde{P}_{uv}(\sigma) = P_{uv} + iQ_{uv} = \text{F.T.}(\text{Covar}_{uv}(\tau))$, where F.T. represents Fourier transformation and P_{uv} and Q_{uv} are the co and quadrature spectra, respectively. A few experiments with fast Fourier transform (FFT) harmonic analysis (Cooley and Tukey, 1965) were carried out. Because the time series analyzed were of limited duration, no significant economic advantage accrued from the use of the FFT, and the use of the present form of FFT requires an undesirable shortening of already short records to make the number of samples equal to a power of 2. Because the spectra do not contain a few discrete lines widely separated in

frequency, no obvious scientific advantage accrued from the use of the FFT with high resolution. All series were not tested with the FFT, thus the possibility exists that the FFT could be profitably employed on some of the residual series, in particular. The velocity cross spectra sampled by a single sensor have been given a semi-principal axis transformation, Appendix III. The time series observed by different sensors have been treated as complex-valued series and the cross spectra of the complex-valued series computed, which maximizes the coherence squared for the clockwise and anti-clockwise rotating components separately, Appendix III.

The two basic hypotheses on which the theory of spectrum analysis is based are that

i) the time series are statistically stationary, and

ii) the time series are random variables.

Neither hypothesis is true in the case of this study; the first is false due primarily to the low frequency variations associated with several-day waves and modifications in the state of coastal upwelling, while the second is false due primarily to the presence of coherent waves in the series. The failure of these hypotheses is not crucial for the validity of spectrum analysis; it only degrades the ability to interpret the statistical significance of the results. The spectra are the accurate frequency domain representations of the time series. Confidence limits are based on the series being a finite representation of an

infinitely long, stationary Gaussian process, which is probably not true, thus confidence limits are used only as rules-of-thumb. (In the future, ensemble averages of spectra will be possible and confidence intervals can then be determined empirically.)

With the 10-minute samples, the Nyquist sampling frequency, f_N, is 72 cycles per day, or 72 cpd. With the hourly averages, f_N = 12 cpd. In the analysis of digital records, the danger of aliasing the spectra at frequencies less than f_N by spectral values from frequencies greater than f_N is always present. There are only two safeguards against aliasing:

i) To sample sufficiently rapidly to define all the frequencies whose amplitude of oscillation is either detectable by the sensors resolution and time response, or is significant with respect to the spectral levels at lower frequencies.

or

ii) To use a sensor whose time constant is sufficiently great to effectively damp-out all the oscillations whose frequency is greater than f_N.

To be certain that method i) applies, it is necessary to have sampled sufficiently often at a greater rate than the desired f_N to verify that f_N is sufficient. In the present case, the sensors did not permit sampling significantly faster than f_N and no rapid sampling sensors were available. Examination of the spectra does indicate that they decrease by several orders of mangitude as the frequency

increases from the band of tidal frequencies, about 1 to 2 cpd, to f_N. This argument does not rule out the possibility that aliasing is caused by large, discrete energy peaks at frequencies greater than f_N. For all practical purposes, method ii) does not apply to the current meters employed because they have a very rapid response, of the order of seconds. It does apply to the thermographs because they have an e-folding time response of 10 minutes, which leads to a half-power point at a frequency of about 100 cpd. The use of hourly averages, rather than simply hourly sub-samples, effectively filters the aliased spectrum in the frequency band between 24 cpd and 72 cpd for both the current meters and the thermographs. The equivalent filter has a zero at 24 cpd and its first side lobe occurs at about 36 cpd and yields a 95% reduction of the energy. The spectrum from 0 to 12 cpd is aliased by the spectrum from 12 to 24 cpd due to hourly averaging. The spectra have not been recolored for the effect of hourly averaging; thus, the spectra should be multiplied by a factor which ranges from about 1 at 6 cpd to about 2 at 12 cpd.

Disregarding the possible effects of high frequency surface waves, which were discounted in Section IX. C., the primary aliasing villain is expected to be the oscillations at the Väisälä-Brunt frequency, f_B. The alias f_A, at any frequency, f_n, is $f_A = 2nf_N \pm f_n$, n : integer; equivalently, either $f_n^+ = f_A - 2nf_N$ or $f_n^- = 2nf_N - f_A$. Assuming that the alias is due to Väisälä-Brunt

osciallations, i.e., $f_A = f_B$, then either $f_n^+ = f_B - 2nf_N$ or $f_n^- = 2nf_N - f_B$. From Figure 28, for the sensors at a depth of 20 meters, $288 \leq f_B \leq 480$ cpd, while for those at a depth of 60 meters, $48 \leq f_B \leq 240$ cpd. For the original series, since $f_N = 72$ cpd, then, where (*) connotes no alias,

n	f_n (cpd) at 20 meters	f_n (cpd) at 60 meters
1	$f_1^+ < 0$(*); $f_1^- > f_N$(*)	$f_1^+ < 0$(*); $0 \leq f_1^- \leq f_N$
2	$0 \leq f_2^+ \leq f_N$; $f_2^- \leq 0$(*)	$f_2^+ \leq 0$(*); $48 \leq f_2^- \leq 240$,

etc.

Thus, aliasing of the entire spectrum by f_B must be considered a possibility. For the present study, it is assumed that the aliasing is of no practical consequence. In defense of this assumption, it is remarked that the Väisälä-Brunt oscillations are vertical motions, while the thermographs, which are the only sensors capable of detecting vertical motions, effectively damp oscillations at frequencies greater than or equal to the minimum value for f_B at the thermograph sites. The question of aliasing by f_B, internal celluar waves, surface waves, or other high frequency motions is one which has yet to be put to explicit field test.

In digitizing an analog record, it is necessary to quantize a record which in Nature is presumably continuous. The quantizing operation introduces an error termed quantization (round-off) error

or noise. The quantization noise sets a lower bound, or threshold, on spectral levels which can be detected. An estimate of the quantization noise, $P_N(f)$, is made by assuming that the underlying process, $x(t)$, is uniformly distributed over the quantization interval, $\pm \frac{\Delta x}{2}$,* where Δx is the resolution of the read-out device. Then the mean quantization error, μ_x, is zero, while the mean square quantization error σ_x^2, equals

$$\sigma_x^2 = \frac{1}{\Delta x} \int_{-\frac{\Delta x}{2}}^{\frac{\Delta x}{2}} x^2 dx = \frac{(\Delta x)^2}{12}.$$

If an average over R values is made, then the quantization noise is

$$R\sigma_x^2 = \frac{\sigma_x^2}{R}.$$

Assuming that the quantization error is uniformly distributed over frequency, the estimate of the quantization noise level is then

$$P_R(f) = \frac{R\sigma_x^2}{2\pi f_N},$$

where f_N is the Nyquist sampling frequency.

For the temperature and velocity data, the following values are obtained with $R = 6$ and $f_N = 12$ cpd:

	Temperature	Velocity
Δx	0.2 C°	4 cm/sec
σ_x^2	$1/3 \times 10^{-2}(C°)^2$	$4/3\ (cm/sec)^2$
$R\sigma_x^2$	$1/18 \times 10^{-2}(C°)^2$	$2/9\ (cm/sec)^2$
P_R	$\approx 1 \times 10^{-5}(C°)^2/cpd$	$\approx 3 \times 10^{-3}(cm/sec)^2 cpd.$

The spectra of the observations generally approach a level an order of magnitude greater than the quantization noise level as the frequency increases to $f_N \approx 12$ cpd.

The frequency resolution of a spectrum and the statistical stability of a spectral estimate are competing phenomena. Because the time series are of unequal length, it is impossible to hold both the fundamental bandwidth, Δf, and the degrees of freedom, ν, constant. For convenience in the comparison of spectra, Δf has been held constant. Because the maximum number of lags, M, was chosen to be 72, then $\Delta f = \frac{f_N}{M} = 1/6$ cpd. Since the total number of samples, N, used ranged from 339 to 865, and since $\nu = \frac{2(N-M/3)}{M}$, then ν ranged from 9 to 23. Experiments have been performed to increase ν for the short records and to decrease Δf for the long records but no noteworthy changes occurred in the results. Ideally, it is desirable to center spectral estimates on frequencies with the largest energy peaks, e. g. the lunar semidiurnal (M_2) and the inertial (I) frequencies. Since the M_2 period and

the I period are about 12.5 and 17 hours, respectively, the minimum maximum lag time to center spectral estimates on both M_2 and I simultaneously, would have to be $T_M \approx 12.5 \times 17 \approx 212$ hours. For $\nu \simeq 10$, then a record duration of about 1060 hours would be necessary. The majority of the time series were not nearly that long so such a centering of spectral estimates was not possible. Much longer records are necessary for further resolution of the semidiurnal and dirunal tides. Many of the interpretations in the following sections are probably limited by the occurrence of many tidal lines in a measurement bandwidth. All indications are that the choice of $M = 72$ was as effective as any value for satisfying the conflicting objectives.

The mean was removed from each time series prior to covariance and spectrum calculations. The series were neither pre-whitened nor detrended prior to covariance and spectrum calculations. (Since the intermediate-passed series are essentially detrended, the objectives of the present study could have been accomplished by using the intermediate-passed series and recoloring their spectra. For the least squares tidal analysis, the detrended, intermediate-passed series might be preferable to the hourly-averaged series.) The spectrum estimates have been smoothed by the use of the hamming spectrum window for side lobe suppression. Thus, the effective bandwidth, $(\Delta f)_e$, of the spectra is $(\Delta f)_e \approx 1.3\ \Delta f \approx 0.2$ cpd.

For each spectrum displayed, the following items are indicated:

i) N, M, and ν.

ii) 90% confidence limits for autospectra and the 90% significance level for the coherence squared. The confidence limits for the phase function are not given because they are not well-understood.

iii) Physical units for spectral density, in either $(cm/sec)^2/cpd$ or $(C°)^2/cpd$.

iv) A -5/3-power law spectrum for comparison to the observed spectral continuum, though the spectra must be recolored.

v) The inertial frequency is identified by a vertical dashed line in the upper panel.

vi) The clockwise and anticlockwise sense of rotation is noted on each phase function by A for anticlockwise and C for clockwise.

vii) The spectra of the original series are shown by heavy, solid lines. The spectra of the residual series are shown by light lines at frequencies where there is a distinguishable difference between the residual and original series.

viii) The cohernece squared, phase, and axis functions are shown by dots or dotted lines for the semi-principal axis calculations. They are only shown for the coherence squared and phase functions when they can be distinguished from the

values for the original and residual series in geographic coordinates.

ix) In the complex spectra, the anticlockwise components are indicated by solid lines, while the clockwise components are indicated by dashed lines.

The frequency axis is in units of cycles per day (cpd), which facilitates comparison with the results of Collins (1968). The variance in a measurement bandwidth is given by $P(f) \cdot 2\pi\Delta f$. The sensor identification is given in each figure caption.

C. The Resolvable Coherent Tides

Least squares analysis has been used to determine the tidal constants for the resolvable diurnal, semidiurnal, and quarterdiurnal frequencies in each time series. The inertial frequency has also been fit to the residual series. This analysis determines the amplitude and temporal phase of the coherent[26] motion for each frequency fit to the time series. The resultant residual series are subsequently used to study the unresolvable and the incoherent motions by spectrum analysis. Inspection of the amplitude and phase relations permits deducing which tidal components are most significant and how the tidal

[26]The term coherent motion is used in the sense of amplitude-and-phase-stable motion, not in the sense of motion statistically correlated at different spatial positions. The amplitude and phase values for series of finite length are the effective stable values.

components compare at different spatial locations.

In Table 5, the resolvable tidal frequencies are tabulated and identified for each of the three common record durations. Rayleigh's criterion[27] was used for determining the resolvability. An adequate set of diurnal tides were resolvable, but only a limited number of semidiurnal tides could be resolved. Additional quarterdiurnal and higher frequency tides could have been resolved. The sequence of fit was largely based on the tidal analysis of current observations reported by Godin (1967). The choice of frequencies was also influenced by the manual authored by Schuremann (1941) and some preliminary tests. The amplitude and phase of the oscillations at the inertial frequency are usually found to be so time-varying that least squares analysis is ineffective (Webster, 1968a) for time series whose duration exceeds a few inertial cycles. For time series spanning only a few inertial cycles on the continental shelf off Oregon, Collins et al. (1968) were able to perform a tidal analysis for the inertial amplitude and phase. It was anticipated that it would be impossible to find coherent inertial oscillations in the present study, thus the inertial frequency was not included in the original list. Subsequently, it was found productive to fit the inertial frequency to the residual series,

[27] Rayleigh's criterion states that to resolve two frequencies, $f_1 > f_2$, the record duration must exceed $\frac{1}{(f_1 - f_2)}$.

Table 5. Resolvable tidal frequencies.

Tide name	Symbol	Speed (deg/hour)	Frequency (rad/hour)	Period (hours)	Record duration (hours) 339	568	865
Principal lunar semidiurnal	M2	28.9841	.505868	12.4206	1	1	1*
Principal solar semidiurnal	S2	30.0000	.523599	12.0000	-	2	2
Smaller lunar elliptic semidiurnal	L2	29.5285	.515370	12.1916	-	-	3
Larger lunar elliptic semidiurnal	N2	28.4397	.496367	12.6583	-	-	4
Variational Semidiurnal	$\mu 2$	27.9680	.488134	12.8718	-	-	5
Luni-solar diurnal	K1	15.0411	.262516	23.9345	2	3	6
Principal lunar diurnal	O1	13.9430	.243352	25.8193	3	4	7
Smaller lunar elliptic diurnal	NO1	14.4972	.253024	24.8324	-	-	8
Larger lunar elliptic diurnal	Q1	13.3987	.233851	26.8684	-	-	9
Smaller lunar elliptic diurnal	OO1	16.1391	.281681	22.3061	4	5	10
Smaller lunar elliptic diurnal	J1	15.5854	.272018	23.0985	-	-	11
Lunar quarterdiurnal	M4	57.9682	1.01174	6.2103	5	6	12
Luni-solar quarterdiurnal	MS4	58.9841	1.02947	6.1033	6	7	13
Solar quarterdiurnal	S4	60.0000	1.04720	6.0000	7	8	14
Inertial	I	21.3000	0.371755	16.9000			A1**
Inertial minus principal lunar semidiurnal	IMM	76.9000	1.342159	4.6814			A2
Inertial plus principal lunar semidiurnal	IMP	50.0000	0.872665	7.2000			A3
Solar terdiurnal	S3	45.0000	0.785399	8.0000			A4
Lunar terdiurnal	M3	41.8000	0.729548	8.6124			A5

* Numerical entries indicate the sequence of fit for the three categories of record duration; the symbol (-) indicates that the record duration is not sufficiently long to permit the resolution of the associated frequency.

** A1 through A5 were fit sequentially to the residual series after completion of the analysis for the tidal constants of the frequencies above the dashed line.

as well as two terdiurnal and the difference and summation frequencies of the inertial motion and the principal lunar semidiurnal tide.

The results from the tidal analysis are presented in Table 6. The tidal component at angular frequency, σ of a time series, $x(t)$ is represented by $x_\sigma(t) = cx \cdot \cos(\sigma t) + sx \cdot \sin(\sigma t)$, where cx and sx are amplitude factors. For the horizontal velocity series, the constants of the hodograph are given as well as the cosine and sine amplitudes of the velocity components of the motions. (A discussion of the terminology of the hodograph is given in Appendix III.) The tidal frequencies were fitted sequentially. At the Nth step, the variance of the residual was computed. Then the N+1st frequency was added to the least squares analysis of the original record, not the residual. Thus, the entry for the Nth frequency in the column labelled "RESX" gives the percent of the original variance remaining in the residual series after inclusion of the Nth frequency in the analysis. It does not represent the percent of the original variance accounted for by the Nth frequency in the final step of the analysis, i. e., when all frequencies are accounted for simultaneously. After the final step, the variance of the residual series is termed the incoherent variance; the difference between the original and the incoherent variance is termed the coherent variance. The system of equations resulting from the least squares calculation was solved by Gauss-Seidel iteration. The solution was iterated until

Table 6. Estimates of tidal constants.

Explanatory Notes:

The quantities which are used in this table are defined below:

U:	x component of the velocity
V:	y component of the velocity
T:	temperature
Z:	sea level
$\overline{U}$:	mean of U
$\overline{V}$:	mean of V
$\overline{T}$:	mean of T
$\overline{Z}$:	mean of Z
UVAR:	variance of U
VVAR:	variance of V
TVAR:	variance of T
ZVAR:	variance of Z
CU:	cosine amplitude of U
SU:	sine amplitude of U
CV:	cosine amplitude of V
SV:	sine amplitude of V
CT:	cosine amplitude of T
ST:	sine amplitude of T
CZ:	cosine amplitude of Z
SZ:	sine amplitude of Z
W1:	amplitude of the semi-major axis of the hodograph
W2:	amplitude of the semi-minor axis of the hodograph
θ1:	orientation of the semi-major axis measured anticlockwise from east
θ2:	orientation of the semi-minor axis measured anticlockwise from east
a:	temporal phase of the semi-major axis referenced to the common start time
ROT:	rotational sense of the hodograph; C is clockwise and A is anticlockwise
ϵ:	eccentricity
AT:	amplitude of T
θT:	phase of T
AZ:	amplitude of Z
θZ:	phase of Z
RESU:	percentage of the original variance in the residual series of U
RESV:	percentage of the original variance in the residual series of V
REST:	percentage of the original variance in the residual series of T
RESZ:	percentage of the original variance in the residual series of Z

When the five additional frequencies have been fit to the residual series, the quantities RESU, etc. represent the percentage of the residual variance in the new residual series.

All units are in the c.g.s. system; i.e., U and V are given in cm/sec, T is given in C^{o}, and Z is given in cm. The standard errors, s.e.'s, are given for tidal amplituddes, where

$$\text{s.e.} = \left(\frac{\text{Incoherent variance}}{\text{No. of samples}}\right)^{1/2}.$$

The s.e.'s are not given for the angular quantities among the tidal quantities. They are determined by dividing the s.e. for the amplitude by the amplitude itself; the result is in units of a fraction of a half-circle.

Table 6. (Continued)

Tide	CU	SU	CV	SV	RESU	RESV	W_1	θ_1	W_2	θ_2	a	ROT	ϵ
6a. (Site: DB5; Depth: 20 meters; Variable: Horizontal Velocity)													
No. of Samples: 339; $\bar{U}$ = -2.2, UVAR = 117.5; $\bar{V}$ = -17.9, VVAR = 132.5													
M2	-0.7	4.9	0.5	2.7	89.8	97.1	5.6	28	0.7	298	94	C	0.77
K1	-0.7	-.05	3.2	-0.3	89.4	92.9	3.3	282	0.5	12	177	A	0.74
O1	-1.7	-1.3	1.7	2.4	87.5	89.7	3.6	126	0.5	36	48	C	0.74
OO1	1.0	-0.3	-0.3	0.1	87.0	89.6	1.1	161	0.0	251	163	A	0.94
M4	-1.0	-0.3	0.1	0.8	86.6	89.4	1.1	154.	0.7	64	33	C	0.23
MS4	0.1	-1.4	0.0	-0.3	85.7	89.4	1.5	193	0.0	283	95	A	0.99
S4	0.4	0.4	0.8	0.1	85.5	89.1	1.0	58	0.2	328	18	C	0.58
			U	V			U	V					
Incoherent variance			100.5	118.1		s.e.	0.5	0.6					
Coherent variance			17.0	14.4									
6b. (Site: DB5; Depth: 60 meters; Variable: Horizontal Velocity)													
No. of Samples: 339; $\bar{U}$ = 2.8, UVAR = 31.5; $\bar{V}$ = 0.7, VVAR = 86.2													
M2	2.2	-1.1	-3.1	0.2	90.3	94.5	3.9	128	0.8	38	168	C	0.65
K1	0.5	0.1	2.2	-1.1	89.9	90.7	2.5	261	0.3	171	154	C	0.80
O1	0.3	-0.4	2.0	1.0	89.4	87.9	2.2	86	0.5	176	26	A	0.62
OO1	0.2	-0.0	-0.2	-0.2	89.4	87.9	0.3	296	0.1	206	27	C	0.42
M4	0.3	-0.1	0.1	-0.2	89.2	87.8	0.4	222	0.2	132	144	C	0.44
MS4	-0.4	0.3	-0.0	-0.1	88.8	87.8	0.5	349	0.1	79	135	A	0.67
S4	0.2	-0.1	-0.3	-0.1	88.7	87.8	0.4	313	0.2	223	3	C	0.39
			U	V			U	V					
Incoherent variance			27.9	75.8		s.e.	0.3	0.5					
Coherent variance			3.6	10.4									
No. of Samples: 568; $\bar{U}$ = 2.4, UVAR = 44.0; $\bar{V}$ = 0.5, VVAR = 126.7													
M2	4.0	-0.9	-3.4	-0.8	77.9	95.9	5.2	140	1.2	50	178	C	0.63
S2	-0.9	1.8	-0.5	1.1	73.5	95.2	2.4	32	0.0	302	115	C	0.96
K1	0.1	-0.0	2.0	-0.4	73.5	93.8	2.0	268	0.0	358	167	A	0.97
O1	0.4	-0.4	1.3	0.3	73.1	93.1	1.4	74	0.5	164	6	A	0.46
OO1	0.1	-0.4	-0.5	0.2	72.9	93.0	0.6	126	0.4	36	139	C	0.28
M4	0.1	-0.6	0.2	0.1	72.5	93.0	0.6	174	0.2	264	99	A	0.52
MS4	-0.1	0.2	-0.1	-0.2	72.4	93.0	0.2	314	0.1	44	91	A	0.47
S4	0.4	-0.0	-0.4	-0.1	72.2	92.9	0.6	315	0.1	225	5	C	0.74
			U	V			U	V					
Incoherent variance			31.8	117.8		s.e.	0.2	0.4					
Coherent variance			12.2	8.9									

Tabel 6. (Continued)

Tide	CU	SU	CV	SV	RESU	RESV	W_1	θ_1	W_2	θ_2	a	ROT	ϵ
No. of Samples: 865; $\bar{U}$ = 2.7, UVAR = 39.8; $\bar{V}$ = 5.1, VVAR = 157.3													
M2	3.9	-1.8	-3.7	-0.2	79.7	95.7	5.5	140	1.4	50	167	C	0.60
S2	-0.6	2.0	-0.3	0.9	75.1	95.4	2.3	23	0.0	113	108	A	1.0
L2	-0.7	-1.2	-0.7	1.1	72.4	94.8	1.6	142	1.0	52	84	C	0.23
N2	-1.6	0.8	0.7	1.3	68.8	94.1	1.8	352	1.5	262	160	C	0.08
μ2	0.1	-0.3	-0.1	0.2	68.6	94.1	0.4	145	0.0	55	117	C	0.84
K1	-0.2	0.0	2.4	-0.2	68.6	92.7	2.4	274	0.0	184	175	C	1.0
O1	0.3	-0.4	1.4	0.8	68.4	91.7	1.6	85	0.5	175	28	A	0.54
NO1	0.1	-0.2	-0.3	0.2	68.3	91.7	0.4	121	0.0	31	133	C	0.75
Q1	0.2	0.3	0.5	-0.3	68.2	91.6	0.6	271	0.3	181	148	C	0.34
OO1	-0.0	-0.4	-0.3	-0.2	68.0	91.5	0.5	229	0.2	139	54	C	0.35
J1	0.2	0.1	0.2	-0.5	68.0	91.4	0.6	275	0.2	185	106	C	0.42
M4	0.2	-0.3	0.1	0.0	67.8	91.4	0.4	186	0.1	276	219	A	0.64
MS4	0.3	0.2	-0.1	-0.2	67.7	91.4	0.4	331	0.1	241	41	C	0.45
S4	0.4	-0.1	-0.3	0.0	67.5	91.4	0.5	147	0.0	57	167	C	0.82
			U	V			U	V					
Incoherent variance			26.9	143.7		s.e.	0.2	0.4					
Coherent variance			12.9	13.6									
I	-0.6	-0.6	-0.6	0.7	98.7	99.7	0.9	107	0.8	17	115	C	0.07
IMM	-0.1	0.2	0.1	0.2	98.6	99.7	0.3	35	0.1	305	93	C	0.59
IMP	-0.1	-0.1	0.1	0.2	98.6	99.7	0.2	125	0.1	35	45	C	0.57
S3	-0.1	0.2	-0.2	0.3	98.5	99.6	0.4	62	0.0	152	121	A	0.85
M3	-0.3	-0.2	-0.2	-0.3	98.3	99.6	0.5	227	0.0	317	44	A	0.88

6c. (Site: DB10; Depth; 20 meters; Variable: Horizontal Velocity)

No. of Samples: 339; $\bar{U}$ = 4.5, UVAR = 109.3; $\bar{V}$ = -12.1, VVAR = 74.1													
M2	8.7	-1.2	-2.6	-2.7	65.0	90.7	9.0	164	3.0	74	177	C	0.51
K1	-2.0	1.0	2.3	0.0	62.8	86.9	3.1	314	0.8	224	167	C	0.61
O1	-1.1	1.1	1.5	0.6	61.8	85.0	1.9	312	1.3	222	170	C	0.20
OO1	1.8	1.0	1.3	-0.0	59.9	83.9	2.3	30	0.6	300	21	C	0.61
M4	0.8	1.0	0.9	-1.1	59.1	82.4	1.6	299	1.2	209	106	C	0.13
MS4	1.0	-0.6	-0.4	0.6	58.5	82.0	1.3	148	0.2	238	143	A	0.72
S4	-0.3	0.5	0.5	-0.8	58.4	81.5	1.1	302	0.0	32	124	A	0.97
			U	V			U	V					
Incoherent variance			63.8	60.3		s.e.	0.4	0.4					
Coherent variance			45.5	13.8									

Table 6. (Continued)

Tide	CU	SU	CV	SV	RESU	RESV	W_1	θ_1	W_2	θ_2	a	ROT	ϵ
			No. of Samples: 568; $\overline{U}$ = 1.3, UVAR = 106.3; $\overline{V}$ = -13.1, VVAR = 63.1										
M2	7.5	-0.8	-3.0	-2.6	70.1	89.8	8.1	338	2.7	248	1	C	0.50
S2	-2.8	1.4	-0.5	2.7	65.5	84.0	3.7	38	1.8	308	132	C	0.35
K1	-1.1	1.0	1.8	-0.1	64.7	81.8	2.2	308	0.8	218	162	C	0.50
O1	-0.4	0.7	1.4	0.0	64.5	80.0	1.5	291	0.7	201	171	C	0.37
OO1	1.1	1.2	1.0	0.4	63.3	79.0	2.0	33	0.4	303	40	C	0.68
M4	-0.3	0.8	0.9	-0.6	62.9	78.0	1.3	307	0.5	217	133	C	0.48
MS4	0.7	-0.6	-0.3	0.3	62.6	77.8	1.0	154	0.0	244	137	A	0.92
S4	-0.7	-0.2	0.3	-0.2	62.4	77.8	0.8	160	0.2	250	7	A	0.54
			U	V			U	V					
Incoherent variance			66.3	49.0		s. e.	0.3	0.3					
Coherent variance			40.0	14.1									
			No. of Samples: 865; $\overline{U}$ = -0.7, UVAR = 108.7; $\overline{V}$ = -13.5, VVAR = 67.6										
M2	7.7	-0.4	-3.6	-2.7	69.2	86.4	8.5	334	2.7	244	.6	C	0.52
S2	-1.2	1.1	-1.0	1.8	68.1	83.4	2.6	52	0.4	322	127	C	0.73
L2	1.8	0.6	0.1	-0.6	66.4	83.2	1.9	356	0.6	266	20	C	0.51
N2	-0.2	-0.7	0.5	1.0	66.2	82.3	1.3	121	0.1	211	64	A	0.82
μ2	-1.0	0.1	-0.2	-0.0	65.7	82.2	1.0	12	0.0	102	174	A	0.92
K1	-0.7	0.9	1.9	-0.5	65.3	79.7	2.2	295	0.6	205	157	C	0.56
O1	-0.4	0.7	1.8	0.0	64.9	77.0	1.9	285	0.7	195	175	C	0.46
NO1	-0.1	-0.0	0.3	-0.5	64.9	76.9	0.6	271	0.1	1	120	A	0.73
Q1	-0.5	0.9	1.2	0.2	64.5	75.9	1.4	301	0.8	211	166	C	0.23
OO1	0.8	1.1	0.6	0.1	63.7	75.6	1.4	20	0.4	290	48	C	0.53
J1	-0.2	-0.7	-0.6	-0.4	63.5	75.3	0.9	224	0.3	134	53	C	0.45
M4	0.3	0.7	0.4	-0.8	63.3	74.8	1.1	309	0.4	219	96	C	0.42
MS4	0.7	-0.6	-0.5	0.3	62.9	74.5	1.1	148	0.1	58	145	C	0.86
S4	-0.6	-0.1	0.1	-0.0	62.8	74.5	0.6	172	0.0	262	9	A	0.85
			U	V			U	V					
Incoherent variance			68.2	50.3		s. e.	0.3	0.2					
Coherent variance			40.5	17.3									
I	0.0	0.4	0.1	-0.3	99.8	99.9	0.5	329	0.1	239	92	C	0.70
IMM	-0.4	0.2	-0.0	0.1	99.7	99.9	0.4	7	0.1	277	153	C	0.67
IMP	0.4	0.0	0.1	-0.8	99.6	99.3	0.8	272	0.4	182	94	C	0.33
S3	0.5	-0.1	-0.0	0.1	99.4	99.3	0.5	175	0.1	265	166	A	0.59
M3	-0.0	-0.3	0.2	-0.1	99.4	99.2	0.3	195	0.2	285	95	A	0.20

Table 6. (Continued)

Tide	CU	SU	CV	SV	RESU	RESV	W_1	θ_1	W_2	θ_2	a	ROT	ϵ
6d. (Site: DB15; Depth: 60 meters; Variable: Horizontal Velocity)													
			No. of Samples: 339; $\bar{U}$ = 5.9, UVAR = 35.2; $\bar{V}$ = 7.8, VVAR = 44.0										
M2	0.9	-1.2	1.7	-0.3	99.1	97.7	2.1	230	0.8	320	154	A	0.44
K1	-1.1	0.8	-1.4	0.7	97.2	96.0	2.0	49	0.2	139	150	A	0.86
O1	-0.6	0.9	0.6	1.3	95.9	93.6	1.6	59	0.8	329	85	C	0.31
OO1	0.4	-0.6	-0.6	0.2	95.6	93.4	0.9	139	0.3	49	141	C	0.46
M4	-0.9	-0.1	-0.1	0.4	97.5	93.8	0.9	184	0.4	94	6	C	0.37
MS4	0.1	-0.0	0.6	-0.3	97.5	94.7	0.7	263	0.0	173	151	C	1.00
S4	-0.0	0.5	0.5	0.1	98.2	95.4	0.5	68	0.5	338	26	C	0.05
			U	V		U	V						
Incoherent variance			34.6	41.9	s.e.	0.3	0.4						
Coherent variance			0.6	2.1									
			No. of Samples: 568; $\bar{U}$ = 5.6, UVAR = 33.8; $\bar{V}$ = 4.8, VVAR = 55.7										
M2	1.3	-0.0	0.8	1.3	97.4	97.8	1.7	54	1.0	144	36	A	0.28
S2	0.5	0.3	-0.3	0.5	96.9	97.5	0.6	348	0.6	78	20	A	0.01
K1	-0.8	0.1	-0.5	-0.1	95.9	97.3	0.9	209	0.2	299	0	A	0.72
O1	-0.7	-0.2	-0.3	0.5	95.0	97.0	0.8	33	0.5	303	167	C	0.26
OO1	0.3	-0.4	-0.3	0.7	94.6	96.5	0.9	124	0.1	214	118	A	0.74
M4	0.6	-0.6	-0.4	-0.6	93.7	96.1	0.9	218	0.6	128	104	C	0.15
MS4	0.3	-0.6	0.0	0.1	93.6	06.1	0.3	179	0.1	269	170	A	0.61
S4	0.6	-0.2	-0.2	0.5	93.1	95.8	0.6	52	0.5	322	144	C	0.10
			U	V		U	V						
Incoherent variance			31.5	53.4	s.e.	0.2	0.3						
Coherent variance			2.3	2.3									
			No. of Samples: 865; $\bar{U}$ = 4.8, UVAR = 45.5; $\bar{V}$ = 3.8, VVAR = 63.2										
M2	1.1	0.1	1.0	0.6	98.5	98.4	1.6	45	0.4	135	19	A	0.57
S2	0.6	0.0	0.2	0.8	98.1	97.7	0.9	62	0.6	152	54	A	0.22
L2	-0.3	0.0	1.0	1.0	98.0	96.3	1.4	99	0.2	9	45	C	0.70
N2	0.3	-0.7	-0.3	0.2	97.5	96.2	0.8	155	0.2	65	122	C	0.65
μ2	0.3	0.8	0.3	-0.2	96.8	96.1	0.8	352	0.3	262	69	C	0.44
K1	-0.9	0.4	0.1	-0.4	95.5	96.0	1.0	340	0.3	70	150	A	0.50
O1	-0.8	-0.3	-0.2	-0.1	94.8	96.0	0.8	195	0.1	285	22	A	0.85
NO1	-0.2	0.8	-0.3	0.6	94.1	95.6	1.0	40	0.1	130	111	A	0.78
Q1	0.0	0.9	0.3	0.0	93.2	95.5	1.0	0	0.3	270	89	C	0.54
OO1	0.2	-0.3	-0.1	0.8	93.0	95.1	0.9	111	0.2	201	101	A	0.65
J1	-0.1	0.2	-0.5	-0.2	93.0	95.0	0.5	253	0.2	343	4	A	0.46
M4	-0.1	-0.5	-0.4	-0.0	92.7	94.8	0.5	214	0.4	124	53	C	0.11
MS4	0.2	0.2	0.0	0.2	92.6	94.8	0.4	35	0.1	125	50	A	0.46
			U	V		U	V						
Incoherent variance			42.1	59.5	s.e.	0.2	0.3						
Coherent variance			3.4	3.3									

Table 6. (Continued)

Tide	CU	SU	CV	SV	RESU	RESV	W_1	θ_1	W_2	θ_2	a	ROT	ϵ
I	1.2	-1.2	-2.0	-3.0	96.5	90.8	3.3	265	1.7	175	56	C	0.32
IMM	-0.2	0.1	-0.0	0.1	96.5	90.8	0.2	20	0.1	290	150	C	0.34
IMP	-0.1	-0.3	-0.6	0.6	96.3	90.2	0.9	102	0.3	12	128	C	0.49
S3	0.4	0.2	0.2	-0.6	96.1	89.8	0.6	269	0.4	179	114	C	0.16
M3	0.1	-0.3	-0.4	-0.4	96.0	89.6	0.6	245	0.3	155	58	C	0.38

6e. (Site: DB 5 ; Depth: 20-60 meters; Variable: Horizontal Velocity Difference)

No. of Samples: 339; $\overline{\Delta U}$ = -5.0, ΔUVAR = 171.5; $\overline{\Delta V}$ = -18.6, ΔVVAR = 116.2

M2	-2.8	6.0	3.6	2.5	87.1	91.6	6.7	10	4.3	280	109	C	0.22
K1	-1.2	-0.5	1.0	0.9	86.5	90.8	1.8	135	0.3	45	32	C	0.74
O1	-2.1	-0.9	-0.3	1.4	85.1	89.9	2.3	168	1.4	78	30	C	0.25
OO1	0.8	-0.2	-0.1	0.3	84.9	89.9	0.9	166	0.3	256	159	A	0.53
M4	-1.3	-0.2	-0.1	1.0	84.4	89.4	1.3	171	1.0	81	16	C	0.12
MS4	0.5	-1.8	0.0	-0.2	83.4	89.4	1.8	186	0.0	96	105	C	0.99
S4	0.2	0.5	1.1	0.2	83.3	88.9	1.1	75	0.4	345	18	C	0.48

	ΔU	ΔV		$\frac{\Delta U}{0.6}$	$\frac{\Delta V}{0.6}$
Incoherent variance	142.9	103.3	s. e.		
Coherent variance	28.6	12.9			

I	0.6	2.0	1.5	0.4	98.6	98.8	2.3	32	1.2	302	55	C	0.32
IMM	0.7	-0.2	-0.1	0.2	98.3	98.8	0.7	164	0.1	254	159	A	0.68
IMP	1.2	-0.4	-1.1	-0.6	97.8	98.0	1.6	315	0.7	255	6	C	0.37
S3	-0.9	0.3	-0.0	0.4	97.6	98.0	1.0	10	0.3	280	158	C	0.50
M3	0.9	-0.6	0.0	-0.9	97.1	97.5	1.2	218	0.6	128	123	C	0.35

Tide	CT	ST	REST	AT	θT

6f. (Site:DB5; Depth: 20 meters; Variable: Temperature)

No. of Samples: 339; $\overline{T}$ = 8.44, TVAR = 0.32

M2	0.10	0.20	91.9	0.23	63
K1	0.01	0.00	91.8	0.01	21
O1	0.03	0.07	90.9	0.08	71
OO1	0.04	0.05	90.3	0.06	53
M4	0.07	-0.10	88.1	0.12	306
MS4	0.02	-0.07	87.4	0.07	284
S4	-0.02	-0.02	87.3	0.03	217

	T		T
Incoherent variance	0.28	s. e.	0.03
Coherent variance	0.04		

Table 6. (Continued)

Tide	CT	ST	REST	AT	θT
	No. of Samples: 482; $\overline{T}$ = 8.34, TVAR = 0.40				
M2	0.03	0.23	95.3	0.23	82
S2	0.19	-0.04	90.8	0.19	347
K1	-0.00	0.02	90.8	0.02	96
O1	0.02	0.03	90.7	0.03	61
OO1	0.02	0.00	90.6	0.02	3
M4	0.08	-0.06	89.5	0.10	323
MS4	0.01	-0.04	89.3	0.04	279
S4	-0.02	-0.02	89.2	0.03	217
	T	T			
Incoherent variance	0.36	s.e. 0.03			
Coherent variance	0.04				
	No. of Samples: 568; $\overline{T}$ = 8.24, TVAR = 0.41				
M2	0.04	0.20	96.5	0.20	77
S2	0.17	-0.02	93.2	0.17	352
K1	0.01	0.02	93.1	0.02	62
O1	0.01	0.03	93.0	0.03	77
OO1	0.02	-0.01	93.0	0.03	345
J4	0.07	-0.04	92.3	0.08	327
MS4	0.02	-0.05	92.0	0.06	286
S4	-0.02	-0.01	92.0	0.03	206
	T	T			
Incoherent variance	0.38	s.e. 0.03			
Coherent variance	0.03				
	No. of Samples: 865; $\overline{T}$ = 8.71, TVAR = 1.10				
M2	-0.00	0.25	96.8	0.25	90
S2	0.08	0.07	96.3	0.11	41
L2	-0.15	0.02	95.4	0.15	171
N2	0.05	-0.07	95.1	0.09	306
μ2	0.01	0.08	94.8	0.08	84
K1	-0.02	0.04	94.7	0.04	118
O1	-0.01	-0.04	94.7	0.04	260
NO1	-0.04	0.02	94.6	0.04	160
Q1	-0.01	-0.00	94.6	0.01	214
OO1	0.04	-0.01	94.6	0.04	343
J1	0.02	0.01	94.5	0.02	30
M4	0.02	-0.05	94.4	0.05	290
MS4	-0.03	-0.04	94.4	0.04	233
S4	0.00	0.03	94.3	0.03	90
	T	T			
Incoherent variance	1.04	s.e. 0.03			
Coherent variance	0.06				
I	-0.05	-0.04	99.8	0.06	216
IMM	-0.00	0.02	99.8	0.02	100
IMP	-0.03	-0.02	99.7	0.04	217
S3	-0.02	0.01	99.7	0.02	156
M3	-0.01	0.04	99.7	0.04	112

Table 6. (Continued)

Tide	CT	ST	REST	AT	θT
6g. (Site: DB15; Depth: 60 meters; Variable: Temperature)					
	No. of Samples: 339; $\bar{T}$ = 10.19, TVAR = 1.38				
M2	0.42	-0.24	91.6	0.49	330
K1	-0.24	0.02	89.4	0.24	176
O1	-0.04	-0.26	86.9	0.27	262
OO1	-0.10	0.10	86.1	0.14	134
M4	-0.18	-0.04	85.0	0.18	193
MS4	-0.05	0.15	84.0	0.16	109
S4	-0.04	-0.03	83.9	0.05	216
	T		T		
Incoherent variance	1.15	s.e.	0.03		
Coherent variance	0.23				
	No. of Samples: 482; $\bar{T}$ = 10.73; TVAR = 2.36				
M2	0.61	-0.25	90.3	0.66	338
S2	-0.03	0.14	89.9	0.14	102
K1	-0.21	-0.02	89.6	0.21	186
O1	-0.10	-0.20	88.6	0.22	244
OO1	-0.14	0.20	87.5	0.24	124
M4	-0.18	-0.08	86.8	0.19	204
MS4	-0.02	0.08	86.7	0.08	101
S4	0.06	-0.02	86.6	0.06	346
	T		T		
Incoherent variance	2.05	s.e.	0.03		
Coherent variance	0.31				

Tide	CZ	SZ	RESZ	AZ	θZ
6h. (Site: Newport, Oregon; Variable: Sea Level)					
	No. of Samples: 900; $\bar{Z}$ = 270, ZVAR = 5080				
M2	-69.6	45.1	36.4	82.9	147
S2	-28.7	- 2.6	27.9	28.9	185
L1	1.2	5.9	27.4	6.0	78
N2	- 0.1	18.9	24.1	18.9	90
μ2	1.8	1.8	24.1	2.5	45
K1	32.2	-11.1	12.3	34.0	341
O1	22.1	20.5	4.0	30.1	43
NO1	0.2	- 1.4	4.0	1.5	279
Q1	7.2	0.1	3.5	7.2	1
OO1	1.5	1.2	3.5	1.9	38
J1	3.4	- 1.5	3.4	3.8	336
M4	0.1	0.2	3.4	0.2	53

Table 6. (Continued)

Tide	CZ	SZ	RESZ	AZ	θZ
MS4	0.9	0.6	3.3	1.1	34
S4	- 0.1	0.5	3.3	0.5	102
	Z		Z		
Incoherent variance	170	s.e.	0.4		
Coherent variance	4910				
I	- 0.3	- 0.5	99.9	0.6	240
IMM	- 0.1	- 0.2	99.9	0.2	235
IMP	- 0.3	- 0.4	99.8	0.5	226
S3	0.2	0.9	99.5	1.0	77
M3	0.0	0.3	99.5	0.3	87

all cosine and sine amplitudes differed by no more than 0.5% from the preceding iterate. Three to six iterations were required. The number of significant figures tabulated for each tidal constant is consistent with the standard error based on the residual variance. The first frequency fit was the M2; the values for its constants varied as much as 50% from the first to the last step in the sequential fit for the sensor at a depth of 60 meters, 30 kilometers offshore.

The most significant features of Table 6 are summarized below:

i) The coherent variance ranged from 2 to 37% of the original variance. In one case, DB15, 60 meters, 339 samples, the incoherent variance increased in the last few steps, so the estimates of tidal constants at the high frequencies are unstable in that case.

ii) Without exception, the M2 component accounted for more of the variance than any other component, ranging from about 1 to 14% of the original variance.

iii) The inertial frequency was generally the second largest component of the variance. In addition, K1, O1, and S2 were generally large components.

iii) There was appreciable variability in the tidal constants estimated for different spatial points and for different record lengths at a single point. The variability was most marked at DB15, 60 meters, even for the M2 component.

Not all of the information in Table 6 is discussed in detail. For the present study, the M2 tide and I, the inertial frequency, are analyzed in detail. The M2 tide had the following properties:

i) At DB5, the hodograph was oriented nearly parallel to the bottom contours at a depth of 20 meters and nearly normal to them at a depth of 60 meters. The two hodographs were about equal in size but were nearly in-quadrature temporally. The coherent vertical shear vector had a maximum amplitude of 1.7×10^{-3} sec^{-1}, which is a factor of 3 less than the mean shear. The temperature oscillation at 20 meters was about 30° out-of-phase temporally with the adjacent hodograph.

ii) At DB10, 20 meters, the size of the hodograph was not highly variable for the different record lengths, though its orientation and phase changed. The hodograph was about five times the size of those at DB5, and was oriented normal to the bottom contours. For the common record length, it led the hodograph at DB5, 20 meters by 83°, consistent with onshore propagation and nearly a quarter-wavelength separation.

iii) At DB15, the temperature at a depth of 20 meters led that at DB5, 20 meters by 263°, which is consistent with onshore propagation and about a 3/4-wavelength separation. The

size of the hodograph at a depth of 60 meters was about half the size of that at DB5, 60 meters. It was the only hodograph which rotated anticlockwise. Disregarding the shortest common record, the two 60 meter hodographs were about 215° out-of-phase; the hodograph at DB15 assumed its largest value first, consistent with onshore propagation and about 7/12-wavelength separation.

In summary, the M2 hodographs were not of uniform amplitude, orientation, temporal phase, or rotational sense at the sensor sites. The temporal phase differences between sensor sites were consistent with the phase differences predicted in Figure 31 for an internal tide propagating shoreward. The spatial and temporal non-uniformity of the coherent M2 tide was consistent with the occurrence of a phase-unstable internal tide.

The estimates of the I component of the motion were obtained for all the long records, i. e., those in excess of five weeks duration. I was statistically significant in all the records. All hodographs rotated clockwise. The largest amplitude for I was found at DB15, 60 meters, where the hodograph was oriented nearly parallel with the bottom contours, the semi-major axis was 3. 3 cm/sec, while at DB10, 20 meters I had an amplitude of 0. 5 cm/sec. I was also significant in the sea level record and the temperature record at DB5, 20 meters. The sea level oscillation

had an amplitude of 0.6 cm, and was virtually in-phase with the hodograph at DB15, 60 meters. These results are consistent with the theory for topographically trapped waves along a coastal barrier, see Appendix I. I also had a significant, coherent shear at DB5; its value was about 0.6×10^{-3} sec^{-1}, i.e., about 1/3 of the value for the M2 shear.

D. The Temperature Spectra and Their Correlation Between Two Spatial Points

The autospectra and coherence squared phase functions for the temperature series are shown in Figure 33. The principal features of the autospectra are summarized:

i) The two spectra had similar shapes, but the spectrum sampled at DB15 had higher values than those of the one sampled at DB5. From Table 2, the variance at DB15, 20 meters was twice that at DB5, 20 meters. This difference is consistent with the fact that, though the vertical temperature gradients at both sensors were essentially equal at the beginning and at the end of the sample period, the gradients were observed to differ by a factor of three in the middle of the period. A factor of two difference in the gradients would account for a factor of four difference in the spectra, and the variance too. Since the gradient measurements were based

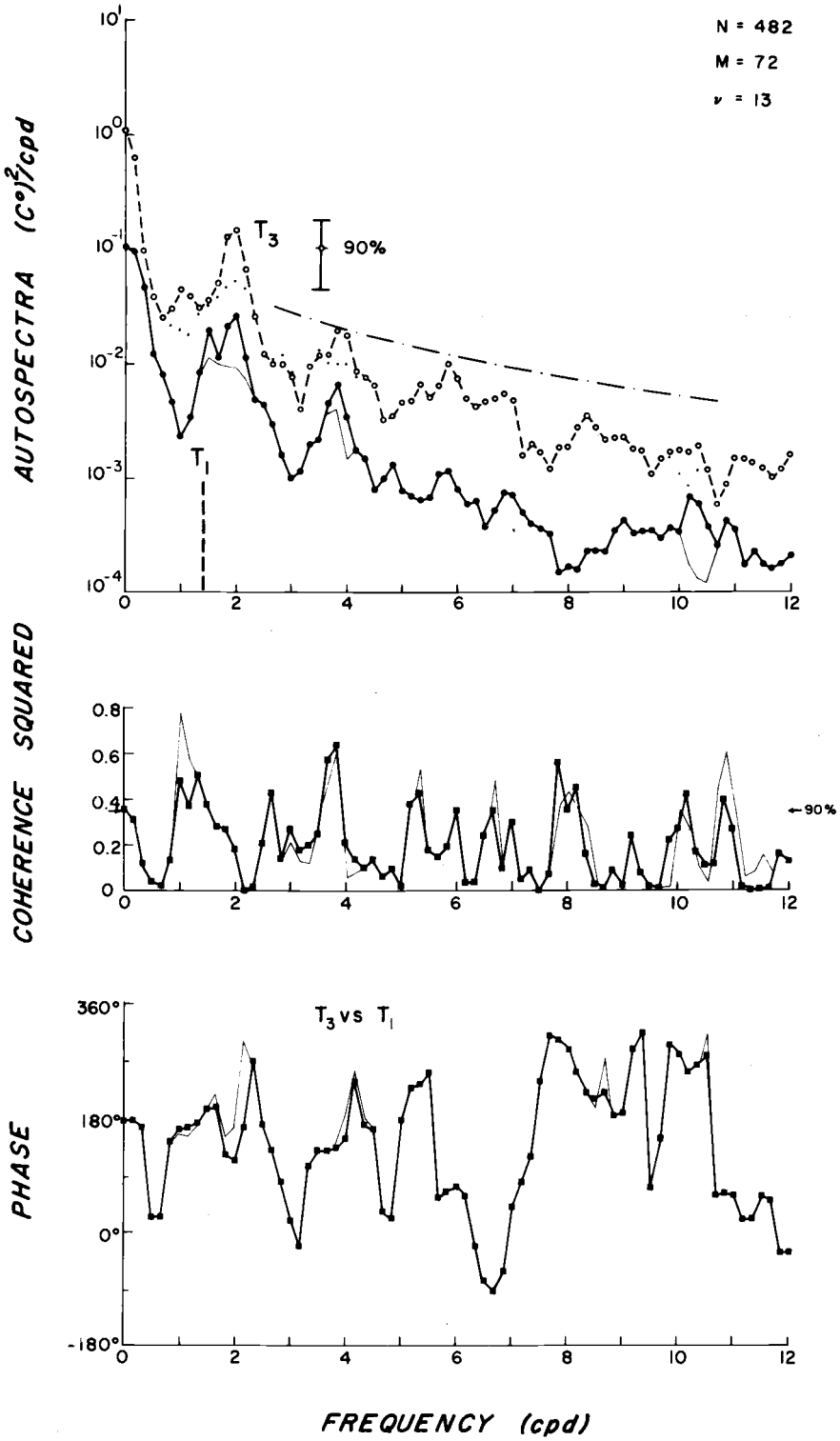

Figure 33. The temperature auto spectra and the coherence squared and phase functions between DB15 and DB5 at a depth of 20 meters. (T_1 and T_3 are the temperature series at DB5 and DB15, respectively.)

on only three samples acquired in the observation period, this explanation is only plausible. The vertical temperature structure at DB15 was nearly linear while that at DB5 was nonlinear, which could produce spurious harmonics. However, there is no evidence of the generation of spurious harmonics in the spectrum at DB5.

ii) Both spectra had their maximum at the low frequency limit and decreased sharply as the frequency increased to 1 cpd.

iii) At the semidiurnal frequency, both spectra achieved their secondary maximum, corresponding to a vertical amplitude of about 5 meters. The spectrum at DB15 rose sharply in the band $f_I \leq f \leq 2$ cpd, while that at DB5 rose sharply in the band $1 \leq f \leq 2$ cpd, with a distinct peak at $f = f_I$. The peak at $f = f_I$ may be indicative of the frontal interaction, since the frontal interaction may open the inertial-internal wave passband to frequencies less than $f = f_I$, thus motion at $f = f_I$ would have had a vertical component. Alternatively, horizontal displacements in the presence of strong horizontal temperature gradients may have produced the peak at $f = f_I$. Longer records and additional temperature sensors are required to investigate this feature in detail.

iv) Both spectra decreased sharply for $2 \leq f \leq 3$ cpd; they then rose to their tertiary peak at 4 cpd. The ratio of the

secondary to the tertiary peak was about 10:1 at DB15, while it was only about 5:1 at DB5. This difference suggests a factor of two growth for the second harmonic of the semidiurnal motion as the wave propagated shoreward, as deduced below.

v) At $f > 4$ cpd, the spectra continued to decrease and there were peaks at higher harmonics of the semidiurnal motion. The most significant peak was at about 6 cpd which was the third harmonic.

vi) The spectra of the residual series indicate a reduction in the spectral peaks at 2 and 4 cpd, and the peak was essentially removed at 1 cpd for DB15, 20 meters.

The coherence squared (γ^2) and phase (θ) of the two temperature series provide essential information about the semidiurnal tide, but, as can be seen from Figure 33, the results are complicated. The principal features of γ^2 and θ are summarized:

i) Overall, γ^2 was statistically insignificant, but it had numerous significant peaks, primarily at tidal harmonics.

ii) The 4 cpd motion was the most strongly correlated, while the motions at the low frequency limit and in the band of $1 \leq f \leq f_I$ were also significantly correlated. The motion at 2 cpd was virtually incoherent; clearly something was awry with the semidiurnal tide. It is not clear what could have

have been wrong; among the possibilities are that the wave was not phase stable due to time variable generation or that the wave's interaction with the time-variable frontal regime phase modulated the wave. It is difficult to explain the lack of coherency of the 2 cpd wave when confronted with the high coherency of the 4 cpd wave.

iii) Overall, θ was variable. Because γ^2 was generally small, θ generally had low statistical significance through most of the band. Since θ did show some piecewise continuity, it is discussed further.

iv) The two series were out-of-phase at the low frequency limit. Though θ was not expected to be highly significant at $f = 0$ due to the nature of the calculation, visual inspection of the low-passed series (Mooers et al., 1968) shows that the two temperature series were out-of-phase. While the temperature decreased by about 1C° at DB5 during the observation period, it increased by 2.5C° at DB15, which is consistent with a long period variation in coastal upwelling associated with the observed wind shift.

v) The large variations in phase at 2 cpd are curious features. The presence of the semidiurnal barotropic tides and of several internal tides in a measurement bandwidth may have complicated and degraded θ, as well as γ^2, at 2 cpd.

iv) θ had a surprising value at 1 cpd; it equaled 170° rather than 0°. A similar phase difference for diurnal components was determined in the tidal analysis recorded in Table 6. The dirunal wave should be essentially in-phase at both sites, if it propagated as a barotropic wave. The only existing theoretical mechanism for this feature is the frontal interaction, which may have allowed the diurnal tide to propagate as an internal tide.

vii) The unexpected behavior of γ^2 and θ at 1 and 2 cpd appears in the spectra of the residual as well as that of the original series.

viii) If the motion was that of a standing wave in the onshore-offshore direction, θ should have equaled 0° or 180°. Since θ was seldom 0° or 180°, the phase function is interpreted with a progressive wave model. The slope of θ versus f indicates the direction of propagation of progressive waves; positive values indicate onshore propagation. The θ versus f template of Figure 32 is used for interpreting the observed θ versus f. The theoretical θ vs f function for $N^2 = 3 \times 10^{-4} \text{sec}^{-2}$ gives the best agreement. The waves propagated onshore in the frequency bands of about 1 to 2 cpd, 3 to 4 cpd, and 7 to 8 cpd. Consistent with theoretical expectations, the semidiurnal tide was about

100° to 150° out-of-phase between DB15 and DB5, with DB15 leading DB5. In the non-dispersive range of the phase speed, the progressive waves traveled at a phase speed of about 60 cm/sec.

E. The Horizontal Velocity Component Spectra and Their Correlation at Individual Spatial Points

The horizontal velocity component spectra, and their coherence squared and phase functions, are presented in Figure 34 for each of the four current sensors. The spectra of the original series are shown by heavy solid lines and by heavy dashed lines for the u and v spectra, respectively. The residual spectra are shown by light lines and by dots for the u and v spectra, respectively. The coherence squared and phase functions for the original and residual series are shown by the heavy and light solid lines, respectively; Their values for the semi-principal axis transformation of the residual series are shown by dots.

The principal properties of the autospectra are summarized:

i) All four pairs of spectra were similar to those generally observed elsewhere in the Ocean (Webster, 1968b), and resembled the spectra previously computed from observations taken off Oregon (Collins, 1968). The maximum of each spectrum tended to occur at the low frequency limit. For $f > 0$, there was a sharp decrease in spectral level followed

a

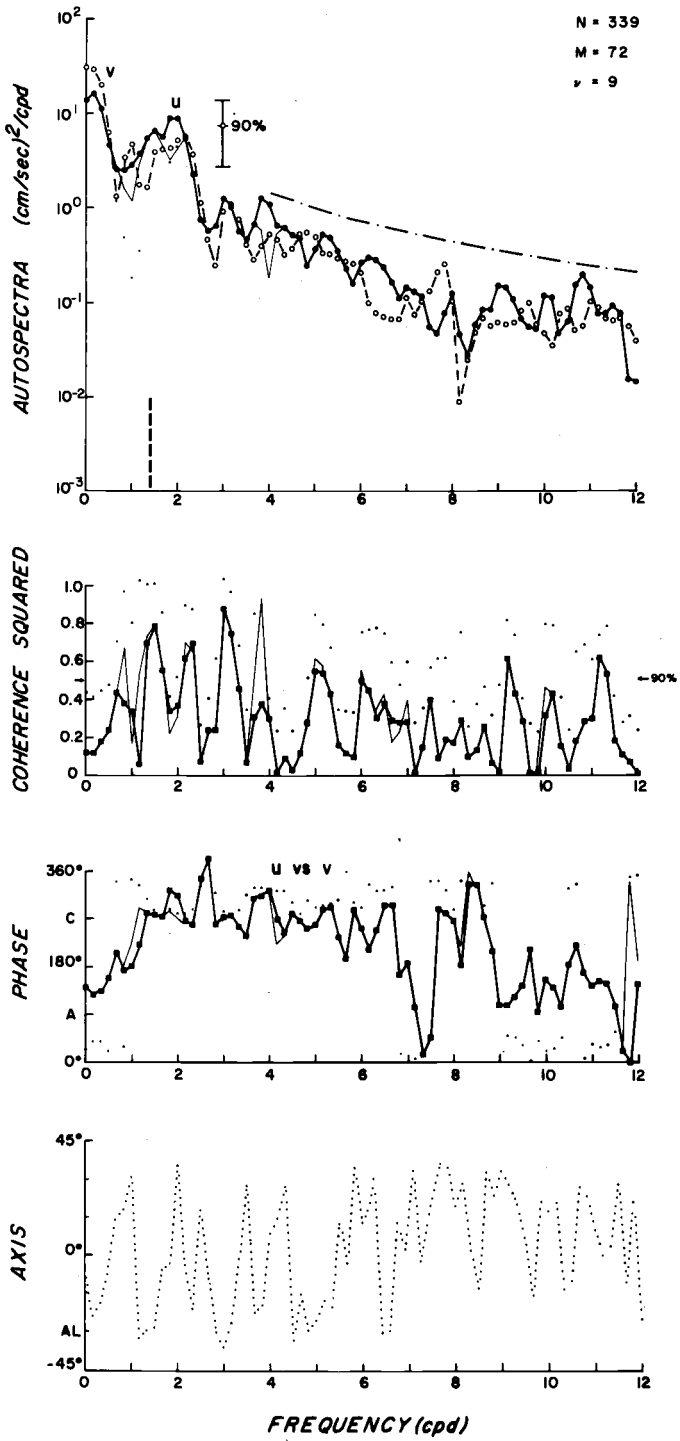

Figure 34a. The horizontal velocity autospectra and their coherence squared, phase, and axis functions at DB5, 20 meters.

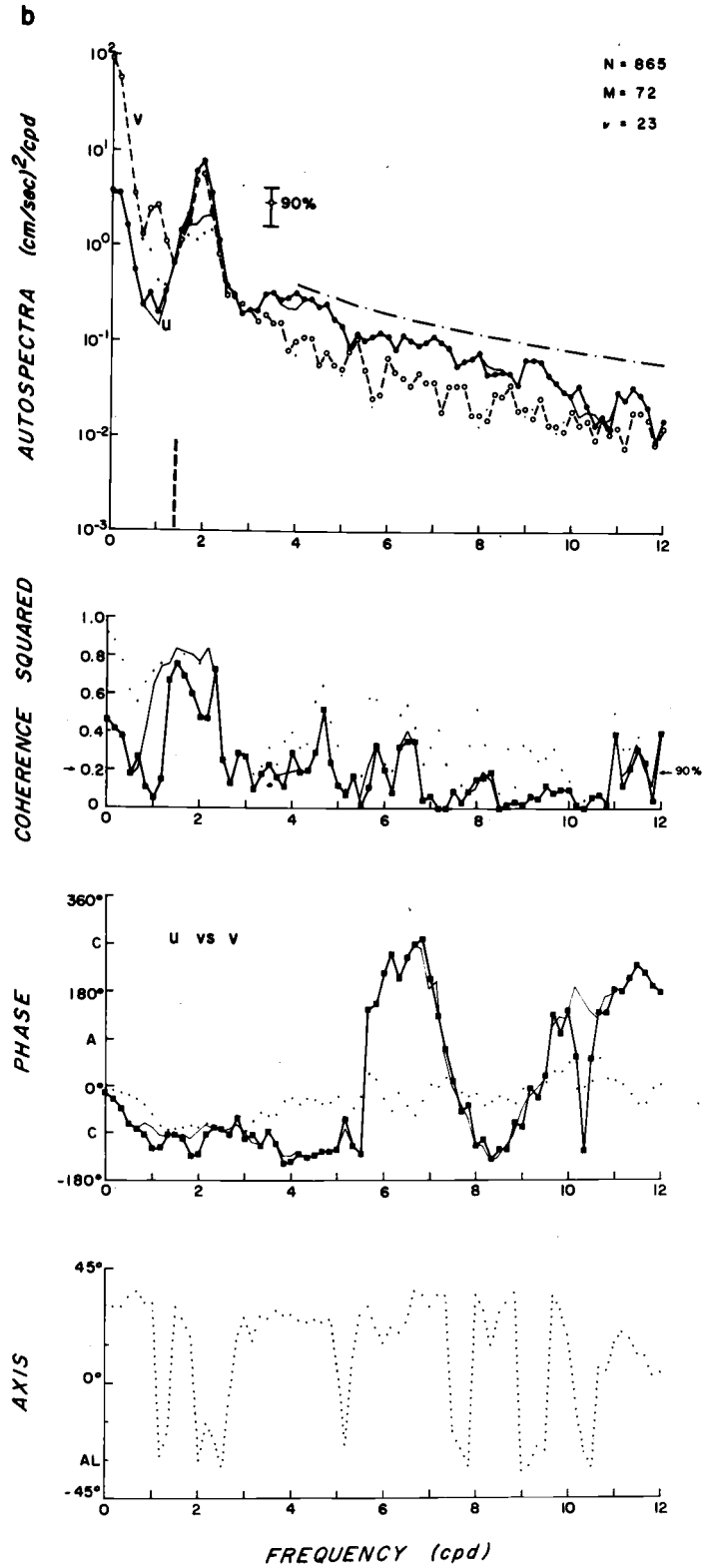

Figure 34b. The horizontal velocity autospectra and their coherence squared, phase, and axis functions at DB5, 60 meters.

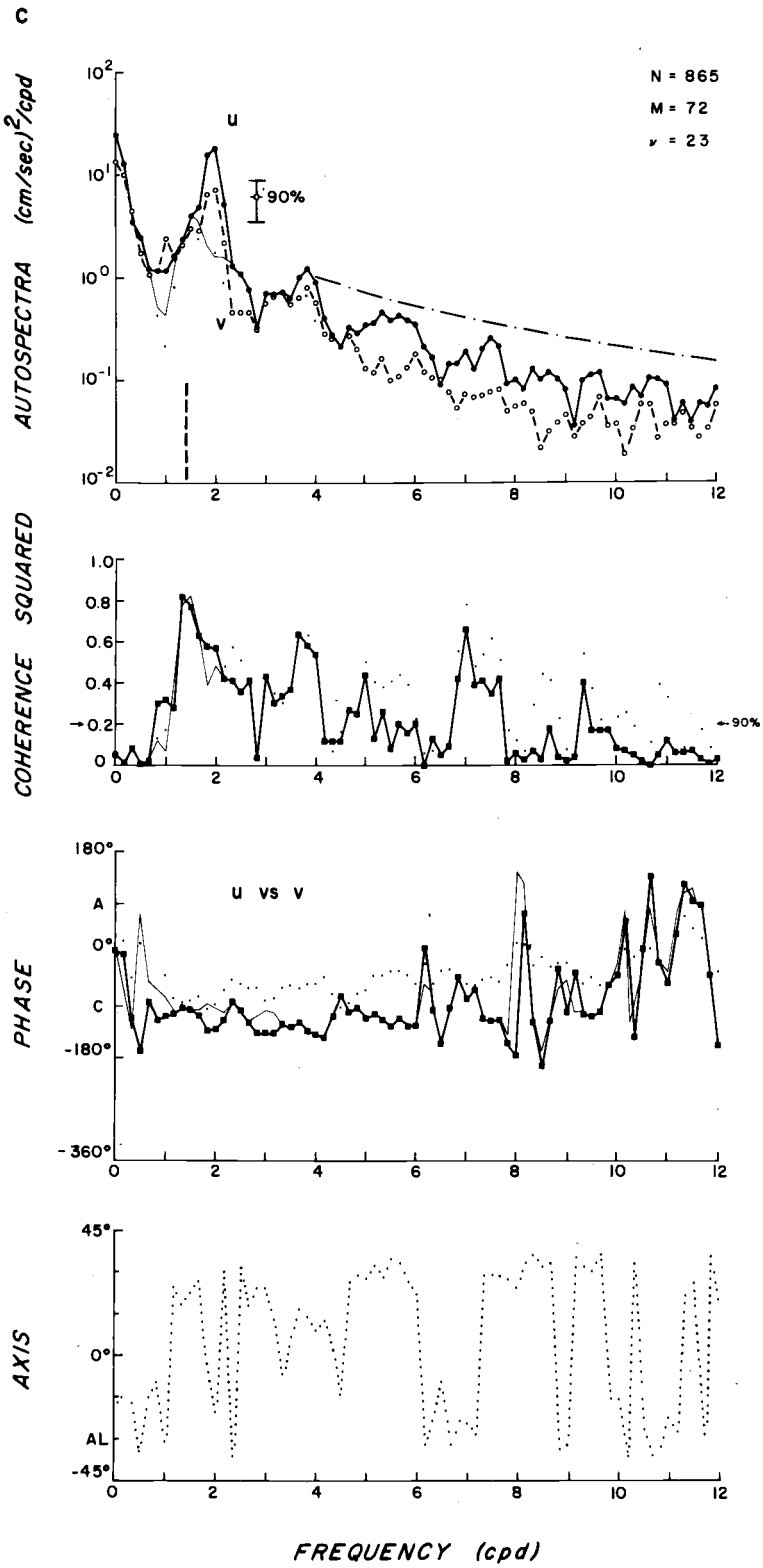

Figure 34c. The horizontal velocity autospectra and their coherence squared, phase, and axis functions at DB10, 20 meters.

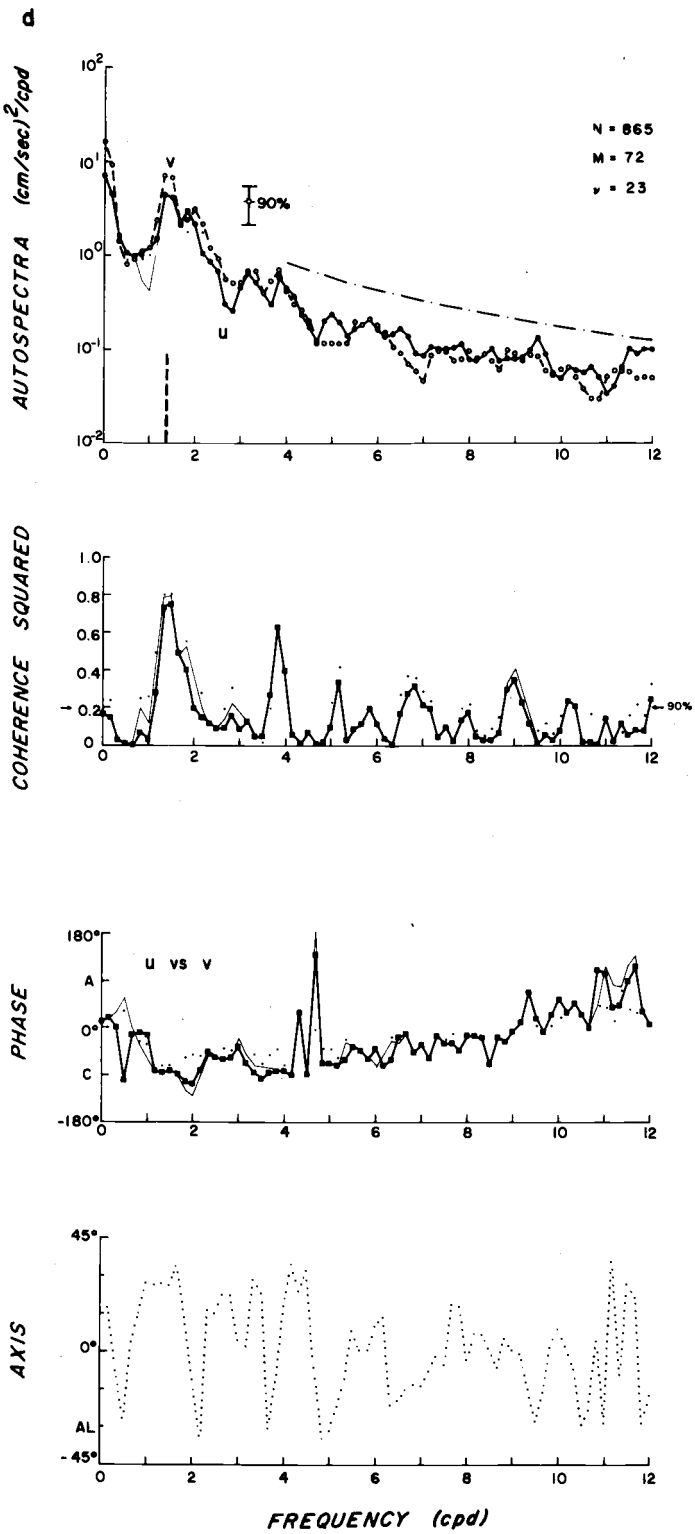

Figure 34d. The horizontal velocity autospectra and their coherence squared, phase, and axis functions at DB15, 60 meters.

by peaks in the region of the diurnal, inertial, and semidiurnal frequencies. There was a tendency for a decrease in spectral level at higher frequencies.

ii) With the exception of DB10, 20 meters, the v spectra were greater than the u spectra at the low frequency limit. This feature reflects the asymmetry imposed by the coastal boundary and bottom contours, since it is natural to expect the low frequency, large scale motions to be oriented in the alongshore direction.

iii) With the exception of DB15, 60 meters, the u spectra tended to dominate the v spectra in the frequency band of $f_I \leq f \leq 2$ cpd; the notable exception was probably related to the location of that sensor at the seaward edge of the continental shelf.

iv) At the diurnal frequency, there was a definite peak in the v spectra, but not the u spectra, at DB5, 20 and 60 meters and DB10, 20 meters. There was no discernable diurnal peak in the spectrum of either component at DB15, 60 meters, though the value of the spectra at the diurnal frequency was about the same as that found in the other spectra.

v) In all the spectra, there was a sharp rise in spectral level at the inertial frequency, or slightly below, which was consistent with inertial-internal wave theory. Yet, only in the

case of DB15, 60 meters was there a distinct peak at the inertial frequency, which actually dominated the semidiurnal peak. From the spectra, an estimate of the average peak amplitude of the inertial motion is made:

Sensor site	Depth (meters)	u (cm/sec)	v (cm/sec)	Ratio of u to v
DB5	20	4.5	3.5	1.3
DB5	60	1.2	1.2	1.0
DB10	20	2.2	2.0	1.1
DB15	60	2.8	3.7	0.8.

The amplitude of the inertial motion was a function of spatial position. There was a tendency for the inertial motion to be isotropic, with possible exceptions at the shelf edge and in the steepest part of the frontal layer, where the component amplitudes were also greatest. The former result is consistent with the theoretical concept that the inertial motion tended to be trapped along the shelf edge, see Appendix I. The latter result is consistent with the inertial-internal wave bandpass concept of this dissertation, which can account for motion present at the inertial and lower frequencies in an inclined frontal layer. Since all of the inertial motion did not persist as a steady wave, the above values are lower bounds on the largest inertial amplitudes. The above values are greater than the amplitudes of the coherent inertial motion given in Table 6.

vi) In all the spectra there was a significant peak at the semidiurnal frequency, though its qualitative shape and absolute value were functions of spatial position. From the spectra, an estimate of the average peak amplitude of the semidiurnal motion is made:

Sensor site	Depth (meters)	u (cm/sec)	v (cm/sec)	Ratio of u to v
DB5	20	5. 2	4. 3	1. 2
DB5	60	3. 9	3. 3	1. 2
DB10	20	6. 2	3. 8	1. 6
DB15	60	2. 2	2. 6	0. 8

The semidiurnal amplitudes tended to be greatest at 20 meters and inshore. Their total range was only 2. 2 to 6. 2 cm/sec while the inertial amplitudes had a range of 1.2 to 4.5 cm/sec, or a spread of less than 1 to 3 compared to one of nearly 1 to 4. Thus, the semidiurnal amplitude was more uniform spatially than the inertial amplitude.

vii) The velocity sepctra were excited in the frequency band $3 \leq f \leq 4$ cpd. The quarterdiurnal peak is attributed to the second harmonic of the semidiurnal motion, which was also noted as significant in the temperature spectra. The spectral peak near the terdiurnal frequency may have been the third harmonic of the diurnal motion.

viii) The residual series have had their diurnal components substantially removed, while the semidiurnal peak has not been eliminated in most cases. The latter is especially true at

DB15, 60 meters.

The coherence squared and phase functions for the component spectra are discussed below:

i) In the band $0 \leq f < 1$ cpd, γ^2 was generally negligibly small. The single exception is DB5, 60 meters, where the two velocity components were nearly in-phase at the low frequency limit. At $f = 1$ cpd, γ^2, for the residual series, and its semi-principal axis transformation, were generally significant.

ii) For $f = f_I$, γ^2 was unequivocally significant, with the components rotating in-quadrature in a clockwise sense, thus the inertial motion was highly coherent at each spatial point.

iii) There was a general tendency for the u and v series to be in-quadrature and to rotate clockwise in the band $f_I \leq f \leq 6$ cpd. At $f = 6$ cpd, the Coriolis restoring force's effectiveness is reduced in the ratio $(\frac{f_I}{6})^2 \approx 0.06$, thus it is not unexpected that the inertial effects on rotation were small at frequencies greater than 6 cpd.

iv) At $f = 2$ cpd, γ^2 was not significant in the original series for DB5, 20 meters. Even the semi-principal axis transformation resulted in only marginal significance for the semidiurnal motion. Otherwise, there was a tendency for

high values of γ^2 in the band of $f_I \leq f \leq 2$ cpd, which is consistent with the fact that a continuum of inertial-internal waves may exist in this region of the spectrum. In this band, there was a tendency for γ^2 of the residual series, and its semi-principal axis transformation, to be appreciably greater than that of the original series, except at DB10, 20 meters. At the latter site, γ^2 was large in the original series.

v) γ^2 was significant near $f = 3$ and 4 cpd after semi-principal axis transformation, indicating that the terdiurnal and quarterdiurnal waves were also coherent motions.

vi) For $f = 3.5$ cpd, γ^2 was significant at DB5, 60 meters and DB10, 20 meters. The corresponding autospectra also show excitation at this frequency. Within the limits of the spectral resolution, this frequency corresponds to the summation frequency for the inertial and semidiurnal frequencies, suggesting an interaction between the two.

The semi-principal axis transformation had its greatest effect on γ^2 for DB5, 20 meters; it generally smoothed the phase functions. The orientation of the semi-principal axis is displayed in the lowest panel of each figure, where AL denotes the orientation of the bottom contours. The pattern of the semi-principal axes is rather erratic in all cases, but, with the exception of DB5, 20 meters, the

axis orientation was aligned with the bottom contours for the semidiurnal motion.

F. The Spectra of Complex-Valued Horizontal Velocity Series and Their Correlation Between Different Spatial Points

The spectrum calculations which result from treating pairs of horizontal velocity series measured at different spatial positions as pairs of complex-valued time series, W_1 and W_2, are presented in Figure 35. The results for both the original and the residual series are shown. The pairs chosen for analysis are DB15, 60 meters versus DB5, 60 meters; DB10, 20 meters versus DB5, 20 meters; and DB5, 20 meters versus DB5, 60 meters. The upper panel shows the autospectra of anticlockwise (A) components, corresponding to positive frequencies, for the two velocity series; similarly, the next panel shows the autospectra of the clockwise (C) components, corresponding to negative frequencies. For the original series, the values for the A and C components are given by heavy solid lines and dashed lines, respectively. For the residual series, the values for W_1 and W_2 are given by light solid lines and dots, respectively. The coherence squared and phase functions of the original series are shown in the lower panels by solid and dashed lines for the A and C components, respectively. The values for the residual series are shown by light solid lines and dots for the A and C components, respectively.

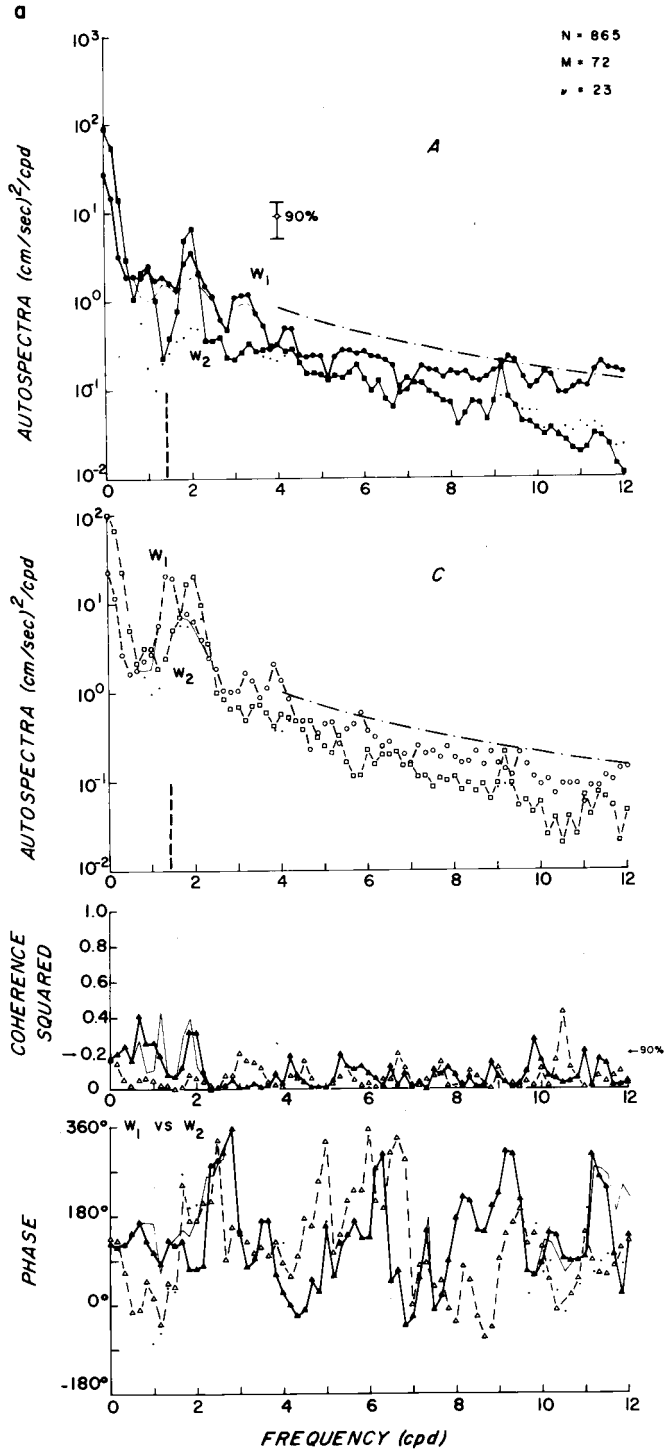

Figure 35a. The autospectra of complex-valued horizontal velocity series and their coherence squared and phase functions for DB15, 60 meters versus DB5, 60 meters. (W_1 and W_2 are the complex-valued horizontal velocities at a depth of 60 meters for DB15 and DB5, respectively. A and C are the anticlockwise and clockwise component spectra, respectively.)

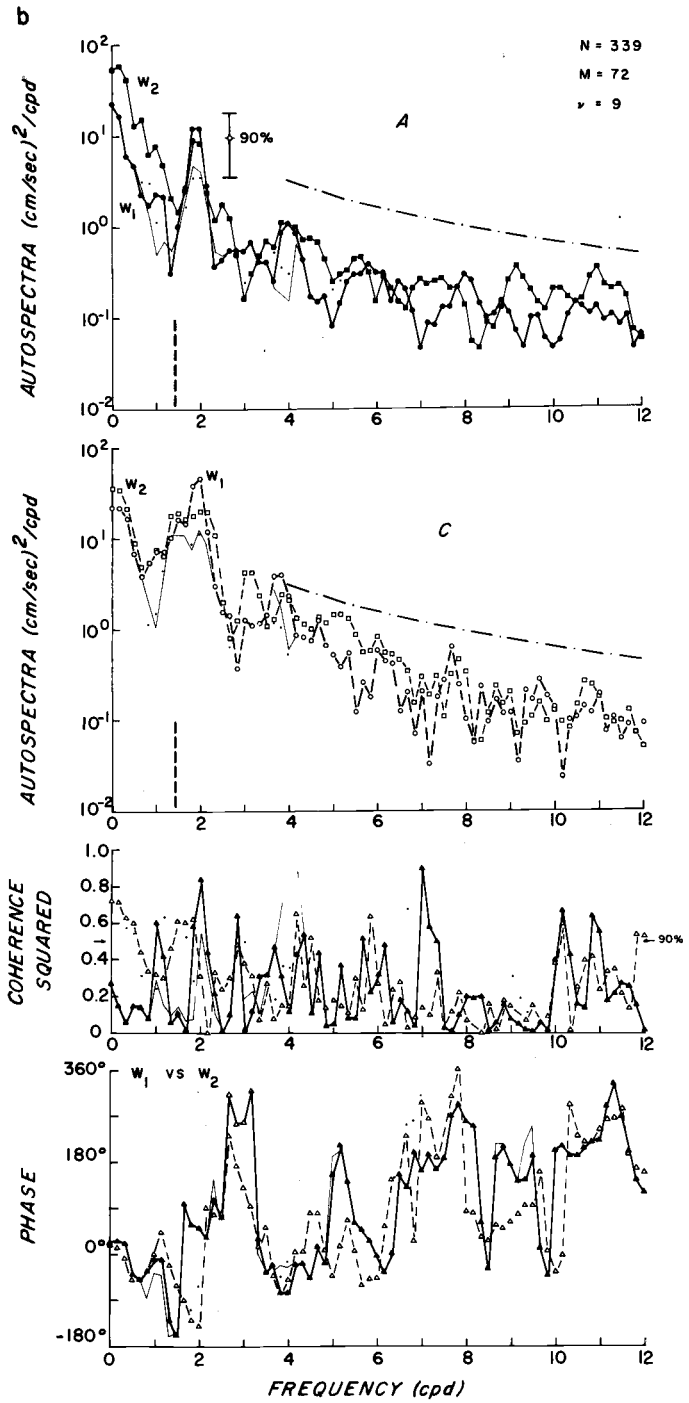

Figure 35b. The autospectra of complex-valued horizontal velocity series and their coherence squared and phase functions for DB10, 20 meters versus DB5, 20 meters. (W_1 and W_2 are the complex-valued horizontal velocities at a depth of 20 meters for DB10 and DB5, respectively. A and C are the anticlockwise and clockwise component spectra, respectively.)

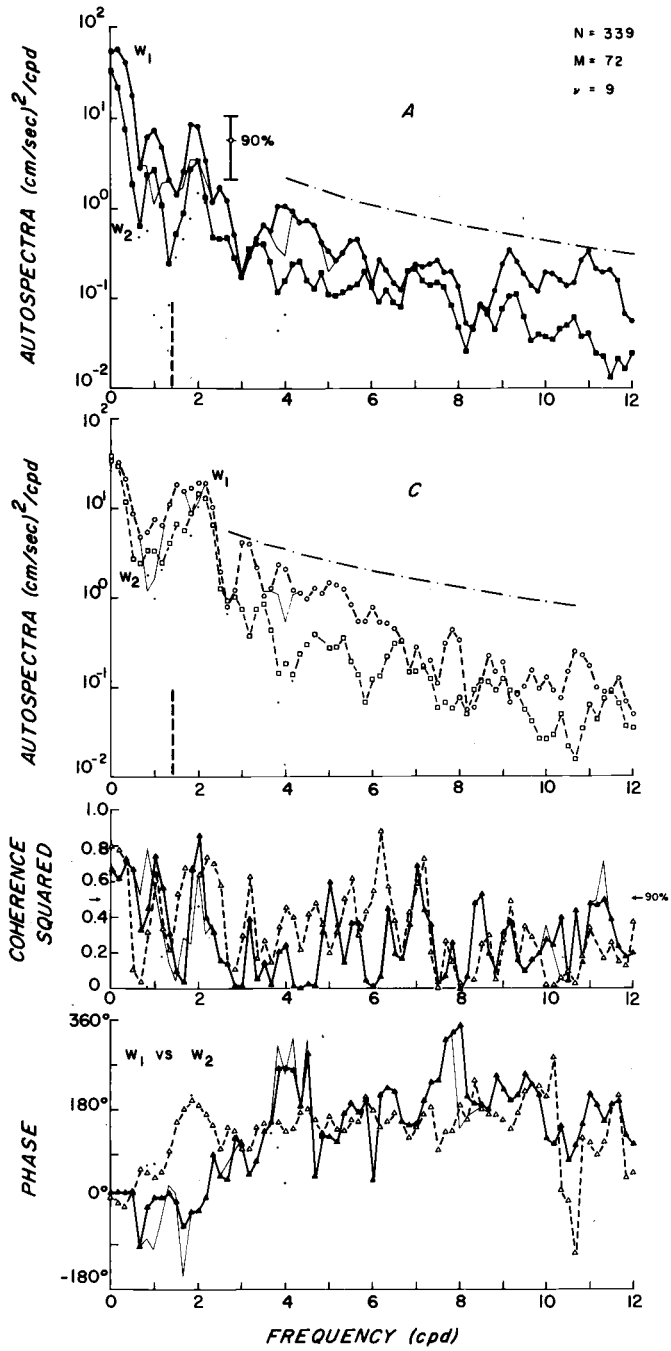

Figure 35c. The autospectra of complex-valued horizontal velocity series and their coherence squared and phase functions for DB5, 20 meters versus DB5, 60 meters. (W_1 and W_2 are the complex-valued horizontal velocities at DB5 for 20 meters and 60 meters, respectively. A and C are the anticlockwise and clockwise component spectra, respectively.)

From Appendix III, γ^2 is automatically maximized in this type of analysis.

The principal properties of the autospectra are summarized:

i) The A and C component spectra were similar in shape and value except that the C component generally predominated in the band $f_I \leq f \leq 4$ cpd.

ii) The A component spectra generally had a diurnal but no inertial peak, while the opposite situation generally prevailed for the C component spectra.

iii) The semidiurnal frequency had an energy peak in both the A and C component spectra, with the latter predominating. The C component of the residual series was only slightly less than that of the original series at DB15, 60 meters, which was in contrast to the A component. This result is consistent with finding the M2 motion rotating anticlockwise at this site from tidal analysis in Section C.

iv) Energy peaks corresponding to tidal harmonics abounded.

v) The separation into A and C components gives a sharper definition of the spectral peaks than observed in Figure 34.

The coherence squared and phase functions for the pairs of series are discussed below:

i) γ^2 was generally significant for both the A and C components at the low frequency limit, except for the A component at

DB10, 20 meters versus DB5, 20 meters.

ii) γ^2 was significant at $f = 1$ cpd for the A component; it was only significant for the C component at DB5, 20 meters versus 60 meters.

iii) γ^2 was not significant at $f = f_I$ except for the C component between DB10, 20 meters and DB5, 20 meters. Thus, the inertial motion was coherent over a horizontal separation of 10 kilometers, though it was incoherent over a vertical separation of 40 meters and a horizontal separation of 20 kilometers.

iv) γ^2 was significant at $f = 2$ cpd for both components, except for the C component between DB15, 60 meters and DB5, 60 meters and between DB10, 20 meters and DB5, 20 meters.

v) For $f \geq 4$ cpd, there was little significance to γ^2 for DB15, 60 meters versus DB5, 60 meters, while there were numerous significant peaks, primarily at tidal harmonics, for the other pairs.

vi) For DB15, 60 meters versus DB5, 60 meters, the velocity series were about 120° out-of-phase at low frequencies. The C component was about 200° out-of-phase at $f = 2$ cpd. The overall pattern of θ vs f was consistent with the theoretical θ vs f template of Figure 32a and $N^2 = 1 \times 10^{-4} \text{sec}^{-2}$. The slope of θ vs f indicated onshore motion in the

frequency bands 2 to 3 cpd, 4 to 6 cpd, and 7 to 9 cpd.

vii) For DB10, 20 meters versus DB5, 20 meters, the velocity series were in-phase at low frequencies. The C component was out-of-phase at $f = 2$ cpd. θ sustained complex variations at higher frequencies. The overall pattern of θ vs f was consistent with the theoretical θ vs f template of Figure 32b and $N^2 = 3 \times 10^{-4} \text{ sec}^{-2}$. The slope of θ vs f indicated onshore motion in the frequency bands 2 to 3 cpd, 4 to 5 cpd, and 6 to 8 cpd.

viii) For DB5, 20 meters versus DB5, 60 meters, the velocity series were in-phase at low frequencies. For $f > f_I$, the C component was essentially 180° out-of-phase. The A component was roughly 180° out-of-phase for $f > 4$ cpd.

G. Spectra of Complex-Valued Horizontal Velocity and Temperature and Their Correlation at a Single Point

The spectral quantities for the complex-valued velocity and the temperature at DB5, 20 meters are presented in Figure 36. The complex-valued velocity autospectra have already been discussed in Section F. Similar to the preceding figures, the values for the original series are given by heavy lines and those for the residual series by light solid lines and dots. The temperature autospectrum has been computed for a record length about two-thirds of that used for the

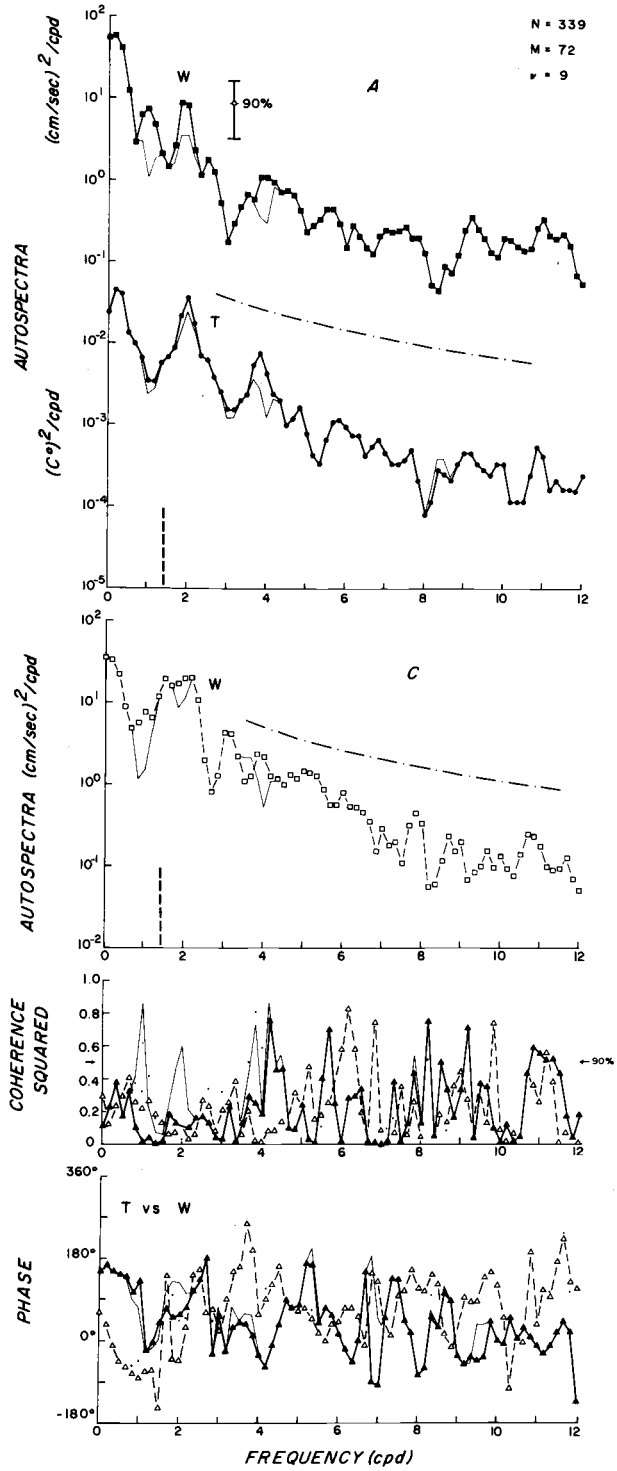

Figure 36. The autospectra of the complex-valued horizontal velocity and of the temperature and their coherence squared and phase functions for DB5, 20 meters. (W is the complex-valued horizontal velocity and T is the temperature at DB5, 20 meters. A and C are the anticlockwise and clockwise component spectra, respectively.)

calculations in Section D. From the autospectra, it is observed that:

i) There were spectral peaks near the low frequency limit, 2 cpd, and 4 cpd in all of the spectra.

ii) There was a diurnal peak at 1 cpd in the A component spectrum but not in the C component spectrum or the temperature spectrum.

The coherence squared and phase functions are discussed below:

i) Except for the A component spectrum of the residual at $f = 1$ and 2 cpd, γ^2 was statistically insignificant in the band $0 \leq f < 4$ cpd, where most of the energy occurred.

ii) For $f \geq 4$ cpd, γ^2 had significant peaks which were generally associated with tidal harmonics.

iii) The peak in γ^2 for 4 cpd is the peak of greatest interest; for the residual series, it was significant in both the A and the C components.

It is difficult to interpret these results. The difficulty may relate to the fact that temperature oscillations are primarily manifestations of vertical motions while velocity oscillations occur in the horizontal plane. At the low frequencies, the hodographs of inertial-internal waves are essentially confined to the horizontal plane. At the high frequencies, the hodographs have a significant vertical component. The ratio of the vertical to the horizontal velocity component is given by the slope of a characteristic:

$$\frac{dz}{dx})_{\eta}^{\pm} \approx \pm \left(\frac{f^2 - f_I^2}{f_B^2 - f^2}\right)^{1/2} .$$

The absolute value for $\frac{dz}{dx})_{\eta}^{\pm}$ increases from about 0.7×10^{-2} to about 1.4×10^{-2} as the frequency increases from 2 to 4 cpd. Thus, the pattern for γ^2 as the frequency increases may be associated with the shift from the predominance of the Coriolis restoring force to that of the buoyancy restoring force.

H. The Spectra of Horizontal Velocity Differences and Their Correlation

Barotropic motions are uniform in the vertical, hence the barotropic component has been removed from time series sampled at different depths on a common vertical by subtraction. Analogously, the barotropic component could be extracted by averaging numerous series sampled at points distributed uniformly from the surface to the bottom on a common vertical. The barotropic component has been removed from records sampled at the same depth and separated horizontally by a small fraction of a barotropic wavelength but by a large fraction of a baroclinic wavelength. Since the horizontal phase speed of baroclinic motions is at least an order of magnitude less than that of barotropic motions, the barotropic component has been removed by subtraction. Analogously, the barotropic component could be extracted by averaging series sampled at numerous points distributed

uniformly over at least one baroclinic wavelength. The difference series are considered the baroclinic series.

Because only a limited number of sensors were employed, the barotropic component could not be extracted, but three baroclinic series were formed. The effectiveness of the effort to remove the barotropic component can be judged by applying several criteria to the results:

i) In general, the spectra should be consistent with theoretical inertial-internal wave passband.

ii) The diurnal tide should be essentially barotropic, thus there should be little evidence for diurnal motion in the spectra of the difference series.

iii) The semidiurnal tide should have an appreciable baroclinic component, hence there should be a significant spectral peak for semidiurnal motion in the difference series.

One vertical and two horizontal difference series were formed from the horizontal velocity series; their spectra are discussed below. The residual and the semi-principal axis series are analyzed only for the case shown in Figure 37a. The spectral quantities of the vertical difference series for DB5, 20 meters minus DB5, 60 meters are shown in Figure 37a. The autospectra had the following properties.

i) The spectra had the same form, with that of Δu generally greater than that of Δv but by less than a factor of three.

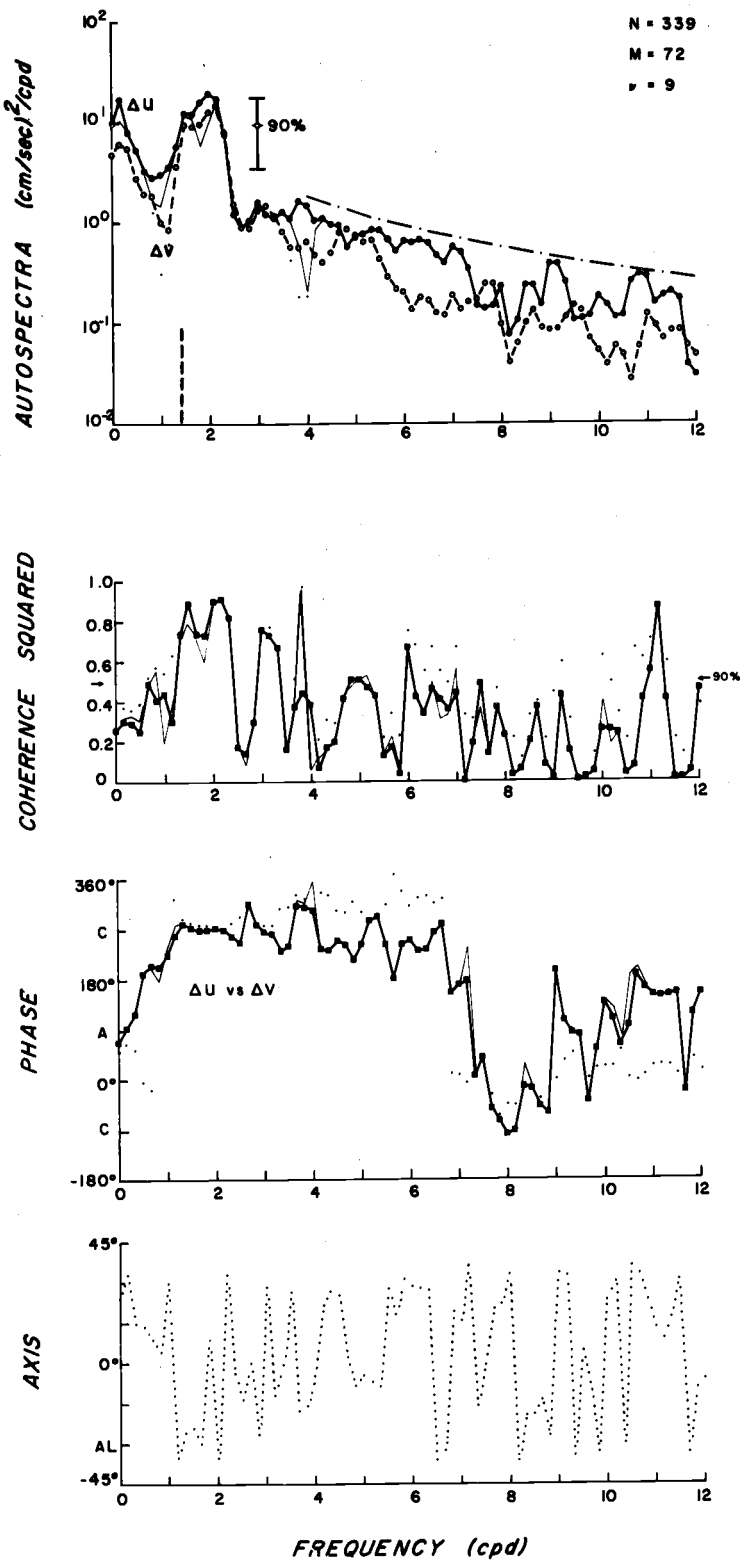

Figure 37a. The autospectra of horizontal velocity difference series and their coherence squared, phase, and axis functions for DB5, 20 meters minus DB5, 60 meters.

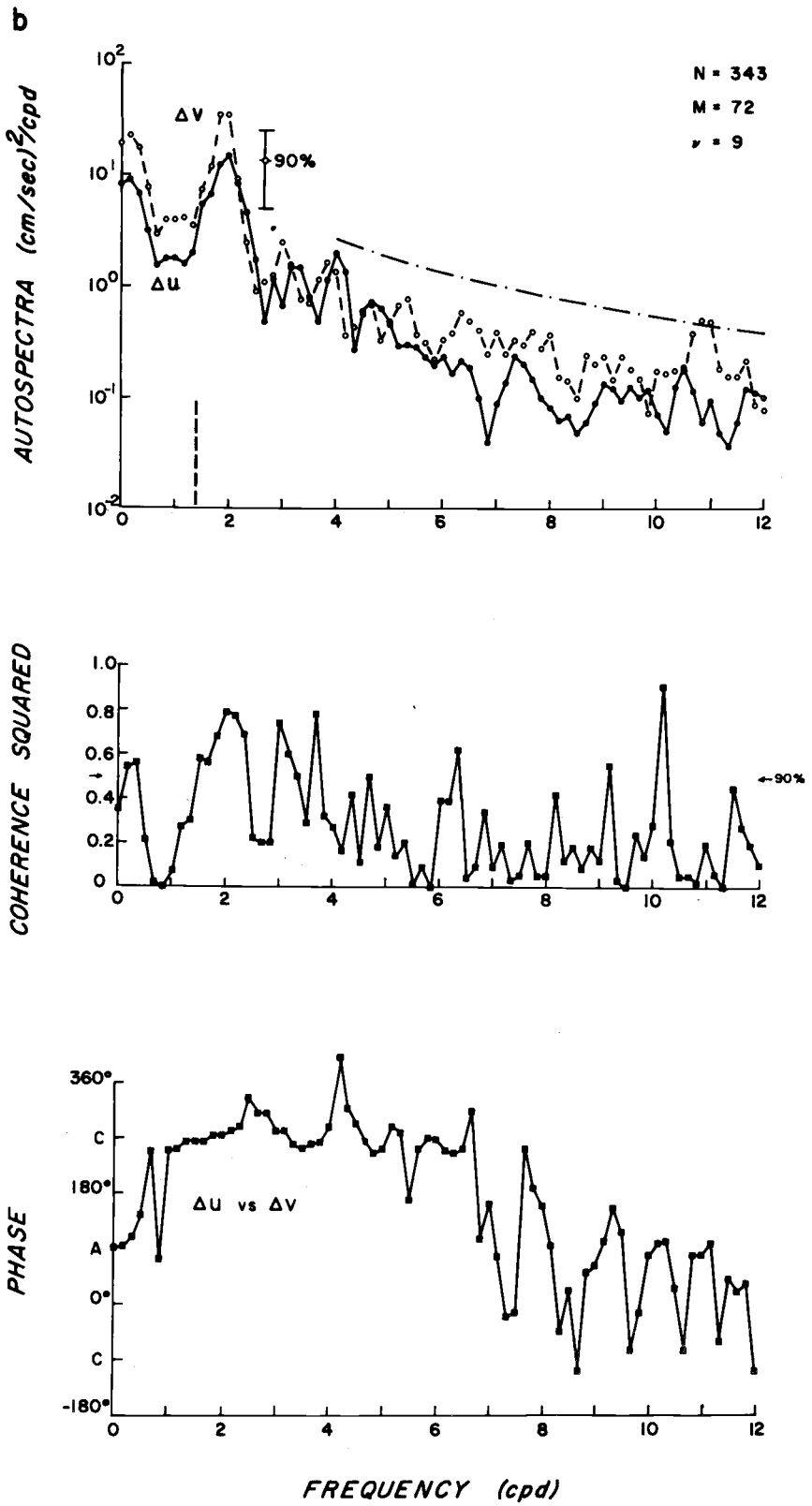

Figure 37b. The autospectra of horizontal velocity difference series and their coherence squared and phase functions for DB5, 20 meters minus DB10, 20 meters.

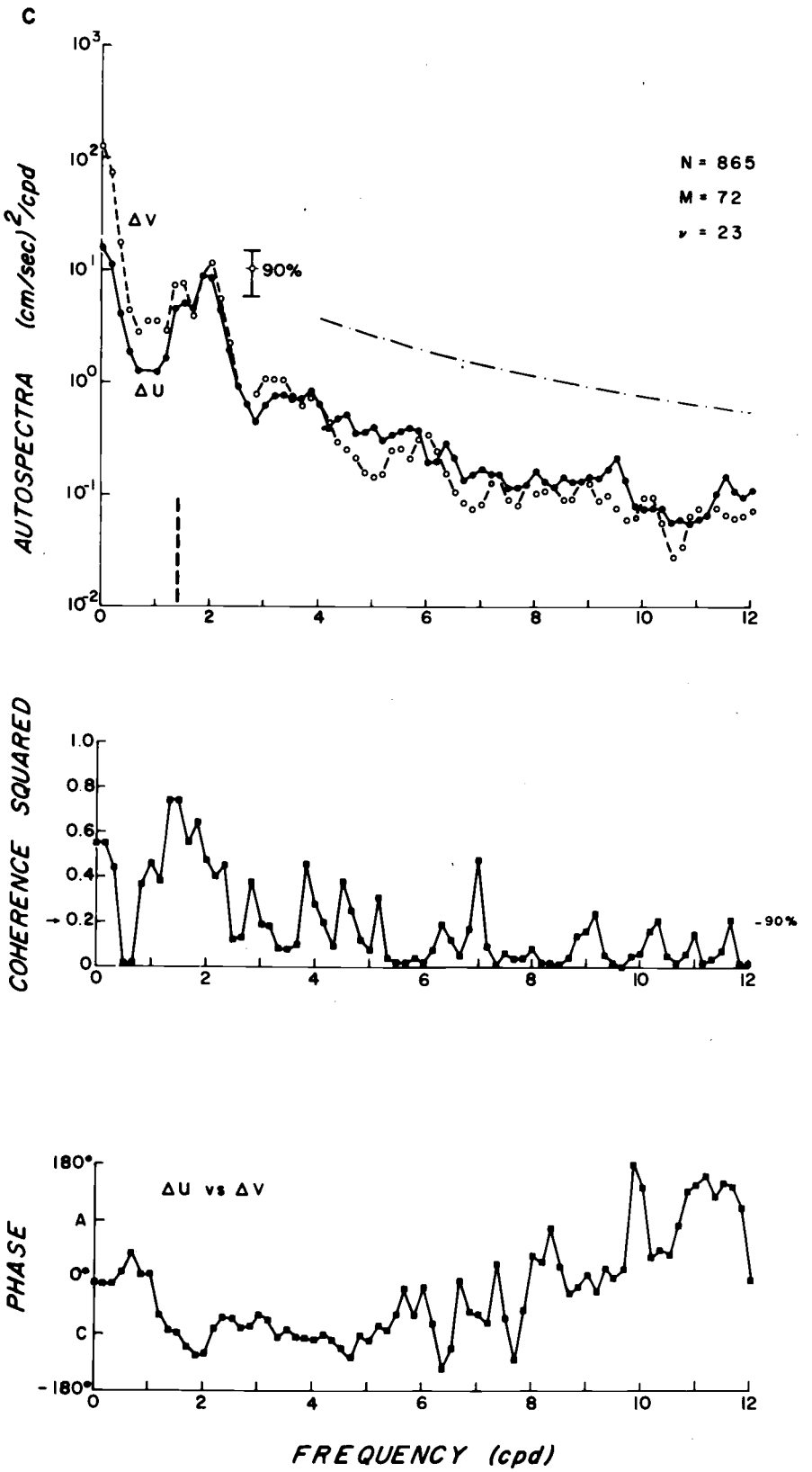

Figure 37c. The autospectra of horizontal velocity difference series and their coherence squared and phase functions for DB5, 60 meters minus DB5, 60 meters.

ii) At low frequencies, the spectral levels rose and peaked.

iii) There was a decided trough in the spectra at the diurnal frequency, as predicted.

iv) There was a rise in the spectra at the inertial, or slightly lower, frequency, which is consistent with inertial-internal wave theory for the frontal interaction, as predicted.

v) There was a maximum in both spectra at the semidiurnal frequency, as predicted.

vi) There was a sharp decrease in the level of both spectra for $2 \leq f \leq 3$ cpd.

vii) At frequencies greater than 3 cpd, the spectral levels continued to decrease but at a lesser rate.

viii) The results for the residual series indicate a reduction in the tidal peaks.

The coherence squared and phase functions are discussed below:

i) In the low frequency limit, γ^2 had marginal statistical significance, but it was significant at $f = f_I$, or slightly lower. At the low frequency limit, θ corresponded to anticlockwise rotation of the shear vector; it smoothly shifted to indicate clockwise rotation of the shear vector at $f = f_I$, or slightly lower.

ii) In the frequency band of $f_I \leq f \leq 2$ cpd, γ^2 remained significant, while θ indicated that the shear vector rotated clockwise. γ^2 had its maximum at $f = 2$ cpd.

iii) In the frequency band $2 \text{ cpd} \leq f \leq 6 \text{ cpd}$, γ^2 had peaks at 3, 4, 5 and 6 cpd, while the phase slowly varied within $\pm 40^{\circ}$ of -90°.

iv) At frequencies greater than 6 cpd, γ^2 continued to fluctuate and θ departed from -90°, indicating the reduced effect of the Coriolis force on the shear vector at high frequencies.[28]

The spectral quantitites of the horizontal difference series for DB5, 20 meters minus DB10, 20 meters are shown in Figure 37b. The principal properties of the autospectra are remarked:

i) The spectra were quite similar, with that of Δv generally greater than that of Δu but by less than a factor of two.

ii) The Δu and Δv spectra were similar to those of the preceding figure and a detailed discussion is not necessary.

γ^2 and θ had the following properties:

i) γ^2 and θ were similar to those of the preceding figure in the frequency band $0 \leq f \leq f_I$, except for the decrease to $\gamma^2 = 0$ near $f = 1$ cpd, which is consistent with predictions.

ii) In the band $f_I \leq f \leq 12$ cpd, γ^2 and θ were similar to

---

[28] The only other spectra of vertical difference series known to the author are those computed by Dr. G. Seidler (1968). His calculations were based on observations in the deep ocean separated by only 3 meters, yet his spectra exhibit the same qualitative features that these do.

those of the preceding figure, except that a well-formed peak in γ^2 did not occur at f = 5 cpd.

The spectral quantities of the horizontal difference series for DB5, 60 meters minus DB15, 60 meters are shown in Figure 37c. From the autospectra, the following results are remarked:

i) Again, the Δu and Δv autospectra were quite similar; the spectrum of Δv was greater than that of Δu by less than a factor of three for $0 \leq 3 \leq f \leq 4$ cpd. At higher frequencies, Δu and Δv were essentially equal.

ii) Δu and Δv were so similar to the two preceding cases that only the exceptions are noted.

iii) The values for both Δu and Δv at the low frequency limit appreciably exceeded those at the inertial and semidiurnal frequencies.

iv) The semidiurnal peak dominated the distinct inertial peak for both Δu and Δv.

The following remarks derive from the plots of γ^2 and θ:

i) γ^2 and θ were similar to the two preceding cases, except there were no peaks in γ^2 for f = 6 and 8 cpd; however, there were peaks at f = 7 and 9 cpd.

ii) At the low frequency limit, γ^2 was significant and θ was zero, thus Δu and Δv were correlated and in-phase at low frequencies.

iii) The peak at the inertial frequency was more significant than the semidiurnal and quarterdiurnal peaks.

iv) In the frequency band $f_I \leq f \leq 6$ cpd, θ tended to be $-90°$.

The horizontal difference spectrum for the temperature series at a depth of 20 meters at DB5 and DB15 has been computed but it is not discussed for the following reasons:

i) The temperature autospectrum at DB15 dominated that at DB5 by up to an order of magnitude, hence their difference series was essentially the same as that for the series at DB15, and

ii) The significant difference series to examine is that of vertical displacement, which was not computed since the vertical temperature gradient is not sufficiently well-known at either site to justify converting the temperature series to vertical displacement series.

From the spectra of the vertical difference series in Figure 37a, deductions about the spectral Richardson Number, RIS, can be made. RIS(f) had its minimum value at the semidiurnal frequency. For the shear amplitude at $f = 2$ cpd, $|\frac{\Delta u}{\Delta z}| \approx 1.5 \times 10^{-3} \text{sec}^{-1}$ and $|\frac{\Delta v}{\Delta z}| \approx 1.2 \times 10^{-3} \text{sec}^{-1}$. With $E \approx 2 \times 10^{-4}$, then $RISU(2) \approx 90$ and $RISV(2) \approx 133$. There was appreciable shear in the band $1.3 \leq f \leq 2.2$ cpd. Integrating over this band,

$$|\overline{\frac{\Delta u}{\Delta z}}| \approx 3.0 \times 10^{-3} \text{sec}^{-1} \quad \text{and} \quad |\overline{\frac{\Delta v}{\Delta z}}| \approx 2.5 \times 10^{-3} \text{sec}^{-1}$$

then $\overline{RISU} \approx 20$ and $\overline{RISV} \approx 30$ represent minimum Richard Numbers when all the motions in the band are in-phase. From Section X. C., for the mean flow

$$\frac{\Delta \bar{u}}{\Delta z} \approx -1.2 \times 10^{-3} \text{sec}^{-1} \quad \text{and} \quad \frac{\Delta \bar{v}}{\Delta z} \approx -4.6 \times 10^{-3} \text{sec}^{-1},$$

thus

$$RI\bar{U} \approx 150 \quad \text{and} \quad RI\bar{V} \approx 8.$$

When the conditions for the band-average of $\overline{\frac{\Delta u}{\Delta z}}$ apply, and considering the shear of the mean flow:

$$RIU_{min} \approx 75;$$

when they apply for the band-average of $\overline{\frac{\Delta v}{\Delta z}}$, and again considering the mean shear:

$$RIV_{min} \approx 4,$$

Thus, on the average, the low frequency inertial-internal shear waves were insufficient to produce critically low dynamic stability. Shear was also contributed by the low frequency motions with a time scale of several days; it was of the same order of magnitude as that in the band $1.5 \leq f \leq 2.2$ cpd, and, on the average, it was not sufficient alone or in combination with the mean and low frequency inertial-internal wave shears to produce critically low dynamic stability.

Thus, if the regime becomes dynamically unstable, it must be on an instantaneous basis rather than in an average sense. The maximum magnitude of the shear vector of the 10-minute samples was $1.4 \times 10^{-2} sec^{-1}$. Then, the minimum Ri was 1, which is the critical value. Values very close to the minimum value occurred frequently with a semidiurnal periodicity. The large values of the shear vector were also associated with short period oscillations superimposed on the tidal oscillation. The estimate of minimum Ri is limited by the lack of knowledge of the instantaneous value for E, as well as by the sampling rate and the sensor spacing.

In summary, the spectra were basically consistent with the theory for inertial-internal waves, thus they supported hypothesis i) of Section IX. B. There is some evidence, though not conclusive, for the lowering of the low frequency end of the passband due to the effects of the frontal interaction. Increased spectral resolution is necessary to settle this point. The use of residual series, and their semi-principal axis transformations, generally improved the significance of the spectrum calculations and their interpretation. The behavior of the A component spectra, particularly at the diurnal frequency, was generally consistent with the model for barotropic motions along a coastal boundary in Appendix I. The spectra of complex-valued horizontal velocity series are useful quantities and indicate a general onshore propagation of waves within the inertial-internal wave

passband, though some of the significant tidal harmonics appear to have been propagating offshore, which is plausible if they were generated inshore. Thus, hypotheses iii) and vi) of Section IX. B. have been substantiated. In particular, the vertical difference series of horizontal velocity at DB5 was an effective measure of the baroclinic motion. It can be speculated that, if additional vertical difference series had been calculable from observations, that the technique of spectrum analysis of complex-valued series would have been effective for the analysis of inertial-internal waves. The possible analyses of complex-valued horizontal velocity series were complicated by the presence of the barotropic tides. The values of dynamic stability computed, the general presence of tidal harmonics, and the complications in the coherence squared and phase functions at the semidiurnal frequency were all consistent with hypothesis viii) in Section IX. B. about the stability of the internal tide. The tidal and spectrum analyses indicated the coexistence of the semidiurnal internal tide and inertial motions in all the series, consistent with hypothesis ix) of Section IX. B. More complete observational arrays are necessary to gain insight into the generation and interaction of internal tides and inertial motions.

XII. CONCLUSIONS AND RECOMMENDATIONS

It is premature to expect a detailed, quantitative agreement between observations of inertial-internal waves and the linear theory for inertial-internal waves in the frontal zone of a coastal upwelling region. The principal difficulties are fundamental questions regarding the phase stability, amplitude stability, the spatial coherence, and the linearity of the waves, which can only be answered by further observation. There are other questions involving the effects of the low frequency variations of the frontal regime and the effects of the mean cross-stream flow on inertial-internal waves. Nevertheless, the existent observations and theory permit making several deductions.

The observations have been used to infer the key features of the general, three-dimensional flow pattern in the frontal zone of the coastal upwelling region off Oregon. The general flow pattern in the coastal region during upwelling season is summarized:

For the alongshore flow,

i) The flow is equatorward in the upper 40 meters of the water column.

ii) The flow is poleward beneath a depth of about 40 meters; it tends to be concentrated beneath the inclined, permanent frontal layer as a pycnoclinic jet.

For the cross-stream flow,

iii) The flow is offshore in the surface Ekman layer, which is about 10 to 20 meters thick.

iv) Upwelled water sinks beneath the seasonal pycnocline and flows offshore in a layer at a depth of about 10 to 30 meters.

v) The flow is onshore in the upper portion of the permanent pycnocline in a layer at a depth of about 20 to 60 meters.

vi) The newly formed water mass, which is marked by a temperature inversion, sinks beneath the inclined, permanent frontal layer and flows offshore in a layer at a depth of about 40 to 80 meters.

vii) Beneath the flow described in vi) and above the bottom Ekman layer, the flow is onshore.

viii) Within 10 to 20 meters of the bottom, the flow is also onshore in the bottom Ekman layer.

Since this picaresque flow pattern is based on both deductive and inductive reasoning, and since time-dependent effects may be substantial, it is necessary to make time series observations with increased vertical and horizontal detail to further verify and define the pattern. The observations, and the inferences made from them, indicate that a quite general study of frontal flows is feasible with existent techniques and in the frontal zone of the coastal upwelling region off Oregon.

In August-September 1966, the mean horizontal flow field had appreciable vertical shear, yet it was dynamically stable on the average, though there was evidence for significant mixing, e. g., the formation and sustenance of the temperature inversion. Appreciable vertical shears were produced by low frequency inertial-internal waves in the inclined frontal layer, especially by the semidiurnal internal tide and by motions with a temporal scale of several days. On the average, these motions were not sufficient to produce critically low dynamic stability over a vertical scale of 40 meters. The time series of ten-minute averages of vertical shear gave values for the dynamic stability which approached critical values over a vertical scale of 40 meters on a large fraction of the semidiurnal tidal cycles. At the DB25 anchor station over the continental slope, and on a vertical scale of five meters, the dynamic stability reached critical values on a semidiurnal cycle in the center of the temperature inversion, which was at the base of the inclined frontal layer. It is suggested, if observations are made at a more rapid sampling rate (about once per minute or faster) and over a smaller vertical scale (about five meters or less), that direct evidence will be found for turbulent mixing at the base of the inclined frontal layer and that it will be associated with the semidiurnal internal tide, inertial oscillations, and internal celluar waves.

The tidal and spectrum analyses of the horizontal velocity and

temperature time series indicate:

i) The several-day, the semidiurnal, and the inertial motions predominated in the spectra.

ii) The semidiurnal motion was less coherent than expected over spatial separations less than a horizontal wavelength, while the inertial motion was more temporally coherent than expected.

iii) The semidiurnal internal tide propagated onshore, and the array of sensors spanned about a half wavelength. Several bands of the spectra indicated onshore propagation, while others indicated offshore propagation.

iv) The semidiurnal internal tide was not phase stable, either due to unsteady generation and dissipation, to modification by low frequency modulations of the frontal zone, or to a complex vertical modal structure.

v) The tidal harmonics were richly excited, which is indicative of nonlinearities and interactions. The quarterdiurnal motion was especially marked and suprisingly coherent. The summation frequency for the inertial frequency and the semidiurnal tide had an energy peak in some of the spectra and was temporally coherent, as indicated by tidal analysis.

vi) The inertial motion had an amplitude of 2 to 4 cm/sec at the seaward edge of the continental shelf, where it was temporally

coherent. This may be evidence for a topographically trapped wave motion at a frequency slightly less than the inertial frequency. The inertial motion also had a baroclinic component 10 kilometers offshore.

The time series analyses suggest the following data analysis recommendations:

i) Since a significant collection of time series for the coastal region has been analyzed, or is in the process of analysis, it is timely to consider making ensemble averages of spectral quantities and determining confidence limits for the spectral quantities on an empirical basis.

ii) Optimum methods for the analysis of the coherent and incoherent components of the spectra are in demand. Further exploration for significant, coherent waves in the coastal regime at frequencies other than the ordinary tidal frequencies may be profitable. For instance, least squares tidal analyses of time series observed in the coastal region should routinely include the inertial frequency in the set of frequencies fit to each time series.

iii) Statistical experiments are necessary for the improvement of the estimates of coherency, cf. Tick (1967) and Jenkins and Watts (1968). The technique of alignment (Jenkins and Watts, 1968) should be attempted in the cross spectrum

analyses; i. e., the analyses should be tried with the Fourier transform of the covariance offset an amount equal to the lag value of the maximum covariance plus the ratio of the sensor separation to the inertial-internal wave phase speed. Experiments are also necessary to determine the practical limits and benefits of narrow-band spectrum analysis.

iv) Consideration should be given to routinely presenting all of the one-dimensional spectral quantities in the coordinate system of the array.

v) Least squares tidal analyses should be done on intermediate-passed series to attempt to improve the reliability of the results by suppressing the effects of low frequency, large amplitude oscillations, especially in the horizontal velocity series.

On the basis of the observations, several field observations are suggested. Though the field observations are not mutually exclusive, practical problems of logistics may make them so, and thus they are listed separately:

i) A study of long waves (at tidal, inertial, and lower frequencies) trapped, scattered, and generated over the continental slope could be made with five stations at 20-kilometer spacings from 20 to 100 kilometers offshore, each equipped with recording current meters at 10-meter or 20-meter

vertical increments in the upper 100 meters and at 25-meter or 50-meter vertical increments below a depth of 100 meters. Each station should also be equipped with three recording thermographs at 5-meter increments (in order to define the temperature gradients) in the upper 15 to 25 meters of the water column. Since there is evidence for motions with periods of two days to two weeks, the record durations should be 100 to 200 days long. Bottom mounted pressure gauges at each site would assist in mapping the waveforms of the barotropic motions. Time series of atmospheric pressure and of the winds would be necessary for the interpretation of the results.

ii) A study of low frequency inertial-internal waveforms over the continental slope and shelf could be made with two parallel arrays separated by 10 to 40 kilometers in the alongshore direction, each with five stations at 18, 20, 24, 30, and 40 kilometers offshore, and each equipped with recording current meters and salinographs at 5-meter or 10-meter vertical increments in the upper 100 meters, and 10-meter or 20-meter vertical increments below. Within 20 meters of the bottom, a sensor spacing of 5 meters would be useful for detection of the "bounded beam" phenomenon predicted by Sandstrom (1966). Record durations of 25 to 50 days should

be adequate.

iii) A detailed study throughout the spectral band of inertial-internal waves in the coastal upwelling frontal zone and of the fine structure of the mean flow could be made with five stations at 6, 8, 11, 15, and 20 kilometers offshore, each with recording current meters and thermographs or salinographs at 5-meter or 10-meter vertical increments. Of particular interest is the study of the mean flow and of wave motions in the bottom and surface Ekman layers, as well as in the interior frontal layers, especially near the surface front. An increase in sampling rate to once per minute is necessary for defining the Väisälä-Brunt oscillations. Record durations of 15 to 30 days should be adequate.

iv) In conjunction with i) to iii), lunar-day anchor stations should be conducted alongside sensor sites. The measurement techniques employed on anchor stations should be extended to include STD's and pairs of profiling current meters. Of particular interest is the use of simultaneous anchor stations to study the temperature inversion and the dynamic stability in the frontal layer both over the continental slope and in the region of the most intense frontal slopes over the continental shelf, i.e., near the surface front 5 to 15 kilometers offshore. Simultaneous anchor stations taken 10 to 40

kilometers apart in the alongshore direction over the continental shelf and slope could answer, at least roughly, the questions about long-crestedness and directionality of the internal tides. More hydrographic casts to near the bottom over the continental slope and shelf are necessary to compute $E(x, z)$ in detail and to determine for which frequencies the bottom slopes are critical.

The above list suggests an abundance of sensors for three reasons:

i) To obtain a redundancy in sensors to guard against malfunctions and loss.

ii) To obtain spatial detail so the the modal structure and the coherence squared and phase of the waves can be studied carefully. With good vertical detail, the barotropic and baroclinic components can be accurately separated.

iii) With sufficient vertical detail, observations of horizontal velocity and vertical displacement would enable the calculation of horizontal energy flux through a vertical column. Also, Cauchy data as a function of frequency could be empirically determined at one site. Then, as a function of frequency, solutions to the mixed initial-boundary value problem could be calculated and compared to the observations at the other sensor sites.

The observations could be profitably attempted throughout the year because the seasonal effects are likely to be marked; the observations are also worth repeating in subsequent years. The recommendations listed do not exhaust the possibilities of observational objectives, of sensor types, or of observational design; the recommendations are restricted to topics discussed and to the instrumentation, with the exception of the recording salinographs, employed in this dissertation. For instance, the recommendations do not include the objective of linking the long-period variations in the flow regime to the atmospheric-forcing functions. They also do not include the observational technique of deploying Lagrangian current meters, e.g., parachute drogues or free-fall instruments, to map the offshore distribution of long-period horizontal displacements in the frontal zone and over the continental slope.

The linear theory for the interaction of an inertial-internal wave with a frontal zone has been derived, explored analytically for cases with variable coefficients, and solved for cases with constant coefficients and for a continental shelf with a rigid surface boundary and with parallel and sloping bottom boundaries. The technique of analytical extension of the Cauchy data is an effective means for the construction of solutions for cases of subcritical, critical, and supercritical bottom slopes, with either a rigid or a free sea surface boundary condition.

The principal properties of the inertial-internal wave solutions in the frontal zone of a coastal upwelling region are:

i) The frontal interaction gives the characteristics an asymmetry, which induces alternating zones of increased and decreased shear. The asymmetry also tilts the lines of constant phase within an effective wavelength for a progressive wave. The effective wavelength differs from the wavelength without the frontal interaction.

ii) A sloping bottom boundary, with subcritical slope, produces zones of ever-increasing shear in the waves upon successive reflections of the waves from the bottom. If the isopycnals are inclined in the same sense as the bottom boundary, the value of the critical bottom slope is greater than if $s = 0$. If they are inclined in the opposite sense, the value of the critical bottom slope is less than if $s = 0$. Thus, the upwarped isopycnals over the continental shelf during coastal upwelling season exert a stabilizing influence by tending to make the bottom slope subcritical. Conversely, when the isopycnals close to the bottom become downwarped, they tend to make the bottom slope supercritical.

iii) From i) and ii), temporal variations in the state of coastal upwelling alter the positions of the lines of constant phase, thus the phase stability of the waves is reduced. The

temporal variations also alter the criticality of the bottom slope, and, thus, probably the wave generation process.

iv) An inclined frontal layer affects the inertial-internal waves. The frontal layer serves as a waveguide. If the frontal layer is inclined, it can either open the inertial-internal wave passband to frequencies less than the inertial frequency or close the passband to frequencies greater than the inertial frequency, depending upon the sign of $(f\bar{v}_x - s^2N^2)$. The inclined frontal layer also opens the passband to frequencies greater than the Väisälä-Brunt frequency. Somewhat analogous to the concept of critical bottom slope, the concept of critical frontal slope, s_c, is introduced:

$$s_c^2 = \frac{-(N^2-\sigma^2)(\sigma^2 - f(f+\bar{v}_x))}{N^4},$$

where $s_c^2 > 0$ when $\sigma^2 > N^2$ and when $\sigma^2 < f(f+\bar{v}_x)$. For $s > s_c$, and for $N^2 < \sigma^2 < N^2(1+s^2)$ or $(f(f+\bar{v}_x) - s^2N^2) < \sigma^2 < f(f+\bar{v}_x)$, both the upgoing and downgoing characteristics are oriented either downwards or upwards, respectively. Waves for which $s > s_c$ are blocked by the inclined frontal layer, i.e., back reflection occurs from the sea surface or the sea bottom in the case of low frequency or high frequency waves, respectively.

v) The field of characteristics for the continental shelf off Depoe Bay, Oregon in August-September 1966 indicates that the semidiurnal internal tide had an effective wavelength of about 25 kilometers, measured onshore from the seaward edge of the continental shelf. It also indicates that the array of sensors spanned about a half wavelength of the semidiurnal internal tide and that very little bottom and frontal amplification of the wave occurred over the half wavelength, except near the surface front about 10 to 15 kilometers offshore. Both deductions are consistent with the time series analyses based on the observed time series. If observations had been made between 2 and 10 kilometers offshore, appreciable amplification of the wave would habe been observed, especially near the bottom and near the surface in the inclined frontal layer.

In a coastal upwelling region, an inertial-internal wave is amplified by bottom reflection and tends to be concentrated in the inclined frontal layer, thus the lowest values of dynamic stability are anticipated in the steepest part of the frontal layer over the continental shelf, i. e., near the surface front. Therefore, when coastal upwelling intensifies, which causes s and $|\bar{v}_x|$ to become greater, the conditions for low dynamic stability of the frontal layer caused by an internal tide are enhanced.

In the general case of variable coefficients, a sloping bottom,

a free surface, and the frontal interaction, the following general analyses have been made for inertial-internal waves over a continental shelf:

i) The action integral has been found by which the governing equation can be derived from the calculus of variations. This analysis has led to the identification of the horizontal and vertical components of the kinetic and potential energies and to a spatially-averaged equipartition principle.

ii) The energy integral has been derived. The horizontal energy flux is expressed in terms of the vertical integral of the time-averaged product of the two linearly independent elements of the Cauchy data. If the horizontal energy flux is zero, energy is conserved and a standing wave occurs over the shelf; if it is non-zero, energy is not conserved and a progressive wave occurs, whose direction of propagation is given by the sign of the horizontal energy flux. This analysis has led to the deduction that observations must be made which are equivalent to determining the vertical and temporal structure of the Cauchy data at the seaward edge of the shelf. Once the Cauchy data are determined, the solution theory can be used to construct the solution over the shelf with the temporal phase taken into account.

iii) The spatial conservation law has been derived; it determines the growth of the solution inshore of the initial line. The

interrelation between the Cauchy data, the bottom slope, the potential energy of the free surface, and the inhomogeneities of the mean velocity and density fields enter this analysis. The criticality of the bottom slope determines if the solution decays or grows spatially shoreward of the initial line. The sea surface boundary condition can play a crucial role in determining whether or not the energy of the wave becomes unbounded in the vertex of the coastal wedge for the case of subcritical bottom slopes; i.e., allowing the sea surface to be free and to have potential energy can remove the singularity in the velocity fields at the vertex.

iv) The analysis of baroclinic instability has been carried out from both the integral and the differential viewpoints. Not surprisingly, the conditions for instability coincide with those for frontal blocking.

The theoretical and observational studies suggest the following recommendations for future theoretical work:

i) An analytical assault on the inertial-internal wave generation problem in a coastal region is necessary. The problem should be considered in its full three-dimensional form and for a continuous density structure and a continuous bottom topography. Cases with and without the frontal interaction should be examined.

ii) The free surface boundary condition's capacity for removing the singularity in the velocity field at the vertex of a coastal wedge should be exploited for constructing solutions.

iii) The mean cross-stream flow should be introduced into the analysis of the frontal interaction, especially in shallow water where the advective acceleration terms may become significant.

iv) The frontal interaction problem should be considered for a slowly-varying mean flow. The analysis may be best conducted in wave number-frequency space, i.e., with the use of the techniques of geometrical optics and ray tracing.

v) The interaction of barotropic and baroclinic motions at the inertial and tidal frequencies should be examined.

vi) More observables should be developed, and the hypotheses used for the design of field observations should be refined.

BIBLIOGRAPHY

Abbott, Michael B. 1966. An introduction to the method of characteristics. New York, American Elsevier. 243 p.

Ball, F. K. 1964. Energy transfer between external and internal gravity waves. Journal of Fluid Mechanics 19(3):465-478.

Bateman, Harry. 1953. Higher transcendental functions. Vol. 1. New York, McGraw-Hill. 302 p.

Bendat, Julius S. and Allan G. Piersol. 1966. Measurement and analysis of random data. New York, John Wiley. 390 p.

Benjamin, T. Brooke. 1966. Internal waves of finite amplitude and permanent form. Journal of Fluid Mechanics 25(2):241-270.

Blackman, R. B. and J. W. Tukey. 1958. The measurement of power spectra. New York, Dover. 190 p.

Booker, John R. and Francis P. Bretherton. 1967. The critical layer for internal gravity waves in a shear flow. Journal of Fluid Mechanics 27(3):513-539.

Born, Max and Emil Wolf. 1965. Principles of optics. 3d Ed. Oxford, Pergamon. 808 p.

Boston, Noel E. J. 1964. Observations of tidal periodic internal waves over a three day period off Panama City, Florida. College Station, Tex. 44 numb. leaves. (Texas Agriculture and Mechanics University. Dept. of Oceanography and Meteorology. Reference 64-20T. Office of Naval Research Contract Nonr 2119(4))

Boussinesq, Joseph. 1903. Theorie analytique de la chaleur. Vol. 2. Paris, Gauthier-Villars. 625 p.

Bowden, K. R. 1965. Horizontal mixing in the sea due to a shearing current. Journal of Fluid Mechanics 21(2):83-95.

Brunt, D. 1927. The period of simple vertical oscillations in the atmosphere. Quarterly Journal of the Royal Meteorological Society 53(221):30-32.

Campbell, L. L. and A. Robinson. 1955. Mixed problems for hyperbolic partial differential equations. Proceedings of the London Mathematical Society 3(5):129-147.

Carsola, A. J., D. P. Hamm and J. C. Roque. 1965. Spectra of temperature fluctuations over the continental borderland off southern California. Deep-Sea Research 12(5):685-691.

Collins, Curtis Allan. 1964. Structure and kinematics of the permanent oceanic front off the Oregon coast. Master's thesis. Corvallis, Oregon State University. 53 numb. leaves.

Collins, Curtis Allan. 1968. Description of measurements of current velocity and temperature over the Oregon continental shelf, July 1965-February 1966. Ph. D. thesis. Corvallis, Oregon State University. 154 numb. leaves.

Collins, Curtis Allan, Christopher N. K. Mooers, Merrit R. Stevenson, Robert L. Smith and June G. Pattullo. 1968. Direct current measurements in the frontal zone of a coastal upwelling region. Journal of the Oceanographical Society of Japan 24(6):295-306.

Cooley, J. W. and J. W. Tukey. 1965. Algorithm for the machine calculation of complex Fourier series. Mathematics of Computation 19(90):297-301.

Copson, E. T. 1958. On the Riemann-Green function. Archive of Rational Mechanics and Analysis 1(4):324-348.

Courant, R. and D. Hilbert. 1962. Methods of mathematical physics. Vol. II. Partial differential equations. New York, Interscience. 830 p.

Cox, Charles S. 1962. Internal waves. Part II. In: The seas, ed. by M. N. Hill. Vol. 1. New York, Interscience. p. 752-763.

Cox, Charles S. and Helmuth Sandstrom. 1962. Coupling of internal and surface waves in water of variable depth. In: Journal of the Oceanographical Society of Japan, 20th Anniversary Volume, p. 499-513.

Cox, Charles S. 1968. Professor, University of California at San Diego, Dept. of Oceanography. Personal Communication. Woods Hole, Massachusetts. August 1968.

Davis, Russ E. and Andreas Acrivos. 1967. Solitary internal waves in deep water. Journal of Fluid Mechanics 29(3):593-607.

Defant, Albert. 1949. Internal tidal waves and their stability conditions. Archiv für Metorologie, Geophysik, und Bioklimatologie, ser. A, 1:39-61. (Translation issued by U. S. Naval Electronics Laboratory, San Diego)

Defant, Albert. 1961. Physical oceanography. New York, Macmillan. 2 vols.

Doodson, A. T. and H. D. Warburg. 1941. Admiralty manual of tides. London, Her Majesty's Stationery Office. 270 p.

Dowling, George B. 1966. Low frequency shallow water internal waves at Panama City, Florida. Panama City, Fla. 59 numb. leaves. (U. S. Navy Mine Defense Laboratory. Research Report no. 313)

Eckart, Carl. 1960. Hydrodynamics of oceans and atmospheres. New York, Pergamon. 290 p.

Eckart, Carl. 1961. Internal waves in the ocean. The Physics of Fluids 4(7):791-799.

Fjeldstad, Jonas Ekman. 1933. Interne wellen. Geofysiske Publikasjoner 10(6):1-35.

Fjeldstad, Jonas Ekman. 1958. Ocean currents as an initial problem. Geofysiske Publikasjoner 20(7):1-24.

Fjeldstad, Jonas Ekman. 1964. Internal waves of tidal origin. Part I. Theory and analysis of observations. Geofysiske Publikasjoner 25(5):1-73.

Fofonoff, Nicholas P. 1966. Internal waves of tidal period. Unpublished manuscript. Woods Hole, Mass. Woods Hole Oceanographic Institution. 8 numb. leaves.

Fofonoff, Nicholas P. 1968a. Current measurements from moored buoys, 1959-1965. Woods Hole, Mass. 12 p. (Woods Hole Oceanographic Institution. Reference no. 68-30)

Fofonoff, Nicholas P. 1968b. Measurements of internal waves from moored buoys. In: Notes on the 1968 Summer Study Program in Geophysical Fluid Dynamics at the Woods Hole Oceanographic Institution, Woods Hole, Mass. Vol. 1. p. 123-132.

Forsythe, George E. and Wolfgang R. Wasow. 1960. Finite-difference methods for partial differential equations. New York, John Wiley. 444 p.

Garabedian, Paul R. 1964. Partial differential equations. New York, John Wiley. 672 p.

Garret, C. J. R. 1968. On the interaction between internal gravity waves and a shear flow. Journal of Fluid Mechanics 34(4):711-720.

Gaul, Roy D. 1961. Observations of internal waves near Hudson Canyon. Journal of Geophysical Research 66(11):3821-3830.

Gelfand, I. M. and S. V. Fomin. 1963. Calculus of variations, tr. and ed. by Richard A. Silverman. Rev. English ed. Englewood Cliffs, N. J., Prentice-Hall. 232 p.

Godin, Gabriel. 1967. The analysis of current observations. The International Hydrographic Review 44(1):149-165.

Gossard, Earl and Walter Munk. 1954. On gravity waves in the atmosphere. Journal of Meteorology 11(4):259-269.

Gossard, Earl E. 1962. Vertical flux of energy into the lower ionosphere from inertial gravity waves generated in the troposphere. Journal of Geophysical Research 67(2):745-757.

Granger, C. W. J. 1964. Spectral analysis of economic time series. Princeton, Princeton University. 299 p.

Griscom, Clement A. 1965. The application of a perturbation technique to the nonlinear equations of internal wave motion and a comparison of the resultant theoretical wave forms with those observed in nature. New York. 58 numb. leaves. (New York University. Dept. of Meteorology and Oceanography. Geophysical Sciences Laboratory. Report 65-8 on Office of Naval Research Contract Nonr 285(57))

Groen, P. 1948. Contribution to the theory of internal waves. Mendelingen en Verhandelingen, ser. B, 2(11):1-23. (Koninklijk Nederlands Meteorologisch Instituut de Bilt (Nederland) No. 125)

Halpern, David. 1968. Observation of short period internal waves. (Abstract) Transactions of the American Geophysical Union 49(1):210-211.

Haurwitz, B. 1954. The occurrence of internal tides in the ocean. Archiv fur Meteorologie, Geophysik und Bioklimatolgie, ser. A: Meteorologie and Geophysik, 7:406-424.

Haurwitz, Bernard, Henry Stommel and Walter H. Munk. 1959. On the thermal unrest in the ocean. In: The atmosphere and the sea in motion, ed. by Bert Bolin. New York, Rockefeller Institute. p. 74-94.

Healey, David and Paul H. LeBlond. 1969. Internal wave propagation normal to a geostrophic current. Journal of Marine Research 27(1):85-98.

Huppert, H. E. 1968. On Kelvin-Helmholtz instability in a rotating fluid. Journal of Fluid Mechanics 33(2):353-359.

Ichiye, Takashi. 1963. Internal waves over a continental shelf. Tallahassee. 21 numb. leaves. (Florida State University. The Oceanographic Institute. Technical Report no. 3 on Office of Naval Research Contract Nonr 988(11) Project NR 083-16612-62.) (Unpublished manuscript)

Jenkins, Gwilym M. and Donald G. Watts. 1968. Spectral analysis and its applications. San Francisco, Holden-Day. 525 p.

Jones, Walter L. 1967. Propagation of internal gravity waves in fluids with shear flow and rotation. Journal of Fluid Mechanics 30(3):439-448.

Jones, Walter L. 1969. Ray tracing for internal gravity waves. Journal of Geophysical Research 74(8):2028-2033.

Kenyon, Kern E. 1968. Wave-wave interaction of surface and internal waves. Journal of Marine Research 26(3):208-231.

Keulegan, Garbis H. and Lloyd H. Carpenter. 1961. An experimental study of internal progressive oscillatory waves. Washington, D. C. 34 numb. leaves. (U. S. National Bureau of Standards. Report 7319)

Korgen, Benjamin J. 1968. Temperature and velocity fields near the deep ocean floor west of Oregon. Ph. D. thesis. Corvallis, Oregon State University. 155 numb. leaves.

Koshlyakov, N. S., M. M. Smirnov and E. B. Gliner. 1964. Differential equations of mathematical physics, tr. by Scripta Technica and tr. ed. by H. J. Eagle. Amsterdam, North-Holland. 701 p.

Krauss, W. 1966a. Internal tides off sourthern California (analysis of data obtained by NEL thermistor chain). San Diego. 53 numb. leaves. (U. S. Navy. Electronics Laboratory. NEL Report 1389)

Krauss, W. 1966b. Internal waves in the sea. In: Oceanography and Marine Biology: an annual review, ed. by Harold Barnes. 4:11-32.

Krauss, W. 1966c. Methoden und ergebnisse der theoretischen ozeanographie. Band II. Interne Wellen. Berlin-Nikolassee, Gerbü der Borntraeger. 248 p.

La Fond, E. C. 1961a. Boundary effects on the shape of internal temperature waves. Indian Journal of Meteorology and Geophysics 12:335-338.

La Fond, E. C. 1961b. Internal wave motion and its geological significance. In: Mahadevan Volume, a collection of geological papers in commemoration of the 61st birthday of Prof. C. Mahadevan. Hyderabad, Andhra Pradesh, India. Osmania University. p. 61-77.

La Fond, E. C. 1962. Internal waves. Part I. In: The seas, ed. by M. N. Hill. Vol. 1. New York, Interscience. p. 731-751.

Lamb, Horace. 1945. Hydrodynamics. 1st American ed. New York, Dover. 738 p.

Larsen, Jimmy Carl. 1966. Electric and magnetic fields induced by oceanic tidal motion. Ph. D. thesis. La Jolla, University of California at San Diego. 99 numb. leaves.

Larsen, Jimmy Carl. 1969. Long waves along a single-step topography in a semi-infinite uniformly rotating ocean. Journal of Marine Research 27(1):1-6.

Le Blond, Paul H. 1966. On the damping of internal gravity waves in a continuously stratified ocean. Journal of Fluid Mechanics 25(1):121-142.

Lee, Owen S. 1961. Observations on internal waves in shallow water. Limnology and Oceanography 6(3):312-321.

Lee, Owen S. 1965. Internal waves in the sea (a summary of published information with notes on applications to naval operations). San Diego. 58 numb. leaves. (U. S. Navy. Electronics Laboratory. NEL Report 1302)

Lin, C. C. 1967. The theory of hydrodynamic stability. Cambridge, Cambridge University. 155 p.

Long, Robert R. 1965. On the Boussinesq approximation and its role in the theory of internal waves. Tellus 17(1):46-52.

Longuet-Higgins, M. S. 1968a. On the trapping of waves along a discontinuity of depth in a rotating ocean. Journal of Fluid Mechanics 31(3):417-434.

Longuet-Higgins, M. S. 1968b. Double Kelvin waves with continuous depth profiles. Journal of Fluid Mechanics 34(1):49-80.

Longuet-Higgins, M. S. 1969. On the reflection of wave characteristics from rough surfaces. Journal of Fluid Mechanics. (In press)

Magaard, Lorenz. 1962. Zur Berechnung interner Wellen in Meeresräumen mit nicht-ebenen Böden bei einer speziellen Dichtererteilung. Kieler Meeresforschungen 18:151-183. (Draft translation prepared for the author by Miss Ute Gorner, Research Associate, Dept. of Oceanography, Oregon State University)

Magaard, Lorenz. 1963. Baroclinic instability. In: Notes on the 1963 Summer Study Program in Geophysical Fluid Dynamics at the Woods Hole Oceanographic Institution, Woods Hole, Mass. Vol. 2. p. 63-79.

Malone, Frank D. 1968. An analysis of current measurements in Lake Michigan. Journal of Geophysical Research 73(22):7065-7081.

Mesecar, Roderick Smit. 1968. Oceanic vertical temperature measurements across the water-sediment interface at selected stations west of Oregon. Ph. D. thesis. Corvallis, Oregon State University. 99 numb. leaves.

Miles, John W. 1961. On the stability of heterogeneous shear flows. Journal of Fluid Mechanics 10(4):496-508.

Miles, John W. 1967. Surface-wave scattering matrix for a shelf. Journal of Fluid Mechanics 28(4):755-767.

Mooers, Christopher N. K. 1968. Cross-stream flows in continuous f-plane frontal models, with application to coastal upwelling fronts. In: Notes on the 1968 Summer Study Program in Geophysical Fluid Dynamics at the Woods Hole Oceanographic Institution, Woods Hole, Mass. Vol. 2. p. 105-142.

Mooers, Christopher N. K., Lillie M. Bogert, Robert L. Smith and June G. Pattullo. 1968. A compilation of observations from moored current meters and thermographs (and of complementary oceanographic and atmospheric data). Corvallis. 98 numb. leaves. (Oregon State University. Dept. of Oceanography. Data report No. 30 on National Science Foundation Grant GA 331, Reference 68-5, June 1968)

Mooers, Christopher N. K. and Robert L. Smith. 1968. Continental shelf waves off Oregon. Journal of Geophysical Research 73(2): 549-557.

Mooers, Christopher N. K., Robert L. Smith, Curtis A. Collins and June G. Pattullo. 1969. Dynamical interpretation of the frontal zone in a coastal upwelling region. (In preparation)

Mortimer, C. H. 1963. Frontiers in physical limnology with particular reference to long waves in rotating basins. In: Publication Number 10, Great Lakes Res. Div. Ann Arbor, Michigan. The University of Michigan. p. 9-49.

Munk, Walter H. 1950. On the wind-driven ocean circulation. Journal of Meteorology 7(2):79-93.

Munk, Walter H., F. Snodgrass and F. Gilbert. 1964. Long waves on the continental shelf: an experiment to separate trapped and leaky modes. Journal of Fluid Mechanics 20(4):529-554.

Munk, Walter H. 1966. Abyssal recipes. Deep-Sea Research 13(4):707-730.

Munk, Walter H. and Norman Phillips. 1968. Coherence and band-structure of inertial motion in the sea. Reviews of Geophysics 6(4):447-472.

Munk, Walter H. 1969. Professor, University of California at San Diego. Institute of Geophysics and Planetary Physics. Personal Communication. 9 May 1969.

Mysak, Lawrence A. 1967. On the theory of continental shelf waves. Journal of Marine Research 25(3):205-227.

Mysak, Lawrence A. 1968. Edgewaves on a gently-sloping, finite-width continental shelf. Journal of Marine Research 26(1):24-33.

Neudeck, Roger. 1969. Photographic study of sediment rippling and scouring mechanisms operating on the continental margin off Oregon and their geological significance (tentative title). Master's thesis. Corvallis, Oregon State University. (In preparation)

Neumann, Gerhard. 1949. Oscillations of stability and the internal thermal agitation in the sea and in the atmosphere. Deutsche Hydrographische Zeitschrift 2(1/2/3):52-67.

Orlanski, Isidoro. 1968a. The influence of bottom topography on the stability of jets in a baroclinic fluid. Unpublished manuscript prepared by the Geophysical Fluid Dynamics Laboratory of the Environmental Science Services Administration, Princeton, New Jersey. 33 numb. leaves.

Orlanski, Isidoro. 1968b. Instability of frontal waves. Journal of Atmospheric Sciences 25(2):178-200.

Ozimidov, R. V. and A. D. Yampolskii. 1965. Some statistical characteristics of velocity and density fluctuations in the ocean. Atmospheric and Oceanic Physics Series 1(6):357-360. (Translated from Akademiia Nauk SSSR, Izvestiia, Fizika Atmosfery I Okeana)

Pak, Hasong, George F. Beardsley, Jr. and Robert L. Smith. 1969. An optical and hydrographic study of a temperature inversion off Oregon during upwelling. (Submitted to Journal of Geophysical Research)

Panofsky, H. A. 1967. Meteorological applications of cross-spectrum analysis. In: Spectral analysis of time series, ed. by Bernard Harris. New York, John Wiley. p. 109-132.

Pattullo, June G. and W. B. McAlister. 1962. Evidence for oceanic frontogenesis off Oregon. Science 135(3498):106-107.

Pavlova, Yu. V. 1966. Seasonal variations of the California current. Oceanology 6(6):806-814. (Translated from Okeanologia)

Pettersson, Otto. 1934. Tide problem. IV. The internal parallactic tide, a study in geophysics. Arkiv für Matematik, Astronomi och Fysik 25A(1):1-13. (Translated by David Kraus for Geophysics Research Directorate, AF Cambridge Research Center, Cambridge, Mass.)

Phillips, Owen M. 1966. The dynamics of the upper ocean. Cambridge, Cambridge University. 261 p.

Phillips, Owen M. 1968. The interaction trapping of internal gravity waves. Journal of Fluid Mechanics 34(2):407-416.

Pollard, R. T. 1968. On the generation by winds of inertial waves in the ocean. Ph. D. dissertation. Cambridge, England, University of Cambridge. 105 numb. leaves.

Proudman, J. 1952. Dynamical oceanography. New York, Dover. 409 p.

Radok, Rainer, W. Munk and J. Issacs. 1967. A note on mid-ocean internal tides. Deep-Sea Research 14(1):121-124.

Rattray, Maurice, Jr. 1960. On the coastal generation of internal tides. Tellus 22(1):54-62.

Reid, Robert O. 1958. Effect of Coriolis force on edge waves. I. Investigation of the normal modes. Journal of Marine Research 16(2):109-144.

Rhines, Peter B. 1963. Internal waves with stratification and an inclined rotation vector. In: Notes on the 1963 Summer Study Program in Geophysical Fluid Dynamics at the Woods Hole Oceanographic Institution, Woods Hole, Mass. Vol. 3. Woods Hole. p. 81-94.

Richardson, Lewis F. 1920. The supply of energy from and to atmospheric eddies. Proceedings of the Royal Society (London), ser. A, 97(686):354-373.

Robinson, Alan R. 1964. Continental shelf waves and the response of sea level to weather systems. Journal of Geophysical Research 69(2):367-368.

Sandstrom, Helmuth. 1966. The importance of topography in generation and propagation of internal waves. Ph. D. thesis. La Jolla, University of California at San Diego. 105 numb. leaves. (Microfilm-zerography)

Seidler, Gerold. 1968. Visiting Scientist. Woods Hole Oceanographic Institution. Personal Communication. Woods Hole, Mass.

Shen, M. C. 1967. On long waves with cross-wind in an atmosphere. Journal of Fluid Mechanics 28(3):481-492.

Smith, Robert L. 1964. An investigation of upwelling along the Oregon Coast. Ph. D. thesis. Corvallis, Oregon State University. 83 numb. leaves.

Smith, Robert L., June G. Patullo and Robert K. Lane. 1966. An investigation of upwelling along the Oregon coast. Journal of Geophysical Research 71:1135-1140.

Smith, Robert L. 1968. Upwelling. In: Oceanography and Marine Biology: an annual review, ed. by Harold Barnes. 6:11-46.

Sneddon, Ian N. 1957. Elements of partial differential equations. New York, McGraw-Hill. 327 p.

Starr, Victor P. 1968. Physics of negative viscosity phenomena. New York, McGraw-Hill. 256 p.

Stern, Melvin E. 1961. The stability of thermoclinic jets. Tellus 13(4):503-508.

Stommel, Henry. 1965. The Gulf Stream, a physical and dynamical description. 2d ed. Berkley, University of California. 248 p.

Summers, H. J. and K. O. Emery. 1963. Internal waves of tidal period off Southern California. Journal of Geophysical Research 68(3):827-839.

Tareev, B. A. 1963. Concerning internal waves in an inhomogeneous ocean. Akademiia Nank, SSSR Doklady, ser. A, 149(4):827-830.

Thorpe, S. A. 1966. On wave interactions in a stratified fluid. Journal of Fluid Mechanics 24(4):737-751.

Tick, Leo J. 1967. Estimation of coherency. In: Spectral analysis of time series, ed. by Bernard Harris. New York, John Wiley. p. 133-152.

Tikhonov, A. N. and A. A. Samarskii. 1963. Equations of mathematical physics, tr. by A. R. M. Robson and P. Basu and tr. ed. by D. M. Brink. Oxford, Pergamon. 765 p.

Tolstoy, Ivan. 1963. The theory of waves in stratified fluids including the effects of gravity and rotation. Reviews of Modern Physics 35(1):207-230.

Väisälä, Vilho. 1925. Über die Wirkung der Windschwankungen aut die Pilobtbeobachtungen. Finska. Vetenskaas-Societatch, Helsingfors, Fennica, Commentationes Physico-Mathematicae 2(19):38-?.

Vapnyar, D. U. 1964. Theoretical model and physical structure of internal tidal waves. Soviet Oceanography 3:1-17. (Translated from Trudy, Morskovo Gidrofisicheskovo Institut)

Warner, James. 1968. Currents over the Scotian shelf. Paper presented at the Physical Oceanography Seminar, Woods Hole Oceanographic Institution, Woods Hole, Mass., Sept. 20, 1968.

Webster, Ferris T. 1965. Measurements of eddy fluxes of momentum in the surface layer of the Gulf Stream. Tellus 17(2):239-245.

Webster, Ferris T. 1968a. Observations of inertia-period motions in the deep sea. Reviews of Geophysics 6(4):473-490.

Webster, Ferris T. 1968b. On the representativeness of direct deep-sea current measurements. Progress in Oceanography. (In press)

Weigand, James Gary. 1962. A model study of internal waves. Mater's thesis. Seattle, University of Washington. 52 numb. leaves.

Weigand, James Gary. 1964. The generation of internal waves by long surface waves. Ph. D. thesis. Seattle, University of Washington. 78 numb. leaves. (Microfilm zerography)

Woods, J. D. 1968. Wave-induced shear instability in the summer thermocline. Journal of Fluid Mechanics 32(4):791-800.

Wooster, Warren S. and Joseph L. Reid, Jr. 1963. Eastern boundary currents. In: The seas, ed. by M. N. Hill. Vol. 2. New York, Interscience. p. 253-280.

Wunsch, Carl. 1968. On the propagation of internal waves up a slope. Deep-Sea Research 15(2):251-258.

Wunsch, Carl. 1969. Progressive internal waves on slopes. Journal of Fluid Mechanics 35(1):131-144.

Yanowitch, Michael. 1962. Gravity waves in a heterogeneous incompressible fluid. Communications on Pure and Applied Mathematics 15(1):45-61.

Yasui, Masashi. 1961. Internal waves in the open ocean. The Oceanographical Magazine 12(2):157-183.

Yih, Chia-Shun. 1965. Dynamics of nonhomogeneous fluids. New York, MacMillan. 306 p.

Yoshida, Kozo and Mizuki Tsuchiya. 1957. Northward flow in lower layers as an indicator of coastal upwelling. Records of Oceanographic Works in Japan 4(1):14-22.

Yoshida, Kozo. 1967. Circulation in the eastern tropical oceans with special references to upwelling and undercurrents. Japanese Journal of Geophysics 4(2):1-75.

Zeilon, Nils. 1934. Experiments on boundary tides. Goteborgs Kungliga Vetenskaps-och Vitterhets-Samhäles Handlingar Femte Följden, ser. 8, 3(10):3-8.

APPENDICES

APPENDIX I

Long Wave Propagation Along a Meridional Boundary

The long wave of primary interest in this study is the semidiurnal tide, yet there are energy peaks in the spectra of Chapter XI at the diurnal, inertial, quarterdiurnal, and other frequencies. Though internal tides are the chief concern of this study, the surface tides have contributed to the spectra of Chapter XI. Also, the surface tides are the ultimate source of the internal tides. For these reasons, the classes of barotropic and baroclinic motion along a coastal boundary oriented parallel to a meridian of longtidue are examined. The objectives are primarily qualitative.

The alongshore wavenumber, ℓ, is not neglected in the following. The topics to be examined are:

i) For the interpretation of the spectra in Chapter XI, the permissible classes of barotropic (in Section A) and baroclinic (in Section B) waves along a meridional boundary with variable depth.

ii) For the exploration of the theory for the three-dimensional problem, the matching of solutions to the inertial-internal wave problem over the continental shelf and slope to those for deep water.

iii) Also for the interpretation of the spectra in Chapter XI, the

spectral and hodograph observables for a simple coastal model (in Sections C and D).

The permissible motions are those basic solutions to the linearized hydrodynamical equations which have no mass flux across the coastal boundary and for which the sea surface and the normal component of the mass flux are continuous at each variation in bottom topography. The BC's place constraints on the solutions which lead to eigenvalue problems and dispersion relations. The general problem types are those of partial reflection of a wave at a vertical barrier and of wave trapping by the barrier. The coastline, depth variations, and pycnoclines all have waveguide effects. The first two effects are analyzed to gain some insight into topographically leaky and trapped modes; the waveguide effects of density variations have been discussed in the text.

Waves with a functional form for the surface displacement, ζ, of $\zeta = F(x, z) \cos(\sigma t - \ell y)$ are assumed. An infinitely long coastline parallel to the y-axis is also assumed, with a monotonic depth, $z_B = -h(x)$, variation in the x-direction only, such that $h_x \leq 0$. $\beta = \frac{df}{dy}$ and f_h are neglected, and f_v is represented by the symbol f.

A. Barotropic Cases

In a barotropic, inviscid, rotating system the linearized

equations of motion are:

EOM's

(1) $$0 = -\pi_z - g, \quad \text{thus} \quad \pi(z) = g(\zeta - z),$$

i. e., hydrostatic equilibrium is assumed,

(2) $$u_t - fv = -\pi_x = -g\zeta_x,$$

and

(3) $$v_t + fu = -\pi_y = -g\zeta_y.$$

With h equal to the time-averaged depth, the linearized, vertically integrated EOC is:

(4) EOC: $$(hu)_x + (hv)_y + \zeta_t = 0, \quad \text{or} \quad \vec{\nabla}_H \cdot (h\vec{U}) = -\zeta_t,$$

where u and v are the depth-averaged horizontal velocity components and $\vec{U} = (u, v)$. Since $F(x, z) = F(x)$ in barotropic cases, and using (2) and (3), the equation for the horizontal velocity components are

(5) $$u = \frac{g}{(\sigma^2 - f^2)}[-\sigma F_x + f\ell F] \sin(\sigma t - \ell y)$$

and

(6) $$v = \frac{g}{(\sigma^2 - f^2)}[\sigma\ell F - fF_x] \cos(\sigma t - \ell y).$$

Substituting (5) and (6) into (4), the GE is obtained:

GE: $$(hF_x)_x + Q(x)F = 0,$$

where

$$Q(x) = \left[\frac{\sigma^2 - f^2}{g} - \frac{f\ell}{\sigma} h_x - \ell^2 h\right].$$

The GE is a Sturm-Liouville equation. With the BC's, i.e., $|\zeta| < \infty$ $(x \to -\infty)$ and hu, or $h(f\ell\zeta - \sigma\zeta_x)$, $\to 0$ $(x \to 0)$ and the fact that $h \to 0$ $(x \to 0)$, the problem constitutes a singular Sturm-Liouville system. The solutions depend upon the sign of $Q(x)$; their x-dependence is sinusoidal-like where $Q > 0$ and exponential-like where $Q < 0$.

Forming the energy equation from the primitive equations,

$$\rho_o h\left(\frac{u^2+v^2}{2}\right)_t = -\rho_o gh[u\zeta_x + v\zeta_y] = -\rho_o g(h\vec{U}) \cdot \nabla_H \zeta$$

and then integrating over a horizontal area, S:

$$\rho_o \int_S h\left(\frac{u^2+v^2}{2}\right)_t dxdy = -\rho_o g\left[\int_B (h\vec{U})\zeta \cdot d\vec{s} - \int_S \zeta \vec{\nabla}_H \cdot (h\vec{U})dxdy\right],$$

if $h\vec{U}\zeta$ is continuous, and where B is the bounding curve of S and $d\vec{s}$ is the incremental arc length along B. With use of the EOC:

$$\rho_o \int_S h\left[\frac{u^2+v^2}{2} + \frac{g\zeta^2}{2}\right]_t dxdy = -\rho_o g \int_B (h\vec{U})\zeta \cdot d\vec{s},$$

The total energy E is E = KE + PE, where

$$KE = \rho_o \frac{u^2+v^2}{2} \quad \text{and} \quad PE = \rho_o g \frac{\zeta^2}{2}.$$

E is conserved if the normal component of the energy flux, $\rho_o h\vec{U}\zeta \cdot \hat{n}$, vanishes on boundaries and if $\rho_o h\vec{U}\zeta \cdot \hat{n}$ is continuous which is assured if $h\vec{U}$ and ζ are separately continuous.

For uniform depth, and with the assumption of SHM, i. e., $F(x) \propto e^{ikx}$, the CR is

$$gh[k^2+\ell^2] - (\sigma^2-f^2) = 0$$

or,

$$k^2 = \frac{\sigma^2-f^2}{gh} - \ell^2.$$

If $\sigma > f$, plane waves occur for $k^2 > 0$; they are called Poincare waves and $\ell > 0$ or $\ell < 0$. The high cut-off wave number, ℓ_{co}, is obtained when $k = 0$, so

$$\ell_{co} = \pm \left(\frac{\sigma^2-f^2}{gh}\right)^{1/2}.$$

Thus, ℓ_{co} decreases to zero as $\sigma \to f$ and as $h \to \infty$. Exponentially damped waves occur for $\ell > \ell_{co}$; they are called Kelvin waves, for which $k^2 < 0$ and $\ell > 0$ only. For σ and ℓ fixed, k increases as h decreases; thus, a wave is refracted as it propagates shoreward, i. e., the orientation of wavefronts is

aligned parallel to the coastline as shallow water is approached.

General Topography. As a consequence of requiring hu and ζ, or, equivalently, $h[-\sigma F_x + f\ell F]$ and F, to be continuous functions of x, hv is discontinuous where h is discontinuous. Therefore, a depth discontinuity produces a vortex sheet, and a variation in depth produces horizontal shears in the flow component tangential to the depth variation.

Reid (1958) analyzed the GE for gently-sloping bottoms of semi-infinite extent, i.e., in the case of $h(x) = mx$, $-\infty \leq x \leq 0$, where $m > 0$ is the bottom slope. When $\sigma > f$, ℓ has a positive and a negative roots. When $\sigma < f$, ℓ has only positive roots. When $\sigma = f$, a singular case occurs which is discussed below. For $\sigma > f$, Reid termed the permissible north- and south-going modes free edge waves; for $\sigma < f$, Reid termed the north-going wave a quasi-geostrophic edge wave. Recently, Robinson (1964), Mysak (1967, 1968), and Longuet-Higgins (1967, 1968) have examined the case of $\sigma < f$ in greater generality; they have considered the effect of a depth transition of finite width on wave trapping. Robinson and Mysak have discovered continental shelf waves theoretically which are different from the quasi-geostrophic waves; they are due to a resonance involving the finite shelf width, the Coriolis force, and the alongshore wavelength of the atmospheric excitation function. Mysak (1968) discussed his results, and the results of Reid,

in a unified fashion. The phase speed, c, of the two types of low-frequency waves is greatly different: for quasi-geostrophic waves $c_q = gm/f \sim 10^5$ cm/sec, while for continental shelf waves $c_c = Lf \sim 2 \times 10^2$ cm/sec. For an ordinary Kelvin wave, $c_k = (gh)^{1/2} \sim 1.7 \times 10^4$ cm/sec, thus $c_k \approx (c_q c_c)^{1/2}$. Mooers and Smith (1968) have detected continental shelf waves off Oregon; since the period of continental shelf waves is of the order of several days, these waves are not in the spectral band of interest to the present study. Longuet-Higgins' studies (1967, 1968) are general analyses of double Kelvin waves, which can only propagate northwards along a topographical barrier in the Northern Hemisphere. He has studied these waves for an infinite domain, $-\infty \leq x \leq +\infty$, with the geometry $h \to h^+, h^- < \infty$, $x \to \pm\infty$ and with the BC's $\zeta \to 0$, $|x| \to \infty$ hence they are not strictly applicable to waves trapped on a coastline. They exhibit much the same qualitative behavior as that of the other low frequency, topographically trapped waves mentioned, viz. the inertial frequency is the upper frequency bound and the zero frequency is the lower frequency bound for the first mode. Of special significance is the fact that the double Kelvin waves are predicted to produce jet-like currents over a continental slope.

Sketches of the depth profile and Q(x) off Depoe Bay, Oregon, are given in Figures 38a and b, respectively. The bottom profile is based on Coast and Geodetic Survey Chart No. 1308N-22, 1968; it

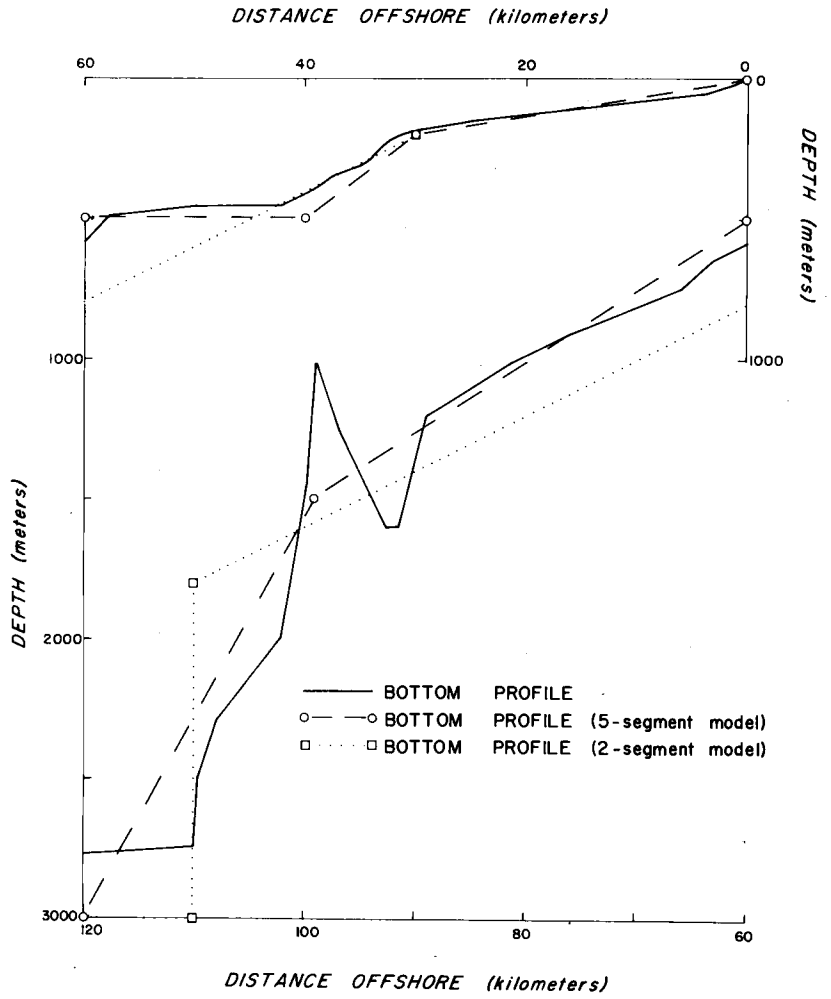

Figure 38a. Depth profile off Depoe Bay, Oregon.

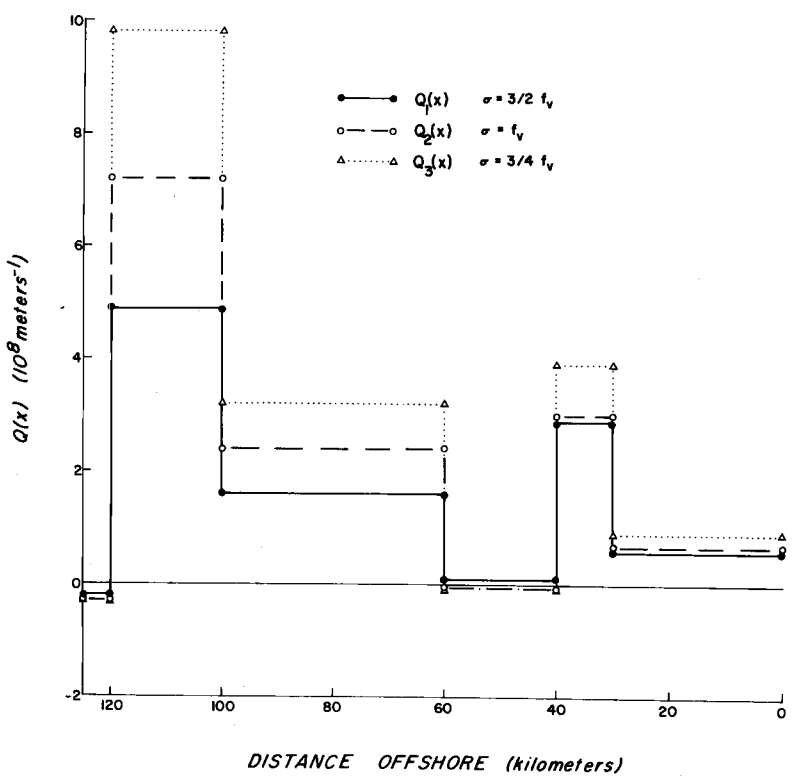

Figure 38b. The function Q(x) off Depoe Bay, Oregon.

corresponds to the Depoe Bay hydrographic line, which is oriented normal to the bottom contours. The upper portion of the figure shows the bottom profile from the coastline to 60 kilometers offshore, while the lower portion of the figure shows the bottom profile from 60 to 120 kilometers offshore, which is effectively in deep water. The bottom profile has been approximated by a 5-segment and by a 2-segment model. The 5-segment model was used in the plot of $Q(x)$. The 2-segment model was used for the calculation of the dispersion law for inertial Kelvin waves. A single-step model has also been used for dispersion calculations for the semidiurnal tide and other frequencies of interest. The parameters of the models are tabulated below:

Bottom profile parameters

Distance offshore (kilometers)	Depth (meters)	Slope (x 10^2)
5-Segment Model		
0	0	0.67
30	200	3
40	500	0
60	500	2.5
100	1500	7.5
$\geq$120	3000	
2-Segment Model		
0	0	0.67
30	200	2
110	1800	∞
$\geq$110	3000	
Single-Step Model		
0	200	
30		∞
$\geq$ 30	3000	

There are an infinite number of discrete values of ℓ permissible for a fixed σ and a given $h(x)$. The value of ℓ chosen, $\ell = 10^{-8}\,cm^{-1}$, is an order of magnitude estimate for the lowest mode of the semidiurnal tide, but there is no reason to believe that it corresponds exactly to a permissible ℓ. $Q(x)$ is plotted for $\sigma = 3/4\,f$, f, and $3/2\,f$, where $f = 10^{-4}\,sec^{-1}$, to indicate its form for the diurnal, inertial, and semidiurnal motions, respectively. Where $Q(x) > 0$, the region has the nature of a potential well. It is remarked that

i) Potential wells occur over the continental shelf, the upper reach of the continental slope, and the lower reach of the continental slope,

ii) The potential wells have their greatest and least values for the diurnal and semidiurnal frequencies, respectively, and

iii) The potential wells have their greatest and least values over the lower reaches of the continental slope and over the continental shelf, respectively.

On the basis of $Q(x)$, waves at the three frequencies are expected to be most strongly trapped over the lower reaches of the continental slope; a secondary wave trap is expected over the upper reaches of the continental slope.

Inertial Kelvin Waves. The degenerate case, $\sigma = f$, serves to introduce Kelvin waves. Take $\zeta = Ae^{\ell x}\cos(ft - \ell y)$; substitute

ζ and $u = u(x) \sin(ft-\ell y)$ into (2) to find v:

$$v = [g\frac{\ell A}{f} e^{\ell x} + u(x)] \cos(ft-\ell y).$$

Substituting v into the EOC, and dropping the common $\sin(ft-\ell y)$ factor, then

$$(hu)_x + h\ell[\frac{g\ell}{f} Ae^{\ell x} + u] - fAe^{\ell x} = 0$$

or

$$(hue^{\ell x})_x = (f - g\frac{h\ell^2}{f})Ae^{2\ell x}.$$

With the BC $hu = 0$ at $x = 0$, then

$$hu = Ae^{-\ell x}[\frac{f}{2\ell}(e^{2\ell x} - 1) - \frac{g\ell^2}{f}\int_0^x e^{2\ell x} h(x)dx].$$

Since $|hu| \overset{\text{(must)}}{<} \infty$ as $x \to -\infty$, then

$$f^2 + 2g\ell^3 \int_0^{-\infty} e^{2\ell x} h(x)dx = 0,$$

which is the dispersion relation. At the coast,

$$(hv)_{x=0} = A\frac{g\ell h(0)}{f} = 0.$$

In the deep ocean, $(hv) \to 0$ as $x \to -\infty$, by the dispersion relation. Using the parameters from the 2-segment model to represent the bottom

profile off Depoe Bay, Oregon, the dispersion relation yields:

$$\ell = 6.1 \times 10^{-9} \text{cm}^{-1}.$$

When the continental shelf and slope are neglected, the dispersion relation for uniform depth,

$$\ell = \frac{f}{(gh)^{1/2}},$$

yields $\ell = 5.8 \times 10^{-9} \text{cm}^{-1}$, hence there is only a 5% increase in wave number when variable depth is considered in this case. Yet, the solutions for variable depth have more interesting functional forms than those for uniform depth, which require $u(x) = 0$ for all x, as seen below. The functions $u(x)$ and $v(x)$ are plotted in Figure 39. The shear-inducing effect of variable depth is apparent. $u(x)$ has its greatest values over the continental shelf, while $v(x)$ has its greatest value at the boundary between the continental slope and the deep ocean. Over the continental shelf, the wave's hodograph has an eccentricity of about 0.5 and rotates anticlockwise. This case is rather unrealistic since it neglects the beta effect, thus it is only valid at a single latitude. The model is not consistent with the observations reported in Chapter XI.

Uniform Depth. The case of uniform depth admits Kelvin wave and standing wave solutions, which are the basic building blocks for the case of stepped topography, which is considered next. The Kelvin

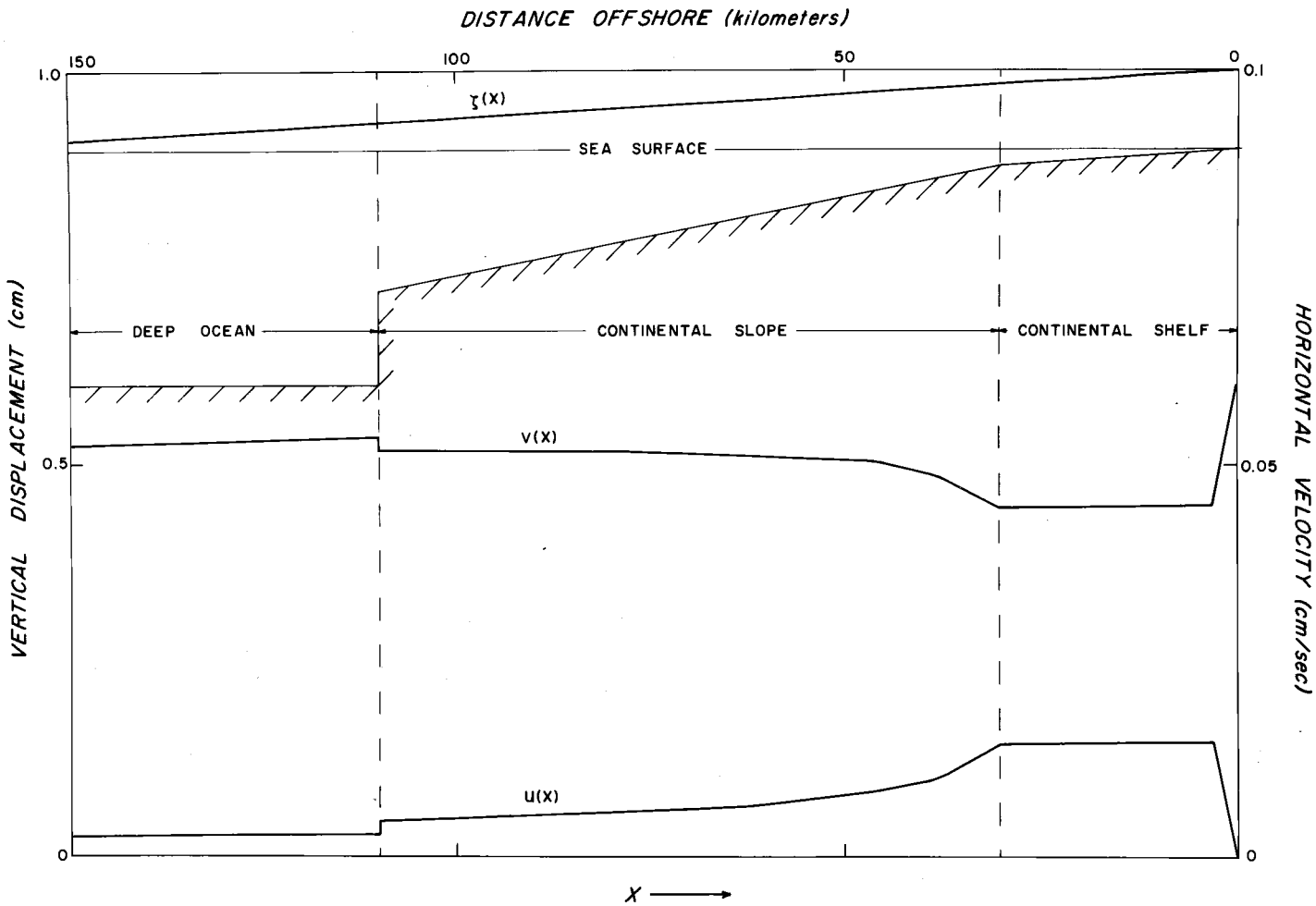

Figure 39. Theoretical velocity field for a barotropic inertial Kelvin wave off Depoe Bay, Oregon. (Normalized to a 1 cm sea surface amplitude at the coastline.)

wave case is limited by the fact that u (must) $= 0$ at $x = 0$, which implies, from (5), that $-\sigma F_x + f\ell F = 0$. The form for F then implies that $u = 0$ for all x. In this case, v is determined from (6):

$$v = \frac{g\ell}{\sigma} Ae^{\frac{f\ell}{\sigma}x} \cos(\sigma t - \ell y).$$

The EOC yields the dispersion relation:

$$\ell = \frac{\sigma}{(gh)^{1/2}} .$$

For standing waves, $-\sigma F_x + f\ell F = 0$ implies that, for $F = A \sin(kx) + B \cos(kx)$, then

$$\frac{A}{B} = \frac{f\ell}{\sigma k} .$$

From the CR,

$$k^2 + \ell^2 - \frac{(\sigma^2 - f^2)}{gh} = 0,$$

there are Poincare wave solutions for $\sigma > f$; for Poincare waves, ℓ is not constrained to be positive. When $\sigma < (f^2 + gh\ell^2)^{1/2}$, k becomes imaginary and only Kelvin waves are permissible.

Thus, in the degenerate case of uniform depth, the topographic waves have their recognizable counterparts:

i) In a gross sense, the quasi-geostrophic waves become the Kelvin waves but exist for all σ.

ii) The edge waves become the Poincare waves.

Stepped Bottom. A single topographical step is considered, though the analysis is readily extended to an arbitrary number of steps (Munk, Snodgrass, and Gilbert, 1964). The depth is given by

$$h(x) = \begin{cases} h_S, \; S : x \in (0 \leq x < L), & \text{where } S \text{ is shallow water} \\ h_D, \; D : x \in (-\infty \leq x < 0), & \text{where } D \text{ is deep water.} \end{cases}$$

The CR's for regions S and D are

$$(\sigma^2 - f^2) = gh_S(k_S^2 + \ell^2)$$

and

$$(\sigma^2 - f^2) = gh_D(k_D^2 + \ell^2).$$

Then

$$h_S(k_S^2 + \ell^2) = h_D(k_D^2 + \ell^2),$$

thus

$$k_S^2 = \frac{h_D}{h_S} k_D^2 + (\frac{h_D}{h_S} - 1)\ell^2 > k_D^2, \quad \text{since} \quad h_D > h_S.$$

As noted by Ichiye (1963), for $\sigma > f$, the case divides into three subcases:

I: $0 < k_D^2 < k_S^2$, yielding Poincare waves in D and S, thus there are a total of four waves possible (two in D and

two in S),

II: $k_D^2 < 0 < k_S^2$, yielding Kelvin waves in D and Poincare waves in S, thus there are a total of three waves possible (one in D and two in S), and

III: $k_D^2 < k_S^2 < 0$, yielding Kelvin-type waves in both D and S, thus there are a total of three waves possible (one in D and two in S).

It is recognized that

i) There can be waves from D incident on S with complete or partial reflection, subcase I.

ii) There can be waves in S which "leak" to D, subcase I above without an incident wave in D.

iii) There can be waves trapped on the continental shelf, subcases II and III above.

The BC's are then:

i) No net mass flux across the coastline,

$$h_S u_S \Big|_{x=L} = 0,$$

ii) Continuity of the sea surface at the shelf edge,

$$\zeta_D \Big|_{x=0} = \zeta_S \Big|_{x=0},$$

and

iii) Continuity of mass flux at the shelf edge,

$$h_D u_D\Big|_{x=0} = h_S u_S\Big|_{x=0}.$$

There are three BC's to be satisfied and from three to four possible waves. The following notation is used for the various wave types S_a and D_a, where S_a and D_a are amplitudes of waves in regions S and D, respectively. a = I, R, or K, which denote incident-plane, reflected-plane and Kelvin waves, respectively. Incident waves propagate in the positive x-direction and reflected waves in the negative x-direction.

Subcase I (Poincare waves only): The surface displacements in S and D are

$$\zeta_S = [S_I e^{-ik_S x} + S_R e^{ik_S x}] \cos(\sigma t - \ell y)$$

and

$$\zeta_D = [D_I e^{-ik_D x} + D_R e^{ik_D x}] \cos(\sigma t - \ell y),$$

respectively. This case admits several possible subcases but, barring waves with complex wave numbers and waves confined to the shelf, the leaky mode subcase is of most interest, i.e., where $\zeta_D = D_o \cos(k_D x + \theta) \cos(\sigma t - \ell y)$.

Application of the three BC's leads to:

i) $S_I e^{i(\phi - k_S L)} + S_R e^{-i(\phi - k_S L)} = 0,$

where $\phi = \tan^{-1}\left(\frac{\sigma k_S}{f\ell}\right)$,

ii) $D_o \cos\theta = S_I + S_R$, and

iii) $D_o[\sigma k_D \sin\theta + f\ell \cos\theta]h_D = [S_I e^{i\phi} + S_R e^{-i\phi}]h_S$.

The compatability condition for i) to iii) requires that

$$[k_D \tan\theta + \frac{f\ell}{\sigma}][k_S \cot(k_S L) + \frac{f\ell}{\sigma}] = \frac{h_S}{h_D}[(\sigma k_S)^2 + (f\ell)^2],$$

which is the dispersion relation. Since θ is arbitrary, a continuum of waves can exist for $|\ell| < |\ell_{c.o.}|$.

Subcase II (Two Poincare waves in shallow water and a Kelvin wave in deep water): The surface displacements in S and D are

$$\zeta_S = [S_I e^{-ik_S x} + S_R e^{ik_S x}] \cos(\sigma t - \ell y)$$

and

$$\zeta_D = D_K e^{k_D x} \cos(\sigma t - \ell y), \text{ respectively.}$$

Application of the three BC's leads to a compatibility condition which is the dispersion relation:

$$\frac{h_S}{h_D}(k_S^2 + (\frac{f\ell}{\sigma})^2) - (k_D - \frac{f\ell}{\sigma})(k_S \cot(k_S L) - \frac{f\ell}{\sigma}) = 0.$$

Subcase III (Two Kelvin waves in shallow water and a Kelvin wave in deep water): The surface displacements in S and D are

$$\zeta_S = [S_{KN} e^{-k_S x} + S_{KP} e^{k_S x}] \cos(\sigma t - \ell y)$$

and

$$\zeta_D = D_K e^{k_D x} \cos(\sigma t - \ell y),$$

respectively. Analogous to Subcase II, the dispersion relation is

$$\frac{h_S}{h_D}(k_S^2 - (\frac{f\ell}{\sigma})^2) + (k_D - \frac{f\ell}{\sigma})(k_S \coth(k_S L) - \frac{f\ell}{\sigma}) = 0.$$

Larsen (1966) computed the M2 tidal constants along the west coast of North America from observations. Figure 40 is an adaption of a figure given by Larsen. The phase speed and the amplitude of the M2 tide are fairly consistent with Kelvin wave-type behavior.

The dispersion relation for trapped waves has been evaluated for the semidiurnal and diurnal tides at the latitude of the Depoe Bay array, 45° N. For the semidiurnal tide, values of

$$\ell = 8.7 \times 10^{-9} \text{cm}^{-1},$$

$$k_S = 2.2 \times 10^{-8} \text{cm}^{-1},$$

and

$$k_D = 6.2 \times 10^{-9} \text{cm}^{-1}$$

were obtained. For the diurnal tide, values of

$$\ell = 4.2 \times 10^{-9} \text{cm}^{-1},$$

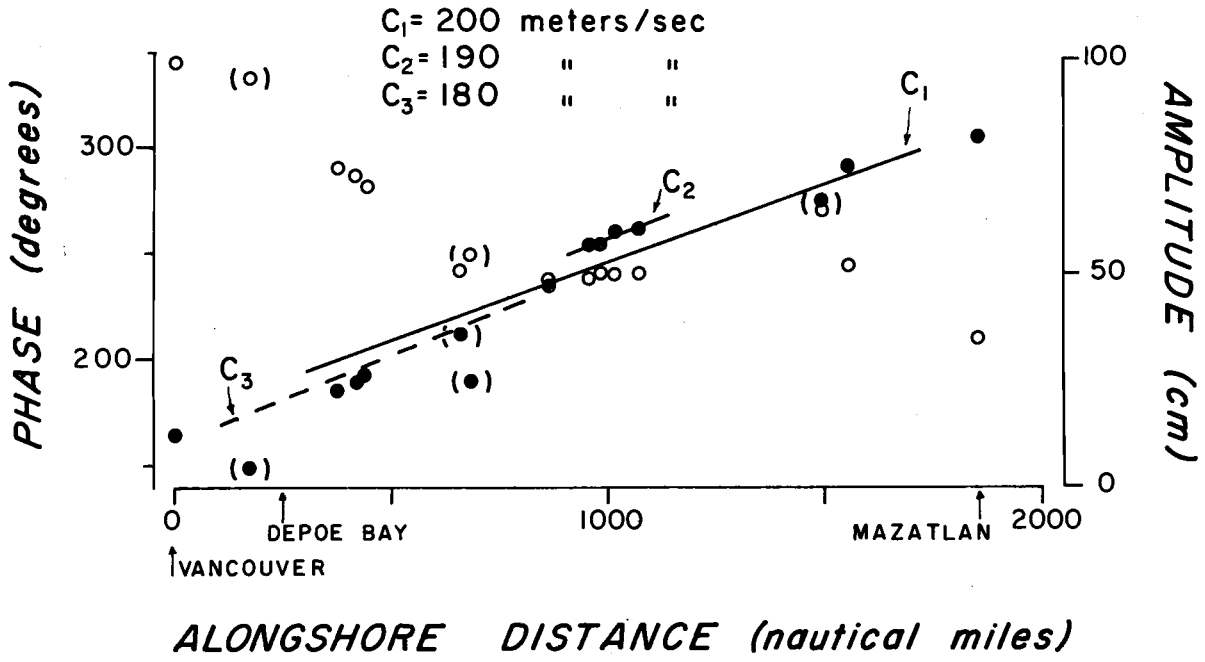

Figure 40. M2 tidal constants along the west coast of North America, adapted from Larsen (1966).
- ● phase value
- o amplitude value
- C phase speed

$$k_S = 1.7 \times 10^{-8} \text{cm}^{-1},$$

and

$$k_D = 6.0 \times 10^{-9} \text{cm}^{-1}$$

were obtained. The waveforms for ζ, u, and v are shown in Figure 41 for both the semidiurnal and diurnal tides. The horizontal velocity fields rotate anticlockwise for both the semidiurnal and diurnal tides, while the eccentricity of the diurnal tide is greater than that of the semidiurnal tide over the continental shelf. The model is not unequivocally consistent with the observations reported in Chapter XI.

B. Baroclinic Cases

The baroclinic cases exhibit qualitative behavior similar to the barotropic cases, but they have vertical structure, which admits vertical modes to the analysis. Because of the existence of vertical modes, with modal number m, energy can be transferred between vertical modes whenever a reflection process occurs at a discontinuity in depth. When a barotropic wave is treated as the zeroth order baroclinic mode, then energy can also be transferred from a barotropic tide, $m = 0$, to higher order, baroclinic modes.

Rattray (1960) considered a two-layered model with a barotropic tide striking a continental shelf at normal incidence; he considered one case with a continental shelf of uniform depth and another case with a shelf of uniform bottom slope. His model gives the conditions under which the incident barotropic wave is partially converted

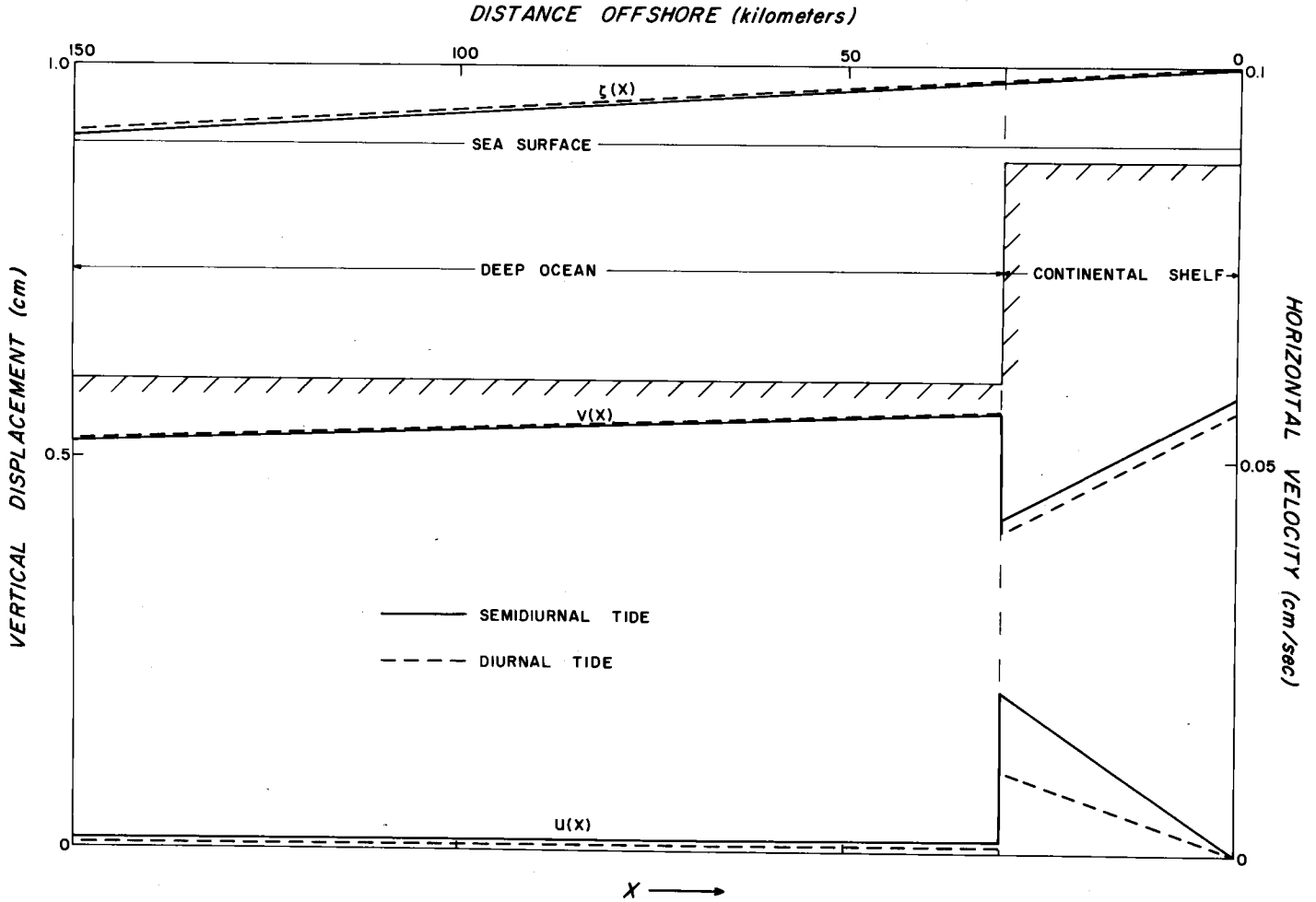

Figure 41. Theoretical velocity field for the barotropic M2 and K1 tides off Depoe Bay, Oregon. (Normalized to a 1 cm sea surface amplitude at the coastline.)

to a baroclinic wave propagating seaward and to another wave propagating shoreward, which reflects and then propagates seaward, too. Weigand (1962) experimentally verified Rattray's model in the laboratory. Ichiye (1963) extended Rattray's theory to include waves incident at an arbitrary angle and to include Kelvin waves as well as plane waves. He found that, as a function of frequency, resonance conditions could favor the surface Kelvin wave solutions over the plane wave solutions as the most effective generation mechanism for internal waves propagating offshore. Weigand (1964) extended his own and Rattray's theoretical and experimental work to include the effects of non-normal angles of incidence and dissipation. The two-layered models can be extended to an arbitrary number of layers, but they are interfacial waves rather than the inertial-internal (body) waves. Since the basic principles of wave propagation along a coast have been illustrated in the barotropic case, and since it is the case of continuous density stratification that is of interest, layered-models are not discussed in detail.

Stepped Bottom. The case of continuous density stratification and of a stepped bottom is outlined. Since the depth is uniform but different in D and S, then SOV applies:

$$\pi = X(x)Z(z) \cos(\sigma t - \ell y).$$

With the FBC, and with N^2 constant, the CR is

$$\ell^2 + (k^{(n)})^2 = {}^{(n)}k^2 \frac{(\sigma^2 - f^2)}{(N^2 - \sigma^2)} \sim \frac{(n\pi)^2}{h} \frac{(\sigma^2 - f^2)}{g'}$$

where g' is the reduced gravity, i.e.,

$$g' = \frac{\Delta\rho g}{\rho_o} \sim 10^{-3} g.$$

Thus, for fixed ℓ and σ, there exists a set of $k^{(n)}$, $n = n_c$, $n_c + 1, \ldots$ which are real. The cut-off wave number for the barotropic wave is

$$\ell_{co}^2 = \frac{\sigma^2 - f^2}{hg},$$

while the cut-off wave number for the nth mode baroclinic wave is

$$\ell_{cn}^2 \sim (n\pi)^2 \frac{(\sigma^2 - f^2)}{hg'},$$

thus

$$\frac{\ell_{cn}}{\ell_{co}} \sim 100\, n.$$

Thus, conditions for trapping baroclinic modes in shallow water deteriorate as the modal number increases. The effect of baroclinicity on refraction can be seen from the relations for the orientation of the wave number vector: with

$$R_o = \left(\frac{\sigma^2 - f^2}{gh}\right)^{1/2}$$

and

$$R_n = n\pi\left(\frac{\sigma^2 - f^2}{g'h}\right)^{1/2} \sim 100\, nR_o,$$

where R is the radius of the wave number locus. With

$$\sin(\theta_o) = \frac{\ell}{R_o} \quad \text{and} \quad \sin(\theta_n) = \frac{\ell}{R_n} \sim \frac{1}{100\, n} \sin(\theta_o),$$

where θ is the orientation of the wave number measured from east, then $\theta \sim \frac{\theta_o}{100\, n}$. Thus, for a barotropic mode whose wave number is oriented at an angle, θ_o, with respect to the coastline, the wave numbers of the corresponding baroclinic modes tend to orient nearly perpendicular to the coastline. These qualitative remarks demonstrate that Rattray's modeling of the generation of interfacial tides by a surface wave of normal incidence was quite realistic. They also support the two-dimensionalization of the inertial-internal wave problem over the continental shelf, which was postulated in Chapter II.

For brevity, only the case of Poincare waves in S and D is considered. Kelvin waves are also admissible, and a mixture of Poincare and Kelvin waves can occur, depending upon the vertical modal number. Solutions of the following form are sought:

$$\beta^{\pi} = \sum_{n=0}^{\infty} \left[{}^{(n)}_{\beta}A_I e^{-i\,{}^{(n)}k_{\beta}x} + {}^{(n)}_{\beta}A_R e^{i\,{}^{(n)}k_{\beta}x} \right] {}^{(n)}_{\beta}Z(z) \cos(\sigma t - \ell y),$$

where

$$\beta = S, D, \qquad {}^{(n)}_{\beta}Z_{(z)} = \begin{cases} (\zeta - z), & n = 0 \\ \cos\left({}^{(n)}K_{\beta}(z+h_{\beta})\right), & n \geq 1, \end{cases}$$

and

$$\tan\left({}^{(n)}K_{\beta}h_{\beta}\right) = \frac{(N^2-\sigma^2)}{g\,{}^{(n)}K_{\beta}},$$

by the FBC. There are three BC's which must yet be satisfied:

i) ${}_{S}u = 0$ for all $z \in (-h_S, 0)$, at $x = L$, the coastline,

ii) ${}_{D}\pi = {}_{S}\pi$ for all $z \in (-h_S, 0)$, at $x = 0$, the shelf edge, and

iii) ${}_{D}u = \begin{cases} {}_{S}u & \text{for all } x \in (-h_S, 0) \\ 0 & \text{for all } z \in (-h_D, h_S), \end{cases}$ at $x = 0$.

The first BC implies:

$$\frac{{}^{(n)}_{S}A_R}{{}^{(n)}_{S}A_I} = -e^{-2i\left({}^{(n)}_{S}kL - {}^{(n)}_{S}\theta\right)},$$

where

$${}^{(n)}_{S}\theta = \tan^{-1}\left(\frac{{}^{(n)}_{S}k\sigma}{\ell f}\right);$$

this relation must hold for all n, then i) is satisfied exactly for all z. The second and third BC's can be satisfied in only a vertically-integrated sense, or mean-square sense, because the vertical modes of D and S are different. Define δ_{mn} to be

$$\delta_{mn} = \frac{2}{h_S} \int_{-h_S}^{0} {}^{(m)}_{D}Z(z)\,{}^{(n)}_{S}Z(z)dz.$$

Then the second BC implies:

$${}^{(n)}_{S}A_I + {}^{(n)}_{S}A_R = \sum_{m=0}^{\infty} ({}^{(m)}_{D}A_I + {}^{(m)}_{D}A_R)\delta_{mn}$$

for all n. Similarly, the third BC implies:

$${}^{(n)}_{S}K({}^{(n)}_{S}A_I - {}^{(n)}_{S}A_R) = \sum_{m=0}^{\infty} {}^{(m)}_{D}K({}^{(m)}_{D}A_I - {}^{(m)}_{D}A_R)\delta_{mn}$$

At this point, infinite-dimensional scattering, reflection, and transmission matrices can be written formally. If conditions such as perfect reflection are imposed, an infinite number of dispersion relations result, one for each vertical mode. One solution procedure is to solve interatively for an N-dimensional set of modes and to then increase N until a satisfactory approximation is achieved. Analogous to the approach made by Miles (1967b) for the problem of surface wave diffraction at a continental shelf edge, the problem can be attacked by defining excitations functions, $E_1(z)$ and $E_2(z)$, at the shelf edge. Then $E_1(z)$ and $E_2(z)$ can be expanded in terms of ${}^{(n)}_{D}\pi|_{x=0}$ and ${}^{(n)}_{S}\pi|_{x=0}$ and ${}^{(n)}_{D}u|_{x=0}$ and ${}^{(n)}_{S}u|_{x=0}$ or, equivalently, ${}^{(n)}_{D}\pi_x|_{x=0}$ and ${}^{(n)}_{S}\pi_x|_{x=0}$. Such a procedure can be generalized to

the case of variable depth where the deep water solution is treated as above and the shallow water solution is found by treating $E_1(z)$ and $E_2(z)$ as Cauchy data on the initial line.

Baroclinic Inertial Kelvin Waves with Variable Topography.

This is the degenerate case, $\sigma = f$; it has more flexibility than when $\sigma \neq f$, as in the barotropic case. Assume N is constant and take $\pi = e^{\ell x} Z(z) \cos(ft - \ell y)$, $u = u(x, z) \sin(ft - \ell y)$, and $v = v(x, z) \cos(ft - \ell y)$. Then, from the primitive equations

$$v(x, z) = u(x, z) + \frac{\ell}{f} Z e^{\ell x}.$$

Substituting into the EOC, it follows that

$$(u_x + \ell u) + e^{\ell y}\left(\frac{\ell^2}{f} Z + \frac{fZ''}{(N^2 - f^2)}\right) = 0$$

or, neglecting the constant of integration and BC's for the moment:

$$u(x, z) = -\frac{f}{2\ell}\left[\frac{\ell^2}{f^2} Z + \frac{Z''}{(N^2 - f^2)}\right] e^{\ell x}.$$

From the primitive equations,

$$w = w(x, z) \sin(ft - \ell y),$$

where

$$w(x, z) = \frac{Z' f}{(N^2 - f^2)} e^{\ell x}.$$

These forms are used to satisfy the BC's:

i) RBC: $w = 0$, at $z = 0$ for all x, or $Z'(0) = 0$, and

ii) RBC: $w = mu$ or, $Z'' + \frac{2\ell}{m(x)} Z' + \frac{\ell^2}{f^2}(N^2 - f^2)Z = 0$, at $z = z_b(x)$ for all x.

From ii), the equation for Z is then a function of one parameter, viz. $s = z_b(x)$, since $m(x) = s_x$. The form for s can be quite arbitrary but a simple example suffices for the present.

A simple case which imposes the constraint of finite depth in the deep ocean, $h(x) \to h_o$, $x \to -\infty$, is given by $z_b(x) = -h_o(1-e^{\alpha x})$, hence $h(0) = 0$. Then

$$m(x) = \alpha h_o e^{\alpha x} = \alpha(h_o - h(x)).$$

Take $s = z_b$, thus $m(x) = \alpha(h_o + s)$ and the equation for Z is:

$$Z_{ss} + \frac{2\ell}{\alpha(h_o+s)} Z_s + K^2 Z = 0,$$

where

$$K^2 = \frac{\ell^2}{f^2}(N^2 - f^2).$$

Changing variables to $t = h_o + s$, thus $t \to h_o$, $x \to 0$ and $t \to 0$, $x \to -\infty$ then

$$Z_{tt} + \frac{2\ell}{\alpha t} Z_t + K^2 z = 0.$$

In normal form, $Z = F(t)G(t)$, where $F(t) = t^{-\frac{\ell}{\alpha}}$ and

$$G_{tt} + [K^2 - \frac{1}{t^2}(\frac{\ell}{a})(\frac{\ell}{a}-1)]G = 0.$$

G has solutions of the form

$$G = AJ_\nu(kt) + BN_\nu(kt),$$

where

$$\nu = \frac{\ell}{a}(\frac{\ell}{a}-1).$$

If the condition $\pi \to 0$ ($x \to -\infty$) is imposed, $e^{\ell x}Z \to 0$ ($t \to 0$) or

$$\lim_{x \to -\infty} [e^{\ell x}Z] = \lim_{\substack{x \to -\infty \\ t \to 0}} [e^{\ell x}(At^{(\frac{\ell}{a})^2 - 2(\frac{\ell}{a})} + Bt^{-(\frac{\ell}{a})^2}] \to 0,$$

which requires $B = 0$ and $\frac{\ell}{a} \geq 2$, thus $\nu \geq 2$. The SBC requires that

$$[(h_o+z)^{-(\frac{\ell}{a})} J_\nu(K(h_o+z))]' = 0 \quad \text{at} \quad z = 0$$

or

$$-\frac{\ell}{a} J_\nu(Kh_o) + h_o J'_\nu(Kh_o) = 0,$$

which is the dispersion relation. The solution is not sought here, but the basic principle has been illustrated, i. e., baroclinic inertial Kelvin waves can be trapped along a coastal barrier with variable topography. As in the barotropic case, this case is rather unrealistic since the beta effect is neglected.

Variable Topography. The problem of general topographical variation is approached formally and reduced to quadratures in the three-dimensional case. The problem is posed with a deep water region of uniform depth and a coastal region of non-uniform depth. The coordinate of the intersection of the deep water and shallow water regions is again $x = 0$. A rational approach is to treat $x = 0$ as an initial line, forming a MIBVP. The GE is written in terms of π:

$$\text{GE:} \qquad (N^2-\sigma^2)(\pi_{xx}+\pi_{yy}) - (\sigma^2-f^2)\pi_{zz} = 0.$$

The GE is a two-dimensional wave equation in the spatial variables and could be treated in a general way as such, but the information that the semidiurnal tide tends to propagate along the positive y-axis, i.e., $\pi = P(x, z) \cos(\sigma t - \ell y)$, is used to reduce the GE:

$$\text{GE:} \qquad P_{xx} - R^2 P_{zz} - \ell^2 P = 0,$$

where

$$R^2 = \left(\frac{\sigma^2-f^2}{N^2-\sigma^2}\right).$$

Assuming constant coefficients, the GE is recognized as a telegraph equation. The Riemann-Green's function for this equation is known, Sneddon, (1957). Take $F(z) = \pi(0, z)$ and $G'(z) = \pi_x(0, z)$, then the solution for the initial value problem is

$$P(x, z) = \frac{1}{2}[F(z+Rx) + F(z-Rx)]$$

$$+ \frac{1}{2R}\int_{z-Rx}^{z+Rx} G'(\xi)J_o(\frac{\ell}{R}((\xi-z)^2-R^2x^2)^{1/2})d\xi$$

$$+ \frac{1}{2}\ell x\int_{z-Rx}^{z+Rx} F(\xi)\frac{J_o'(\frac{\ell}{R}((\xi-z)^2-R^2x^2)^{1/2})d\xi}{((\xi-x)^2-R^2x^2)^{1/2}} .$$

The Riemann-Green function,

$$W(\rho, \xi; x, z) = J_o(\frac{\ell}{R}((z-\xi)^2-R^2(x-\rho)^2)^{1/2}),$$

and its first derivative have been evaluated on the initial line, $\rho = 0$, in the integrals. The complete solution to the MIBVP can be computed using the solution theory in Section V.F. Several points are noted:

i) For uniform depth in shallow water, the effect of the coastal BC is to remove the independence of $F(z)$ and $G(z)$,

ii) The issue of onshore-offshore energy flux is again settled on the basis of the temporal phase relation between $F(z)$ and $G(z)$,

iii) Since u, v, and w can be expressed in terms of π, the RBC and FBC can be written in terms of π, giving the full constraint to the arbitrariness of $F(z)$ and $G(z)$, i.e., the algorithms for analytic extension of the CD can be

derived.

Because the details of the analysis are lengthy, they are not given here. The RBC applied at the sea surface requires that $F(z)$ and $G(z)$ be even functions of z with respect to the origin. The RBC applied at the sea bottom imposes a subtle rule for extension of $F(z)$ and $G(z)$; it involves Volterra integral equations of the third kind,

iv) Once $F(z)$ and $G(z)$ have been completely specified, they can be expanded in terms of the deep water normal modes for the deep water solution, and

v) It is not yet clear how to treat the problem of converting alongshore energy flux of the barotropic tide to onshore-offshore energy flux of the baroclinic tide.

C. Spectral Observables

It is assumed that the depth and the density gradient are uniform and that a locally valid model of the internal tide consists of a northward propagating Poincare wave over the continental shelf. Attention is focused on a discrete frequency and a single vertical mode.

π is chosen to be of the form such that when it is substituted into the equation for U the CBC is satisfied:

$$\pi = A \cos(\sigma t - \ell y) \cos(k(x-L) - \theta) + B \cos(\sigma t - \ell y - k(x-L) + \theta),$$

where

$$\theta = \tan^{-1}\left(\frac{f\ell}{\sigma k}\right)$$

and A and B are the depth-dependent amplitudes of the standing and progressive wave components, respectively.

$$u(x, y, z) = \frac{\pi_{xt}+f\pi_y}{(\sigma^2-f^2)} = \frac{[(\sigma k)^2+(f\ell)^2]^{1/2}}{(\sigma^2-f^2)}$$

$$\times \{A \sin(k(x-L)\sin(\sigma t-\ell y)+B\cos(\sigma t-\ell y-k(x-L))\},$$

and

$$u\big|_{x=L} = \frac{[(\sigma k)^2+(f\ell)^2]^{1/2}}{(\sigma^2-f^2)} B \cos(\sigma t-\ell y).$$

B represents the coastal energy "sink," or "source." Similarly, v's dependence on π is:

$$v(x, y, z) = \frac{\pi_{yt}-f\pi_x}{(\sigma^2-f^2)}$$

$$= \frac{[(\sigma\ell)^2+(fk)^2]^{1/2}}{(\sigma^2-f^2)}$$

$$\times \{A \sin(k(x-L)-(\theta-\phi))\cos(\sigma t-\ell y) - B\sin(\sigma t-\ell y-k(x-L)$$

$$+ (\theta-\phi))\},$$

where

$$\phi = \tan^{-1}\left(\frac{\sigma\ell}{fk}\right).$$

Using the relations

$$\eta_t = w = \frac{\pi_{zt}}{(N^2 - f^2)}$$

and

$$T = \eta \left(\frac{d\overline{T}}{dz}\right),$$

where η is the vertical displacement and T is the temperature,

$$T(x, y, z) = -\left(\frac{d\overline{T}}{dz}\right)\pi_z$$

$$= \frac{-\left(\frac{d\overline{T}}{dz}\right)}{(N^2 - \sigma^2)}$$

$$\times \{A'\cos(\sigma t - \ell y)\cos(k(x-L)-\theta) + B'\cos(\sigma t - \ell y - k(x-L)+\theta)\},$$

where

$$A' = \frac{dA}{dz} \quad \text{and} \quad B' = \frac{dB}{dz}.$$

For the computation of spectral quantieis, it is convenient to set $y = 0$ and rewrite the expressions for u, v, and T in orthogonal components:

$$u = u(\sigma)[(A+B)\sin(k(x-L))\sin(\sigma t) + B\cos(k(x-L))\cos(\sigma t)],$$

$$v = v(\sigma)[(A+B)\sin(k(x-L)-(\theta-\phi))\cos(\sigma t) - B\cos(k(x-L))-(\theta-\phi))\sin(\sigma t)],$$

and

$$T = T(\sigma)[(A'+B')\cos(k(x-L)-\theta\cos(\sigma t) + B'\sin(k(x-L)-\theta)\sin(\sigma t)],$$

where

$$u(\sigma) = \frac{[(\sigma k)^2+(f\ell)^2]^{1/2}}{(\sigma^2-f^2)},$$

$$v(\sigma) = \frac{[(\sigma \ell)^2+(fk)^2]^{1/2}}{(\sigma^2-f^2)},$$

and

$$T(\sigma) = \frac{-(\frac{d\overline{T}}{dz})}{(N^2-\sigma^2)}.$$

The autospectra are then

$$P_{uu}(\sigma, x) = \frac{u^2(\sigma)}{2}[(A^2+2AB)\sin^2(k(x-L))+B^2]$$

$$P_{vv}(\sigma, x) = \frac{v^2(\sigma)}{2}[(S^2+2AB)\sin^2(k(x-L)-(\theta-\phi))+B^2]$$

and

$$P_{TT}(\sigma, x) = \frac{T^2(\sigma)}{2}[(A^2+2AB)\cos^2(k(x-L)-\theta)+B^2].$$

Thus, with a source or sink only $(A = 0)$, the spectra of the corresponding progressive wave component are spatially uniform; with perfect reflection, the resultant spectra have the spatial structure of a standing wave. The presence of the phase terms θ and ϕ means that the spectra for u, v, and T are not in-phase spatially. Since

$$\theta - \phi = -\tan^{-1}[\frac{(\sigma^2-f^2)\ell k}{(k^2+\ell^2)\sigma f}],$$

P_{uu} and P_{vv} have the same spatial structure only if $\ell = 0$, $\sigma = f$, or $A = 0$.

If $A = 0$, the ratio of the energy spectra of u and v is

$$\frac{P_{uu}}{P_{vv}} = \frac{(\frac{\sigma}{f})^2 + (\frac{\ell}{k})^2}{(\frac{\sigma}{f})^2(\frac{\ell}{k})^2 + 1} = R_o.$$

If the hypothesis that $\ell \ll k$ is valid, then $\frac{P_{uu}}{P_{vv}} \approx (\frac{\sigma}{f})^2$.

If $B = 0$, the ratio of the energy spectra of u and v is

$$\frac{P_{uu}}{P_{vv}} = R_o \frac{\sin^2(k(x-L)}{\sin^2(k(x-L)-(\theta-\phi))};$$

If the hypothesis that $\ell \ll k$ is valid, this ratio becomes

$$\frac{P_{uu}}{P_{vv}} \approx (\frac{\sigma}{f})^2.$$

If the hypothesis is not valid, the ratio assumes all possible positive values as a function of x; one consequence is that the nodal points for u and v do not coincide.

Similarly, the cospectrum and quadrature spectrum are

$$P_{uv}(\sigma;x, z) = \frac{-u(\sigma)v(\sigma)}{2} (A+B)B \sin(\theta-\phi)$$

and

$$Q_{uv}(\sigma;x,z) = \frac{-u(\sigma)v(\sigma)}{2}\{[(A^2+2AB)\sin^2(k(x-L))+B^2]\cos(\theta-\phi)$$

$$-(A^2+2AB)\sin(k(x-L)\cos(k(x-L))\sin(\theta-\phi)\}.$$

The coherence squared is unity; the phase function has spatial structure:

$$\theta_{uv}(\sigma;x,z) = \tan^{-1}\left(\frac{Q_{uv}}{P_{uv}}\right)$$

$$= \tan^{-1}\{[(A^2+2AB)\sin^2 k(x-L)+B^2]\cot(\phi-\theta)$$

$$-(A^2+2AB)\sin(k(x-L))\cos(k(x-L))\}.$$

The cross spectral quantities can be used to test the hypothesis that $\ell \ll k$; if the hypothesis is valid, $\theta = \phi$, then

$$P_{uv} = 0,$$

$$Q_{uv} = \frac{-u(\sigma)v(\sigma)}{2}[(A^2+2AB)\sin^2(k(x-L))+B^2],$$

and

$$\theta_{uv} = \pm\frac{\pi}{2}.$$

When there is no source or sink at the coastal boundary $(B = 0)$,

$$Q_{uv} = \frac{-u(\sigma)v(\sigma)}{2}A^2\sin(k(x-L))\sin(k(x-L)-(\theta-\phi)),$$

and the signs of Q_{uv} and θ_{uv}, oscillate spatially unless $\theta = \phi$, i.e., when $\theta \neq \phi$, the direction of rotation will reverse whenever

$k(x-L) = (\theta-\phi)$, (mod 2π) and whenever $k(x-L) = 0$, (mod 2π).

The cross spectrum for u measured at two different spatial points, (x_1, z_1) and (x_2, z_2) is examined: where $A(z) = Z(z)A$ and $B(z) = Z(z)B$,

$$P_{u_1u_2}(\sigma;(x_1, z_1), (x_2, z_2))$$

$$= \frac{u^2(\sigma)}{2} Z(z_1)Z(z_2)[(A+B)^2 \sin(k(x_1-L)\sin(k(x_2-L)$$

$$+B^2\cos(k(x_1-L)\cos(k(x_2-L))]$$

and

$$Q_{u_1u_2}(\sigma;(x_1, z_1), (x_2, z_2) = \frac{u^2(\sigma)}{2} Z(z_1)Z(z_2)(A+B)B \sin(k(x_2-x_1)).$$

Again, the coherence squared is unity and

$$\theta_{u_1u_2} = \tan^{-1}\left\{\frac{(A+B)B \sin (k(x_2-x_1))}{A(A+2B)\sin(k(x_1-L))\sin(k(x_2-L)+B^2\cos(k(x_2-x_1))}\right\}.$$

If $B = 0$, then

$$P_{u_1u_2} = \frac{u^2(\sigma)}{2} Z(Z_1)Z(z_2)A^2 \sin (k(x_1-L)) \sin (k_2(x_2-L)),$$

$$Q_{u_1u_2} = 0, \quad \text{and} \quad \theta_{u_1u_2} = 0 \quad \text{or} \quad \pi,$$

depending on $k(x_2-x_1)$, (mod 2π).

If either (x_1, z_1) or (x_2, z_2) is a nodal point, all cross spectral quantities are null. If $A = 0$, then

$$P_{u_1u_2} = \frac{u^2(\sigma)}{2} Z(z_1)Z(z_2)B^2 \cos(k(x_2-x_1)),$$

$$Q_{u_1u_2} = \frac{u^2(\sigma)}{2} Z(z_1)Z(z_2)B^2 \sin(k(x_2-x_1)),$$

and

$$\theta_{u_1u_2} = k(x_2-x_1).$$

Within the limitation of this simple model, the spectral quantities calculated from observations potentially provide the means of testing several basic hypotheses, viz.,

i) $\ell \ll k$, i. e., the motion is essentially homogeneous in the alongshore direction,

ii) $A \neq 0$, there is a standing wave component to the motion, and

iii) $B \neq 0$, there is a progressive wave component to the motion.

Analogous results would follow for an analysis of the solution to the complete problem with variable depth and the frontal interaction.

D. Hodograph Observables

A hodograph, the spatial locus of a velocity vector as a function of time, is a useful device for the analysis of wave fields. Since the velocity vector at tidal frequencies is principally horizontal, the

hodograph determined by the horizontal velocity vector is considered. This, the projection of the hodograph on to the horizontal plane, is most familiar from its common usage as the tidal ellipse. A continuum of hodographs exists, though custom has focused on discrete frequencies for which a statistically stationary wave component is anticipated; otherwise, the hodograph is more difficult to interpret. The principal properties of the hodograph are:

i) The orientation of the major axis with respect to a fixed reference axis, such as geographic east,

ii) The length of the semi-major and semi-minor axes, R_1 and R_2, respectively.

iii) The ratio $\epsilon = \frac{R_1 - R_2}{R_1 + R_2}$, where ϵ is termed the eccentricity.

iv) The sense of rotation of the velocity vector, and

v) The time phase of the radial vector with respect to a time base.

The hodograph is generally a function of spatial position and its orientation relates to the direction of wave propagation. The formulae of Doodson and Warburg, (1941, p. 180-181), are used for calculations based on the velocity functions introduced in the previous section. Since the algebraic and trignometric manipulations are tedious, the standing wave and progressive wave components are treated separately. Once the hodograph for each of these has been found they

can be combined to form the effective hodograph.

First, a standing wave only is assumed to exist (B = 0); the formulae lead to

$$R_1 = u(\sigma)A \sin (k(x-L))$$

and

$$R_2 = v(\sigma)A \sin (k(x-L)-(\theta-\phi)).$$

R_2 is in-phase with the pressure field. R_1 and R_2 can interchange their relative size and sign as a function of offshore position, and thus the orientation of the ellipse. The sense of rotation also varies as a function of offshore position. The eccentricity is

$$\epsilon = \frac{v(\sigma)\sin(k(x-L)-(\theta-\phi))-u(\sigma)\sin(k(x-L))}{v(\sigma)\sin(k(x-L)-(\theta-\phi))+u(\sigma)\sin(k(x-L))}.$$

At the coastal boundary, (x = L), R_2 tends to zero and the motion becomes rectilinear with amplitude

$$R_1 = -vA \sin (\theta-\phi),$$

which also tends to zero for small ℓ. When $\ell \ll k$, all hodographs rotate clockwise, and, for $\sigma > f$,

$$R_1 = A\left(\frac{\sigma k}{\sigma^2-f^2}\right) \sin (k(x-L)),$$

$$R_2 = \frac{f}{\sigma}R_1,$$

and

$$\epsilon = \frac{\sigma - f}{\sigma + f}.$$

For a progressive wave only, $A = 0$ and $B \neq 0$, the formulae yield:

$$R_1 = \frac{B}{(2)^{1/2}} \{u^2+v^2+[u^4+v^4-2u^2v^2\cos(2(\theta-\phi))]^{1/2}\}^{1/2}$$

and

$$R_2 = \frac{B}{(2)^{1/2}} \{u^2+v^2-[u^4+v^4-2u^2v^2\cos(2(\theta-\phi))]^{1/2}\}^{1/2}.$$

When $\ell \ll k$,

$$R_1 = \frac{\sigma k B}{(\sigma^2 - f^2)}$$

$$R_2 = \frac{f}{\sigma} R_1$$

and

$$\epsilon = \frac{\sigma - f}{\sigma + f}.$$

The phase relation of R_1 with respect to the pressure field is given by the angle a, where

$$a = \frac{-1}{2} \tan^{-1} \left[\frac{v^2 \sin(2(\theta-\phi))}{u^2 - v^2 \cos(2(\theta-\phi))} \right].$$

The orientation of the major axis, ω, with respect to east is given by the formula

$$\omega = -\tan^{-1} \left[\frac{v(\sigma)}{u(\sigma)} \frac{\sin(a+(\theta-\phi))}{\cos(a)} \right],$$

thus when $\ell \ll k$, $\omega = 0°$ or $180°$. In other words, when $\ell \ll k$ the hodograph is oriented east or west depending upon whether there is a coastal sink or source. ω can be computed from observations, thus the ratio ℓ/k can be estimated.

When $\ell \ll k$, and $\sigma \sim f$, then, if there is both a progressive and a standing wave component to the motion:

$$u = \left(\frac{\sigma k}{\sigma^2 - f^2}\right)\left[(A+B)\sin(k(x-L))\sin(\sigma t)+B\cos(k(x-L))\cos(\sigma t)\right]$$

and

$$v = \left(\frac{fk}{\sigma^2 - f^2}\right)\left[(A+B)\sin(k(x-L))\cos(\sigma t)-B\cos(k(x-L))\sin(\sigma t)\right],$$

or

$$u = \sigma c \cos(\sigma t-\psi), \text{ thus } R_1 = \sigma c \text{ and}$$

$$v = -fc \sin(\sigma t-\psi), \text{ thus } R_2 = fc,$$

where

$$c = \left(\frac{k}{\sigma^2 - f^2}\right)\left[(A+B)^2\sin^2(k(x-L))+B^2\cos^2(k(x-L))\right]^{1/2}$$

$$\psi = \tan^{-1}\left[\left(1+\frac{A}{B}\right)\tan(k(x-L))\right],$$

and

$$\epsilon = \frac{\sigma - f}{\sigma + f}.$$

Therefore the horizontal velocity rotates clockwise, which is consistent with the observations reported in Chapter XI. The observations have yet to be examined thoroughly enough to test the other relationships found in this and the preceding section.

APPENDIX II

The Consequences of the Assumptions of Alongshore Uniformity and of the Traditional Approximation

Since $f_h = f_v$ at 45° latitude, the latitude of the observations, and since the alongshore wavelengths of inertial-internal waves are uncertain, the consequences of neglecting these two quantities for both the GE and the hodograph are examined. For simplicity, the frontal interaction terms are neglected but f_h is assumed not zero and all variables are assumed to have a y- as well as an x- and z-dependence; SHM is assumed for the time dependence. The system of equations is then:

i) $i\sigma u - f_v v - f_h w = -\pi_x$

ii) $i\sigma v + f_v u = -\pi_y$

iii) $i\sigma w + f_h u = -\pi_z - \frac{\rho}{\bar{\rho}} g,$

iv) $u_x + v_y + w_z = 0,$ and

v) $i\sigma\rho + w\bar{\rho}_z = 0$

Eliminating ρ between iii) and v), then

vi) $(N^2 - \sigma^2)w + i\sigma f_h u = -i\sigma\pi_z.$

Eliminating v and u successively between i) and ii), then

vii) $(\sigma^2 - f_v^2)u + i\sigma f_h w = i\sigma\pi_x + f_v\pi_y$

and

viii) $(\sigma^2 - f_v^2)v - f_v f_h w = -f_v\pi_x + i\sigma\pi_y$.

Eliminating u and w successively between vi) and vii), the equations for u and w in terms of π are:

$$\text{ix)} \quad w = \frac{[-i(\sigma^2 - f_v^2)\sigma\pi_x + f_h(\sigma^2\pi_x - if_v\sigma\pi_y)]}{D}$$

and

$$\text{x)} \quad u = \frac{[(N^2 - \sigma^2)(i\sigma\pi_x + f_v\pi_y) - \sigma^2 f_h\pi_z]}{D},$$

where

$$D = (\sigma^2 - f_v^2)(N^2 - \sigma^2) + \sigma^2 f_h^2.$$

Then w is eliminated from viii):

$$\text{xi)} \quad v = \frac{[-if_v f_h\sigma\pi_x - f_v(N^2 - \sigma^2)\pi_x + i\sigma((N^2 - \sigma^2) + f_h^2)\pi_y]}{D}$$

To avoid unnecessary detail, the coefficients are assumed constant; then the expressions for u, v, and w are substituted into iv), the EOC. The GE in terms of π is then:

$$\text{GE:} \quad (N^2 - \sigma^2)\pi_{xx} + (N^2 - \sigma^2 + f_h^2)\pi_{yy} - (\sigma^2 - f_v^2)\pi_{zz} - 2f_v f_h\pi_{yz} = 0.$$

Hence, the neglect of $(\ )_y$ in the GE removes all the terms

containing f_h but not conversely; with the neglect of f_h, the term π_{yy} remains. Unless either f_h or $(\ )_y$ is neglected, the variables will not separate in y and z, inducing asymmetry in the solution and in the characteristics of the GE.

With the traditional approximation, $f_h = 0$, the hodograph is:

$$(u, v, w) = \left(\frac{i\sigma\pi_x + f_v\pi_y}{(\sigma^2 - f_v^2)}, \frac{-f_v\pi_x + i\sigma\pi_y}{(\sigma^2 - f_v^2)}, \frac{-i\sigma\pi_z}{(N^2 - \sigma^2)} \right).$$

The singularities in the hodograph are at $\sigma = N$ and $\sigma = f_v$; they correspond to the singularities of the GE.

With the alongshore uniformity hypothesis, $(\ )_y = 0$, the hodograph is:

$$(u,v,w) = \frac{[((N^2-\sigma^2)i\sigma\pi_x - \sigma^2 f_h\pi_z), (-(N^2-\sigma^2)f_v\pi_x - i\sigma f_v f_h\pi_z), (-(\sigma^2-f_v^2)i\sigma\pi_z + f_h\sigma^2\pi_x)]}{D}$$

While the neglect of $(\ )_y$ removes the influence of f_h in the GE, it does <u>not</u> remove f_h from the hodograph. In this case, the singularities of the GE are at $\sigma = f_v$ and $\sigma = N$, while the singularities of the hodograph, are at

$$\sigma^{\pm} = \left(\frac{1}{2}[f^2+N^2 \pm ((f^2+N^2)^2 - 4f_v^2N^2)^{1/2}]\right)^{1/2},$$

where

$$f^2 = f_h^2 + f_v^2.$$

Since $\sigma^+ > N$ and $\sigma^- < f_v$, the singularities of the hodograph lie outside the inertial-internal wave passband, causing no difficulty for the velocity fields which are solutions to the GE.

The principle effect of f_h on the velocity fields is to couple the vertical pressure gradient to the horizontal velocity and the horizontal pressure gradient to the vertical velocity. This effect may be significant for the interpretation of observations.

APPENDIX III

The Spectrum Analysis of Singletons and Pairs of Two-Dimensional Velocity Vectors

The study of two-dimensional velocity vectors considers properties of the components of the motion such as their cospectrum (for a measure of the Reynolds stress spectrum) and coherence squared (for a measure of the coherence of wave motion). The results for one-dimensional spectrum analysis are dependent upon the coordinate system in which the calculations are made. The analysis of this appendix allows removing the ambiguity in spectral quantities caused by their dependence on the coordinate system of their measurement.[29] In Section A, the techniques for maximizing the Reynolds stress and coherence squared are derived for a single two-dimensional velocity vector. In Section B, the geography of the hodograph is discussed and the concept of negative frequency is introduced to current measurements. In Section C, the technique for analyzing a pair of two-dimensional velocity vectors as complex-valued functions is

[29] On his visit to Oregon State University in December, 1967, Dr. N. P. Fofonoff, Woods Hole Oceanographic Institution, stated that he had derived these results recently, but they are not published. He has applied the results to flow models based on the linearized equations of geophysical fluid dynamics.

derived.[30, 31]

A. The Semi-Principal Axis Transformation

Velocity measurements are usually made in an arbitrary coordinate system, e.g., geographic coordinates. To study such quantities as the Reynolds stress and the spectral coherence squared, it is of interest to perform a rotation of axes. The rotation of axes is a real orthogonal transformation. Rotation to the semi-principal axis[32] of the covariance maximizes the Reynolds stress. Rotation to the semi-principal axis of the cospectrum (or Reynolds stress spectrum) for each frequency maximizes the Reynolds stress and coherence squared at that frequency. The basic results are derived by using trigonometric identities and differential calculus; they have also been derived using Hermitian operator and matrix theory. The former

---

[30] Many of the concepts contained in this appendix have analogues in optics, cf. Born and Wolf, 1965, with the study of polarized and partially coherent light, as brought to my attention by Professor M. S. Longuet-Higgins, Department of Oceanography, Oregon State University. In optics, right-handed and left-handed elliptical polarizations correspond to the two-dimensional clockwise and anticlockwise motions of marine hydrodynamics. In Born and Wolf (1965), the concept of negative frequencies is not exploited for optics as it is in Sections B and C.

[31] The author is indebted to Mr. Michael Ho, Graduate Student, Department of Oceanography, Oregon State University for his meticulous proofreading of this appendix.

[32] The term semi-principal axis is used because the transformation is real and involves the eigenvalues of the corresponding two-dimensional matrix, while the term principal axis is its analogue for complex transformation.

approach is used here because it is more familiar, while the latter has the advantages of being more efficient and of leading to analogues with operators and variables of classical and quantum mechanics.

Maximum Reynolds Stress. The time-averaged horizontal component of the Reynolds stress is $\overline{u(t)v(t)}^t$. Changing variables by rotation through an arbitrary angle, θ, from the unprimed to the primed coordinates, then

$$x' = x \cos \theta + y \sin \theta$$

and

$$y' = -x \sin \theta + y \cos \theta,$$

where $\theta > 0$ for anticlockwise rotation.

The Reynolds stress in the primed coordinates is

$$\overline{u'v'}\,(\theta) = \overline{uv} \cos (2\theta) + \frac{1}{2}(\overline{v^2} - \overline{u^2}) \sin (2\theta),$$

where the time argument, t, has been dropped for convenience.

Maximizing $\overline{u'v'}$ with respect to θ and solving for the corresponding θ, say $\bar{\theta}$, it follows that

$$\bar{\theta} = \frac{1}{2} \tan^{-1} \left[\frac{(\overline{v^2} - \overline{u^2})}{2\overline{uv}} \right].$$

There ia an ambiguity of $\pm\pi$ in $2\bar{\theta}$, but $2\bar{\theta}$ is chosen to be the root which occurs in either the first or fourth quadrant. Since

$$\sin(2\bar{\theta}) = \frac{(\overline{v^2}-\overline{u^2})}{2[(\overline{uv})^2+(\overline{v^2}-\overline{u^2})^2/4]^{1/2}}$$

and

$$\cos(2\bar{\theta}) = \frac{\overline{uv}}{[(\overline{uv})^2+(\overline{v^2}-\overline{u^2})^2/4]^{1/2}},$$

then

$$\max u'v' = [(\overline{uv})^2 + (\overline{v^2}-\overline{u^2})^2/4]^{1/2}$$

If $\overline{v^2} = \overline{u^2}$, then $\bar{\theta} = 0$, i.e., no rotation is required for maximization, and $\overline{u'v'} = \overline{uv}\cos(2\theta)$.

The preceding discussion serves as a model for the subsequent development of its covariance and spectral analogues.

Autovariance and Covariance Functions. The autovariance functions in the primed coordinates are given by

$$R_{u'u'}(\tau) = \overline{u'(t)u'(t+\tau)}$$
$$= R_{uu}(\tau)\cos^2(\theta) + R_{vv}(\tau)\sin^2\theta + [R_{uv}(\tau)+R_{vu}(\tau)]\sin\theta\cos\theta$$

and

$$R_{v'v'}(\tau) = \overline{v'(t)v'(t+\tau)}$$
$$= R_{uu}(\tau)\sin^2(\theta) + R_{vv}(\tau)\cos^2(\theta) - [R_{uv}(\tau)+R_{vu}(\tau)]\sin\theta\cos\theta.$$

Since

$$R_{u'u'}(\tau) + R_{v'v'}(\tau) = R_{uu}(\tau) + R_{vv}(\tau),$$

for all τ, then

$$R_{u'u'}(0) + R_{v'v'}(0) = R_{uu}(0) + R_{vv}(0);$$

therefore, the total variance and kinetic energy are conserved under coordinate rotation. Similarly, the covariance functions in the primed coordinates are given by

$$R_{u'v'}(\tau) = \overline{u'(t)v'(t+\tau)}$$
$$= [R_{vv}(\tau)-R_{uu}(\tau)] \sin\theta \cos\theta + R_{uv}(\tau) \cos^2\theta - R_{vu}(\tau) \sin^2\theta$$

and

$$R_{v'u'}(\tau) = \overline{v'(t)u'(t+\tau)}$$
$$= [R_{vv}(\tau)-R_{uu}(\tau)] \sin\theta \cos\theta + R_{vu}(\tau) \cos^2\theta - R_{uv}(\tau) \sin^2\theta.$$

The symmetry relation of the covariance function, viz. $R_{uv}(\tau) = R_{vu}(-\tau)$, is used to break the covariance functions into their even and odd parts, which are denoted $E_{uv}(\tau)$ and $O_{uv}(\tau)$, respectively:

$$E_{u'v'}(\tau) = \frac{1}{2}[R_{u'v'}(\tau)+R_{v'u'}(\tau)] = \frac{1}{2}[R_{vv}(\tau)-R_{uu}(\tau)] \sin(2\theta)$$
$$+ E_{uv}(\tau) \cos(2\theta)$$

and

$$O_{u'v'}(\tau) = \frac{1}{2}[R_{u'v'}(\tau)-R_{v'u'}(\tau)] = O_{uv}(\tau).$$

Thus, the odd part of the covariance is conserved but not the even part. (The covariance could be maximized as a function of θ for each τ by maximizing $E_{uv}(\tau)$.) Since

$$R_{u'u'}(\tau) = R_{uu}(\tau)\cos^2(\theta) + R_{vv}(\tau)\sin^2(\theta) + E_{uv}(\tau)\sin(2\theta)$$

and

$$R_{v'v'}(\tau) = R_{uu}(\tau)\sin^2(\theta) + R_{vv}(\tau)\cos^2(\theta) - E_{uv}(\tau)\sin(2\theta),$$

then, with reduction, it follows that

$$E^2_{u'v'}(\tau) - R_{u'u'}(\tau)R_{v'v'}(\tau) = E^2_{uv}(\tau) - R_{uu}(\tau)R_{vv}(\tau).$$

In summary, the three covariance invariants of real orthogonal transformations are

$$I_1(\tau) = R_{uu}(\tau) + R_{vv}(\tau),$$

$$I_2(\tau) = O_{uv}(\tau) = \frac{R_{uv}(\tau) - R_{vu}(\tau)}{2},$$

and

$$I_3(\tau) = R_{uu}(\tau)R_{vv}(\tau) - E^2_{uv}(\tau),$$

which are true for all τ. These invariants are used below to note their similarity in form to equivalent spectral quantities. The invariants can also be found from the covariance matrix:

$$CM_{uv}(\tau) = \begin{pmatrix} R_{uu}(\tau) & R_{uv}(\tau) \\ R_{vu}(\tau) & R_{vv}(\tau) \end{pmatrix} = \begin{pmatrix} R_{uu}(\tau) & E_{uv}(\tau)+O_{uv}(\tau) \\ E_{uv}(\tau)-O_{uv}(\tau) & R_{vv}(\tau) \end{pmatrix}.$$

Since

i) trace $(CM_{uv}) = I_1$,

and

ii) $\det\ (CM_{uv}) = -I_2^2 + I_3$,

then $\text{trace}\ (CM_{uv}(\tau))$ and $\det\ (CM_{uv}(\tau))$ are conserved under real orthogonal transformation. The reason for three invariants under coordinate rotation rather than merely two is that: (i) the odd part of the correlation matrix is skew symmetric, so the odd part is invariant (I_2), and (ii) the even part is symmetric, so the even part's trace (I_1) and determinant (I_3) are also invariant.

Autospectrum and Crossspectrum. The spectral functions are defined in the usual way. Take

F. T. to be the Fourier transform,

C. F. T. to be the Fourier cosine transform, and

S. F. T. to be the Fourier sine transform,

i) The u-autospectrum is $P_{uu}(\sigma) = \text{C. F. T.}[R_{uu}(\tau)]$, since $R_{uu}(\tau)$ is an even function,

ii) Similarly, the v-autospectrum is $P_{vv}(\sigma) = \text{C. F. T.}[R_{vv}(\tau)]$, and

iii) The uv-crossspectrum is

$$\tilde{P}_{uv}(\sigma) = P_{uv}(\sigma) + iQ_{uv}(\sigma) = \text{C.F.T.}(E_{uv}(\tau)) + i\text{S.F.T.}(O_{uv}(\tau)),$$

where $P_{uv}(\sigma)$ is the uv-cospectrum, and $Q_{uv}(\sigma)$ is the uv-quadrature spectrum. The basic forms for the covariance functions in the primed coordinates are Fourier transformed directly to obtain

$$P_{u'u'} = P_{uu} \cos^2(\theta) + P_{vv} \sin^2(\theta) + P_{uv} \sin(2\theta),$$

$$P_{v'v'} = P_{uu} \sin^2(\theta) + P_{vv} \cos^2(\theta) - P_{uv} \sin(2\theta),$$

$$Q_{u'v'} = Q_{uv},$$

and

$$P_{u'v'} = P_{uv} \cos(2\theta) + \frac{1}{2}[P_{vv} - P_{uu}] \sin(2\theta),$$

where the frequency argument, σ, has been suppressed for convenience. The above relations provide three spectral invariants analogous to those for the covariance functions of the preceding section:

i) $J_1 = P_{uu} + P_{vv}$, which is proportional to the total horizontal kinetic energy, whose time average is conserved,

ii) $J_2 = Q_{uv}$, which is proportional to frequency times the angular momentum, and which is constant for a particle undergoing elliptical motion,

and

iii) $J_3 = P_{uu}P_{vv} - P_{uv}^2$, which is related to the eccentricity of the hodograph.

A spectral matrix can be formed:

$$SM_{uv} = \begin{pmatrix} P_{uu} & \tilde{P}_{uv} \\ \tilde{P}_{vu} & P_{vv} \end{pmatrix} = \begin{pmatrix} P_{uu} & P_{uv}+iQ_{uv} \\ P_{uv}-iQ_{uv} & P_{vv} \end{pmatrix},$$

where

i) $\text{trace}(SM_{uv}) = J_1$ and

ii) $\Delta_{uv} = \det(SM_{uv}) = -J_2^2 + J_3$.

Since SM_{uv} is Hermitian, the alternative analysis by Hermitian operator and matrix theory is convenient.

Maximization of the Coherence Squared and Cospectrum. The spectral coherence squared is:

$$\gamma^2_{uv} = \frac{P^2_{uv} + Q^2_{uv}}{P_{uu} P_{vv}} .$$

The spectral invariants are used to re-render the form for γ^2_{uv}: since

$$-P^2_{uv} - Q^2_{uv} + \gamma^2_{uv} P_{uu} P_{vv} = 0$$

and

$$P^2_{uv} + Q^2_{uv} - P_{uu} P_{vv} = -\Delta_{uv},$$

then

$$\gamma^2_{uv} = 1 - \frac{\Delta_{uv}}{P_{uu} P_{vv}} .$$

The objective is to find the angle of rotation, θ_o, which maximizes $\gamma^2_{u'v'}(\sigma;\theta)$. Since $\Delta \geq 0$, because $|\tilde{P}_{u'v'}|^2 \leq P_{u'u'} P_{v'v'}$ by the C-B-S inequality,[33] and since Δ_{uv} is invariant under coordinate rotation, θ_o also corresponds to $[P_{u'u'} P_{v'v'}]$ maximum. Define H to be

---

[33] The C-B-S inequality is the Cauchy-Bounakowski-Schwarz inequality, viz. $\left(\int uvds\right)^2 \leq \left(\int u^2 ds\right) \cdot \left(\int v^2 ds\right)$ in integral form.

$$H(\theta) = P_{u'u'}P_{v'v'} = \{\frac{1}{4}[P_{uu}+P_{vv}]^2 - P_{uv}^2\} \sin^2(2\theta) + P_{uu}P_{vv}\cos^2(2\theta)$$
$$+ P_{uv}[P_{vv}-P_{uu}] \sin(2\theta)\cos(2\theta).$$

Maximizing $H(\theta)$ with respect to θ while σ is held fixed, then

$$\theta_o = \frac{1}{2}\tan^{-1}[\frac{P_{vv}-P_{uu}}{2P_{uv}}].$$

Again, $2\theta_o$ is chosen to be the root which occurs in either the first or fourth quadrant. It follows that

$$\text{Max}(\gamma_{uv}^2) = \gamma_{u'v'}^2(\theta_o) = \frac{P_{uv}^2 + \frac{1}{4}[P_{vv}-P_{uu}]^2 + Q_{uv}^2}{\frac{1}{4}[P_{uu}+P_{vv}]^2}.$$

It is noted that:

i) If $P_{vv} = P_{uu}$, no rotation is required for maximization and $P_{u'v'} = P_{uv}\cos(2\theta)$,

ii) The C-B-S inequality can be used to verify that

$$\gamma_{uv}^2 \leq \gamma_{u'v'}^2(\theta_o) \quad \text{and} \quad P_{uv} \leq P_{u'v'}(\theta_o),$$

iii) The maximum cospectrum is an invariant

$$\text{Max}(P_{uv}) = P_{u'v'}(\theta_o) = [P_{uv}^2 + \frac{1}{4}(P_{vv}-P_{uu})^2]^{1/2}$$
$$= [P_{uv}^2 - P_{uu}P_{vv} + \frac{1}{4}(P_{uu}+P_{vv})^2]^{1/2}$$
$$= [-J_3 + \frac{1}{4}J_1^2]^{1/2},$$

iv) The component energy spectra in the semi-principal axis coordinates are

$$P_{u'u'} = P_{v'v'} = \frac{P_{uu}+P_{vv}}{2} = \frac{J_1}{2},$$

v) From iii) and iv), $\text{Max}(\gamma^2_{uv})$ can be expressed in terms of the invariants

$$\text{Max}(\gamma^2_{uv}) = \frac{[-J_3+(J_1/2)^2]+J_2^2}{(J_1/2)^2}, \quad \text{or}$$

$$\text{Max}(\gamma^2_{uv}) = \frac{(\text{Reynolds stress spectrum})^2 + (\sigma \text{ x angular momentum spectrum})^2}{(\text{kinetic energy spectrum})^2},$$

and

vi) The phase, ϕ, of the cross spectrum in the primed coordinates is:

$$\phi_{u'v'}(\theta_o) = \tan^{-1}\left[\frac{Q_{u'v'}}{P_{u'v'}}\right]$$

$$= \tan^{-1}\left[\frac{\sigma \text{ x angular momentum spectrum}}{\text{Reynolds stress spectrum}}\right].$$

Reynolds Stress. Using the form established for the maximum Reynolds stress, $\overline{u'v'}_{max}$, it follows that:

$$(\overline{u'v'}_{max})^2 = \overline{uv}^2 + \frac{1}{4}(\overline{v^2}-\overline{u^2})^2,$$

or

$$\overline{u^2v^2} + (\overline{u'v'}_{max})^2 = \overline{uv}^2 + \frac{1}{4}(\overline{v^2}+\overline{u^2})^2,$$

but

$$\overline{uv}^2 \leq \overline{u^2 v^2}$$

by the C-B-S inequality; therefore

$$0 \leq \overline{u'v'}_{max} \leq \frac{\overline{v^2}+\overline{u^2}}{2},$$

i.e., the maximum Reynolds stress is less than or equal to the total kinetic energy.

Cospectrum. In a similar manner, for the cospectrum, or Reynolds stress as a function of frequency, it follows that

$$0 \leq \max_{\theta} P_{u'v'} \leq \frac{P_{uu}+P_{vv}}{2}.$$

Since

$$\int_0^\infty P_{uu} d\sigma = \overline{u^2} \quad \text{and} \quad \int_0^\infty P_{vv} d\sigma = \overline{v^2},$$

then

$$0 \leq \int_0^\infty \max_{\theta} P_{u'v'} d\sigma \leq \frac{\overline{u^2}+\overline{v^2}}{2}.$$

Also, since

$$\int_0^\infty P_{u'v'}(\theta) d\sigma = \overline{u'v'(\theta)}$$

then

$$\max_{\theta} (u'v'(\theta)) = \max_{\theta} \int_0^\infty P_{u'v'}(\theta) d\sigma \leq \int_0^\infty \max_{\theta} P_{u'v'} d\sigma.$$

Finally,

$$\max_{\theta} \overline{u'v'} \leq \int_0^{\infty} \max_{\theta} P_{u'v'} d\sigma \leq \frac{\overline{u^2}+\overline{v^2}}{2} .$$

Thus, the integral of the maximum value of the cospectrum is bounded below by the value of the maximum Reynolds stress and above by the value of the kinetic energy. This result suggests that the proper technique for integrating the Reynolds stress spectrum should be sought.

Vector Reynolds Stress Spectrum. Since $P_{u'v'}$ is the magnitude of the Reynolds stress as a function of frequency oriented along $2\theta'$, then it is useful to define the Reynolds stress spectrum to be the vector[34] $(P_{u'v'}, 2\theta')$, in polar coordinates. The integral of the cospectrum is used in momentum flux calculations when the frequency-dependent contribution of spectral bands to the Reynolds stress is sought. To perform the integration, the concept of the vector Reynolds stress spectrum is essential.

Since $P_{u'v'} = P_{uv} \cos(2\theta') + \frac{1}{2}[P_{vv}-P_{uu}] \sin(2\theta')$, the following geometric relation is recognized:

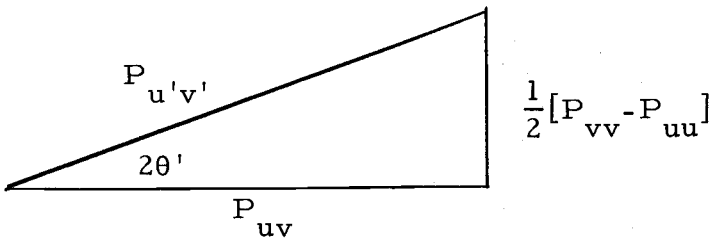

[34] Dr. Stephen G. Pond, Department of Oceanography, Oregon State University, suggested treating the cospectrum as the vector Reynolds stress spectrum.

Then $\vec{P}_{u'v'} = (P_{uv}, \frac{1}{2}[P_{vv}-P_{uu}])$ in Cartesian coordinates. The vector sum of $\vec{P}_{u'v'}$ over all frequencies is

$$\int_0^\infty \vec{P}_{u'v'} d\sigma = \left(\int_0^\infty P_{uv} d\sigma, \int_0^\infty \frac{[P_{vv}-P_{uu}]d\sigma}{2} \right)$$

$$= \left(\overline{uv}, \frac{[\overline{v^2}-\overline{u^2}]}{2} \right) ,$$

in Cartesian coordinates. In polar coordinates,

$$\int_0^\infty \vec{P}_{u'v'} d\sigma = (\max \overline{u'v'}, 2\bar{\theta})$$

When band-averaging a Reynolds stress spectrum over the interval $\sigma_1 \leq \sigma \leq \sigma_2$, the correct formula is then

$$(P_{uv})_{ave} = \left(\sum_{\sigma=\sigma_1}^{\sigma_2} P_{uv}, \sum_{\sigma=\sigma_1}^{\sigma_2} \frac{(P_{vv}-P_{uu})}{2} \right) .$$

The contribution, $\Delta\overline{uv}$, to the maximum Reynolds stress produced by the Reynolds stress spectrum in the frequency interval $\sigma_1 \leq \sigma \leq \sigma_2$ is calculated by projecting $P_{u'v'}$ onto $2\bar{\theta}$ and integrating over the interval:

$$\Delta\overline{uv} = \int_{\sigma_1}^{\sigma_2} P_{u'v'} \cos\,(2(\theta'-\bar{\theta}))d\sigma$$

$$= \cos\,(2\bar{\theta}) \int_{\sigma_1}^{\sigma_2} P_{u'v'} \cos\,(2\theta')d\sigma + \sin\,(2\bar{\theta}) \int_{\sigma_1}^{\sigma_2} P_{u'v'} \sin\,(2\theta')d\sigma$$

$$= \cos\,(2\bar{\theta}) \int_{\sigma_1}^{\sigma_2} P_{uv} d\sigma + \sin\,(2\bar{\theta}) \int_{\sigma_1}^{\sigma_2} \frac{[P_{vv}-P_{uu}]d\sigma}{2}$$

$$= \frac{\overline{uv} \int_{\sigma_1}^{\sigma_2} P_{uv} d\sigma + \frac{[\overline{v^2}-\overline{u^2}]}{2} \int_{\sigma_1}^{\sigma_2} \frac{[P_{vv}-P_{uu}]d\sigma}{2}}{[(\overline{uv})^2 + \frac{(\overline{v^2}-\overline{u^2})^2}{4}]^{1/2}} .$$

B. The Geography of the Hodograph and Negative Frequencies

To clarify the discussion of Section A, and to prepare for the discussion of Section C, an examination of the geography of the hodograph is made with simple models.

The hodographs considered here involve the total energy of the motion, i. e., both the coherent and incoherent components, based on the energy spectra. In tidal analysis, the usual procedure is to examine hodographs (tidal ellipses) constructed from only the coherent component of the motion through least squares calculations.

At this stage, formulae are available to find the transformation

of velocity components from the measurement coordinate frame to the semi-principal axis coordinate frame.

There is another coordinate frame of special interest; it is the set of axes coincident with the major and minor axes of the hodograph. In this coordinate frame,

$$u'' = (A+C)\cos(\sigma t).$$

and

$$v'' = (A-C)\sin(\sigma t),$$

where A and C are amplitude factors. A and C can assume any non-negative, finite value. The eccentricity, ϵ, is $\epsilon = A/C$ or C/A, whichever is less than one. Since, in the semi-principal axis coordinate system,

$$P_{u'u'} = P_{v'v'} = \frac{P_{u''u''} + P_{v''v''}}{2}$$

$$= \frac{1}{2}(A^2+C^2),$$

the radius, R_o, of the hodograph along the semi-principal axes is $R_o = (A^2+C^2)^{1/2}$. By inspection,

$A = C$ gives rectilinear motion along the x"-axis,

$A = -C$ gives rectilinear motion along the y"-axis,

$C = 0$ gives anticlockwise circular motion,

$A = 0$ gives clockwise circular motion,

and

$A > C$ gives anticlockwise elliptical motion,

while

$C > A$ gives clockwise elliptical motion.

Thus, A is the amplitude of the anticlockwise component of the motion, while C is the amplitude of the clockwise component. The characterizing property of the ellipse-axes coordinate system is that $P_{u"v"} = 0$. The rotation from the (u, v) to the $(u", v")$ velocity components through the angle θ_1 is then given by

$$\theta_1 = \frac{-1}{2} \tan^{-1}\left[\frac{2P_{uv}}{P_{vv} - P_{uu}}\right],$$

or

$$\theta_1 = \theta_o \pm \frac{\pi}{4}.$$

The component energy spectra in the ellipse-axes coordinate system are of special significance:

$$P_{u"u"} = \frac{P_{uu}+P_{vv}}{2} - \cos(2\theta_1)\frac{[P_{vv}-P_{uu}]}{2} + P_{uv}\sin(2\theta_1)$$

$$= \frac{P_{uu}+P_{vv}}{2} - \sin(2\theta_o)\frac{[P_{vv}-P_{uu}]}{2} - P_{uv}\cos(2\theta_o)$$

$$= \frac{P_{uu}+P_{vv}}{2} \pm \max P_{uv}$$

and, similarly,

$$P_{v''v''} = \frac{P_{uu}+P_{vv}}{2} \mp \max P_{uv},$$

which demonstrates that the Reynolds stress spectrum is related to the eccentricity of the hodograph. It is recognized that $P_{u''u''}$ and $P_{v''v''}$ are the eigenvalues of the real (or, even) part of the spectral matrix, thus they represent the squares of the lengths of the ellipse semi-axes, as they must.

There is an efficient means for solving for the amplitude and eccentricity of the hodograph from the spectral values:

since

$$P_{u''u''} = \frac{(A+C)^2}{2}$$

and

$$P_{v''v''} = \frac{(A-C)^2}{2},$$

then

$$A \pm C = \sqrt{P_{uu}+P_{vv} + 2 \max P_{uv}} = G$$

and

$$A \mp C = \sqrt{P_{uu}+P_{vv} - 2 \max P_{uv}} = H,$$

thus

$$\epsilon = \frac{G-H}{G+H}.$$

Several properties of the hodograph can be deduced from the preceding formulae and model:

i) $J_1 = P_{uu} + P_{vv} = A^2 + C^2$,

ii) $J_2 = Q_{uv} = \frac{1}{2}(A^2 - C^2)$,

($Q_{uv} = 0$ for $\epsilon = 1$, i.e., for rectilinear motion)

iii) $J_3 = P_{uu}P_{vv} (= (P_{uv})^2 = \frac{1}{4}(A+C)^2(A-C)^2 = (J_2)^2$, in the case of a single sinusoid), and

iv) $\max P_{uv} = [P_{uv}^2 + \frac{1}{4}(P_{vv} - P_{uu})^2]^{1/2}$

$= AC$, thus

$P_{uv} = 0$ for $\epsilon = 0$, i.e., for circular motion.

An Example Hodograph. The geography of the hodograph is illustrated in Figure 42a for the following model. In the measurement coordinates, take

$$u = C \cos \sigma t + D \sin \sigma t$$

and

$$v = E \cos \sigma t + F \sin \sigma t;$$

then

$$P_{uu} = \frac{1}{2}(C^2 + D^2)$$

$$P_{vv} = \frac{1}{2}(E^2 + F^2)$$

$$P_{uv} = \frac{1}{2}(CE + DF)$$

and

$$Q_{uv} = \frac{1}{2}(CF - DE).$$

For a quantitative example, take

$$C = \sqrt{3}, \qquad D = 1/2, \qquad E = -1, \qquad F = \sqrt{3/2}\ ;$$

then

$$P_{uu} = 3/2 + 1/8 = 13/8,$$

$$P_{vv} = 1/2 + 3/8 = 7/8\ ,$$

$$P_{uv} = -\frac{\sqrt{3}}{2} + \frac{\sqrt{3}}{8} = -3\sqrt{3/8}\ ,$$

$$Q_{uv} = 3/4 + 1/4 = 1\ ,$$

$$P_{u'u'} = P_{v'v'} = \frac{P_{uu}+P_{vv}}{2} = 5/4,$$

$$P_{u'v'} = [P_{uv}^2 + \frac{(P_{vv}-P_{uu})^2}{4}\ ]^{1/2} = [\frac{27}{64} + \frac{9}{64}]^{1/2} = 3/4,$$

$$\theta_0 = \frac{1}{2}\tan^{-1}\ (\frac{P_{vv}-P_{uu}}{2P_{uv}}) = \frac{1}{2}\tan^{-1}\ (\frac{1}{\sqrt{3}}) = 15^\circ\ ,$$

and

$$\theta_1 = -30^\circ.$$

Since

$$G = (5/2 + 3/2)^{1/2} = 2$$

and

$$H = (5/2 - 3/2)^{1/2} = 1,$$

then

$$\epsilon = \frac{1}{3}, \qquad A = \frac{G+H}{2} = \frac{3}{2}\ , \qquad C = \pm\ (\frac{G-H}{2}) = \pm\ \frac{1}{2}\ .$$

Choose $C = +\frac{1}{2}$, then

$$u'' = (A+C)\cos(\sigma t) = 2\cos(\sigma t)$$

and

$$v'' = (A-C) \sin(\sigma t)$$

$$= 1 \sin(\sigma t).$$

The Concept of Negative Frequencies. In the coordinates of the ellipse-axes, since

$$u = (A+C) \cos(\sigma t)$$

and

$$v = (A-C) \sin(\sigma t),$$

then

$$u = u^{+} + u^{-} = A \cos(+\sigma t) + C \cos(-\sigma t)$$

and

$$v = v^{+} + v^{-} = A \sin(+\sigma t) + C \sin(-\sigma t).$$

Thus, the hodograph can be conceived to consist of two counter-rotating velocity vectors:

i) An anticlockwise motion with amplitude A and frequency $+\sigma$, and

ii) A clockwise motion with amplitude C and frequency $-\sigma$.

The complex-valued velocity vector, w, is defined to be $w = u + iv$. It is clear that the autospectrum for w^{+} is $P^{+}_{ww} = A^2$ and that for w^{-} it is $P^{-}_{ww} = C^2$. Thus, there is physical meaning for spectra with negative as well as positive frequencies. The total autospectrum for w is

$$P_{ww} = P^{+}_{ww} + P^{-}_{ww} = A^2 + C^2 = P_{uu} + P_{vv}.$$

It also follows that

$$P^{+}_{ww} - P^{-}_{ww} = (A^2 - C^2) = 2Q_{uv}.$$

Thus, P^{+}_{ww} and P^{-}_{ww} are invariant under coordinate rotation.

The two counter-rotating vectors corresponding to the hodograph of Figure 42a are shown in Figure 42b.

C. Spectral Quantities for Pairs of Complex-Valued Time Series

For the study of the coherency of a pair of two-dimensional velocity vectors, in addition to the component-wise coherence and phase matrices, there is a quantity which measures the overall coherency of two velocity vectors. In essence, the coherency of a pair of horizontal hodographs is considered. Each horizontal velocity vector series is written as a complex-valued series with real argument, t, i.e., $w(t) = u(t) + iv(t)$. The material of this section was derived in a search for a technique which would provide quantitative results which were invariant under coordinate rotation.

Autovariance and Autospectrum Functions. The autovariance function for w is defined as, Jenkins and Watt (1968)

$$R_{ww}(\tau) = \overline{w(t)w^*(t+\tau)}^{t},$$

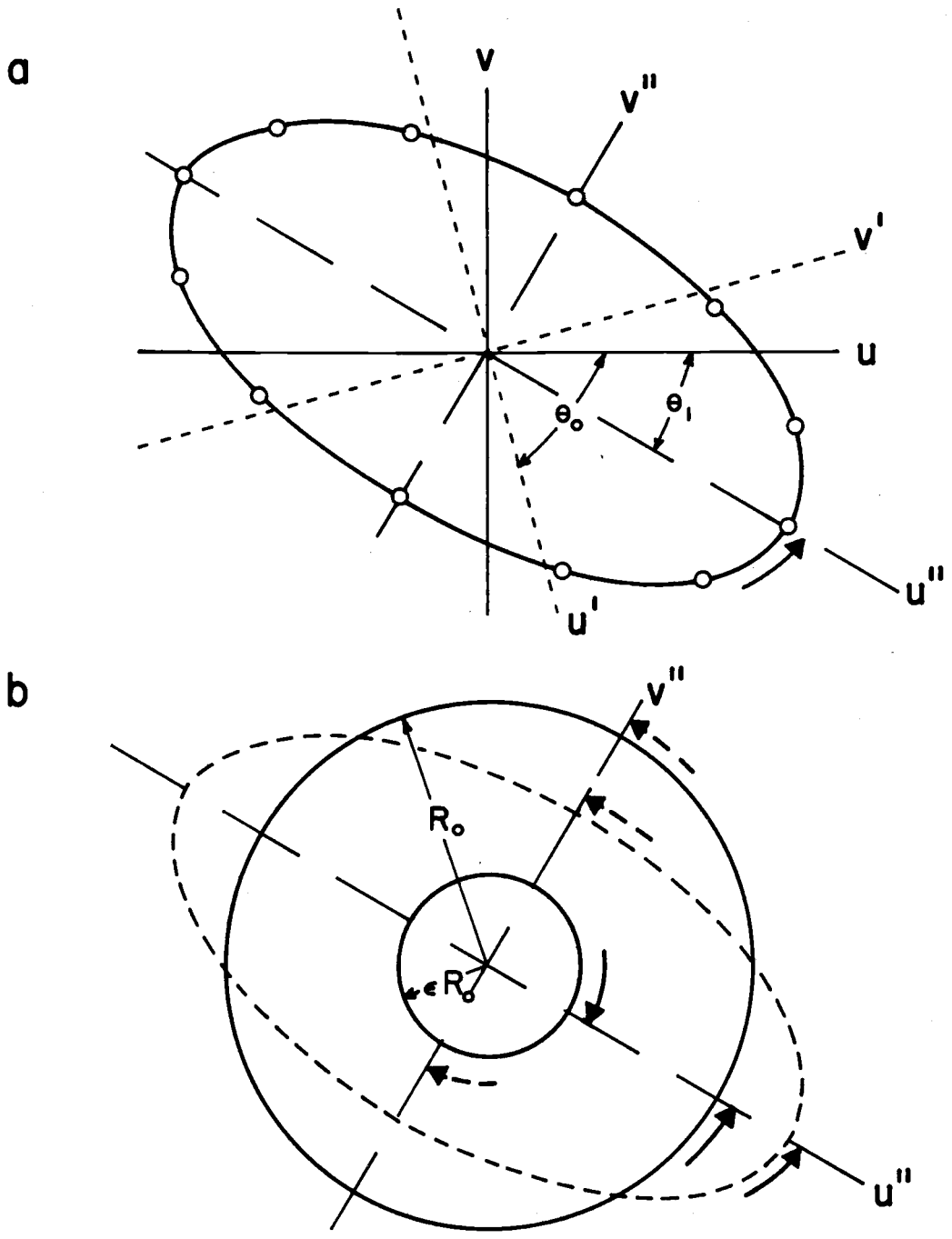

Figure 42. The geography of the hodograph.
a. The hodograph ((u, v): geographic coordinates; (u', v'): semi-principal axes coordinates; (u", v"): ellipse-axes coordinates)
b. Decomposition of the hodograph into clockwise and anticlockwise components

where $(\ )^*$ is the conjugate operator; in coordinate form,

$$R_{ww}(\tau) = [R_{uu}(\tau)+R_{vv}(\tau)] + i[R_{vu}(\tau)-R_{uv}(\tau)],$$

$$= [R_{uu}(\tau)+R_{vv}(\tau)] - i2O_{uv}(\tau),$$

which is invariant under coordinate rotation by Section A. Then the autospectrum is

$$P_{ww}(\sigma) = F.T.(R_{ww}(\tau))$$

$$= [P_{uu}(\sigma)+P_{vv}(\sigma)] + 2Q_{uv}(\sigma),$$

which is also invariant. $P_{ww}(\sigma)$ is not an energy spectrum in the usual physical sense because it is two-sided; i.e., it is neither odd nor even as a function of frequency. The variance of w does equal

$$\int_{-\infty}^{\infty} P_{ww}(\sigma)d\sigma .$$

Covariance and Cross Spectrum Functions. The covariance function for w_1 and w_2 is defined as

$$R_{w_1w_2}(\tau) = \overline{w_1(t)w_2^*(t+\tau)}$$

$$= [R_{u_1u_2}(\tau)+R_{v_1v_2}(\tau)] + i[R_{v_1u_2}(\tau)-R_{u_1v_2}(\tau)].$$

When w_1 and w_2 undergo a coordinate transformation to w_1'

and w_2' by a rotation through an angle of θ_1 and θ_2, respectively, it follows that

$$R_{w_1'w_2'}(\tau) = R_{w_1w_2}(\tau)e^{i(\theta_2-\theta_1)}.$$

Thus, the absolute value of the covariance function is invariant. The cross spectrum is

$$\tilde{P}_{w_1w_2}(\sigma) = F.T.(R_{w_1w_2}(\tau)) = P_{w_1w_2}(\sigma) + iQ_{w_1w_2}(\sigma),$$

where the cospectrum is

$$P_{w_1w_2}(\sigma) = [P_{u_1u_2}(\sigma)+P_{v_1v_2}(\sigma)] - [Q_{v_1u_2}(\sigma)-Q_{u_1v_2}(\sigma)]$$

and the quadrature spectrum is

$$Q_{w_1w_2}(\sigma) = [Q_{u_1u_2}(\sigma)+Q_{v_1v_2}(\sigma)] + [P_{v_1u_2}(\sigma)-P_{u_1v_2}(\sigma)].$$

The absolute value of the cross spectrum is invariant under coordinate rotation from the above. The forms of $P_{w_1w_2}(\sigma)$ and $Q_{w_1w_2}(\sigma)$ contain terms accounting for the component-wise coupling of the two velocity vectors; these terms are the elements of the component-wise cross spectral matrix.

Coherence Squared and Phase Functions. The coherence

squared, γ^2, and phase, ϕ, are defined in the usual way, dropping the frequency argument, σ, for convenience:

$$\gamma^2_{w_1w_2} = \frac{|\tilde{P}_{w_1w_2}|^2}{P_{w_1w_1} P_{w_2w_2}}$$

$$= \frac{[P_{u_1u_2} + P_{v_1v_2} + Q_{u_1v_2} - Q_{v_1u_2}]^2 + [Q_{u_1u_2} + Q_{v_1v_2} + P_{v_1u_2} - P_{u_1v_2}]^2}{[P_{u_1u_1} + P_{v_1v_1} + 2Q_{u_1v_1}][P_{u_2u_2} + P_{v_2v_2} + 2Q_{u_2v_2}]}$$

and

$$\phi_{w_1w_2} = \tan^{-1}\left[\frac{Q_{w_1w_2}}{P_{w_1w_2}}\right]$$

$$= \tan^{-1}\left(\frac{[Q_{u_1u_2} + Q_{v_1v_2} + P_{v_1u_2} - P_{u_1v_2}]}{[P_{u_1u_2} + P_{v_1v_2} + Q_{u_1v_2} - Q_{v_1u_2}]}\right).$$

By the preceding remarks, γ^2 is invariant under coordinate rotation and $\phi'_{w'_1w'_2} = \phi_{w_1w_2} + (\theta_2 - \theta_1)$.

It remains to prove that $\gamma^2_{w_1w_2}$ is bounded above by 1.0. The most instructive way to do this is to use a model for w_1 and w_2 composed of a sum of sinusoids in each hypothetical measurement bandwidth. Form w_1 and w_2 from a set of sinusoids:

$$u_1 = A_1 \cos(\sigma t) + B_1 \sin(\sigma t),$$

$$v_1 = C_1 \cos(\sigma t) + D_1 \sin(\sigma t),$$

$$u_2 = A_2 \cos(\sigma t) + B_2 \sin(\sigma t),$$

and

$$v_2 = C_2 \cos(\sigma t) + D_2 \sin(\sigma t),$$

thus

$$w_1 = \sum_k [(A_1^{(k)} \cos(\sigma_k t) + B_1^{(k)} \sin(\sigma_k t)) + i(C_1^{(k)} \cos(\sigma_k t) + D_1^{(k)} \sin(\sigma_k t))],$$

and similarly for w_2, where k is summed over the number of frequencies in a measurement bandwidth. Dropping the superscript k for convenience, it is straightforward to show that

$$P_{w_i w_j} = \frac{1}{2} \sum_k [(A_i + D_i)(A_j + D_j) + (B_i - C_i)(B_j - C_j)]$$

and

$$Q_{w_i w_j} = \frac{1}{2} \sum_k [(A_i + D_i)(B_j - C_j) - (A_j + D_j)(B_i - C_i)].$$

Now take

$$\vec{I}(k) = [(A_i + D_i),\ (B_i - C_i)]$$

and

$$\vec{J}(k) = [(A_j + D_j),\ (B_j - C_j)],$$

thus

$$P_{w_i w_j} = \frac{1}{2} [\sum_k \vec{I} \cdot \vec{J}] = \frac{1}{2} \sum_k |\vec{I}|\,|\vec{J}| \cos\phi$$

and

$$Q_{w_i w_j} = \frac{1}{2} [\sum_k \vec{I} \times \vec{J}] = \frac{1}{2} \sum_k |\vec{I}|\,|\vec{J}| \sin\phi,$$

where ϕ is the angle between $\vec{I}(k)$ and $\vec{J}(k)$.

With use of the C-B-S inequality in summation form, it follows that

$$|\tilde{P}_{w_i w_j}|^2 = \frac{1}{4}\{[\Sigma_k |\vec{I}||\vec{J}| \cos\phi]^2 + [\Sigma_k |\vec{I}||\vec{J}| \sin\phi]^2\}$$

$$\leq \frac{1}{4}\{[\Sigma_k |\vec{I}|^2(\Sigma_k |\vec{J}|^2 \cos^2\phi + \Sigma_k |\vec{J}|^2 \sin^2\phi)\}$$

$$= \frac{1}{4}\Sigma_k |\vec{I}|^2 \Sigma_k |\vec{J}|^2$$

$$= P_{w_i w_i}(\sigma) P_{w_j w_j}(\sigma).$$

Therefore,

$$\gamma^2_{w_i w_j}(\sigma) \leq 1.0;$$

the equality holds only when $\vec{I} = \vec{J}$ for all k or when there is only one sinusoid in a measurement band. γ^2 and ϕ for complex-valued series obey the same statistics as they do for real series. The equations for the cospectrum and quadrature spectrum are in the proper form for use in band-averaging a set of Fourier coefficients.

Since $P_{ww} = \frac{1}{2}\Sigma_k [(A+D)^2 + (B-C)^2]$, then $P_{ww} = 0$ if and only if $A^{(k)} = -D^{(k)}$ and $B^{(k)} = C^{(k)}$ for all k. Thus, when the denominator of γ^2 vanishes, the numerator also vanishes.

Degenerate Cases. If one series is complex, e.g., velocity, and a second real, e.g., temperature, set $w_1 = w = u + iv$ and $w_2 = s$. Then

$$P_{w_1 w_2} = P_{ws} = P_{us} - Q_{vs}$$

and

$$Q_{w_1 w_2} = Q_{ws} = Q_{us} + P_{vs},$$

thus

$$\gamma^2_{ws} = \frac{[P_{us}-Q_{vs}]^2+[Q_{us}+P_{vs}]^2}{P_{ss}[P_{uu}+P_{vv}+2Q_{uv}]}$$

and

$$Q_{ws} = \tan^{-1}\left(\frac{Q_{us}+P_{vs}}{P_{us}-Q_{vs}}\right).$$

If both series are real, i.e., v_1 and $v_2 = 0$, then the above formulae reduce to the ordinary forms in the cross spectrum analysis of real-valued series.

The Complex Spectrum of a Pair of Hodographs. As seen in Section B, the hodograph can be reduced to components with positive and negative frequencies. The spectrum of the hodograph, Section B, for positive and negative frequencies is recognized as the spectrum of a complex-valued series as discussed above. The detailed steps are illustrated for a pair of hodographs. Take $u_1 = (A_1+C_1)\cos(\sigma t+\theta_1)$ and $v_1 = (A_1-C_1)\sin(\sigma t+\theta_1)$, then

$$w_1 = u_1 + iv_1 = [A_1 e^{i(\sigma t+\theta_1)} + C_1 e^{-i(\sigma t+\theta_1)}]$$

and an analogous form is used for w_2. Thus,

$$R_{w_1w_1}(\tau) = A_1^2 e^{-i\sigma\tau} + C_1^2 e^{+i\sigma\tau},$$

$$R_{w_2w_2}(\tau) = A_2^2 e^{-i\sigma\tau} + C_2^2 e^{i\sigma\tau},$$

and

$$R_{w_1w_2}(\tau) = A_1A_2 e^{-i(\sigma\tau-(\theta_1-\theta_2))} + C_1C_2 e^{i(\sigma\tau-(\theta_1-\theta_2))}.$$

Then

$$P_{w_1w_1}(\sigma_o) = A_1^2\delta(\sigma-\sigma_o) + C_1^2\delta(\sigma+\sigma_o),$$

$$P_{w_2w_2}(\sigma_o) = A_2^2\delta(\sigma-\sigma_o) + C_2^2\delta(\sigma+\sigma_o),$$

and

$$\tilde{P}_{w_1w_2}(\sigma_o) = A_1A_2\delta(\sigma-\sigma_o)e^{i(\theta_1-\theta_2)} + C_1C_2\delta(\sigma+\sigma_o)e^{-i(\theta_1-\theta_2)},$$

thus

$$\left|\tilde{P}_{w_1w_2}(\sigma_o)\right|^2 = A_1^2A_2^2\delta(\sigma-\sigma_o) + C_1^2C_2^2\delta(\sigma+\sigma_o),$$

where $\delta(\ )$ is a Dirac delta function.

For a sum of sinusoids in a measurement band, the coherence squared is then

$$\gamma^2_{w_1w_2} = \begin{cases} \dfrac{(\Sigma A_1A_2)^2}{\Sigma(A_1)^2\Sigma(A_2)^2}, & \sigma \geq 0 \\ \dfrac{(\Sigma C_1C_2)^2}{\Sigma(C_1)^2\Sigma(C_2)^2}, & \sigma \leq 0 \end{cases}.$$

Thus, there is a value of $\gamma^2_{w_1w_2}$ defined for the anticlockwise

($\sigma \geq 0$) portion of w_1 and w_2 and a value for the clockwise, ($\sigma \leq 0$) portion. Several special cases exist for the spectrum of the hodograph:

i) $A = C$, $P_{ww}(-\sigma) = P_{ww}(\sigma)$, rectilinear motion,

ii) $C = 0$, $P_{ww}(-\sigma) = 0$, pure anticlockwise motion,

iii) $A = 0$, $P_{ww}(\sigma) = 0$, pure clockwise motion.

In general, $P_{ww}(-\sigma) < P_{ww}(\sigma)$ for net anticlockwise motion and vice versa for net clockwise motion.

APPENDIX IV

Two Analogues of the Free Surface Boundary Value Problem for Inertial-Internal Waves

Since the free surface boundary value problem, viz.

i) GE: $\psi_{xx} - R^2\psi_{zz} = 0$, where $R^2 = \left(\frac{\sigma^2 - f^2}{N^2 - \sigma^2}\right)$,

ii) RBC: ψ = constant = 0 at $z = -H$, and

iii) FBC: $\psi_{xx} + \gamma\psi_z = 0$ at $z = 0$, where $\gamma = \left(\frac{\sigma^2 - f^2}{g}\right)$,

is rather unfamiliar, it is useful to examine a mechanical analogue. As noted by Tikhonov and Samarskii (1963, p. 44), the boundary value problem for the angular rotation of a rod undergoing small amplitude torsional vibrations, θ, with a fixed end $(x = \ell)$ and a pulley on the other end $(x = 0)$, is formulated as:

iv) $\theta_{tt} - a^2\theta_{xx} = 0$, where $a^2 = \frac{GJ}{k}$, $[0 \leq x \leq \ell;\ 0 < t < \infty]$,

k is Young's modulus,

G is the shear modulus, and

J is the moment of inertia,

v) $\theta = 0$ at $x = \ell$, and

vi) $\theta_{tt} + b^2\theta_x = 0$ at $x = 0$,

where

$$t \sim x, \quad x \sim z, \quad a^2 \sim R^2$$

and

$$b^2 \sim \gamma$$

in the inertial-internal wave problem.

The behavior of ψ in x is similar to that of θ in time, t. The effect of motion of a free surface on inertial-internal waves is similar to that of a torque applied by a pulley, situated at the end of a rod, on torsional vibrations of a rod. (If SOV applies, the FBC becomes:

$$\psi - \frac{(\sigma^2 - f^2)}{gk^2} \psi_z = 0,$$

where k is the horizontal wave number. Then an analogy can be made to a vibrating spring with an elastic attachment at $x = 0 \sim z = 0$ in the inertial-internal wave problem.) To model the variable density structure of the ocean, a rod of variable a^2, i.e., density, diameter, etc. would be appropriate. To model propagation of inertial-internal waves into shallow water, shortening the rod from the fixed end as a function of time would be appropriate.

A close analogy can be made to the problem of the motion of an infinite string with a mass in the center which has been given an initial velocity, Tikhonov and Samarskii (1963, p. 81). For the inertial-internal wave problem, consider a periodic point source perturbing the free surface at $x = 0$. The domain is an infinite half-plane ($-\infty < x < \infty$, $-\infty < z \leq 0$), since the only conditions that can be

applied in this case are at the free surface and the origin.

The formulation of the problem is:

i) and iii) as before, plus

vii) $\psi = 0$ at $x = 0,\ z = 0,$

viii) $\psi_x = w_o$ at $x = 0,\ z = 0,$ and

ix) $\psi \underset{|x|\to\infty}{\to}$ constant along $z = 0.$

Since the GE has general solutions of the form $f(z+ax)$ and $g(z-ax)$, the FBC is used to find the permissible forms of f and g. For example, since

$$f''(\zeta) + (\frac{b}{a})^2 f(\zeta) = 0, \quad (\zeta = z+ax),$$

then

$$f(\zeta) = C_1 e^{-(\frac{b}{a})^2 \zeta} + C_2$$

and g has the same form. The condition vii) implies that $C_2 = -C_1$; the condition viii) implies that $-C_1(\frac{b}{a})^2 a = w_o$ or $C_1 = -\frac{a}{b^2} w_o$. If g is written as

$$g(\eta) = C_3 e^{-(\frac{b}{a})^2 \eta} + C_4, \quad (\eta = z-ax),$$

then $C_3 = \frac{a}{b^2} w_o$ and $C_4 = -C_3$. Thus,

$$\psi = \begin{cases} \frac{a}{b^2} w_o\left[1 - e^{-\left(\frac{b}{a}\right)^2 (z+ax)}\right], & D_1 = \{(z+ax) > 0;\ (x > 0,\ z < 0)\}, \\ -\frac{a}{b^2} w_o\left[1 - e^{-\left(\frac{b}{a}\right)^2 (z-ax)}\right], & D_2 = \{(z-ax) > 0;\ (x < 0,\ z < 0)\}, \\ 0, & D_3 = \{\text{otherwise}\}, \end{cases}$$

where condition ix) is satisfied by inspection.

The streamlines are characteristics. The free surface and body motion decay exponentially away from the origin and away from the characteristics through the origin, respectively. Since this is a linear theory, a general, harmonic surface perturbation can be decomposed into such motions. Of course this problem is idealized, but it illustrates the influence of a harmonically perturbed free surface on a stratified medium, without regard for the effect of finite depth.

APPENDIX V

Derivation of the Governing Equation for Inertial-Internal Waves With the Frontal Interaction and Without the Boussinesq Approximation

The Boussinesq approximation was made in deriving the GE for inertial-internal waves with the frontal interaction in Chapter II. Since horizontal density gradients are significant in the case of frontal interaction, and since the basis of the Boussinesq approximation is the neglect of horizontal variations of density in the momentum equations, a rigorous derivation of the GE must not make the Boussinesq approximation (Healey and Le Blond, 1969).

The zero-order equations are those for geostrophic equilibrium in the alongshore component of flow and hydrostatic equilibrium:

$$-\rho_1 f \bar{v} = -\bar{p}_x \tag{1}$$

and

$$0 = -\bar{p}_z - \rho_1 g, \tag{2}$$

where $\rho_1 = \rho_o + \bar{\rho}$ and ρ_o and $\bar{\rho}$ are defined as in Chapter II.

The only first-order term neglected in the derivation of the GE in Chapter II is one involving $\rho f \bar{v}$, where ρ is the perturbation density, in the x-component EOM. Hence, the system of equations is

(3) $$\rho_1(u_t - fv) - \rho f\bar{v} = -p_x,$$

(4) $$\rho_1(v_t + fu + u\bar{v}_x + w\bar{v}_z) = 0,$$

(5) $$\rho_1 w_t = -p_z - g\rho,$$

(6) $$u_x + w_z = 0,$$

and

(7) $$\rho_t + u(\rho_1)_x + w(\rho_1)_z = 0.$$

The ρ, v, and p variables are eliminated from (3) through (7) by cross-differentiation and subtraction and the stream function is introduced into the resulting equation to yield:

(8) $$(N^2 - \sigma^2)\psi_{xx} - 2M^2\psi_{xz} - (\sigma^2 - f(f+\bar{v}_x))\psi_{zz}$$

$$+ \left[f\bar{v}\frac{M^2}{g}\psi_{zz} + \frac{N^2}{g}(\sigma^2 - f^2)\psi_z + \frac{M^2}{g}\sigma^2\psi_x\right] = 0,$$

where the terms inside [ ] are neglected in the GE used in this dissertation.

To assess the significance of the neglected terms, the following nondimensionalization is used:[35]

[35] The nondimensionalization used here differs slightly from that used by Healey and Le Blond (1969). Their horizontal scale for the perturbation flow was the same as their vertical scale. They also introduced the slope of the sea surface into the analysis for $\bar{v}$ and a separate horizontal scale for the mean flow. Their conclusions are identical to those made in this appendix. They took z to be positive downwards which accounts for the sign differences between their work and the author's work.

i) $\dfrac{(\rho_1)_z}{\rho_1} = -a, \quad (a \sim 10^{-7} \text{ c. g. s.})$

ii) $\dfrac{(\rho_1)_x}{\rho_1} = b, \quad (b \sim 10^{-10} \text{ c. g. s.})$

iii) $\Omega = \dfrac{\sigma}{N}$,

iv) $(\ )_x = \dfrac{1}{L}(\ )_{x'}$,

v) $(\ )_z = \dfrac{1}{H}(\ )_{z'}$,

vi) $\psi = \psi_o \psi'$

vii) $f\bar{v} = v'gbH$,

where H is the scale depth, L is the scale length, and ψ_o is a scale stream function.

Dropping the primes, (8) becomes

$$(9) \qquad \epsilon_3^2(1-\Omega^2)\psi_{xx} + 2\epsilon_2\epsilon_3\psi_{xz} - (\Omega^2 - \frac{f^2}{N^2} - v_x\epsilon_2\epsilon_3)\psi_{zz}$$

$$+ \epsilon_1[-v\epsilon_2^2\psi_{zz} + (\Omega^2 - \frac{f^2}{N^2})\psi_z - \epsilon_2\epsilon_3\Omega^2\psi_x] = 0,$$

where

$$\epsilon_1 = aH(= \frac{N^2H}{g}) \sim 10^{-3},$$

$$\epsilon_2 = \frac{b}{a}\ (=s) \sim 10^{-3},$$

and

$$\epsilon_3 = \frac{H}{L} \sim 10^{-2}$$

for the continental shelf region and low frequency inertial-internal waves.

Because $\Omega \sim \epsilon_3$ for the low frequency inertial-internal waves, i. e., for $\sigma \sim f$, then (9) is identical to the GE derived in Chapter II to $O(\epsilon_1)$. The neglect of the terms with the factor ϵ_1 is identical to making the Boussinesq approximation. Therefore, the GE derived in this dissertation neglects effects which are only the order of 10^{-3} compared to those included.